Towards high-chi block copolymers at the industry scale : routes for a possible integration as a new nanostructuring technology

Sophie Böhme

Communauté
UNIVERSITÉ Grenoble Alpes

THÈSE

Pour obtenir le grade de

DOCTEUR DE LA COMMUNAUTE UNIVERSITE GRENOBLE ALPES

Spécialité : **Nanoélectronique et Nanotechnologies**

Arrêté ministériel : 7 août 2006

Présentée par

Sophie Böhme

Thèse dirigée par **Jumana Boussey**

préparée au sein du **LTM (CNRS / UJF-Grenoble 1 / CEA)**
dans **l'École Doctorale EEATS**

Towards High-χ Block Copolymers at the Industry Scale – Routes for a Possible Integration as a New Nanostructuring Technology

Vers les copolymères à blocs à forte incompatibilité dans l'industrie – des voies pour l'intégration en tant que nouvelle technologie de nanostructuration

Thèse soutenue publiquement **le 19 octobre 2016**,
devant le jury composé de :

Jérôme Plain
Professeur de l'Université de Technologie de Troyes, Président
Christophe Sinturel
Professeur de l'Université d'Orléans, Rapporteur
Olivier Soppera
Directeur de recherche, CNRS, IS2M, Mulhouse, Rapporteur
Karim Aissou
Chargé de recherche, CNRS, LCPO, Bordeaux, Examinateur
Jumana Boussey
Directrice de recherche CNRS, LTM, Grenoble, Directrice de thèse
Marc Zelsmann
Chargé de recherche, CNRS, LTM, Grenoble, Co-encadrant de thèse
Raluca Tiron
Ingénieure de recherche CEA-Leti, Grenoble, Co-encadrante de thèse

Acknowledgements

First of all I would like to thank Olivier Joubert, director of the LTM, for giving me the opportunity to work at the LTM and the LabeX Minos directory for financing this thesis.

Furthermore, I would like to thank my Ph.D director Jumana Boussey for her support, encouragement and advice. I would also like to express my sincere gratitude to my advisor Marc Zelsmann for the continuous support of my Ph.D study and research, for his patience, motivation, and immense knowledge. His guidance helped me in all the time of research and writing of this thesis while giving me the freedom to explore my own ideas.

I would also like to thank the members of the thesis examination committee, Prof. Christophe Sinturel and Dr. Olivier Soppera for taking the time to referee the thesis, and Prof. Jérôme Plain (chairman of the committee) and Dr. Karim Aissou who agreed to be part of the jury.

I want also to express my gratitude to Raluca Tiron for her insightful comments, her help and encouragement.

A large thanks to all the colleagues at LTM that helped me with various problems regarding plasma etching, STEM or AFM imaging and everything else: Camille, Gilles, JH, Kevin, Laurent, Nathalie, Odile, Philippe, Seb. Great thanks goes also to Céline, Malou, Stéphanie and Sylvaine for all their help in bureaucracy, financial or other issues.

Further I want to thank everybody in the “copo”-team for sharing our passion (or was it?) for BCPs, the advice, support and the enriching discussions: Antoine, Cécile, Javier and Jérôme G.

Not to forget the colleagues that became friends during my time at the LTM and, without whom that time wouldn’t have been as much fun as it was. The long evenings that we spent “chez Emile” are unforgettable and I will definitely miss them: Anthony, Benoît, Jérôme D., Manu, Maxime, Michel, Nico, Olivier, Thibault and Tiphaine.

Last but not least I would like to thank Julien, without whom none of this would have happened, who always knew how to motivate and push me forward and my close friends and family who always believed in me and supported me, no matter what.

Abstract

The increasing cost and complexity of processes needed to keep up with the ever increasing demand for more powerful processors in the IC industry, lead to smaller and smaller feature sizes. Photolithography, once the workhorse for nanostructuration, reaches now its physical limits in terms of resolution. Other, alternative methods have thus to be found in order to continue producing more efficient integrated circuits, while keeping the production costs at a reasonable level. The combination of conventional photolithography and directed self-assembly of block copolymers (BCP) seems to be one promising alternative. Block copolymers have the unique property to phase separate at the nanometer scale driven by the chemical incompatibility (described by the Flory-Huggins interaction parameter χ) of the blocks. This way, when brought onto a substrate, structures like spheres, cylinders or lamellar can be obtained and used as etching masks for nanostructuration. Probably the most used BCP is Polystyrene-b-Polymethylmethacrylate (PS-b-PMMA), which has been studied for over 20 years. PS-b-PMMA is a so called "low- χ" BCP and can reach feature sizes not smaller than ~12 nm. The higher the incompatibility of the blocks (i.e. the higher the χ-value), the smaller the obtainable feature size. This thesis deals primarily with "high-χ" Polystyrene-b-Polydimethylsiloxane (PS-b-PDMS) block copolymers and evaluates its possible integration into IC industry. Processes are developed and optimized in view of their future application in industry. A common annealing method for "high-χ" block copolymers is solvent vapor annealing (SVA), where the BCP layer is exposed to solvent vapors. Solvent molecules swell then the BCP layer, increasing the mobility of polymer chains and allowing long range ordering of the features. Although this method is widely used, it has never been reported on large scale production lines, for example on 300 mm wafers. The SVA is a very complex process that is sensitive to the environment and uses often toxic solvents. During this thesis, mechanisms of solvent vapor annealing are studied and safe solvents that are compatible with industrial environment are studied. Furthermore, alternative solutions for annealing "high-χ" BCPs without solvents are proposed. Blending the BCP with plasticizer molecules, for example, leads to rapid self-assembly with thermal annealing and the feasibility of this process was shown on 300 mm wafers.

Pattern transfer etching is a problematic step in IC nanostructuring. The smaller the features, the higher the aspect ratio, the more challenging the etching process. Different plasma etching procedures, all typically used in industrial gate etching processes, are studied on PS-b-PDMS. Challenging silicon features of down to 10 nm and aspect ratios of up to 6:1 are obtained.

Finally, a simple spin-coating process of metal-oxide inclusion on widespread PS-b-PMMA is introduced in which etch selectivity of the BCP is highly increased. PS-b-PMMA has the advantage of being studied by numerous research groups and the understanding of the BCP is very advanced. However, its etching quality for pattern transfer is very poor as to the poor etch selectivity between PS and PMMA. Complicated

multiple-step etching processes, where wet etching and dry etching are alternated, have to be performed in order to transfer the pattern satisfactorily. By introducing metal salts selectively in one of the blocks, the etch contrast is considerably enhanced and the pattern transfer can be obtained in one single step of dry etching.

Résumé

La complexité et le coût croissant des processus nécessaires pour fabriquer les processeurs de plus en plus puissants de l'industrie microélectronique conduit à des structures de plus en plus petites. La photolithographie, technologie clé pour la nanostructuration, atteint aujourd'hui ses limites en termes de résolution. Des méthodes alternatives doivent donc être trouvées afin de continuer à produire des transistors plus efficaces, tout en gardant les coûts de production à un niveau raisonnable. La combinaison de la photolithographie classique et de l'auto-assemblage de copolymères à blocs (CPB) semble être une alternative prometteuse. Les copolymères à blocs ont la propriété de créer une séparation de phases à l'échelle du nanomètre grâce à l'incompatibilité chimique (décrite par le paramètre d'interaction χ) des blocs. De cette façon, lorsque cette séparation de phase est formée à la surface d'un substrat, des structures telles que des sphères, des cylindres ou des lamelles peuvent être obtenues et utilisées comme masques de gravure pour la nanostructuration. Le CPB le plus utilisé est probablement le Polystyrène-Polyméthacrylate de méthyle (PS-PMMA), qui a été étudié pendant plus de 20 ans. Le PS-PMMA est un CPB de faible χ et ne peut pas atteindre des tailles de structure inférieures à 12nm. Plus l'incompatibilité des blocs (c'est-à-dire le χ) est importante, plus la taille des structures possibles est petite. Cette thèse traite principalement le système Polystyrène-Polydiméthylsiloxane (PS-PDMS), un CPB de haute valeur de χ, et évalue son éventuelle intégration dans l'industrie de la microélectronique. Des procédés ont été développés et optimisés en vue de leur utilisation future dans l'industrie. Un procédé de recuit commun pour les "high-χ" est le recuit sous vapeur de solvant (RVS), où la couche de CPB est exposée aux vapeurs de solvants. Les molécules de solvant gonflent le CPB et augmentent ainsi la mobilité des chaînes de polymère, permettant l'organisation des structures à grande échelle. Bien que ce procédé soit largement utilisé, il n'a jamais été utilisé sur des lignes de production à grande échelle. Le RVS est un processus très complexe qui est sensible à l'environnement et utilise souvent des solvants toxiques. Au cours de cette thèse, des mécanismes de RVS sont étudiés et des solvants non-toxiques qui sont compatibles avec l'environnement industriel sont proposés comme alternative. Une autre solution pour le recuit de CPBs "high-χ" sans solvant est également proposée. En formulant la solution de CPB avec des molécules de plastifiant, un auto-assemblage rapide avec un simple recuit thermique est possible. La faisabilité de ce processus a été démontrée sur des tranches de silicium de 300mm de diamètre.

Le transfert des motifs par gravure est une étape importante et problématique en nanofabrication. Plus les tailles sont réduites, plus le facteur d'aspect est haut et le processus de gravure difficile. Des procédés de gravure par plasma différents, tous utilisés dans des procédés de gravure industriels, sont étudiés sur le matériau PS-PDMS. Des nanostructures de silicium de 10nm de large et des structures avec un rapport d'aspect de 6:1 ont été gravées avec succès.

Enfin, un processus d'inclusion d'oxydes métalliques par simple dépôt par centrifugation a été démontré sur le polymère PS-PMMA. Ce BCP a l'avantage d'être un système bien connu grâce aux nombreux groupes de recherche qui s'y intéresse. Cependant, ses performances en gravure pour le transfert des motifs est peu satisfaisant à cause de la faible sélectivité entre les blocs PS et PMMA. Des procédés de gravure compliqués en plusieurs étapes doivent être effectués afin de transférer les motifs de manière satisfaisante. En introduisant des sels métalliques de manière sélective dans l'un des blocs, le contraste de gravure est considérablement augmenté et le transfert du motif peut être obtenu en une seule étape de gravure plasma.

Table of Contents

Table of Abbreviations

AFM	Atomic force microscopy
ALD	Atomic layer deposition
BCC	Body centered cubic
BCP	Block copolymer
CD	Critical dimension
CDU	Critical dimension uniformity
CW	Continuous wave
D_h	Hydrodynamic diameter
DIS	Disordered
DLS	Dynamic light scattering
DOA	Diisooctyl adipate
DOA42	SD42+DOA
DOA45	SD45+DOA
DOS	Dioctylsebacate
DOS42	SD42+DOS
DOS45	SD45+DOS
DPS	Decoupled plasma source
DSA	Directed self-assembly
ESRF	European synchrotron radiation facility
EtOH	Ethanol
EUV	Extreme ultraviolet
FFT	Fast Fourier transform
FIB	Focused ion beam
finFET	Fin field-effect transistor
GISAXS	Grazing incident small angle X-ray scattering
GYR	Gyroidal
HEX	Hexagonal
HPL	Hexagonally perforated lamellar
HSP	Hansen solubility parameter
IC	Integrated circuit
ICP	Inductively coupled plasma
ITRS	International technology roadmap for semiconductors
L_0	Natural period of BCP
LAM	Lamellar
LER	Line edge roughness
LTM	Laboratoire de technologies de la microélectronique
LWR	Line width roughness
MH	Maltoheptaose
N	Degree of polymerization
NIL	Nanoimprint lithography
ODT	Order-disorder transition

P2VP	Poly-2-vinylpyridine
P4VP	Poly-4-vinylpyridine
PB	Polybutadiene
PDMS	Polydimethylsiloxane
PEO	Polyethylene oxide
PFS	Polyferrocenyldimethylsilane
PGMEA	Propylene glycol methyl ether acetate
PI	Polyisoprene
PLA	Polylactid
PMMA	Poly(methyl methacrylate)
PS	Polystyrene
PtBS	Poly-4-ter-butylstyrene
PTMSS	Poly(para-trimethyl silystyrene)
RF	Radio frequency
RT	Room temperature
SCFT	Self-consistent mean field theory
SD16	PS-b-PDMS: M_w=16kg/mol, L_0=20nm
SD42	PS-b-PDMS: M_w=42kg/mol, L_0=33nm
SD45	PS-b-PDMS: M_w=45kg/mol, L_0=35nm
SEM	Scanning electron microscopy
SiArc	Silicon antireflective coating
SIS	Sequential infiltration synthesis
SOC	Spin-on-carbon
SOI	Silicon on insulator
SSL	Strong segregation limit
STEM	Scanning transmission electron microscopy
SVA	Solvent vapor annealing
TA	Thermal annealing
T_g	Glass transition temperature
TGA	Thermogravimetric analysis
VUV	Vacuum ultra violet
WSL	Weak segregation limit
XPS	X-ray photoelectron spectroscopy
χ	Flory-Huggins interaction parameter
χN	Strength of segregation

Chapter 1 Introduction

1.1 Photolithography

1.1.1 The Beginning of Integrated Circuit Production

In the last decades, many efforts have been made in terms of miniaturization, cost, speed, power consumption and versatility concerning the silicon based integrated circuits (IC) industry. In 1947 the first microprocessor was commercialized by Intel and possessed about 2300 transistors. 1958 Jack Kilby invented the first integrated circuit at Texas Instruments and by the 1960'ies one chip contained about 50 transistors. Ever since, tremendous progress has been made and today's microprocessors contain up to four billion transistors. To illustrate the evolution of transistor, Figure 1-1 shows a replica of the first transistor and a 300 mm wafer that contains hundreds of millions of transistors.

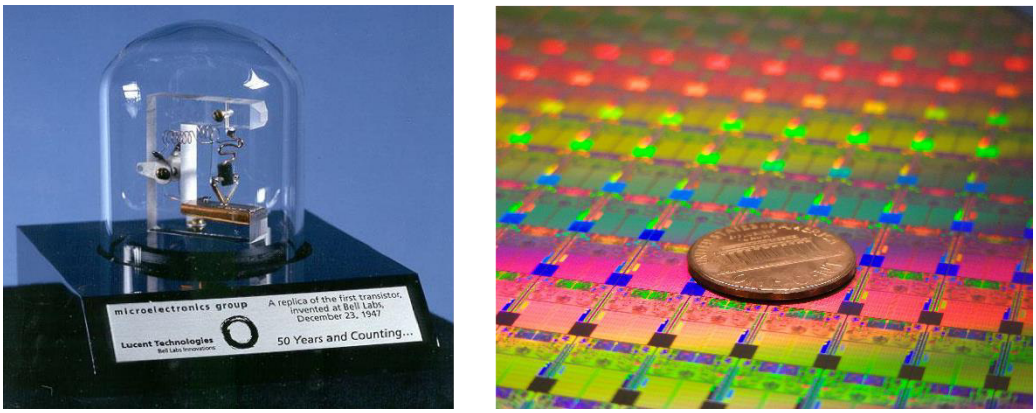

Figure 1-1: Comparison of the first transistor[1] and today's 300 mm wafer containing hundreds of millions of transistors[2]

To build these kinds of processors a series of operations is performed on one piece of silicon, among the process steps are photolithography, etching or deposition. Each of these steps is performed by specialized equipment built by commercial companies. In order for the industry to advance, a roadmap, the so called International Technology Roadmap for Semiconductors (ITRS) was introduced over 20 years ago to anticipate the technological evolution and predict technological needs of the IC industry. With the help of this roadmap, industry was able to double the number of transistors per chip every 2 years, increasing processing power exponentially, while keeping the production cost constant. A schematic of this evolution is depicted in Figure 1-2 and was already predicted by Gordon Moore in 1965: it is known to us today as Moore's law[3]. Today in 2016, the most powerful chips commercially available are at the 14 nm technology node, i.e., the typical half-pitch of a feature is approximately 14 nm. Prior to the 14 nm node was the 22 nm node, introduced in 2012, and next is supposed to be the 10 nm node in 2017.

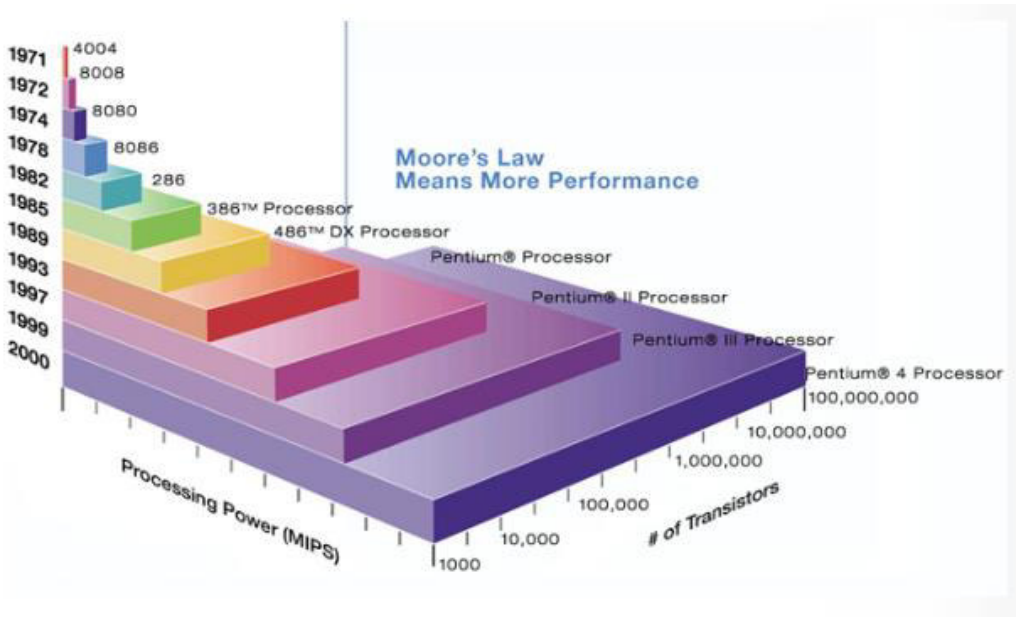

Figure 1-2: Representation of Moore's law [4]

Even though Moore's law has been true for the last 50 years, it seems that technology evolution slows down. Indeed the technological complexity to decrease feature sizes becomes tremendous. The simple and classic photolithography, which was for a long time the microelectronics workhorse, reached its limits at feature sizes of approximately 45 nm due to light diffraction problems. In order to attain the 14 nm node, it was necessary to integrate complex lithography processes, whose prizes grow with decreasing feature size. In order to reduce the cost of nanostructuring, alternative lithography techniques have been introduced in recent years

1.1.2 Conventional Photolithography

Photolithography is a key step in the production of transistors and uses photoresists and light to transfer a geometric pattern from a mask onto a substrate. The parts of the resist that are exposed to light are chemically modified. With a chemical solution, a developer, either the exposed parts (positive resist) or those not exposed to light (negative resist) can be removed, creating an image of the initial pattern at the substrate surface. After developing the resist, the parts free of resist can be processed, while those covered with resist will be protected. That way the pattern can be transferred into the substrate. A schematic of the process is depicted in Figure 1-3

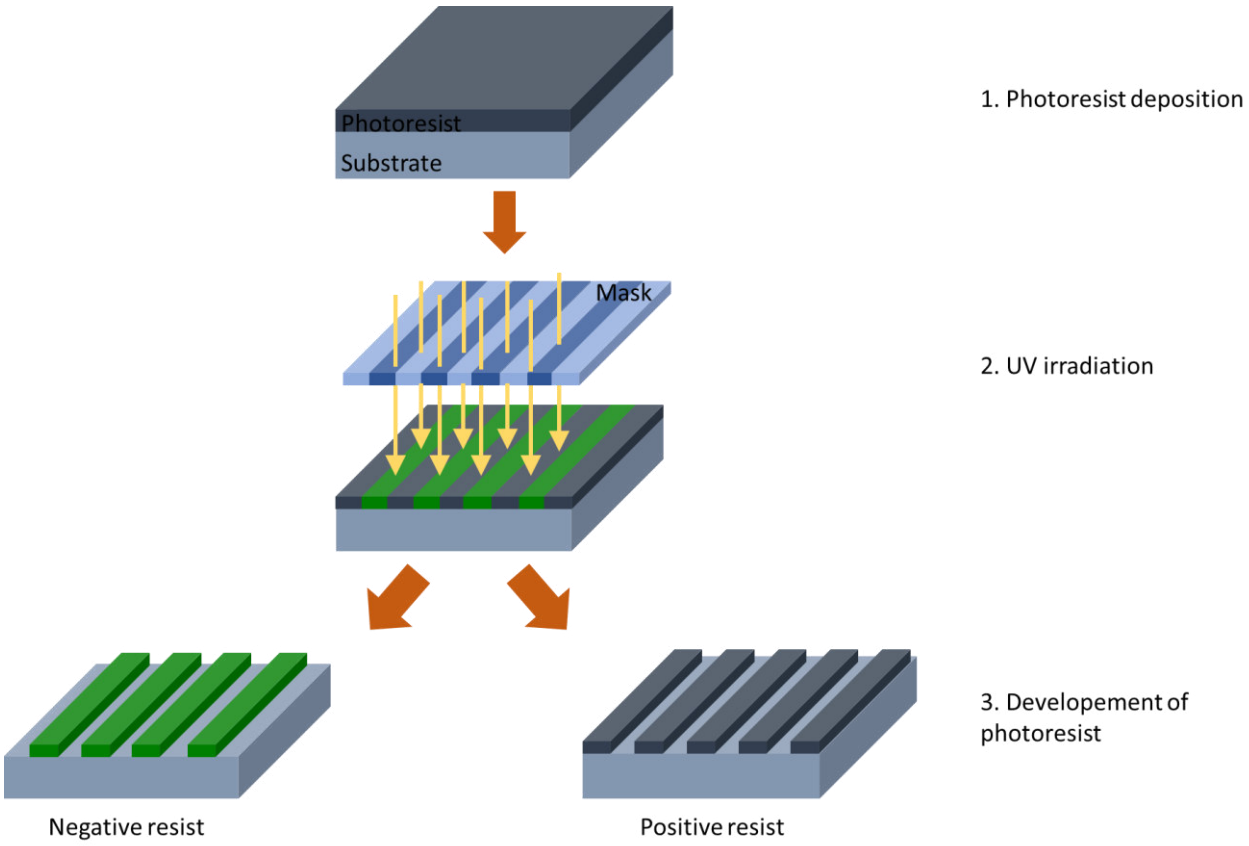

Figure 1-3: Schematic representation of the optical photolithography process

The simplest types of lithography are contact and proximity lithography. In contact mode the mask is in direct contact of the resist, limiting the lifetime of the mask and bringing a risk of contamination into the process. In proximity lithography, the mask is maintained at a certain distance of a few micrometers above the resist, limiting its resolution to the micrometer scale[5]. Further evolution of photolithography led to projection lithography. This technique avoids the direct contact of the mask and wafer, by projecting the pattern onto the photoresist via a refractive optical system, as depicted in Figure 1-4. As can be seen on the schematic, a projection lens is positioned between the photomask and photoresist which allows a demagnification of the pattern of at least 4x in most systems[6]. Projection optical photolithography is today's most used type of nanopatterning.

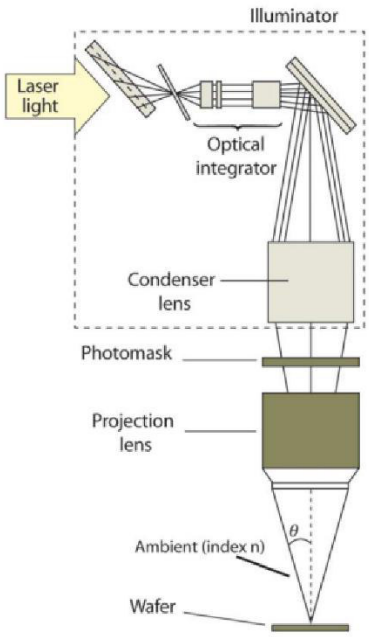

Figure 1-4: Schematic representation of projection lithography[6]

The resolution of the obtained structures depends on the one hand on the material of the resist and on the other hand on the wavelengths that are used. The smaller the wavelength, the higher the possible resolution. Since the beginning of photolithography a great part of the whole photon spectrum was exploited for nanostructuration. In the beginning, when the feature sizes on transistors were as big as a few micrometers, wide spectrum lamp light was used. Since then, light sources used more and more powerful photons, passing by UV-light in the 1980's with a wavelength of 436 nm (G-line) to produce structures of 5 to 6 µm. In the late 1980's lithography moved on to 365 nm (I-line) and produced 1µm features. The next step, to sub-1µm structures was considered challenging but was obtained in the 1990's with deep UV-light at 248 nm and by 1993, 500 nm features were produced commercially. In the 2000's finally, the 193 nm wavelength was introduced which is still today the main photolithography exposure technique in industry[7,8]. The relationship between wavelength and obtainable feature size becomes clear in the Rayleigh equation:

$$\boldsymbol{CD = k_1 \frac{\lambda}{N_A}} \qquad \text{Equation 1-1}$$

Where CD is the critical dimension, λ the wavelength, NA the numerical aperture of the system's lens and k_1 is known as the resolution factor and accounts for all other process variables[9]. Besides using shorter wavelength, only the numerical aperture can be increased or k_1 reduced in order to improve feature sizes. Continuous improvement of the lens systems has helped in the downscaling process of feature size but desired resolutions today are at 20 nm and below, whereas classic dry 193 nm lithography tools attain 90 nm resolution.

1.1.3 193 Immersion Lithography

193 nm immersion lithography (193i) has been introduced in IC manufactory in 2002 in order to attain the 45 nm technology node. In this technique the medium in which lithography takes place is changed from air to a liquid (usually purified water) with a higher refractive index[10]. The introduction of water into the gap between the final lens and wafer changes the optical paths of exposure light, decreasing the effective wavelength of 193 nm to 135 nm. This way the final resolution is improved, enabling the production of 45 nm node circuits.

1.1.4 Extreme Ultraviolet Lithography

Extreme ultraviolet (EUV) lithography uses light with an extreme small wavelength of 11 - 14nm. Most materials, including oxygen and nitrogen, absorb these short wavelengths, which is why EUV lithography machines must operate in vacuum. Also, the optical system, including mask and mirrors, must be coated by materials that are able to reflect the short wavelength light. Mirror materials composed of multilayers of silicon and molybdenum reach reflectivities of 60 - 70% in EUV[11,12]. In order to compensate for the power loss, extreme high power EUV sources are necessary. Due to the high cost and complexity of the system, EUV lithography is not yet used in IC manufacturing.

1.1.5 Double Patterning

Double or multiple patterning lithography has been introduced to bridge the gap between immersion lithography and the delayed readiness of EUV lithography and is now expected to be also used for the upcoming 10 nm node. The principle is based on the sequential exposure with immersion lithography so that a multiplication of feature density can be obtained. The integration of this concept avoids the investment into new equipment and materials, as immersion photolithography is already used in industry. However, due to the increased number of steps (successive lithography and etch), the reduction of the cost of ownership is not evident.

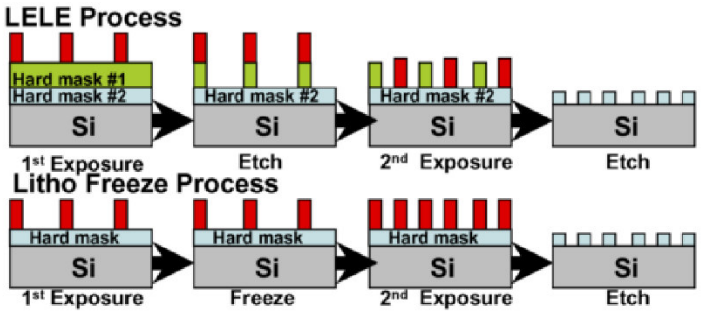

Figure 1-5: Schematic of two double patterning approaches: litho-etch-litho-etch (LELE) and litho freeze process[13]

Numerous variations of this technique exist and one of the first was the litho etch litho etch process. Here two subsequent lithography and etching steps lead to the final density multiplication while in the litho freeze process, only one etching step is required. Here, two different masks are used to obtain two different lithography patterns. By "freezing-in" the first pattern, it is not affected during the second exposure[13]. These two processes are depicted in Figure 1-5. Apart from increased number of process steps, overlay and design issues make the implementation of double patterning for the 10 nm node very challenging[14].

1.2 Alternative Lithography Techniques

1.2.1 Nanoimprint

Nanoimprint lithography was introduced in 1995 in order to propose a cost-effective, high-throughput alternative manufacturing process of nanopatterning in the sub-50 nm scale[15]. This alternative lithography technique uses thickness contrast rather than optical contrast in order to create nanostructures in thin film resists. The basic principle of the method is schematically represented in Figure 1-6. A mold is pressed onto a resist, creating a thickness contrast on the resist. By releasing the mold, a negative image is reproduced to scale. Remaining residues inside the compressed areas can be etched away by reactive ion etching (RIE) and the obtained structures can be transferred to the pattern, similarly to the obtained images in photolithography.

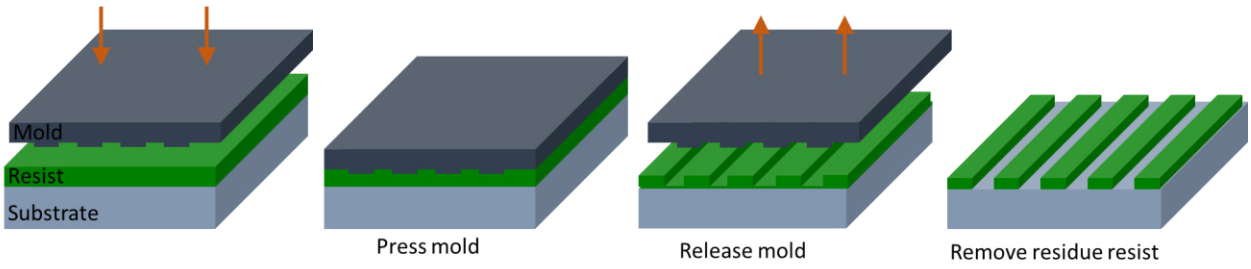

Figure 1-6: Schematic of the nanoimprint lithography process: first, the mold is pressed onto a resist in order to create a thickness contrast, then the mold is removed, and residue resist between features is removed by reactive ion etching

Drawbacks of this technique are the high cost of the master mold when using decreased feature sizes as well as the high defectivity which is not compatible with industry expectations.

1.2.2 Block Copolymer Lithography

Block copolymer (BCP) lithography differs from the other presented nanopatterning methods, as it is a combination of bottom-up and top-down methods. Top-down methods are characterized by the down scaling of bulk materials by lithography and or etching, while bottom-up methods create structures directly at the nanometer scale. In directed self-assembly (DSA) of BCPs, templates created with lithography techniques (top-down method) are used to guide the self-assembly of block copolymers (bottom-up

method). A guiding template is created at a substrate surface with a pitch of tens to hundreds of nanometer. Then the BCP is spin-coated onto the substrate and allowed to phase separate with respect to the guiding patterns. After transfer etching, the resulting structures show a drastic density multiplication of features, having a critical dimension much smaller than the original pattern. The directed self-assembly (DSA) of BCP has been introduced into the ITRS in 2010 to attain resolution of <16nm[16]. Figure 1-7 shows a schematic of such a BCP lithography process.

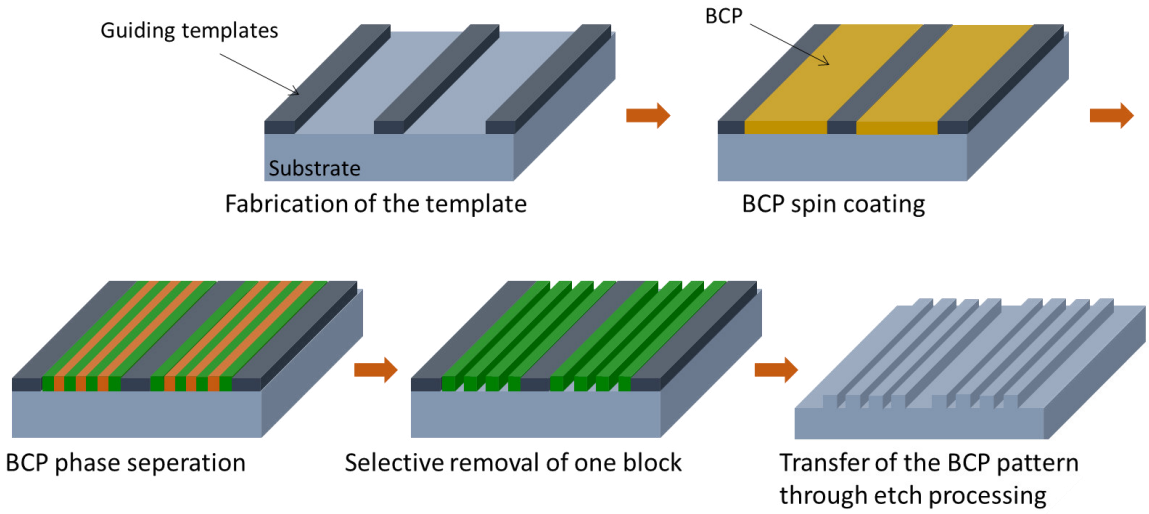

Figure 1-7: Schematic of BCP lithography as a complementary technique to photolithography

Block copolymers are macromolecules, composed of at least two different monomers, separated in different blocks that are linked by a covalent bond. These materials have the unique property to self-assemble into micro and nanodomains, due to non-favorable segment interactions. The domain size and shape is dictated by molecular weight and volume fraction of the blocks. Block copolymer lithography takes advantage of this property and uses shapes like spheres, cylinders or lamellas in the nanoscale dimension in order to propose a cost-effective, high-resolution, high-throughput nanopatterning solution. In the following section an overview of block copolymer phase separation and its use in lithography applications are presented.

1.3 Directed Self-Assembly of Block Copolymers

1.3.1 Thermodynamics of Block Copolymers

The beginning of block copolymer applications was set by the discovery of living-anionic polymerization in 1956, in which anionic polymer chains were grown by the addition of precursors[17,18]. Although, since then, other polymerization techniques have been discovered and complex block copolymers can be synthesized, we will concentrate during this thesis on copolymers consisting of two blocks A and B. For only two blocks, anionic polymerization permits the synthesis of a variety of different architectures as depicted Figure 1-8.

Linear di-, tri- or multiblocks (A-B, A-B-A, $(\text{-A-B-A})_n$) as well as non-linear starblock ($(\text{A-B})_n$) copolymers can be obtained by a composition of only two blocks. We concentrate on the simplest diblock (A-B) copolymer form.

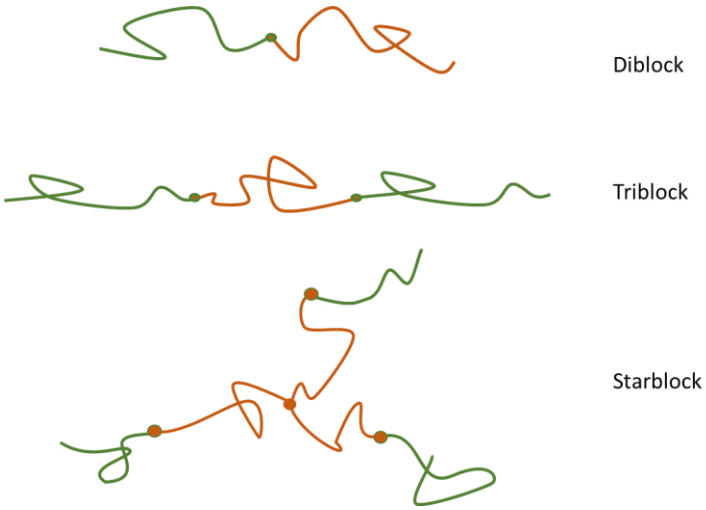

Figure 1-8: Schematic of different architectures obtainable with A-B block copolymers

The phase behavior of block copolymers is governed by an unfavorable mixing of enthalpic and entropic forces and the covalent bond preventing the macroscopic demixing, like it is observed with oil and water for example. Several parameters are important in the microphase separation: the degree of polymerization N (the total number of monomers per chain), the Flory-Huggins interaction parameter between the two blocks χ, and the volume fraction *f* of one block. The χ-parameter describes the incompatibility of the blocks AB and is inversely proportional to temperature. This relationship can be described as follows[19]:

$$\chi_{AB} = \left(\frac{z}{k_B T}\right)\left[\varepsilon_{AB} - \frac{1}{2}(\varepsilon_{AA} + \varepsilon_{BB})\right] \qquad \textbf{Equation 1-2}$$

where k_B is the Boltzman constant, z is the number of nearest neighbours per segment, and ε_{AB}, ε_{AA}, and ε_{BB} are the interaction energies between monomers of A–B, A–A, and B–B, respectively. The χ-parameter is high, when interactions between A and B are strong, for example when ionic charges or hydrogen bondings are present.

The product χN describes the strength of segregation. If either χ or N is small enough, entropic forces dominate and the system is in a disordered state[17]. When χN exceeds a certain value (ODT: order-disorder-transistion), phase separation occurs and the system is ordered. With χN variation as a function of the volume fraction *f*, a phase diagram can be predicted by self-consistent mean field theory (SCFT), depicted in Figure 1-9[20].

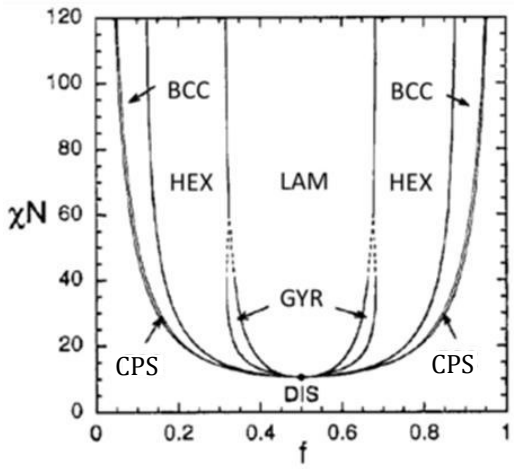

Figure 1-9: Self-consistent mean field theory phase diagram of diblock copolymers[20]. Obtained morphologies are closed-packed spheres (CPS), body centered cubic spheres (BCC), hexagonal cylindrical (HEX), bicontinuous gyroid (GYR) and lamellar (LAM). Below the ODT threshold, the system is disordered (DIS)

In symmetric block copolymers, with f = 0.5, the ODT is at $\chi N \sim 10.5$ in the mean field calculation. When χN is slightly above this value, the system is in the weak segregation limit (WSL), the A-B interactions are then weak and the interfaces are diffuse. The periodic length scales can be described as $L_0 \sim a N^{1/2}$ (a is the statistical segment length)[17]. In the strong segregation limit (SSL), when $\chi N > 100$, interfaces become narrow and microdomains are composed of pure A or B. The interface width becomes proportional to $a\chi^{1/2}$ and the equilibrium domain spacing of microdomains scales as $L_0 \sim a N^{2/3}\chi^{1/6}$ [17]. The system in the SSL region is dominated by the balance between a minimization of the total area of interfaces and the maximization of entropic penalty of extended chain configuration under incompressible conditions[17,21,22].

Given that L_0 is dependent on χ and N, higher values of χ allow lower values for N and thus smaller domain spacing. Taking into account the domain spacing and interfacial width in the SSL regime, Sinturel and coworkers demonstrated a simple calculation in which they showed that for feature sizes ($L_0/2$) of 8 nm a χ of 0,1 at N = 105 would be necessary[23]. Thus, in order to generate sub-10 nm for next generation lithography, high- χ, low-N block copolymers are needed. Furthermore, for lithography applications, it is important to distinguish the segregation regimes, as they describe the sharpness of interfaces from which conclusion of the feature roughness could be drawn[24].

The phase diagram predicts also the shape of the microdomains as a function of the volume fraction f. At a fixed χN value, with growing volume fraction of one block, the system passes from closed-packed spheres (CPS), body centered cubic (BCC) to hexagonal cylindrical (HEX) and bicontinuous gyroid (GYR) to lamellar (LAM) morphology at f = 0.5. This transition is inversely taking place with further increasing f. Figure 1-10 shows a schematic of the morphologies that can be obtained with one diblock copolymer AB with growing volume fraction of block A[25].

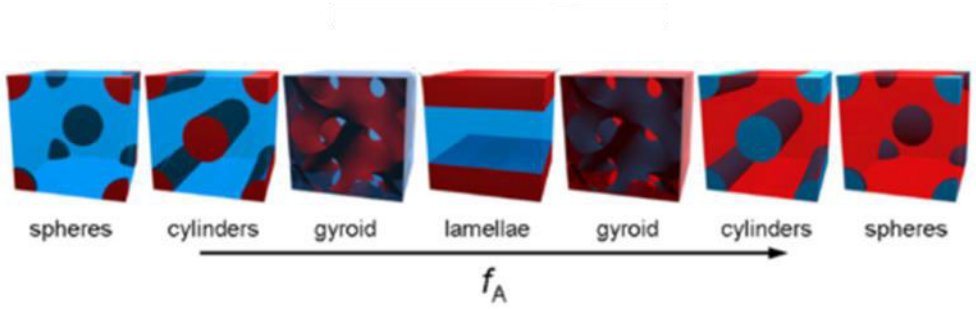

Figure 1-10: Schematic representation of different morphologies of a diblock copolymers depending on the volume fraction of block A[25]

The phase diagram represented in Figure 1-9 was obtained by SCFT calculations. In order to verify the simulated phase diagram, experimental phase diagrams have been developed and show some discrepancies with calculated diagrams. An experimental phase diagram of Polyststyrene-block-Polyisoprene (PS-b-PI) (Figure 1-11) showed for example that the critical ODT point was at $\chi N = 20$ (compared to 10.5 in SCFT diagram)[26]. Moreover, the experimental diagram is not symmetric in terms of volume fraction which is due to monomer volume asymmetry and differences in segment length of PI and PS.

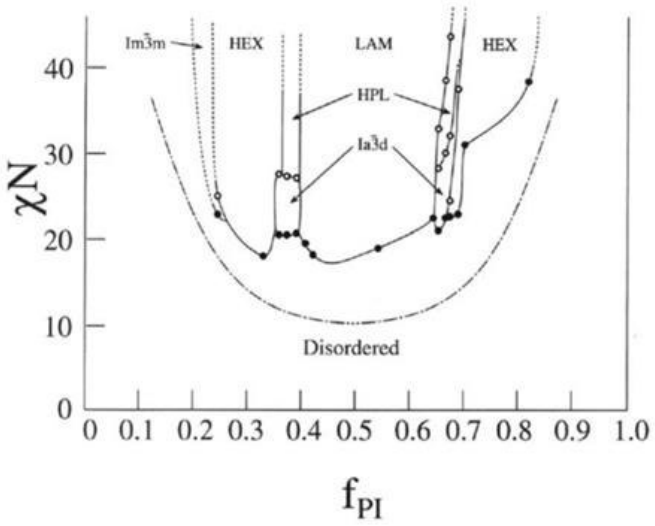

Figure 1-11: Experimental phase diagram of PS-PI[26]. Lm3m and Ia3d are crystallographic space groups

Furthermore, the experimental phase diagram shows an additional morphology, the hexagonally perforated lamellar (HPL) that does not occur in the calculated diagram and is considered as a metastable structure.

1.3.2 Block Copolymer Thin Films

As seen in the previous section, bulk block copolymers can phase separate in different morphologies with different sizes, depending on the structure of each of their blocks with N and *f* and on the interaction of the two blocks with χ. For most lithography applications, however, thin films (< 100 nm) of BCPs are necessary. In thin films, other parameters, like film thickness or surface and interface interactions become important and influence the phase separation and orientation of block copolymers. The total free energy F of a diblock copolymer, AB, in a thin film can be described as the sum of its internal structure F_{bulk} and the interface interactions $F_{surface}$[21]:

$$\boldsymbol{F = F_{bulk+} F_{surface}} \quad \textbf{Equation 1-3}$$

$$\boldsymbol{F_{bulk} = F_{AB} + F_{conformation}} \quad \textbf{Equation 1-4}$$

$$\boldsymbol{F_{surface} = F_{A/sub} + F_{B/sub} + F_{A/air} + F_{B/air}} \quad \textbf{Equation 1-5}$$

Where F_{AB} is the interfacial energy between the blocks A and B, $F_{conformation}$ is the conformation entropy of A and B polymer chains, $F_{A/sub}$ and $F_{B/sub}$ are the interfacial energies of block A and B with the substrate and $F_{A/air}$ and $F_{B/air}$ are the interfacial energies of block A and B with the air[21]. Thin films are usually one or a few times as thick as the natural domain spacing, L_0, of the block copolymer, which is why $F_{surface}$ contributes considerably to the total free energy F. $F_{conformational}$ is influenced by the commensurability between L_0 and the film thickness, t. If t is similar to that of the natural domain spacing of the BCP, thin films are most stable. The conformational entropy increases significantly when the film thickness does not scale as discrete integer or half-integer of L_0, which causes morphology and orientation transitions and or inhomogeneous layer thicknesses[21].

As described above, lithography applications require monolayers of BCP patterns that are transferred into the substrate through etch processing. Hence, the orientation of BCP nanodomains is crucial for their usefulness in lithography. In the next section we will concentrate on the influence of the surface energy $F_{surface}$ on the orientation for the examples of two morphologies, lamellar and cylindrical, which have become the most important morphologies for lithography applications.

1.3.2.a Lamellar Block Copolymers

Lamellar morphology appears when both blocks have equal volume fractions and consist of well-defined stripes of alternating A and B blocks. As described above, the orientation of BCP chains is dictated by the interfacial interactions of the polymer and the substrate and the air. It is known that when, for example block A has lower surface energy than block B, A preferentially wets the substrate and air interfaces[27]. Four different cases of different wetting behaviors can be observed that have influence on the morphology orientation in lamellar BCPs and are illustrated in Figure 1-12. First case, block A shows lower interfacial energy for both surfaces, air and substrate. In this case, both interfaces are wetted symmetrically by block A and the lamellas are oriented horizontally (Figure 1-12a). Furthermore, the film thickness (t) should be

an integer of L_0 ($t = nL_0$), otherwise spatial inhomogeneities in the film thickness can be observed by the formation of terraces with islands or holes. In the second case, block A has lower interfacial energy for only one interface, for example the substrate. This leads to asymmetric wetting were $t = (n-1/2)L_0$, and lamellae are oriented also horizontal (Figure 1-12b). In the third case, block A and B have equal interfacial energies for both substrates. In that case the most stable orientation is perpendicular to the substrate and film thickness commensurabilities do not influence the orientation (Figure 1-12c). Unlimited film thicknesses are here possible. In the fourth case, one surface shows neutral wetting for both blocks and the other preferential wetting for just one of the blocks. In that case it comes to complicated T-shaped structures, were lamellas are oriented perpendicular at the neutral surface and change to horizontal orientation when approaching the preferential interface (Figure 1-12d,e) [21].

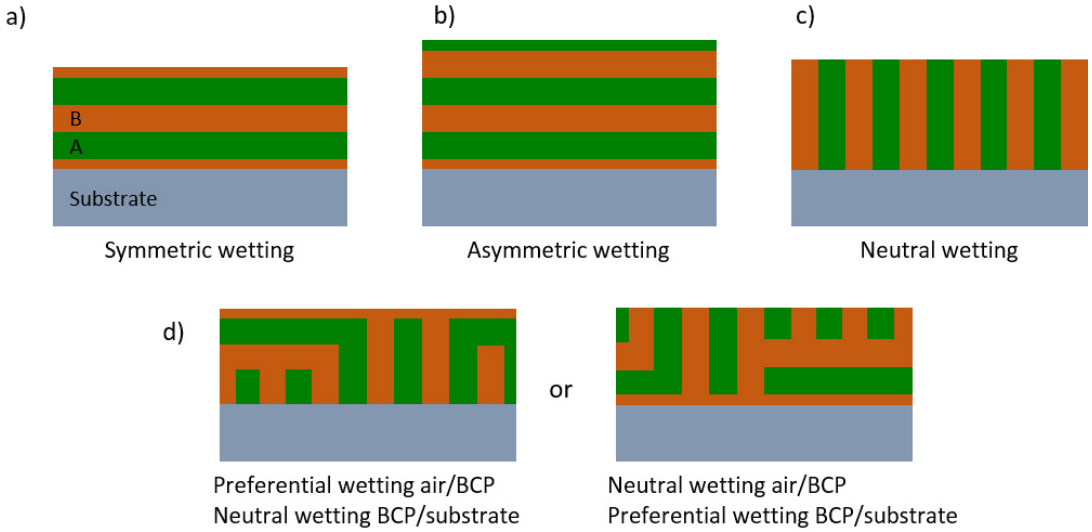

Figure 1-12: Schematic of lamellar AB diblock copolymer with different interfacial wetting. Parallel lamellas under (a) symmetric and (b) asymmetric wetting. Perpendicular lamellas under (c) neutral wetting. (d) Complex structures under mixtures of preferential and neutral wetting[21]

1.3.2.b Hexagonal Arrangements of Cylinders

Cylinder morphology appears in asymmetric BCP, where one block, the minority phase, forms cylinders in the matrix of the other block, the majority phase. Phase behavior in thin films is somewhat more complex for asymmetric morphologies. In contrast to a symmetric lamellar system, not only the orientation but also the shape of the microdomains is influenced in confined thin films. When both interfaces present a preferential wetting of the minority part block, the formation of continuous or structured wetting layers at the interfaces has been observed[28–31]. The shape of these wetting layers seems to depend mostly on the layer thickness and on the strength of the surface energy. For Polystyrene-b-Polydimethylsiloxane (PS-b-PDMS) BCPs, for example, it was shown that the PDMS block always wets the BCP/air interface, due to its

lower surface tension compared to PS[32–35]. Moreover, when monolayers are coated on bare Si substrates, an additional, discontinuous PDMS wetting layer is formed at the interface with the substrate[36,37].

Hybrid structures, a combination of basic structures like parallel cylinders, perpendicular cylinders, perforated lamellar or wetting layers were observed when the film–interface interactions are dissimaler at the two interfaces[30]. Neck forming cylinders, for example, which is a combination of parallel and perpendicular cylinders was observed[38]. Also, perforated lamellas, where one of the block is in a lamellar structure, whereas the other is cylindrical, has been observed for asymmetric BCPs[20].

Depending on the layer thickness, cylinder orientations can be perpendicular or parallel, similar to lamellar BCP behavior[30]. Terrace formation with different layer thicknesses and thus different cylinder orientations are also observed. The parallel orientation is supposed to be preferred due to the energy gain of the two degrees of freedom compared to one in perpendicular orientation[39]. Then, only in very thin films, where the bulk morphology would be too much distorted, a perpendicular orientation would be thermodynamically preferred. When the layer thickness is about $t = (n-1/2)L_0$, the layer ruptures and forms terraces with different heights with integer step heights, leading to the formation of different morphologies and orienations[39,40]. An example of terrace formation and corresponding simulations of a symmetric polystyrene–polybutadiene triblock BCP (PS-b-PB-b-PS) are shown in Figure 1-13 (note that ABA triblocks show similar thermodynamic behavior as AB diblock copolymers[41])[40].

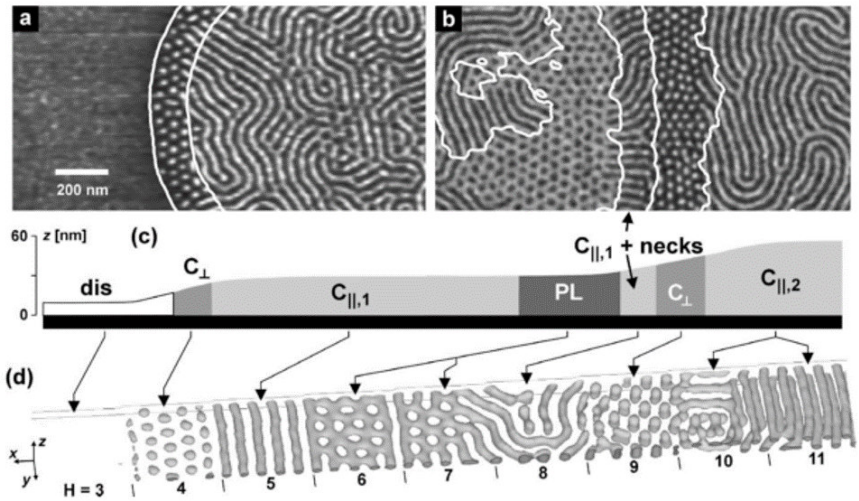

Figure 1-13: (a,b) Scanning force microscopy (SFM) phase images of thin films of PS-b-PB-b-PS on Si substrates after annealing in chloroform vapor. PB wets the substrate and bright areas corresponds to PS microdomains. (c) Schematic height profile of the phase images shown in (a,b). (d) Simulation of an ABA block copolymer film with increasing film thickness. B shows preferential wetting towards the surface[39].

In conclusion, the interplay of the strength of the surface energy of the confining interfaces (substrate and air) and the thickness of the layer, thus the deformability of the bulk structure, defines the arrangement of the microdomains.

1.3.2.c Manipulation of Interfacial Interactions

Over the decades, significant effort have been devoted to controlling the orientation of microdomains, especially for lamellas. Horizontal orientation of lamellae is undesirable in lithography applications, because their structure cannot be transferred into the substrate. The orientation of cylinders, on the other hand can be either horizontal (for semiconductor fins) or vertical (for contact holes) orientation. In order to overcome preferential interactions, several strategies have been presented. Note, that the manipulation of interface interactions becomes even more challenging when the χ-interaction parameter is high due to the high difference in interfacial energies of the blocks. However, for lithography applications, high-χ BCP are desired as they allow for lower molecular weights, so smaller feature sizes.

The most simple method to tune interfacial interactions is probably the grafting of polymer brushes onto the substrate, which was first presented in 1997, by Mansky et al.[42]. An end-functionalized random copolymer of Polystyrene – random – Poly(methyl methacrylate) (PS-r-PMMA) was grafted onto a substrate. When a block copolymer is deposited onto this brush layer, precise control over the orientation could be obtained by varying the composition of the random copolymer brush[43]. When precisely controlled, random copolymer brushes enable the neutral wetting of lamellar BCPs and thus the perpendicular orientation of the lamellae. In a similar way homopolymers can be grafted onto substrates in order to trigger the preferential wetting of just one block in asymmetric BCPs. In cylindrical BCPs for example, this enables the horizontal orientation of cylinders[33,44]. A variation of the grafting procedure is the integration of cross-linkable units into the BCP. Drockenmuller and coworkers demonstrated the neutral wetting of PS-PMMA when the PS block was incorporated with cross-linkable benzocyclobutene, altering its surface tension[45,46].

Substrate surface modification is not always possible or wanted. For brush grafting for example, the substrate has to be specifically altered in order to allow the grafting. For hydroxyl terminated brushes the surface has to be an oxide layer for instance. Sometimes, additional process steps have to be integrated in order to obtain an appropriate substrate surface. An alternative and or complementary effective method is using top-coats that can be deposited on the BCP in order to change the BCP/air interface interactions. Bates and coworkers employed maleic anhydride top-coats on high-χ Polystyrene-block-Polytrimethylsilylstyrene-block-Polystyrene and Polytrimethylsilylstyrene-block-Polylactide. When baked, the top-layer switches polarity, initiating the neutral wetting of the BCP.

Further sophisticated methods to modify the orientation of BCPs is the application of electrical fields[47–49]. Morkved and coworkes applied an electric field on cylindrical PS-b-PMMA and oriented the PMMA cylinders parallel to electric field lines exceeding 30kV/cm[48]. This phenomenon is due to the difference in the dielectric constant of the blocks and was further studied via quasi *in-situ* scanning force microscopy

imaging by Olszowka et al.[49]. Kathrein and coworkers combined the application of an electric field and a topographical guidance of PS-b-PDMS. The orientation of the cylinders was either parallel or perpendicular to the guiding templates depending on the electric field orientation[47].

Surfaces with topographical structures could also induce a specific orientation to BCPs. Bai et al. were able to orient a lamellar PS-b-PDMS perpendicular to the surface within extremely high trenches, taking advantage of the preferential wetting at the vertical sidewalls of these high aspect ratio templates[50].

Orientation and morphology control can also be obtained during solvent vapor annealing (SVA) which will be discussed more in detail later in the next section and in chapter 2[51–53]. A solvent vapor can mediate the BCP/air surface energy and act as a neutral layer to both blocks. Thus perpendicularly orientation of lamellae or cylinders can be obtained without the use of neutral brush layers[53,54].

1.3.2.d Microphase Separation via Annealing

In order to obtain a regular thin film of block copolymers, it is usually solvated in a solvent and then spin-coated onto the substrate. By adjusting the degree of dilution of BCP in the solvent and the spinning speed, the desired thickness can be precisely controlled. This rather simple step implicates already complex mechanisms that are important for the subsequent microphase separation and is schematically illustrated in Figure 1-14.

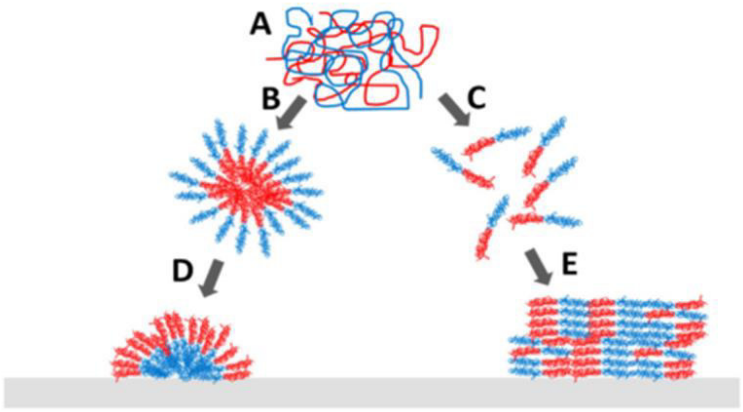

Figure 1-14: Schematic illustration of the spin-coating process[55]

Depending on the BCP and the solvent, either micellar or rod-coil structures are formed in solution (Figure 1-14B and C). When deposited onto the surface via spin-coating, the solvent evaporates quickly and the BCP is trapped in a disordered non-equilibrium state. Well organized morphologies over large areas are unlikely to be produced right after spin-coating. Block-to-block interactions are reduced due the entanglement of the polymer chains and the presence of residual solvent and trapped free volume (Figure 1-14E)[55]. The structure of the film depends on the temperature, spin speed and nature of the solvent (evaporation rate and selectivity). In selective solvents (the solvent favors the solvation of one block) the

BCP can form amphiphilic micelles that are then deposited into hemi-micelles on the substrate (Figure 1-14D)[55]. Under certain conditions, ordering of the micelles can be obtained right after spin[56]. For most applications, regular periodic arrays of structures are desired and hence, in the case where a disordered, metastable structure is obtained after spin-coating, an anneal process is required. The annealing allows an ordered arrangement of nanostructures and can eliminate defects. Kinetically trapped structures, obtained after spin-coating, are usually annealed thermally or by solvent vapor in order to gain enough energy and chain mobility to rearrange into ordered structures. Thermal annealing (TA) is the most simple method to obtain long range ordering as it is easy to be inserted into industrial processes, especially when it comes to up-scaling of the process. During this step, the BCP is typically heated above its glass transition temperature (T_g) but below its decomposition temperature in order to approach T_{ODT} and hold at elevated temperature for a certain amount of time. Then, the BCP is simply left at ambient temperature to cool down. The initial thickness of the film is here crucial and when not correctly chosen, thermal annealing can cause the rupture of the film with hole or island formation[57,58]. For high-χ BCP, the ODT is generally extremely high, and thus not approachable, mainly due to thermal degradation of the polymers at high temperatures[51]. Alternatively very long annealing times of tens of hour or days below the degradation temperature are possible, but not interesting for industrial applications.

Solvent vapor annealing (SVA) is an alternative way to introduce order in BCPs and has been introduced for high-χ BCPs, when the ODT is difficult to attain due to thermal degradation. In this process, the spin-coated BCP film is kept in a controlled atmosphere containing solvent vapors at temperatures usually well below the T_g. The solvent molecules swell the BCP and act like a plasticizer, thus lowering its T_g and enhancing the chain mobility at room temperature[59]. Upon evaporation of the solvent, the BCP forms well-organized nanostructures. Probably the first to present a sort of SVA were Kim and Libera who prepared solutions of polystyrene (PS)-polybutadiene (PB)-polystyrene (SBS) triblock copolymers in toluene and left them to dry at different evaporation rates[54]. The authors obtained well-arranged PS cylinders in a matrix of PB when the sample was exposed to the solvent for a long period of time. Other morphologies and orientations were obtained at different evaporation rates. SVA gained later in popularity after the work of Kim and coworkers that presented the annealing of polystyrene-block-polyethylene oxide (PS-b-PEO) in benzene vapors. Highly ordered hexagonally packed PEO microdomains with long range order were obtained in a PS matrix when the BCP was placed in a benzene saturated chamber at RT. Numerous parameters have an impact on the final nanostructures after SVA. As explained in the previous section, the solvent vapor can mediate surface energies at the BCP/air interface and can change the preferential wetting of the free surface. Also, the solvent can induce a screening effect in mediating the unfavorable interactions of the block, thus

affecting the effective χ_{eff}[32]. Selective solvents can selectively swell only one of the blocks, modifying the effective volume fraction and enabling the access to different morphologies, depending on the solvent[51,60,61].

1.3.3 Large Area Orientation of BCPs

Once annealed on plane substrates, the BCP arranges with short-range lateral ordering in so called "fingerprint" orientation, when showing cylindrical or lamellar morphology and in mulitcrystalline domains for sphere morphology. Small grains of nanostructures, having all a different orientation are formed at the surface. For many applications like bit patterned media or lithography masks, however, periodic domains with a high degree of ordering are required. Controlling the orientation of BCP microdomains with artificial surface modifications (either topographically or chemically) is called the directed self-assembly (DSA) of block copolymers. The use of chemical patterns for orientation control is called chemoepitaxy whereas that of topographical structures is called graphoepitaxy.

1.3.3.a Chemoepitaxy

In chemoepitaxy, chemically modified patterns are used to guide the block copolymer self-assembly. In this technique, the patterns that are created at the surface of a substrate strongly interact with the BCP, and the size of the pattern (L_S) is comparable to that of the BCP period ($L_S \approx L_0$). When a BCP film is deposited on top of this pattern, it minimizes its free energy by minimizing the amount of dissimilar interactions and align perfectly with the underlying pattern[62]. The ideal geometry of the chemical pattern has $L_S \approx L_0$. If the commensurability of the pattern derives from this spacing, the BCP stretches and compresses to a certain amount in order to fit the chemical prepattern[62]. It was shown on lamellar PS-b-PMMA that this mismatch between L_0 and L_S supports ±10% of the ideal L_S before losing the ordering effect and arranging in a fingerprint orientation[63]. The Nealey group extensively worked on the chemoepitaxy of BCP and influenced the progress of this domain greatly[64–67]. In the Liu–Nealey resist trimming or University of Wisconsin (UW) flow[62], a hydroxyl terminated PS monolayer is grafted onto a Si substrate[68]. A resist layer is then patterned and developed on top of this layer. Oxygen plasma treatment of the exposed PS layer led to polar, hydrophilic PS patterns. After resist-stripping, the surface is then alternately covered with hydrophilic and hydrophobic patterns. The deposition and annealing of PS-b-PMMA on these substrates leads to the perfect alignment of the microdomains over large areas. An extension of this works shows the successful alignment of PS-b-PMMA on complex structures with bends (45°, 90° and 135°) and segments, jogs and T-junctions (Figure 1-15)[65,67].

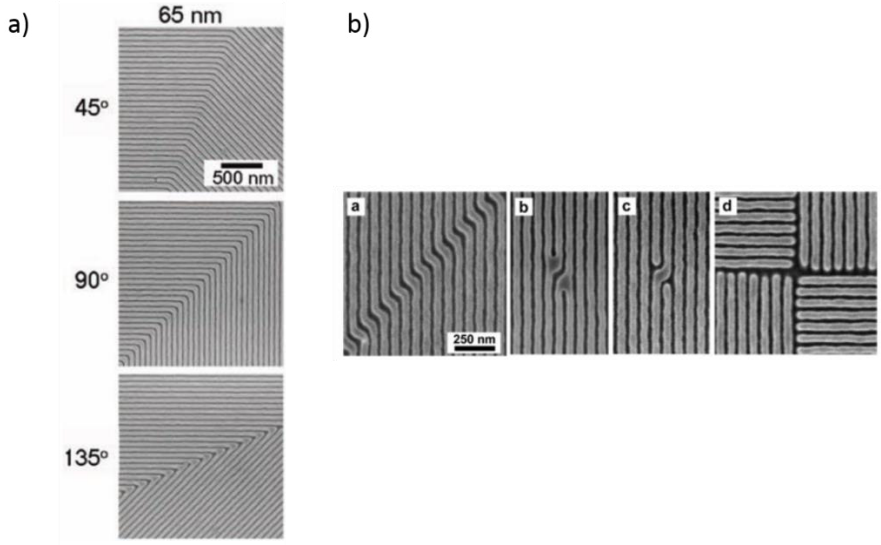

Figure 1-15: Top view scanning electron microscopy (SEM) images of (a) angled lamellae of PS-b-PMMA[65] and (b) PS-b-PMMA directed to assemble into nested arrays of jogs, isolated PMMA jogs, isolated PS jogs and arrays of T-junctions[67]

More interestingly for future lithography applications are also density multiplication structures. In this case sparse chemical patterns, where $L_S = nL_0$, are used to enhance the resolution of the initial pattern. PMMA patterns were found to be able to interpolate additional PMMA domains between guiding patterns, while maintaining its natural L_0, when $L_S = 2L_0$[66,69]. A schematic of this process is depicted in Figure 1-16

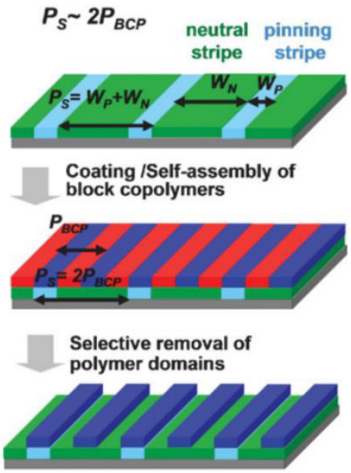

Figure 1-16: Schematic illustration of sparse chemoepitaxy. The chemical patterns have a pitch twice as highs as that of the block copolymers. The self-assembled block copolymer doubles the spatial frequency of the underlying guiding chemical patterns[69]

1.3.3.b Graphoepitaxy

Graphoepitaxy uses structural reliefs to guide the self-assembly of BCP in thin films and enhances lateral ordering of the nanostructures. In contrary to chemoepitaxy, the general pattern size of the topographical structures are a few times larger than the intrinsic domain spacing of the BCP. The topographic patterns are obtained with one of the typical lithography methods presented previously in this chapter. One of the

drawbacks of graphoepitaxy compared to chemoepitaxy is that some of the surface area is lost, due to the guiding patterns. However the extreme density multiplication and ability to align the BCP into complex structures are key advantages.

The first applications of graphoepitaxy on BCP were reported by Segalman and coworkers in the early 2000s[70–73]. Spherical Polystyrene-b-Poly-2-vinylpyridine (PS-b-P2VP) microdomains were aligned within trenches and wells of different depth and width. Large area single crystal of spheres were obtained after thermal annealing when aligned in trenches (Figure 1-17a)[70]. The group found out that the two parameter depth and width of the guiding trenches are crucial for the alignment of the BCP. Good lateral ordering was only obtained when the depth was equal or greater than L_0 and the width not greater than 185*L_0 (5µm) [70].

In parallel, the Ross group also thoroughly investigated the effect of graphoepitaxy on a different spherical BCP. Polystyrene-b-Polyferrocenyldimethylsilane (PS-b-PFS) were chosen because of the high etch selectivity of the iron containing PFS block, which can be used as a hard mask for pattern transfer into an underlying functional material[74–78]. Trench patterns of 80 nm depth and various widths that were a few times larger than the natural period of the BCP were tested. In that way, the number of PS-b-PFS rows inside the trenches was controlled (Figure 1-17b). An integer number N of rows of spherical microdomains was found when the width (W) of the trenches was $(N-0.5)L_0 < W > (N+0.5)L_0$. When the width of the trenches was not commensurate with the period of the BCP ($W \neq nL_0$), the spheres were compressed or extended in order to accommodate the trench width.

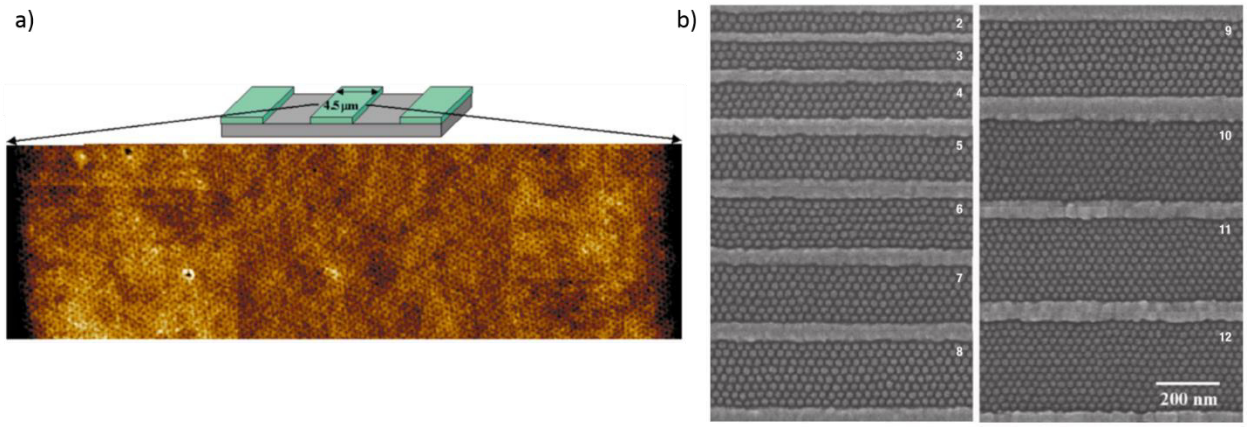

Figure 1-17: a) top view SFM image of a single crystal of PS-b-P2VP on top of a mesa[69]. b) Top view SEM images of aligned PS-b-PFS spheres in trenches of various widths (N=2-12 rows)[75]

Furthermore, they found out that the defect formation can be induced into the microdomain array when defects in the guiding feature were present[79].

The Ross group extended their work on graphoepitaxy with a cylindrical Polystyrene-b-Polydimethylsiloxane (PS-b-PDMS) system[33,80,81]. PDMS shows comparable high etch selectively as PFS, because of its high amount of silicon in the backbone. The PS block can be easily etched away while the

PDMS block transforms into a robust hard mask material. PS-b-PDMS is therefore interesting for pattern transfer. Additionally PS-b-PDMS has a high incompatibility ($\chi \approx 0.26$ at RT[82,83]) and thus smaller N values, which are related to L_0, can be used. However, due to their high surface tension difference, special attention has to be paid to the interface interactions when confined in lateral template patterns. Jung and Ross confined cylindrical PS-b-PDMS microdomains in PDMS-brush coated trenches, in order to obtain vertical orientation of the PDMS cylinders[33]. They obtained selective orientation of cylinders by varying simultaneously the mesa width and solvent annealing parameters. Later, concentric ring patterns with the same BCP system were obtained by the Ross group[80]. By playing with the pattern diameter, the organization of the concentric ring formation could be controlled. Other interesting structures like rectangular, triangles and circles have been used for cylindrical PS-b-P2VP guiding by Chai et al[84] (Figure 1-18b). After alignment of P2VP cylinders inside the templates, the cylinders were loaded with metal ions in order to obtain metal wires after polymer etch.

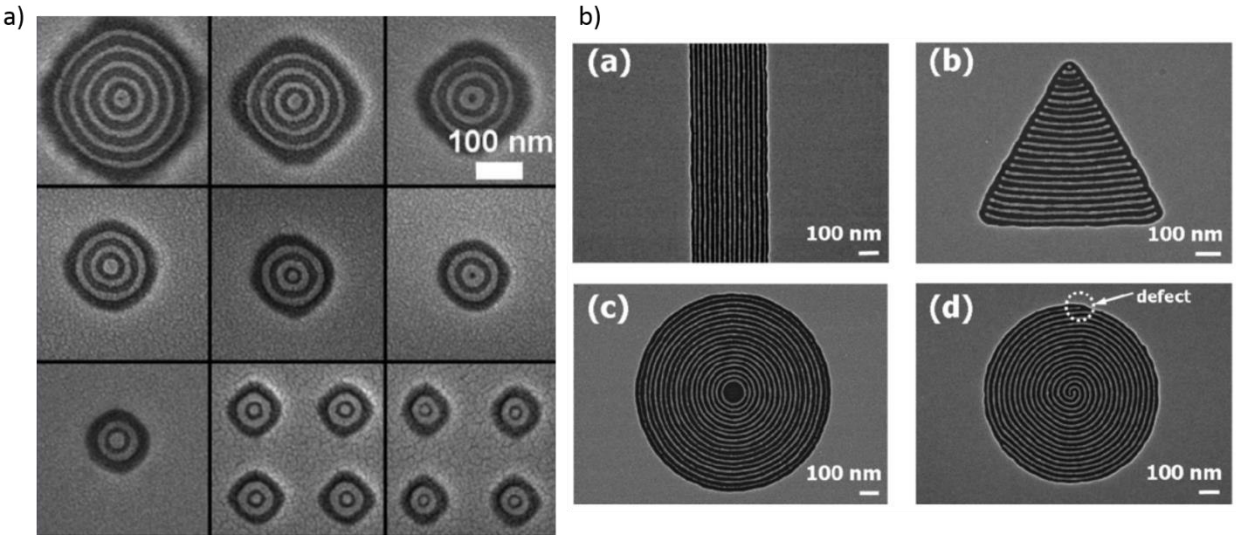

Figure 1-18: top view SEM images of (a) PS-b-PDMS cylinders in concentric ring patterns with varying diameters[79] and (b) Platinum nanowires obtained from self-assembly of PS-b-P2VP in different shaped templates. The different orientations of the cylinders in c) and d) are due to a defect in the template structure[81].

For lamellar systems, the interactions of walls and BCP and the commensurability of the templates govern the orientation and size of the microdomains. Park and coworkers investigated the behavior of lamellar PS-b-PMMA domains in trenches of different surface energies[85]. For perpendicular orientation of the lamellas, it is necessary that the bottom surface of the trenches is neutral for both blocks while the feature sidewalls has to interact selectively to either PS or PMMA. When all sidewalls and bottom surface showed preferential wetting with the PMMA block, the lamellae aligned parallel to the substrate. A neutral brush layer on sidewalls and bottom layer led to perpendicular arrangement but without long range arrangement

of the microdomains. In this case, a precise control of layer thickness, molecular weight and commensurability is important to obtain long range ordering[85].

1.3.4 Application of Directed Self-Assembly in Nanomanufacturing

Recently, the ITRS introduced DSA as a new potential complementary lithography technique for next-generation microelectronic manufacturing[86]. DSA has this great potential due to its ability to create high-throughput, low-cost and high resolution nanopatterns. Several groups have thus investigated the potential of DSA in real applications.

Bit patterned media are hard disk drive technologies that store data in magnetic islands, in which one island contains only one bit. Conventional hard disk drives store data in grains of continuous thin films, where one bit of data consists of around 20 grains. In the attempt to increase storage density and reduce the bit size, thermal stability and media noise problems were caused, that could be solved by using bit patterned media. The magnetic data is here stored in lithographically defined single domain islands, with high area density of 1Tdot/in^2 and beyond[62]. This is where DSA can be interesting by creating large area, high density templates for pattern transfer[87]. Several reports show the directed self-assembly with chemical patterns of large PS-b-PMMA microdomains that are created and transferred into Si substrates. After pattern transfer these templates can serve as a master for nanoimprinting to create disks with magnetic media[88,89]. An example of this process is presented in Figure 1-19

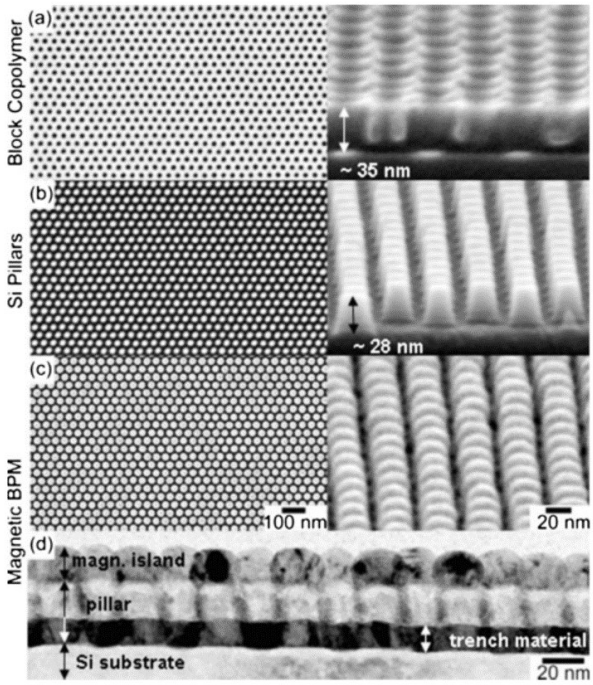

Figure 1-19: top view and tilted SEM images at different stages of the bit patterend media fabrication. (a) BCP template after PMMA removal, (b) Si master template after reactive ion etching, (c) Magnetic islands, (d) Bright field transmission electron microscope (TEM) cross- section image through two consecutive rows of bits[86]

Other reports show the DSA of spherical and cylindrical PS-b-PDMS by graphoepitaxy[90,91]. Guiding patterns were designed to be up to three times as large as the natural period of the PS-b-PDMS. The PS-b-PDMS feature size was down to 6 nm small. By using 2D dots array or 1D groove prepatterns different geometries have been obtained (Figure 1-20). The obtained CoCrPt alloy dots have been demonstrated with highest density of 1.5Tdot/in^2 for a guided media.

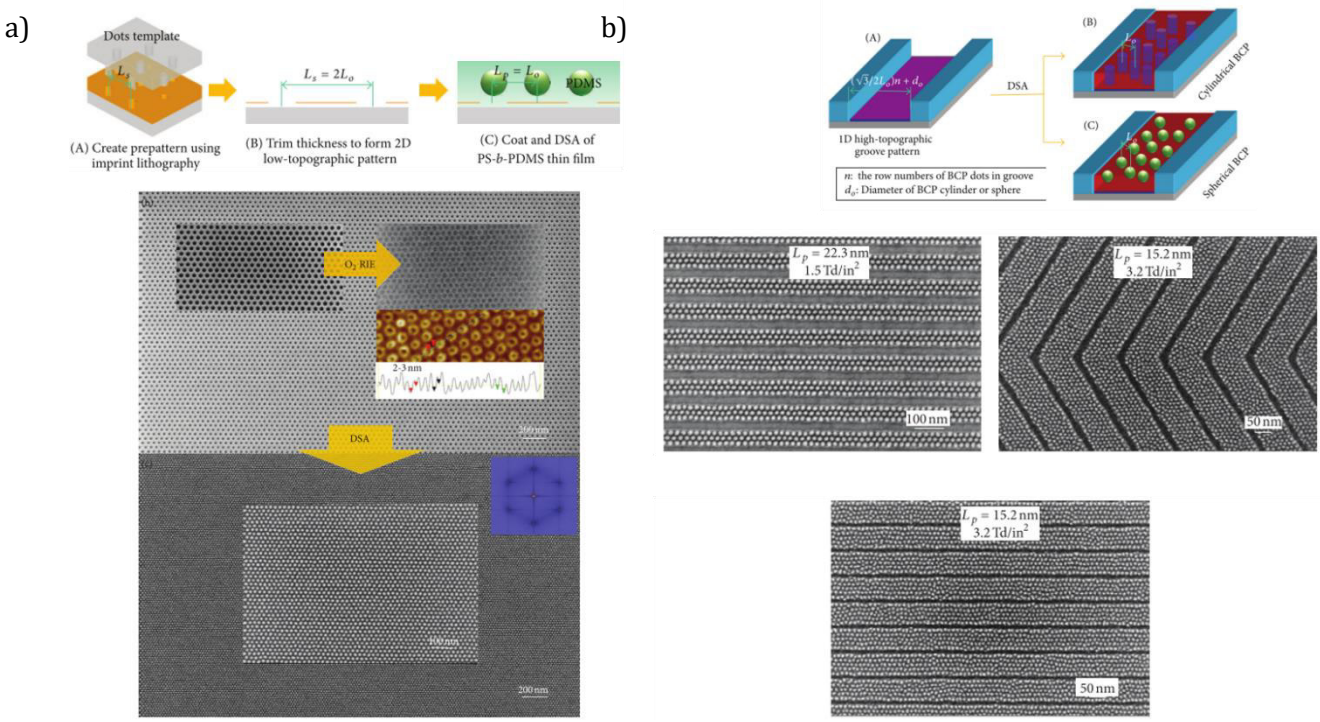

Figure 1-20: (a) Schematic representation of directed self-assembly of sphere-forming PS-b-PDMS thin films by a 2D low-topographic holes array resist prepattern with $L_S=2L_0$ and corresponding SEM top view images. (b) Schematic representation of directed self-assembly of sphere-forming PS-b-PDMS thin films by a 1D high- topographic groove pattern and corresponding SEM images (top L_0=22.3 nm, bottom L_0=15.2 nm)[87]

Fin field-effect transistors (finFET) are another possible application of DSA of BCPs. FinFETs are 3 dimensional double gate transistors that are traditionally build on Silicon on Insulator (SOI) substrates. FinFETs use a conducting channel that stands on the insulator material, shaped like a fin. This fin-shaped gate electrode allows the connection of multiple gates on one single transistor. The implementation of periodic line-shaped BCP patterns could reduce their feature size and improve the performance. By customizing the guiding pattern for graphoepitaxy, Tsai et al. demonstrated the fabrication of a 29 nm pitch finFET device, derived from the DSA of PS-b-PMMA[92]. The authors present the formation of self-aligned pattern-free regions between groups of aligned lines and a cutting of lines by additional lithography and etching processes. The process flow of the finFET fabrication is depicted in Figure 1-21

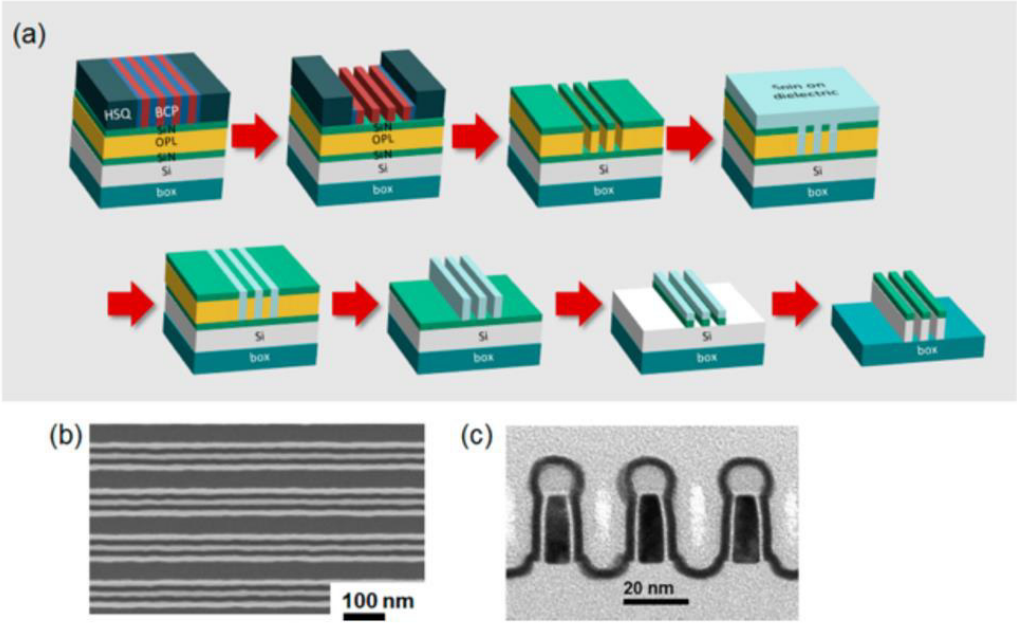

Figure 1-21: (a) Schematic illustration of the process flow for forming groups of silicon on insulator (SOI) fins with PS-b-PMMA templates with a controlled fin spacing. Tone inversion operation is applied after the DSA pattern is transferred into the underlying layer. The tone inverted image is then transferred into a fin hard mask layer and 20nm of SOI. (b) Top view SEM image of a group of fins obtained after the process shown in (a). (c) TEM cross-section image of obtained 29 nm pitch SOI fins[89]

Finally, the translation form laboratory scale DSA samples to industrial scale full 300mm wafers is important to understand mechanisms on a large scale and evaluate if processing steps are adapted for industry. The Liu-Nealey process has been implemented on a 300mm wafer production line[93]. PS-b-PMMA with a pitch of L_0=25 nm were aligned via chemoepitaxy on the wafer. This gives a new basis to study BCP behavior on large surfaces and especially defect origins and propagation.

1.3.5 High-χ Block Copolymers

The most studied system of BCP is PS-b-PMMA due to its easy synthesis and familiarity of the microelectronics industry with the two homopolymers PS and PMMA. However, PS-b-PMMA has a relatively low χ-value of 0.04[94]. As explained above, the χ has great impact on the phase separation. The higher the compatibility (or the lower the χ parameter) the less defined are the microdomains after phase separation. On the contrary when the χ parameter is high and the degree of polymerization, N, is small, the domain spacing of the system can reach its smallest values. In order to phase separate, we have seen that the BCP has to have a χN value of at least 10.5. Taking into account the low value of PS-b-PMMA of 0.04, the polymerization N has to be at least 250 in order to obtain microphase separation. The lowest obtainable period for PS-b-PMMA is hence of about 20 nm. This is why high-χ systems have been introduced. Using BCPs with a higher χ allows to use lower N polymers and thus give access to smaller domain sizes. Numerous BCP with high χ parameter have been reported in the last decade. The incompatibility between

blocks can be increased post-synthesis by blending the polymer with inorganic species for example. Goshal and coworkers presented the amplification of the effective χ_{eff} of polystyrene-b-poly(ethylene oxide) (PS-b-PEO) through the addition of lithium chloride salt[95,96]. Through this technique, vertical lamellar with a feature size of 8 nm were obtained on plane silicon. Similarly, Park et al. presented a hybrid of PS-b-PEO and a low molecular weight organosilicate[97]. They achieved lamellar microdomains with feature sizes of 7 nm. But the amplification of the χ-value post-synthesis means additional process steps in order to obtain the smaller feature sizes. Therefore various polymers that had intrinsically a lower incompatibility were introduced. There are purely organic high-χ BCP, like Polystyrene-b-poly-4-vinylpyridine (PS-b-P4VP) in which the pyridine ring is polar and thus highly repulsive towards PS[98]. This BCP has a χ value of 0.3 to 0.35 and sub 7 nm lamellar microdomains were obtained[99]. Polylactide (PLA) containing BCPs present usually high incompatibility because of the high hydrophobicity of the PLA block. Sinturel and coworkers demonstrated the assembly of PS-PLA with a χ of ≈ 0.13[100]. A more exotic BCP is poly-4-tert-butylstyrene-b-polymethyl methacrylate (PtBS-b-PMMA) where the PtBS block has high hydrophobicity, achieving lamellar patterns of L_0 ≈ 14 nm[101]. When one of the block contains additionally an inorganic specie, like silicon, the block copolymer can profit from higher etch resistance. Polydimethylsiloxane (PDMS) containing block copolymers are the most used BCP of this type. Cylinder forming P4VP-b-PDMS and P2VP-b-PDMS were demonstrated to align in well-organized linear arrays with feature sizes between 6 and 31 nm[24,102]. The triblock polylactide-b-poly(dimethylsiloxane)-b-polylactide (PLA-b-PDMS-b-PLA) was estimated to have a χ of 0.94 and showed lamellar, cylindrical, and spherical arrangements on plane substrates[103]. The authors indicate that theoretical lamellar domain spacing of this BCP could be as small as 3.5nm. PDMS-b-PMMA was synthesized via copper-catalyzed azide–alkyne “click” cycloaddition and showed smallest domain spacing of ≈ 12 nm on plane silicon[94]. Table 1-1 illustrates feature size observations of different BCP systems achieved over the last decades.

Table 1-1: Characteristic dimensions and χ values for selected block copolymers[23]

block polymer	M_n (kg mol^{-1})	morphology	characteristic dimensions (nm)	χ_{eff} 150 °C (and method of estimation)
MH-PTMSS	3.9	Hex	D = 5.5, d = 8.3[34]	not known
P2VP-PDMS	26.0	Hex	D = 6, L_0 = 26[25]	not known
PTMSS-PLA	9.2	Hex	D = 8.8, d = 12.1[33]	0.41[33] (SAXS)
PS-PDMS	16.0	Hex	D = 8, L_0 = 20[45]	0.11[46,40] (ODT)
PS-PLA	18	Hex	D = 10, L_0 = 18[47]	0.075[48] (ODT)
Mal-PS	4.5	Hex	D = 12[35]	not known
PDMS-PLA	9	Hex	D = 13, d = 20[28]	1.1[27] (domain spacing)
PS-PMMA	42	Hex	D = 14, L_0 = 24[49]	0.030[50] (SANS)
PS-PEO	21	Hex	D = 17.4[51]	0.047[52] (SAXS)
PCHE-PMMA	4.9	Lam	L_0 = 9.0[40]	0.18[40] (ODT)
PtBS-PVP	4.5	Lam	L_0 = 9.6[39]	0.11[39] (ODT)
PS-P4VP	6.4	Lam	L_0 = 10.3[37]	0.40[36] (SAXS)
PtBS-*b*-PMMA	17.6	Lam	L_0 = 14.4[38]	0.053[38] (ODT)
PMOST-PTMSS	8.5	Lam	L_0 = 14.4[30]	0.046[30] (ODT, SAXS)
PS-PDMS	16.0	Lam	L_0 = 17.5[24]	0.11[46,40] (ODT)

As depicted in this table, lowest feature sizes reported were at 5.5 nm for maltoheptaose-b-poly(para-trimethyl silylstyrene) (MH-PTMSS)[104]. This polysaccharide based BCPs profits from the strong incompatibility between the saccharidic and synthetic blocks. In theory one could descend to BCPs with feature sizes down to 2 nm but many challenges arise like defect control, dewetting, stability, and pattern transfer[23].

Most of these BCPs however, are still rather exotic and the understanding of their phase separation mechanisms not well developed. The most widely studied high-χ BCP is the PDMS containing PS-b-PDMS, which can be synthesized rather easily[94]. The smallest feature sizes obtained were of 8 nm and the χ value

is estimated to be 0.26 at room temperature[36,82,83,105,106]. PS-b-PDMS can be treated with oxygen plasma to etch the PS block. Simultaneously the PDMS block gets oxidized and transforms into a robust etching mask.

1.4 Motivation and Outline of the Thesis

This thesis deals primarily with the problematic of the implementation of PS-b-PDMS in industry processes. Great progress has been made with PS-b-PMMA over the last years, with first applicational results for finFET or bit patterned media, but PS-b-PMMA can physically not attain feature sizes smaller than 10 nm. However, the semiconductor industry is unlikely to invest in the implementation of DSA for one single generation of products. In order to push DSA forward, reliable processes for sub 10 nm resolutions have to be found. High-χ BCP are here promising candidates as they could assure the downsizing of features for the next several future generation of products. Nonetheless, serious issues arise when increasing the incompatibility of the blocks that have yet to be understood fundamentally. Solvent vapor annealing, for instance, is a very unstable process were numerous parameters influence the phase separation quality. Pattern transfer is a crucial step in DSA that will increasingly be problematic for higher resolutions. Likewise is the pattern quality a crucial issue in integrated circuit fabrication and line edge roughness becomes more and more important with decreasing feature size. During this thesis, some of these problems are addressed in order to find solutions of how to process high-χ BCPs and find answers to the question if this type of material could actually be used soon in large scale manufacturing processes.

Chapter 2 deals with surface interactions of cylindrical PS-b-PDMS with an overall molecular weight of 45kg/mol with several surfaces, including graphoepitaxy templates composed of silicon anti reflective coating (SiArc) / spin-on-carbon (SOC) layers, typically used in photolithography processes. The behavior of PS-b-PDMS during solvent vapor annealing of several solvents is investigated. In order to meet manufacturing standards, the solvents should be non-toxic for human and environment. Therefore several "safe" solvents have been evaluated for the use in SVA for PS-b-PDMS. Further, results of *in-situ* SVA measurements in grazing incident small angle X-ray scattering (GISAXS) are presented. Finally the line edge roughness of obtained cylinders is evaluated.

In chapter 3, a full process of ultra-fast assembly of PS-b-PDMS is presented and first 300 mm wafers were produced. By blending the BCP solution with plasticizers, chain mobility can be greatly increased, allowing thermal annealing of high-χ BCPs. This way, the cumbersome SVA process can be avoided making the upscaling of the process imaginable.

Chapter 4 deals with a small period PS-b-PDMS of $L_0 \approx 20$ nm in order to address next generation devices at the 14 nm technology node and beyond. Surface interactions of this BCP are evaluated and graphoepitaxy in silicon trenches as well as on SiArc/SOC trenches are presented. DSA in SiArc/SOC trenches provides the

possibility to align the BCP via solvothermal annealing. Indeed, the SOC layer is capable of retaining solvent, which evaporates during thermal annealing through the BCP film, participating thus in the annealing step.

In chapter 5, we come to the pattern transfer of the obtained PDMS nanostructures. In order to become of value for the semiconductor industry, features should be transferred into the underlying semiconductor material with plasma etching processes. Several etching procedures that are commercially used for gate etching, are presented and optimized for the transfer etching of PDMS cylinders. Small feature sizes of 10 nm are challenging to be transferred but interesting results are shown, where 10 nm lines in SOI materials are obtained for potential application for finFET fabrication.

Chapter 6 describes uncommon applications of BCP lithography. The first part deals with the sequential patterning with different PS-b-PDMS layers that can create nanomesh structures. Also, density multiplication of nanostructures can be obtained by assembling sequentially two layers of different molecular weight BCPs. In the second part of chapter 6, the infiltration of PS-b-PMMA with metal salts through a straightforward spin-coating technique is addressed and evaluated. This way, DSA can profit from the knowledge on the behavior of PS-b-PMMA while increasing its etch selectively, opening up more possibilities for this system

References

(1) Blais, F. Electronics projects and tutorials http://electronicsbyexamples.blogspot.fr/2013/03/milestones-in-digital-electronics.html (accessed Feb 8, 2016).

(2) Intel. Pressroom: Intel's first high-volume 45nm factoy opens its doors http://www.intel.com/pressroom/kits/manufacturing/Fab32/photos.htm (accessed Feb 8, 2016).

(3) Moore, G. E. Cramming More Components onto Integrated Circuits. *Electronics* **1965**, *38*, 114–117.

(4) Mick, J. Intel's Broadwell-Base Core i-Series SoCs Finally Hits the Market http://www.dailytech.com/Intels+BroadwellBase+Core+iSeries+SoCs+Finally+Hits+the+Market/article37051.htm (accessed Jul 19, 2016).

(5) Mack, C. Semiconductor Lithography (Photolithography) - The Basic Process http://www.lithoguru.com/scientist/lithobasics.html.

(6) Rothschild, M. Projection Optical Lithography. *Mater. Today* **2005**, *8*, 18–24.

(7) Cui, Z. *Nanofabrication*; 2008.

(8) French, R. H.; Tran, H. V. *Immersion Lithography: Photomask and Wafer-Level Materials*; 2009; Vol. 39, pp. 93–126.

(9) Rai-Choudhury, P. *Microlithography, Micromachining, and Microfabrication, Volume 1: Microlithography*; The Society of Photo-Optical Instrumentaion Engineers, 1997.

(10) Wei, Y. 193nm Immersion Lithography: Status and Challenges. *SPIE Newsroom* **2007**, 22–25.

(11) Stulen, R. H.; Sweeney, D. W. Extreme Ultraviolet Lithography. *IEEE J. Quantum Electron.* **1999**, *35*, 694–699.

(12) Wu, B.; Kumar, A. Extreme Ultraviolet Lithography and Three Dimensional Integrated circuit—A Review. *Appl. Phys. Rev.* **2014**, *1*, 011104.

(13) Zimmerman, P. Double Patterning Lithography : Double the Trouble or Double the Fun ? *SPIE Newsroom*. 2009, pp. 2–4.

(14) Cho, M.; Ban, Y.; Pan, D. Z. Double Patterning Technology Friendly Detailed Routing. In *IEEE/ACM International Conference on Computer-Aided Design*; 2008; pp. 506–511.

(15) Chou, S. Y.; Krauss, P. R.; Renstrom, P. J. Imprint of Sub-25nm Vias and Trenches in Polymers. *Appl. Phys. Lett.* **1995**, *67*, 3114.

(16) Garner, M.; Herr, D. Directed Self Assembly - an ITRS Perspective http://www.sematech.org/meetings/archives/litho/9025/Pres/DSA-04-Garner.pdf.

(17) Bates, F. S.; Fredrickson, G. H. Block Copolymer Thermodynamics: Theory and Experiment. *Annu. Rev. Phys. Chem.* **1990**, *41*, 525–557.

(18) Szwarc, M.; Levy, M.; Milkovic, R. Polymerization Initiated by Electron Transfer to Monomer. A New Method of Formation of Block Polymers. *J. Am. Chem. Soc.* **1956**, *78*, 2656 – 2657.

(19) Mai, Y.; Eisenberg, A. Self-Assembly of Block Copolymers. *Chem. Soc. Rev.* **2012**, *41*, 5969–5985.

(20) Matsen, M. W.; Bates, F. S. Unifying Weak- and Strong-Segregation Block Copolymer Theories. *Macromolecules* **1996**, *29*, 1091–1098.

(21) Yoshida, H.; Takenaka, M. Physics of Block Copolymers from Bulk to Thin Films. In *Directed self-assembly of Block Copolymers for Nano-manufacturing*; Gronheid, R.; Nealey, P. F., Eds.; Elsevier Ltd., 2015; pp. 3–26.

(22) Leibler, L. Theory of Microphase Separation in Block Copolymers. *Macromolecules* **1980**, *13*, 1602–1617.

(23) Sinturel, C.; Bates, F. S.; Hillmyer, M. a. High χ–Low N Block Polymers: How Far Can We Go? *ACS Macro Lett.* **2015**, 1044–1050.

(24) Kim, J. M.; Hur, Y. H.; Jeong, J. W.; Nam, T. W.; Lee, J. H.; Jeon, K.; Kim, Y.; Jung, Y. S. A Block Copolymer with an Extremely High Block-to-Block Interaction for a Significant Reduction of Line-Edge Fluctuations in Self-Assembled Patterns. *Chem. Mater.* **2016**, *28*, 5680–5688.

(25) Darling, S. B. Directing the Self-Assembly of Block Copolymers. *Prog. Polym. Sci.* **2007**, *32*, 1152–1204.

(26) Khandpur, A. K.; Förster, S.; Bates, F. S.; Hamley, I. W.; Ryan, A. J.; Bras, W.; Almdal, K.; Mortensen, K. Polyisoprene-Polystyrene Diblock Copolymer Phase Diagram near the Order-Disorder Transition. *Macromolecules* **1995**, *28*, 8796–8806.

(27) Khanna, V.; Cochran, E. W.; Hexemer, A.; Stein, G. E.; Fredrickson, G. H.; Kramer, E. J.; Li, X.; Wang, J.; Hahn, S. F. Effect of Chain Architecture and Surface Energies on the Ordering Behavior of Lamellar and Cylinder Forming Block Copolymers. *Macromolecules* **2006**, *39*, 9346–9356.

(28) Huinink, H. P.; van Dijk, M. A.; Brokken-Zijp, J. C. M.; Sevink, G. J. A. Surface-Induced Transitions in Thin Films of Asymmetric Diblock Copolymers. *Macromolecules* **2001**, *34*, 5325–5330.

(29) Huinink, H. P.; Brokken-Zijp, J. C. M.; van Dijk, M. A.; Sevink, G. J. A. Asymmetric Block Copolymers Confined in a Thin Film. *J. Chem. Phys.* **2000**, *112*, 2452.

(30) Lyakhova, K. S.; Sevink, G. J. A.; Zvelindovsky, A. V.; Horvat, A.; Magerle, R. Role of Dissimilar Interfaces in Thin Films of Cylinder-Forming Block Copolymers. *J. Chem. Phys.* **2004**, *120*, 1127–1137.

(31) Wang, Q.; Yan, Q.; Nealey, P. F.; de Pablo, J. J. Monte Carlo Simulations of Diblock Copolymer Thin Films Confined between Two Homogeneous Surfaces. *J. Chem. Phys.* **2000**, *112*, 450.

(32) Jung, Y. S.; Ross, C. A. . Solvent-Vapor-Induced Tunability of Self-Assembled Block Copolymer Patterns. *Adv. Mater.* **2009**, *21*, 2540–2545.

(33) Jung, Y. S.; Ross, C. A. Orientation-Controlled Self-Assembled Nanolithography Using a Polystyrene-Polydimethylsiloxane Block Copolymer. *Nano Lett.* **2007**, *7*, 2046–2050.

(34) Ndoni, S.; Jannasch, P.; Larsen, N. B.; Almdal, K. Lubricating Effect of Thin Films of Styrene - Dimethylsiloxane Block Copolymers. *Langmuir* **1999**, *15*, 3859–3865.

(35) Wu, N.; Huang, L.; Zheng, A.; Xiao, H. Surface Properties of Block and Graft Polystyrene–Polydimethylsiloxane Copolymers. *J. Appl. Polym. Sci.* **2006**, *99*, 2936–2942.

(36) Garnier, J.; Arias-Zapata, J.; Marconot, O.; Arnaud, S.; Böhme, S.; Girardot, C.; Buttard, D.; Zelsmann, M. Sub-10nm Silicon Nanopillar Fabrication Using Fast and Brushless Thermal Assembly of PS-B-PDMS Diblock Copolymer. *ACS Appl. Mater. Interfaces* **2016**.

(37) O'Driscoll, B. M. D.; Kelly, R. A.; Shaw, M.; Liontos, G.; Ntetsikas, K.; Apostolos, A.; Petkov, N.; Morris, M. A. Achieving Structural Control with Thin Polystyrene- B-Polydimethylsiloxane Block Copolymer Films : The Complex Relationship of Interface Chemistry , Annealing Methodology and Process Conditions. *Eur. Polym. J.* **2013**, *49*, 3445–3454.

(38) Konrad, M.; Knoll, A.; Krausch, G.; Magerle, R. Volume Imaging of an Ultrathin SBS Triblock Copolymer Film. *Macromolecules* **2000**, *33*, 5518–5523.

(39) Van Dijk, M. A.; van den Berg, R. Ordering Phenomena in Thin Block Copolymer Films Studied Using Atomic Force Microscopy. *Macromolecules* **1995**, *28*, 6773–6778.

(40) Knoll, A.; Horvat, A.; Lyakhova, K. S.; Krausch, G.; Sevink, G. J. A.; Zvelindovsky, A. V.; Magerle, R. Phase Behavior in Thin Films of Cylinder-Forming Block Copolymers. *Phys. Rev. Lett.* **2002**, *89*, 035501.

(41) Matsen, M. W.; Thompson, R. B. Equilibrium Behavior of Symmetric ABA Triblock Copolymer Melts. *J. Chem. Phys.* **1999**, *111*, 7139.

(42) Mansky, P. Controlling Polymer-Surface Interactions with Random Copolymer Brushes. *Science (80-.).* **1997**, *275*, 1458–1460.

(43) Ceresoli, M.; Palermo, M.; Ferrarese Lupi, F.; Seguini, G.; Perego, M.; Zuccheri, G.; Phadatare, S. D.; Antonioli, D.; Gianotti, V.; Sparnacci, K.; *et al.* Neutral Wetting Brush Layers for Block Copolymer Thin Films Using Homopolymer Blends Processed at High Temperatures. *Nanotechnology* **2015**, *26*, 415603.

(44) Borah, D.; Rasappa, S.; Senthamaraikannan, R.; Kosmala, B.; Shaw, M. T.; Holmes, J. D.; Morris, M. A. Orientation and Alignment Control of Microphase-Separated PS-B-PDMS Substrate Patterns via Polymer Brush Chemistry. *ACS Appl. Mater. Interfaces* **2013**, *5*, 88–97.

(45) Drockenmuller, E.; Li, L. Y. T.; Ryu, D. Y.; Harth, E.; Russell, T. P.; Kim, H. C.; Hawker, C. J. Covalent Stabilization of Nanostructures: Robust Block Copolymer Templates from Novel Thermoreactive Systems. *J. Polym. Sci. Part A Polym. Chem.* **2005**, *43*, 1028–1037.

(46) Kim, E.; Shin, C.; Ahn, H.; Ryu, D. Y.; Bang, J.; Hawker, C. J.; Russell, T. P. Size Control and Registration of Nano-Structured Thin Films by Cross-Linkable Units. *Soft Matter* **2008**, *4*, 475–479.

(47) Kathrein, C. C.; Bai, W.; Currivan-Incorvia, J. A.; Liontos, G.; Ntetsikas, K.; Avgeropoulos, A.; Böker, A.; Tsarkova, L.; Ross, C. A. Combining Graphoepitaxy and Electric Fields toward Uniaxial Alignment of Solvent-Annealed Polystyrene– B –Poly(dimethylsiloxane) Block Copolymers. *Chem. Mater.* **2015**, *27*, 6890–6898.

(48) Morkved, T. L.; Lu, M.; Urbas, a. M.; Ehrichs, E. E.; Jaeger, H. M.; Mansky, P.; Russell, T. P. Local Control of Microdomain Orientation in Diblock Copolymer Thin Films with Electric Fields. *Science (80-.).* **1996**, *273*, 931–933.

(49) Olszowka, V.; Hund, M.; Kuntermann, V.; Scherdel, S.; Tsarkova, L.; Böker, A. Electric Field Alignment of a Block Copolymer Nanopattern: Direct Observation of the Microscopic Mechanism. *ACS Nano* **2009**, *3*, 1091–1096.

(50) Bai, W.; Gadelrab, K.; Alexander-Katz, A.; Ross, C. A. Perpendicular Block Copolymer Microdomains in High Aspect Ratio Templates. *Nano Lett.* **2015**, *15*, 6901–6908.

(51) Gotrik, K. W.; Hannon, A. F.; Son, J. G.; Keller, B.; Alexander-Katz, A.; Ross, C. A. Morphology Control in Block Copolymer Films Using Mixed Solvent Vapors. *ACS Nano* **2012**, *6*, 8052–8059.

(52) Paik, M. Y.; Bosworth, J. K.; Smilges, D.; Schwartz, E. L.; Andre, X.; Ober, C. K. Reversible Morphology Control in Block Copolymer Films via Solvent Vapor Processing: An In Situ GISAXS Study. *Macromolecules* **2010**, *43*, 4253–4260.

(53) Kim, S. H.; Misner, M. J.; Xu, T.; Kimura, M.; Russell, T. P. Highly Oriented and Ordered Arrays from Block Copolymers via Solvent Evaporation. *Adv. Mater.* **2004**, *16*, 226–231.

(54) Kim, G.; Libera, M. Morphological Development in Solvent-Cast Polystyrene - Polybutadiene - Polystyrene (SBS) Triblock Copolymer Thin Films. *Macromolecules* **1998**, *31*, 2569–2577.

(55) Morris, M. A. Directed Self-Assembly of Block Copolymers for Nanocircuitry Fabrication. *Microelectron. Eng.* **2015**, *132*, 207–217.

(56) Arias-Zapata, J.; Böhme, S.; Garnier, J.; Girardot, C.; Legrain, A.; Zelsmann, M. Ultrafast Assembly of PS-PDMS Block Copolymers on 300 Mm Wafers by Blending with Plasticizers. *Adv. Funct. Mater.* **2016**, *26*, 5690–5700.

(57) Limary, R.; Green, P. F. Hierarchical Pattern Formation in Thin Film Diblock Copolymers above the Order - Disorder Transition Temperature. *Macromolecules* **1999**, *32*, 8167–8172.

(58) Smith, A. P.; Douglas, J. F.; Amis, E. J.; Karim, A. Effect of Temperature on the Morphology and Kinetics of Surface Pattern Formation in Thin Block Copolymer Films. *Langmuir* **2007**, *23*, 12380–12387.

(59) Sinturel, C.; Vayer, M.; Morris, M.; Hillmyer, M. a. Solvent Vapor Annealing of Block Polymer Thin Films. *Macromolecules* **2013**, *46*, 5399–5415.

(60) Stenbock-Fermor, A.; Rudov, A. A.; Gumerov, R. A.; Tsarkova, L. A.; Böker, A.; Möller, M.; Potemkin, I. I. Morphology-Controlled Kinetics of Solvent Uptake by Block Copolymer Films in Nonselective Solvent Vapors. *ACS Macro Lett.* **2014**, *3*, 803–807.

(61) Guo, R.; Huang, H.; Chen, Y.; Gong, Y.; Du, B.; He, T. Effect of the Nature of Annealing Solvent on the Morphology of Diblock Copolymer Blend Thin Films. *Macromolecules* **2008**, *41*, 890–900.

(62) Seidel, R.; Williamson, L.; Segal-Peretz, T.; Wu, G.; Suh, H.; Zhou, C.; Xiong, S.; Craig, G.; Nealey, P. Directed Self-Oriented Self-Assembly of Block Copolymers Using Chemically Modified Structures. In *Directed self-assembly of Block Copolymers for Nano-manufacturing*; Gronheid, R.; Nealey, P. F., Eds.; Elsevier Ltd., 2015; pp. 129–170.

(63) Edwards, E. W.; Montague, M. F.; Solak, H. H.; Hawker, C. J.; Nealey, P. F. Precise Control over Molecular Dimensions of Block-Copolymer Domains Using the Interfacial Energy of Chemically Nanopatterned Substrates. *Adv. Mater.* **2004**, *16*, 1315–1319.

(64) Kim, S. O.; Solak, H. H.; Stoykovich, M. P.; Ferrier, N. J.; Pablo, J. J. De; Nealey, P. F. Epitaxial Self-Assembly of Block Copolymers on Lithographically Defined Nanopatterned Substrates. *Lett. to Nat.* **2003**, *424*, 411–414.

(65) Stoykovich, M. P.; Müller, M.; Kim, S. O.; Solak, H. H.; Edwards, E. W.; Pablo, J. J. de; Nealey, P. F. Directed Assembly of Block Copolymer Blends into Nonregular Device-Oriented Structures. *Science (80-.).* **2005**, *308*.

(66) Ruiz, R.; Kang, H.; Detcheverry, F. A.; Dobisz, E.; Kercher, D. S.; Albrecht, T. R.; Pablo, J. J. De; Nealey, P. F. Density Multiplication and Improved Lithography by Directed Block Copolymer Assembly. *Science (80-.).* **2008**, *321*, 936–940.

(67) Stoykovich, M. P.; Kang, H.; Daoulas, K. C.; Liu, G.; Liu, C.; Pablo, J. J. De; Müller, M.; Nealey, P. F. Directed Self-Assembly of Block Copolymers for Nanolithography : Essential Integrated Circuit Geometries. *ACS Nano* **2007**, *1*, 168–175.

(68) Liu, C.; Han, E.; Onses, M. S.; Thode, C. J.; Ji, S.; Gopalan, P.; Nealey, P. F. Fabrication of Lithographically Defined Chemically Patterned Polymer Brushes and Mats. *Macromolecules* **2011**, *44*, 1876–1885.

(69) Cheng, J. Y.; Rettner, C. T.; Sanders, D. P.; Kim, H.-C.; Hinsberg, W. D. Dense Self-Assembly on Sparse Chemical Patterns: Rectifying and Multiplying Lithographic Patterns Using Block Copolymers. *Adv. Mater.* **2008**, *20*, 3155–3158.

(70) Segalman, R.; Yokoyama, H.; Kramer, E. Graphoepitaxy of Spherical Domain Block Copolymer Films. *Adv. Mater.* **2001**, *13*, 1152–1155.

(71) Segalman, R. A.; Hexemer, A.; Kramer, E. J. Edge Effects on the Order and Freezing of a 2D Array of Block Copolymer Spheres. *Phys. Rev. Lett.* **2003**, *91*, 196101–(1–4).

(72) Segalman, R. A.; Hexemer, A.; Kramer, E. J. Effects of Lateral Confinement on Order in Spherical Domain Block Copolymer Thin Films. *Macromolecules* **2003**, *36*, 6831–6839.

(73) Segalman, R. A.; Hexemer, A.; Hayward, R. C.; Kramer, E. J. Ordering and Melting of Block Copolymer Spherical Domains in 2 and 3 Dimensions. *Macromolecules* **2003**, *36*, 3272–3288.

(74) Chuang, V. P.; Cheng, J. Y.; Savas, T. A.; Ross, C. A. Three-Dimensional Self-Assembly of Spherical Block Copolymer Domains into V-Shaped Grooves. *Nano Lett.* **2006**, *6*, 2332–2337.

(75) Cheng, J. Y.; Ross, C. A.; Thomas, E. L.; Smith, H. I.; Vancso, G. J. Fabrication of Nanostructures with Long-Range Order Using Block Copolymer Lithography. *Appl. Phys. Lett.* **2002**, *81*, 3657–3659.

(76) Cheng, J. Y.; Mayes, A. M.; Ross, C. A. Nanostructure Engineering by Templated Self-Assembly of Block Copolymers. *Nat. Mater.* **2004**, *3*, 823–828.

(77) Cheng, J. Y.; Zhang, F.; Chuang, V. P.; Mayes, A. M.; Ross, C. A. Self-Assembled One-Dimensional Nanostructure Arrays. *Nano Lett.* **2006**, *6*, 2099–2103.

(78) Cheng, J. Y.; Ross, C. A.; Smith, H. I.; Thomas, E. L. Templated Self-Assembly of Block Copolymers: Top-Down Helps Bottom-Up. *Adv. Mater.* **2006**, *18*, 2505–2521.

(79) Cheng, J. Y.; Ross, C. A.; Thomas, E. L.; Smith, H. I.; Vancso, G. J. Templated Self-Assembly of Block Copolymers: Effect of Substrate Topography. *Adv. Mater.* **2003**, *15*, 1599–1602.

(80) Jung, Y. S.; Jung, W.; Ross, C. A. Nanofabricated Concentric Ring Structures by Templated Self-Assembly of a Diblock Copolymer. *Nano Lett.* **2008**, *8*, 2975–2981.

(81) Jung, Y. S.; Lee, J. H.; Lee, J. Y.; Ross, C. A. Fabrication of Diverse Metallic Nanowire Arrays Based on Block Copolymer Self-Assembly. *Nano Lett.* **2010**, *10*, 3722–3726.

(82) Nose, T. Coexistence Curves of Polystyrene/ Poly(dimethylsiloxane) Blends. *Polymer (Guildf).* **1995**, *36*, 2243–2248.

(83) Ross, C. A.; Jung, Y. S.; Chuang, V. P.; Ilievski, F.; Yang, J. K. W.; Bita, I.; Thomas, E. L.; Smith, H. I.; Berggren, K. K.; Vancso, G. J.; *et al.* Si-Containing Block Copolymers for Self-Assembled Nanolithography. *J. Vac. Sci. Technol. B Microelectron. Nanom. Struct.* **2008**, *26*, 2489–2494.

(84) Chai, J.; Buriak, J. M. Using Cylindrical Domains of Block Copolymers To Self-Assemble and Align. *ACS Nano* **2008**, *2*, 489–501.

(85) Park, S.-M.; Stoykovich, M. P.; Ruiz, R.; Zhang, Y.; Black, C. T.; Nealey, P. F. Directed Assembly of Lamellae- Forming Block Copolymers by Using Chemically and Topographically Patterned Substrates. *Adv. Mater.* **2007**, *19*, 607–611.

(86) ITRS. International Technology Roadmap for Semiconductors. **2013**, http://www.itrs.net.

(87) Griffiths, R. A.; Williams, A.; Oakland, C.; Roberts, J.; Vijayaraghavan, A.; Thomson, T. Directed Self-Assembly of Block Copolymers for Use in Bit Patterned Media Fabrication. *J. Phys. D. Appl. Phys.* **2013**, *46*, 503001.

(88) Albrecht, T. R.; Bedau, D.; Dobisz, E.; Gao, H.; Grobis, M.; Hellwig, O.; Kercher, D.; Lille, J.; Marinero, E.; Patel, K.; *et al.* Bit Patterned Media at 1 Tdot / in and Beyond. *IEEE Trans. Magn.* **2013**, *49*, 773–778.

(89) Hellwig, O.; Bosworth, J. K.; Dobisz, E.; Kercher, D.; Hauet, T.; Zeltzer, G.; Risner-Jamtgaard, J. D.; Yaney, D.; Ruiz, R. Bit Patterned Media Based on Block Copolymer Directed Assembly with Narrow Magnetic Switching Field Distribution. *Appl. Phys. Lett.* **2010**, *96*, 052511.

(90) Yang, X.; Xiao, S.; Hsu, Y.; Feldbaum, M.; Lee, K.; Kuo, D. Directed Self-Assembly of Block Copolymer for Bit Patterned Media with Areal Density of 1.5 Teradot / Inch2 and Beyond. *J. Nanomater.* **2013**, *2013*.

(91) Xiao, S.; Yang, X.; Lee, K. Y.; Hwu, J. J.; Wago, K.; Kuo, D. Directed Self-Assembly for High-Density Bit-Patterned Media Fabrication Using Spherical Block Copolymers. *J. Micro/Nanolithography, MEMS, MOEMS* **2013**, *12*, 031110.

(92) Tsai, H.; Pitera, J. W.; Miyazoe, H.; Bangsaruntip, S.; Engelmann, S. U.; Liu, C.; Cheng, J. Y.; Bucchignano, J. J.; Klaus, D. P.; Joseph, E. A.; *et al.* Two-Dimensional Pattern Formation Using Graphoepitaxy of PS - B - PMMA Block Copolymers for Advanced FinFET Device and Circuit Fabrication. *ACS Nano* **2014**, *8*, 5227–5232.

(93) Delgadillo, P. A. R.; Thode, C. J.; Neisser, M.; Nealey, P. F.; Neisser, M. Implementation of a Chemo-Epitaxy Flow for Directed Self-Assembly on 300-Mm Wafer Processing Equipment Self-Assembly on 300-Mm Wafer Processing Equipment. *J. Micro/Nanolith. MEMS MOEMS* **2012**, *11*, 031302–(1–5).

(94) Luo, Y.; Montarnal, D.; Kim, S.; Shi, W.; Barteau, K. P.; Pester, C. W.; Hustad, P. D.; Christianson, M. D.; Fredrickson, G. H.; Kramer, E. J.; *et al.* Poly(dimethylsiloxane- B -Methyl Methacrylate): A Promising Candidate for Sub-10 Nm Patterning. *Macromolecules* **2015**, *48*, 3422–3430.

(95) Ghoshal, T.; Ntaras, C.; Shaw, M. T.; Holmes, J. D.; Avgeropoulos, A.; Morris, M. A. A Vertical Lamellae Arrangement of Sub-16nm Pitch (domain Spacing) in a Microphase Separated PS-B-PEO Thin Film by Salt Addition. *J. Mater. Chem. C* **2015**, *3*, 7216–7227.

(96) Ghoshal, T.; Ntaras, C.; O'Connell, J.; Shaw, M. T.; Holmes, J. D.; Avgeropoulos, A.; Morris, M. a. Fabrication of Ultra-Dense Sub-10 Nm in-Plane Si Nanowire Arrays by Using a Novel Block Copolymer Method: Optical Properties. *Nanoscale* **2016**.

(97) Park, S.-M.; Park, O.-H.; Cheng, J. Y.; Rettner, C. T.; Kim, H.-C. Patterning Sub-10 Nm Line Patterns from a Block Copolymer Hybrid. *Nanotechnology* **2008**, *19*, 455304.

(98) Van Eikenstein, G. O. R. A.; Meyboom, R.; tne Brinke, G.; Ikkala, O. Determination of the Flory - Huggins Interaction Parameter of Styrene and 4-Vinylpyridine Using Copolymer Blends of Poly(styrene. *Macromolecules* **2000**, *33*, 3752–3756.

(99) Chaudhari, A.; Ghoshal, T.; Shaw, M. T.; Cummins, C.; Borah, D.; Holmes, J. D.; Morris, M. A. Formation of Sub-7 Nm Feature Size PS-B-P4VP Block Copolymer Structures by Solvent Vapour Process. *Proc. SPIE 9051, Adv. Patterning Mater. Process.* **2014**, *9051*.

(100) Sinturel, C.; Grosso, D. Structural Transitions in Asymmetric Poly (styrene)-Block-Poly (lactide) Thin Films Induced by Solvent Vapor Exposure. *ACS Appl. Mater. Interfaces* **2014**, *6*, 12146–12152.

(101) Kennemur, J. G.; Hillmyer, M. A.; Bates, F. S. Synthesis, Thermodynamics, and Dynamics of Poly(4-Tert - Butylstyrene - B - Methyl Methacrylate). *Macromolecues* **2012**, *45*, 7228–7236.

(102) Jeong, J. W.; Park, W. I.; Kim, M.-J.; Ross, C. A.; Jung, Y. S. Highly Tunable Self-Assembled Nanostructures from a poly(2-Vinylpyridine-B-Dimethylsiloxane) Block Copolymer. *Nano Lett.* **2011**, *11*, 4095–4101.

(103) Rodwogin, M. D.; Spanjers, C. S.; Leighton, C.; Hillmyer, M. A. Polylactide-Poly(dimethylsiloxane)-Polylactide Triblock Copolymers as Multifunctional Materials for Nanolithographic Applications. *ACS Nano* **2010**, *4*, 725–732.

(104) Cushen, J. D.; Otsuka, I.; Bates, C. M.; Halila, S.; Fort, S.; Rochas, C.; Easley, J. a; Rausch, E. L.; Thio, A.; Borsali, R.; *et al.* Oligosaccharide/silicon-Containing Block Copolymers with 5 Nm Features for Lithographic Applications. *ACS Nano* **2012**, *6*, 3424–3433.

(105) Jeong, J. W.; Park, W. I.; Do, L.-M.; Park, J.-H.; Kim, T.-H.; Chae, G.; Jung, Y. S. Nanotransfer Printing with Sub-10nm Resolution Realized Using Directed Self-Assembly. *Adv. Mater.* **2012**, *24*, 3526–3531.

(106) Huda, M.; Akahane, T.; Tamura, T.; Yin, Y.; Hosaka, S. Fabrication of 10-Nm-Order Block Copolymer Self-Assembled Nanodots for High-Density Magnetic Recording. *Jpn. J. Appl. Phys.* **2011**, *50*, 06GG06.

Chapter 2 Pattern Generation of Lines via Solvent Vapor Annealing of a Cylindrical PS-b-PDMS

2.1 Introduction

This chapter deals with the phase-separation of a cylindrical PS-b-PDMS system with overall molecular weight of M_n = 45kg/mol. The natural domain spacing is of 35 nm. As introduced in chapter 1, in order to overcome the local free energy maximum and trigger the self-assembly process in BCPs, two main methods are used, thermal annealing (TA), where the BCP is heated for a certain amount of time and solvent vapor annealing (SVA) were solvent molecules swell the BCP layer. More atypical annealing methods have also been proposed in the literature, among them electric fields[1], microwaves[2] and soft shears[3]. Thermal annealing is quite simple, the BCP system is raised above its glass transition temperature (T_g) and below the order-disorder transition (ODT) in order to induce sufficient chain mobility[4]. However, high molecular weight or high-χ BCPs in the strong segregation regime (where $\chi N \approx 100$) have a high diffusive energy barrier, and TA would need a considerable amount of time (several tens of hours) in order to achieve satisfactory phase separation[5]. Therefore, high-χ BCPs are often annealed by SVA, where BCPs are exposed to vapors of a solvent or a mix thereof. Vapor molecules enter the polymer film and act as a plasticizer by decreasing the effective T_g and the effective Flory-Huggins interaction parameter, χ_{eff}, of the BCP[6]. Consequently the diffusive energy barrier is lowered and chains acquire sufficient mobility. The self-assembly process can be significantly sped up to some hours or minutes[7]. However, SVA is much more complex than TA. Differences in the solubility of the solvent towards the blocks can cause changes in the volume fraction and consequently in the final morphology. The solvent mediates non-favorable interactions between the blocks if the solvent is neutral, i.e., equal solubility in both blocks. On the other hand, if the solvent is selective, these interactions can be increased. The solvent concentration determines the polymer chain mobility. The higher the concentration of the solvent, the higher the mobility. However, a BCP being initially above the order-disorder transition can be driven below this transition if the solvent concentration is high enough. Drying from a disordered state is different from drying from a micro separated state. Once, the BCP is disordered it can phase separate upon evaporation of the solvent. Ordering starts at the BCP/surface interface, where the evaporation starts, and propagates into the film as depicted in Figure 2-1[8]. In this way the ordering, that was formed initially at the surface, is transferred into the whole film.

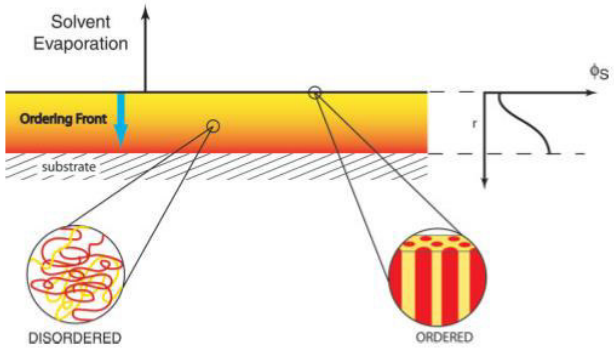

Figure 2-1: Schematic of the ordering front that propagates into the film, when the solvent is evaporated after SVA. [8]

Numerous parameters have great influence on the final dried state, which are more or less easy to be controlled. These include annealing chamber size, surface area of the solvent, proximity of the sample to the solvent surface, vapor pressure of the solvent, temperature, humidity, time in swollen state, time of solvent evaporation. In simple benchmark systems not all of these parameters can scrupulously be controlled and a lack of consistency in results is often observed. However, SVA has been adopted as the most common annealing method to promote microphase separation of PS-b-PDMS.

On plane substrates, self-assembled features are aligned in small areas not larger than a few square micrometers but when the self-assembly of block copolymers is constrained or directed (directed self-assembly=DSA), large area regular patterns can be produced with feature sizes smaller than 10 nm[9–13]. The structure-directing surface pattern can either be a chemical (chemoepitxy) or a topographical (graphoepitaxy) pattern. Both approaches are governed by the size and quality of the lithographically defined surface pattern rather than by the inherent limitations of the self-assembly process. DSA was introduced in the International Technology Roadmap for Semiconductors (ITRS) in order to complement advanced optical lithography techniques by increasing the resolution[18]. In this chapter, the directed self-assembly of high-χ block copolymers (PS-PDMS, M_w=45.5kg/mol, f_{PDMS} = 31%), triggered by SVA is demonstrated as a complement to conventional 193 nm wavelength photolithography. Surface interactions, influence of the solvent solubility and GISAXS *in-situ* measurements will be presented. In the next section, we will briefly describe the experimental conditions adopted for the development of our graphoepitaxy DSA process for PS-b-PMDS

2.2 Experimental Details

The block copolymer of PS-b-PDMS with an overall molecular weight of 45.5 kg/mol is purchased from Polymer Source, Inc. and used as received. All solvents used for annealing or solution preparation are purchased from Sigma Aldrich. The patterned substrates are printed with a photoresist by 193 nm lithography (Nikon S307E 0.85NA dry ArF scanner) on the following stack: 577 nm photolithography

resist/35 nm Si anti-reflective coating layer/50 nm (or 95 nm) spin on carbon/silicon substrate. This stack is generated using a SOKUDO RF3 coating track. All parameters used are set on the basis of suppliers recommendations. Achieved resolution is better than 100 nm. The graphoepitaxy trenches are then created by etching the SiArc/SOC substrates with $Ar/CF_4/CHF_3$ and HBr/O_2 chemistries for SiArc and partial SOC etching, respectively, leading to a guiding trench depth of 45 to 60 nm depending on the initial SOC layer thickness, the mesa and trench width varied between 125 nm and 1.5 µm. The full process of DSA for PS-b-PDMS is depicted in Figure 2-2.

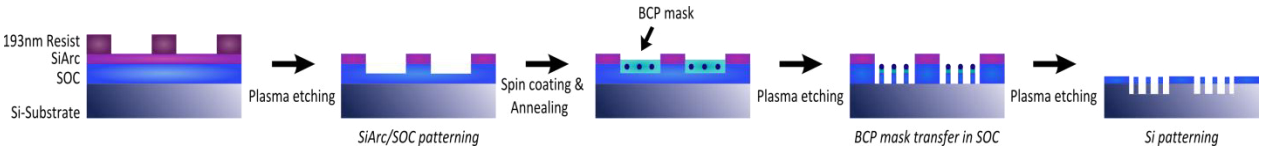

Figure 2-2: Process flow of the directed self-assembly of BCP45 using SiARC/SOC trilayer stacks. First the guiding trenches with desired depth are created using a 193 nm resist and plasma etching. Then the BCP is deposted by spin coating and annealed by solvent vapor annealing. PS and SOC are etched away and simultaneously the PDMS structures are oxidized. Finally, the PDMS nanostructures can be used as a hard mask for Si transfer etching.

The copolymer is spin-coated from a PGMEA-solution of 1% by weight on the substrates. The as-spun film thickness was chosen so that, after solvent vapor annealing, a monolayer of cylinders is present within the trenches. Then the samples are annealed in different solvent vapors in a closed, conventional Petri dish at room temperature for 5 min to 16 hours. The vapor pressure is controlled via the ratio of the surface area of the liquid and the volume of the annealing chamber. The annealed film is then treated with CF_4 plasma (etching time = 7 s, gas flow rate = 100 sccm, working pressure = 4 mTorr and plasma power = 700 W) to remove the top wetting layer of PDMS and then O_2 plasma (etching time = 15 s, gas flow rate = 100 sccm, working pressure = 4 mTorr and plasma power = 700 W) to remove the PS-block leaving oxidized PDMS cylinders at the surface. Subsequent transfer etching is performed in a two-step process. First, the nanopatterns are transferred into the remaining SOC layer and then into the silicon substrate by dedicated plasma etching processes. More details on the pattern transfer etching process will be explained in chapter 5.

After wetting layer removal and PS etching, the surface morphology can be observed by scanning electron microscopy (Hitachi S-5000 or JEOL 7500F). Focused ion beam scanning transmission electron microscopy (FIB-STEM, Helios 450S – FEI) for cross-section images were done without etching. Instead, the samples were covered with a platinum thin layer and a blade was milled by focus ion beam (FIB).

Surface energies were obtained on a Kruss Drop Shape Analyzer 100 by contact angle measurements of three different liquids of known surface tension (water, ethylene glycol and diiodomethane). The surface

energy was then calculated with the Good-van-Oss model by using the mean value of three measurements for each liquid.

The GISAXS measurements were performed on the BM02 beamline at the European Synchrotron Radiation Facility (ESRF) in Grenoble (France). A 1 mm wide and 100 µm high X-ray beam impinged onto the sample at a grazing incidence angle α_i = 0.13°. The X-ray wavelength was 0.083 nm, corresponding to an energy beam of 15 keV; the sample-detector distance was 4.88 m; and the scattered intensity was detected by using a 2D XPAD detector with image sizes of 1148 × 578 pixels with a dimension of 130 × 130 µm^2 for a single pixel. Line roughness measurements for the quantitative analyses of the critical dimension (CD), line width roughness (LWR), and line edge roughness (LER) were performed treating manually obtained SEM images with a commercial image analysis software (TerminalPC from Hitachi). The obtained values are mean values from 10 measurements in the same guiding trench width.

2.3 Effect of Substrate Wetting on PS-b-PDMS (Mw=45.5kg/mol)

The polymer/substrate interface plays a very important role during self-assembly of block copolymers. On untreated Si substrates, a PDMS layer is formed at the substrate/BCP interface due to surface tensions of Si and PDMS. This PDMS layer causes serious difficulties during the subsequent pattern transfer by minimizing the effectiveness of the selective Si:SiO_2 etch chemistry[19]. Furthermore, the strong interaction of PDMS and the hydroxyl-terminated polar native silicon oxide surface lead to dewetting and non-equilibrium morphologies of the BCP[9,19]. These issues make it necessary to pretreat the Si surface with homopolymer-brushes for example. It was shown that a PDMS-brush treatment enhances the diffusivity of the BCP and good alignment of the BCP can be obtained[9,19]. However the PDMS-brush at the substrate/BCP interface is still a problem for transfer etching. Treating the Si surface with a PS-brush seems to be a good trade-off between transfer etch possibilities and alignment of the BCP[19]. Surface wetting of the majority block of the BCP seems to improve the self-assembly, ordering and wetting and minimize defect quantity[20]. This study is concentrated on graphoepitaxial applications of PS-b-PDMS in order to enhance long range ordering and to give indications about technological possibilities of this BCP. In order to prove the concept of DSA lithography, it is important to operate with standard industry equipment and techniques. Trilayers of a 193 nm resist/ silicon antireflective coating/ spin-on-carbon (SiArc/SOC) are standard lithography stacks in industry. In this thesis, all graphoepitaxial studies were performed in these stacks, if not stated otherwise, and a sketch of the layer configuration can be seen in Figure 2-3. A detailed description of the purpose of each layer is given in chapter 5.

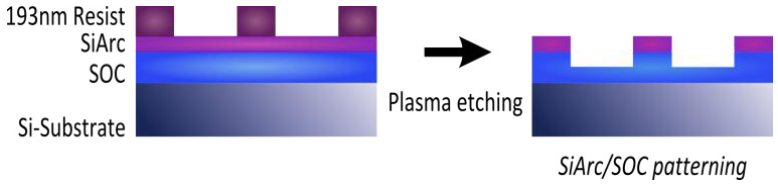

Figure 2-3 Sketch of a 193 nm Resist/SiArc/SOC trilayer before and after trench etching

In order to obtain guiding trenches for BCP assembly, the 193 nm resist is used as etching mask to create trenches in the SOC layer of approximately 45 nm depth. Both sidewalls and the bottom of the trenches should present a preferential attraction to the majority block of the copolymer as explained above, in order to efficiently direct the self-assembly and facilitate the long-range ordering of horizontal cylinders along the patterned trenches. Here, the trenches are mostly composed of SOC, a carbon based material which has similar properties as a PS homopolymer. In order to evaluate further properties of PS-b-PDMS on SOC surfaces further investigations were performed.

The SOC solution was spin-coated on bare silicon substrates to obtain a layer of approximately 30 nm. In order to mimic the activated surface chemistry present in graphoepitaxy trench after trench design etching (see experimental section of this chapter), the substrates were exposed to HBr/O_2 plasma for 20s. In order to simplify the process pure O2 plasma was tested also and it was found that this treatment for 20s resulted in similar results as samples treated with HBr/O2 plasma. In accordance, surface energies were measured to be ≈ 37.6 for HBr/O_2 plasma treated samples and ≈41.1 for O_2 treated samples, thus very similar. Further on, SOC samples were treated with oxygen plasma in O_2 plasma cleaner to "activate" the surface. Figure 2-4 shows a top view SEM micrograph and GISAXS profile of SD45 after SVA on plane SOC surfaces without topography and brush surface treatment. The peak position of the GISAXS scattering profile of Figure 2-4 corresponds to the periodicity of SD45 and gives a value of ≈ 35±1 nm. The corresponding SEM image reveals well aligned cylinders after this solvent vapor annealing without the use of any brush surface treatment. It is suggested that the high chemical similarity between SOC (mostly composed of carbon) and PS leads to advantageous wetting behavior towards PS-b-PDMS, making it unnecessary to treat the surface with additional polymer brushes or other functional layers.

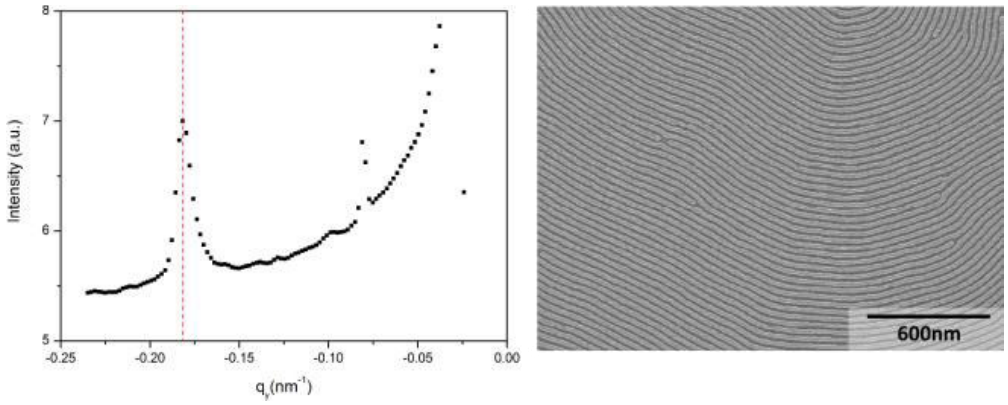

Figure 2-4: (left) GISAXS profile of SD45 on plane SOC surface, annealed for 75min in toluene vapor. (right) SEM top view image of the same sample after plasma etching to reveal PDMS cylinders for SEM observation

In order to analyze the BCP/SOC interface, scanning transmission electron microscopy (STEM) was performed on self-assembled SD45 within SiArc/SOC trenches. In the cross section micrographs of Figure 2-4(a,b), PDMS domains are distinguished by the image contrast appearing as dark patterns.

It is known that PDMS has lower surface tension compared to PS, and preferentially wets the air/polymer interface. Although, not visible in the STEM images due to the thick platinum layer on the trenches, water contact angle measurements on PS-brush, PDMS-brush, and the BCP emphasize the presence of a PDMS surface layer. The water contact angles of PDMS- and PS-brush have been reported to be approximately 114° and 95° respectively. The as-spun BCP film and solvent vapor annealed film on planar SOC substrates were found to have a water contact angle of about 109° and 108°, respectively, indicating PDMS rich surface layers. On SOC substrates, it has been found that plasma etching requires a short CF_4 burst (withdrawal of the PDMS surface layer) to efficiently reveal and transfer the assembled PDMS lines. Consequently, for SEM observations, the thin PDMS surface layer has systematically to be removed by CF_4 plasma in order to reveal the underlying PDMS nanostructures.

At the BCP/SOC interface no dark pattern can be distinguished in the STEM micrograph of Figure 2-5 indicating the absence of a PDMS interlayer that could prevent pattern transfer etching. This observation can further be confirmed by the fact that the transfer etching of the PDMS lines into the SOC layer can be carried out with a simple HBr/O_2 plasma. A PDMS wetting layer at the interface would be oxygen resistant, and would consequently not allow such a transfer etching. This wetting behavior allows indeed the wetting of the PS block (BCP matrix) and thus in addition the rapid formation of horizontal PDMS cylinders parallel to the trenches. These results confirm the fact that it is unnecessary to treat the graphoepitaxy trenches with an additional brush-layer for the assembly of SD45.

It can be noticed that the PDMS cylinders show an elliptic shape, which has already been observed elsewhere[4] and is commonly attributed to the solvent evaporation at the very end of SVA when decreasing from the swollen to the final dried state[6].

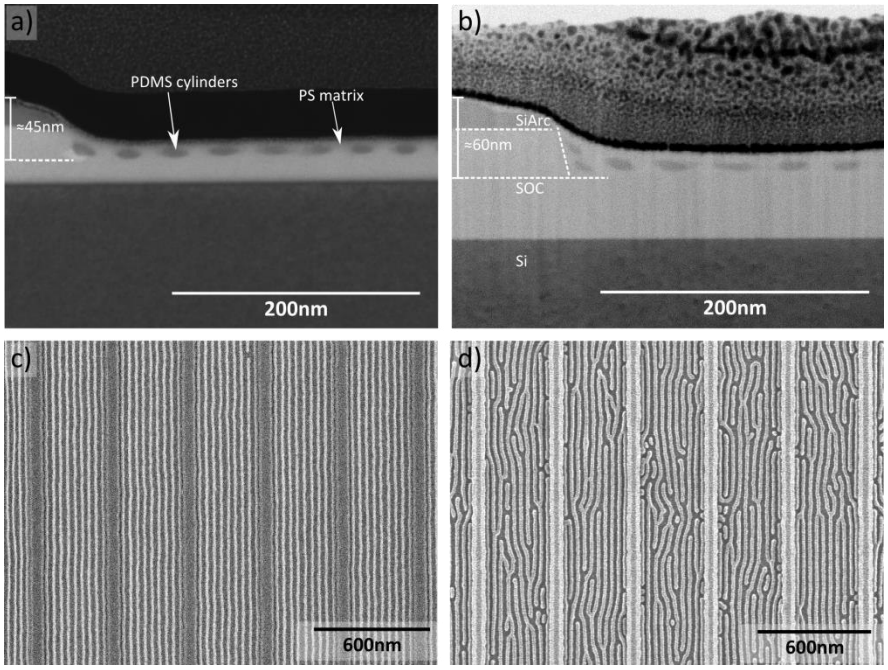

Figure 2-5: (a-b) FIB-STEM cross section images of SD45 in 45 nm (a) deep and 60 nm (b) deep SiArc/SOC trenches after 75min SVA in toluene. (c-d) corresponding SEM top view images

Furthermore, it was discovered that the phase separation process depends also on the depth of the guiding trenches. Therefore two different SiArc/SOC stacks have been investigated. One stack has an initial SOC layer of 95 nm and is etched to obtain 60 nm deep trenches, leaving a 40 nm SOC layer. The other stack has initially a 50 nm high SOC layer and is etched to obtain trenches of about 45nm depth. The remaining SOC layer is approximately 20 nm high. The natural periodicity of SD45 (≈35 nm) is close to the smaller trench depth and can have influence on the obtained PDMS alignment. Figure 2-5(c,d) show top view SEM images of 45 nm deep and 60 nm trenches respectively after the same annealing process (75 min SVA toluene). It can be observed that the quality of the alignment is much more homogeneous with longer correlation length for smaller trench depth. When regarding the corresponding STEM micrographs in Figure 2-5(a,b) it can be seen that in deeper trenches the large wetting of the copolymer with the sidewalls leads to a double layer of cylinders in the edges. This extra layer of cylinders disturbs the self-assembly process, leading to a lower pattern quality, which is why we worked further on with the smaller trench depth to smooth the path for the best alignment results.

2.4 Graphoepitaxy and Solvent-Vapor Annealing of SD45 in SiArc/SOC Trenches

The full DSA process was described above in the experimental section and is depicted in Figure 2-2. In this section we will concentrate on the solvent vapor annealing of SD45. In order to trigger the self-assembly mechanism in high χ and high N BCP the annealing by solvent vapor has been introduced. During this procedure, the BCP thin film is exposed to solvent vapors and the film swells due to thermodynamic driving forces associated with the entropy of mixing inducing a screening effect where the unfavorable interfaces between blocks are diluted[6]. Furthermore, the effective Flory-Huggins interaction parameter (χ_{eff}) is decreased as the volume fraction of the solvent (f_s) in the film is increased[21]. This way phase-separation is possible at room temperature.

The solvent vapor annealing setup of this study is schematized in Figure 2-6, and was performed in Petri dishes. The setup is rather simple: a first, large Petri dish contains a smaller one which serves as sample holder. The larger Petri dish is then filled with a certain amount of solvent and closed with a lid. Numerous parameters, like environmental conditions, solvent selectivity, solvent vapor pressure, time in swollen state, drying speed etc. are known to impact the final dried BCP pattern. In order to precisely control the vapor pressure Gotrik et al. proposed sophisticated set up where an inert gas bubbles through the annealing solvent, transporting it into the annealing chamber towards the sample[22]. Those types of setup are useful in order to control the vapor pressure by controlling the gas flow, but have its limits as the solvent is always diluted in the inert gas. We chose therefore to work with a chamber set up where the solvent is directly exposed to the sample. In order to give a minimum of reproducibility the experiments were carried out in the same Petri dish system and were located in a class100 clean room where humidity and temperature are kept at a constant level. Furthermore the volume of the solvent was kept constant and before each experiment the solvent was introduced into the chamber at least 2h before the sample in order to stabilize the vapor pressure conditions in the chamber.

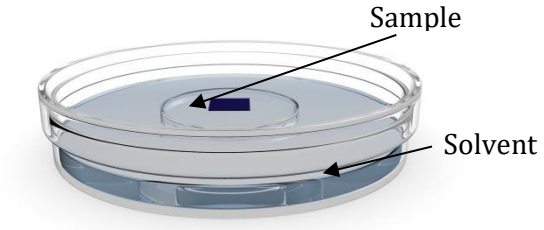

Figure 2-6: Schematic of the solvent vapor annealing setup

Most commonly, the BCP is swelled with solvents that have neutral or only weak selectivity towards both blocks in order to obtain homogeneous swelling. The solvent uptake of each block is related to its compatibility to the solvent and can result in differential swelling, modifying the effective volume fraction

of the blocks and thus the final morphology[6]. In the literature, a common studied solvent for PS-PDMS annealing is toluene [12,19,23–25]. Hence to start our investigation, we first concentrated on solvent annealing with toluene vapor. The solvent vapor pressure was kept as constant as possible by keeping the solvent surface area to annealing chamber volume at approximately 0.6 cm^{-1}. Figure 2-7 shows a systematic trend of cylinder alignment as a function of annealing time (mesa width at constant periodicity). As-spun, SD45 arranges itself as spherical micelles, since the spin solvent is propylene glycol monomethyl ether acetate (PGMEA). PGMEA is a PS selective solvent, which means that PS is more soluble in PMGEA than PDMS. These solubility differences produce micelles in solution as will be described in chapter 3. The obtained as-spun micelles are disordered and show no homogeneity in size. After 15 min annealing the micelles start to grow and one can distinguish a beginning of ordering near to the mesa walls. After 30 min the morphology has completely changed to cylinders but there is no order except at the far edges of the mesa. Finally, after 75min of solvent vapor annealing, cylinders are perfectly aligned with respect to the guiding trenches. We could thus confirm already reported annealing results in toluene vapor and further decrease process time from several hours to 75min thanks to the optimization of the substrate.

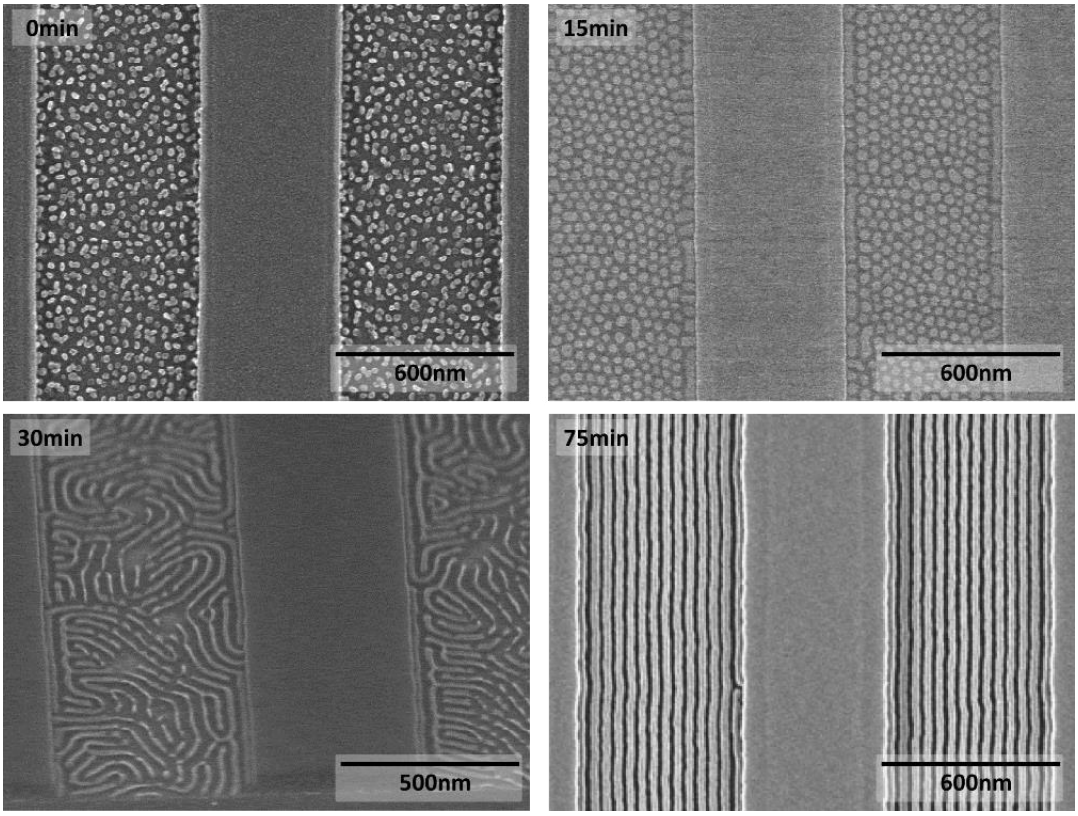

Figure 2-7: SEM micrographs of SD45 in SiArc/SOC trenches after different times of annealing in toluene vapor

Once we obtained first knowledge about the behavior of SD45 in toluene vapor, further studies oriented towards the integration of block copolymers in industry have to be performed. SVA in general and

especially in toluene vapors presents several disadvantages: toluene and other commonly used SVA solvents are toxic, flammable and rarely used in microelectronic industry. The ITRS indicates that all new chemicals introduced in manufacturing need to be cleared to not induce new hazards on human health, safety, and the environment[18]. In order to promote industry application, we now concentrate on safe solvents. A comparison of different safe solvents (Butanone, PGMEA, cyclohexanone, ethylacetate, butylacetate and isobutylacetate) which are more suitable for industry as they are non-toxic for humans and for the environment is presented hereafter.

Apart from safety issues, the choice of the right solvent is conducted by the selectivity of the solvent towards the polymer blocks. Polymers dissolve in solvents whose solubility parameter is similar to their own. Hildebrandt and Scott were the first to introduce the term "solubility parameter" and the Hildebrandt solubility parameter is defined as $\delta = (E/V)^{1/2}$, where V is the volume of pure solvent, and E is its measurable energy of vaporization[26]. The Hildebrandt theory however does not take into account molecular interactions that can influence the affinity of solvent and polymer. One good alternative is the Hansen solubility parameter (HSP) that is a multicomponent parameter and has been widely used[27].

However, solubility parameters were established for bulk solvents in which a polymer is dissolved. In SVA of thin BCP monolayers, the density of the solvent, as it concerns only the vapor, is not the same as the bulk solvent and thus its vapor pressure plays most certainly a crucial role in selectivity[6]. For comparison Figure 2-8 shows total HSPs (for better comparability we have simplified the HSP to the total value) of selected solvents with their corresponding vapor pressures.

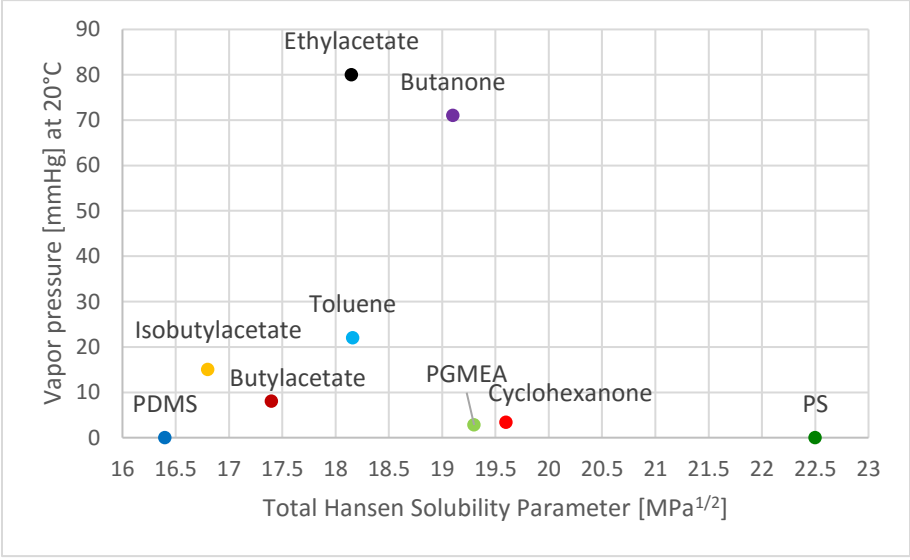

Figure 2-8: Vapor pressure vs. total Hansen solubility parameter of selected safe solvents and the polymers PS and PDMS[27]

The final morphology of a BCP depends on the volume ratio between the two blocks which is first determined by the degree of polymerization of each block. By adding a PS selective solvent, for example,

the total volume fraction of PS increases whereas that of PDMS decreases, resulting in a morphology shift. Self-assembly by SVA is a very sensitive process which is not only dependent on the solvent, but also on BCP layer thickness, mesa size, trench depth, vapor pressure and many more. In order to investigate the influence of all these parameters a very sophisticated experiment setup would be needed where parameters could be changed in all possible variations. This kind of statistical analysis is very complex but in order to get an impression of the influence of solvent, we tested solvent vapor annealing of SD45 with the above shown solvents for 75min to compare with results obtained with toluene. For all samples, SD45 was spin-coated from a 1wt% solution in PGMEA in order to obtain a monolayer of cylinders within the trenches (layer thickness ≈ 22 nm on plane SOC surfaces before annealing, corresponding to approximately 35nm inside the trenches after annealing). Figure 2-9 shows top view SEM images of these samples after annealing in the Petri dish set-up. Note that the revealing etching steps were not always the same, which is why different electron contrasts are observed in different images. This might also affect the PDMS domain size, as the CF4 step was not kept constant for all samples.

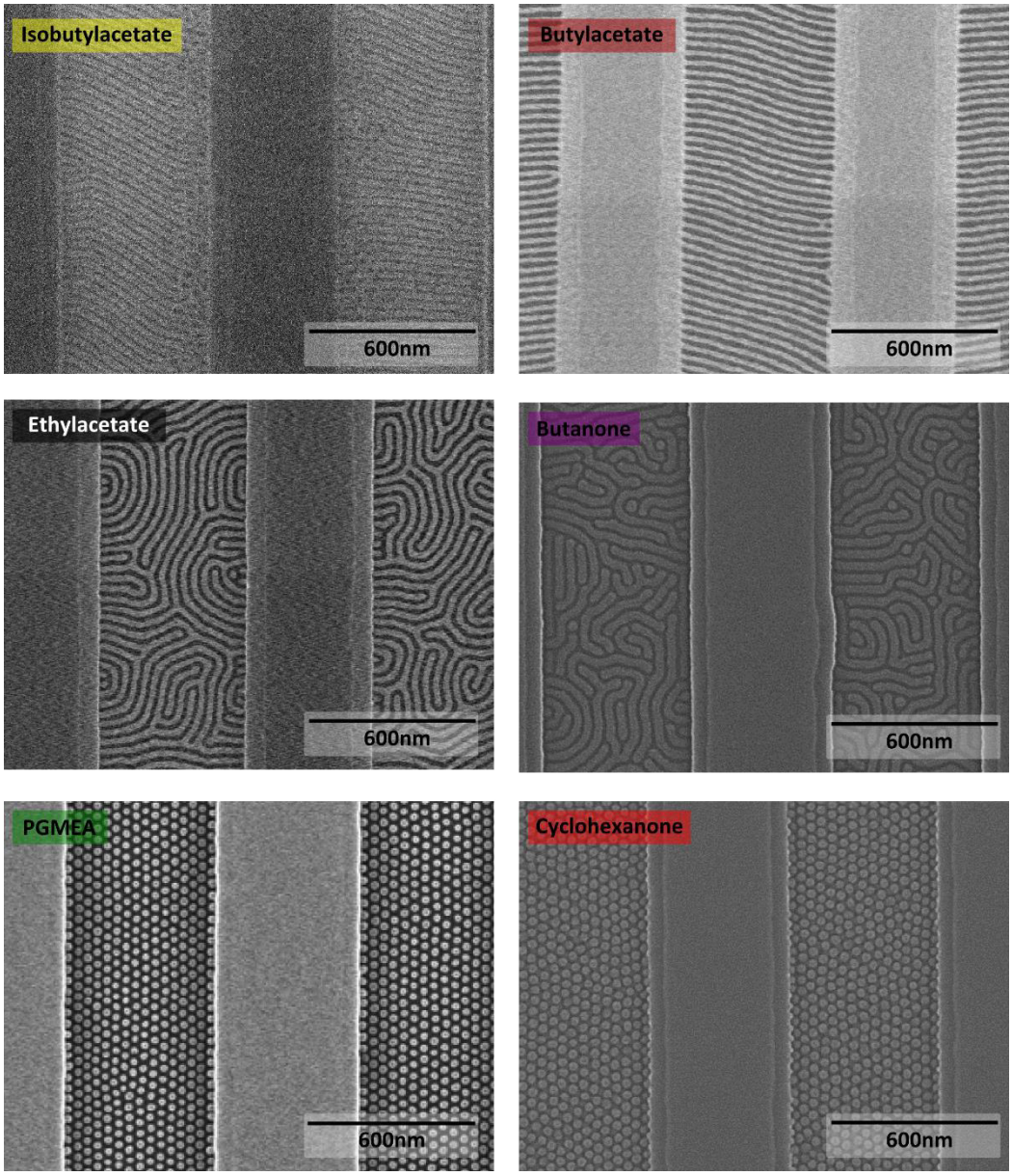

Figure 2-9: Top-view SEM images of SD45 after 75min SVA in different solvent vapors

As we can see, PGMEA and cyclohexanone result completely in what appears to be spherical morphology. Both solvents are PS selective and provide low mobility increase, due to the low vapor pressure. Therefore, the morphology of the cylindrical SD45 results in spherical alignment. However in thin films of approximately 30nm we cannot conclude with certainty that the morphology is spherical. Another possibility is a vertical orientation of the PDMS cylinders triggered by BCP/solvent vapor interface interactions. In order to definitely define the morphology additional in-depth studies of the film have to be made. In any case, we obtain a good alignment of these vertical cylinder or spheres for both solvents.

Ethylacetate and butanone show cylinder morphology but no long-range ordering. Ethylacetate is neutral, it has the same selectivity as toluene, and butanone is slightly more PS selective. In both cases the vapor pressure is very high. It is known that solvent incorporation reduces the X_{eff}. The higher the solvent concentration in the film, the more X_{eff} is decreased. The vapor pressure of the solvent is responsible for the swelling of the film and thus the relative concentrations of polymer and solvent in the film. In the cases of butanone and ethylacetate, as of their high vapor pressure, the solvent concentration becomes very high and the system drops below the order-disorder-transition. When swelled, SD45 is thus disordered and phase separates only when the chamber is opened and the solvent evaporates. As presented in the introduction of this chapter, it was shown that, when the film is in a disordered state when swelled, an ordering front propagates from the BCP/air interface to the BCP/substrate interface upon solvent evaporation, due to solvent concentration differences[8]. As the solvent evaporates very quickly and the layer is very thin in our case, the system phase separates during evaporation but has no time to align in parallel lines, and remains in a "fingerprint" configuration. Moreover, it can be observed that cylinders formed in ethylacetate are longer, i.e. better developed, than those formed in butanone. The selectivity parameter of butanone (19.1 $MPa^{1/2}$) is very close to that of PGMEA (19.3) so at the frontier between neutral and PS-selective solvents. The PS block is thus more plasticized, leading to short cylinders.

Films annealed in isobutylacetate and butylacetate show principally cylindrical morphology, but we see partially perforated lamellas for isobutylacetate (only poorly visible in the edge of the trenches). In this case the high PDMS selectivity of isobutylacetate leads to the inversion of the majority part, making PDMS the matrix block, leading to PS cylinders that are etched away. For both solvents, long range cylinders that are well aligned in perpendicular direction to the trenches are observed. The perpendicular orientation could be due to capillary flow from mesas to trenches. It is assumed that the BCP, while swelled, is higher than the mesas, leading to perpendicular cylinders when flowing back in the trenches, during drying. The spheres and cylinders that can be seen on the edges of the mesas, especially in the case of butylacetate, confirm this assumption. Perpendicular orientation is known to be a metastable condition which could be replaced by parallel orientation when annealing for longer times[9]. Even though the orientation is perpendicular, we think that butylacetate, as it leads to clean cylinders, has the greatest potential for an appropriate safe annealing solvent. After only 20min annealing, SD45 shows long range alignment on structured and on plane surfaces, like PS-brushed silicon, as can be seen in Figure 2-10.

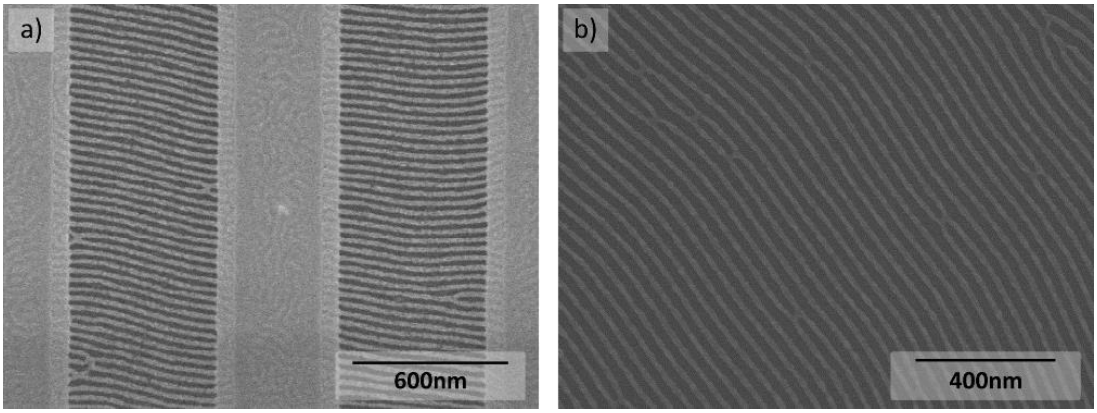

Figure 2-10: Top view SEM images of SD45 after 20min annealing in butylacetate on (a) SiArc/SOC trenches and (b) on plane SOC surface

Even though we were not able to align SD45 horizontally along the guiding trenches, it is reasonable to say that when adjusting annealing time, it will be possible to align SD perfectly horizontal with butylacetate.

After close analysis of the obtained data, we were able to develop a cartography of different morphologies as a function of vapor pressure and selectivity of the solvent, as shown in Figure 2-11. Areas in which perforated lamellar, cylinders or spheres can be obtained are defined. A vapor pressure limit is estimated above which ordering becomes difficult as the BCP is too much diluted and X_{eff} passes the ODT while swelled. As we tested only solvents with "extreme" vapor pressures, the exact limit is not definitely known.

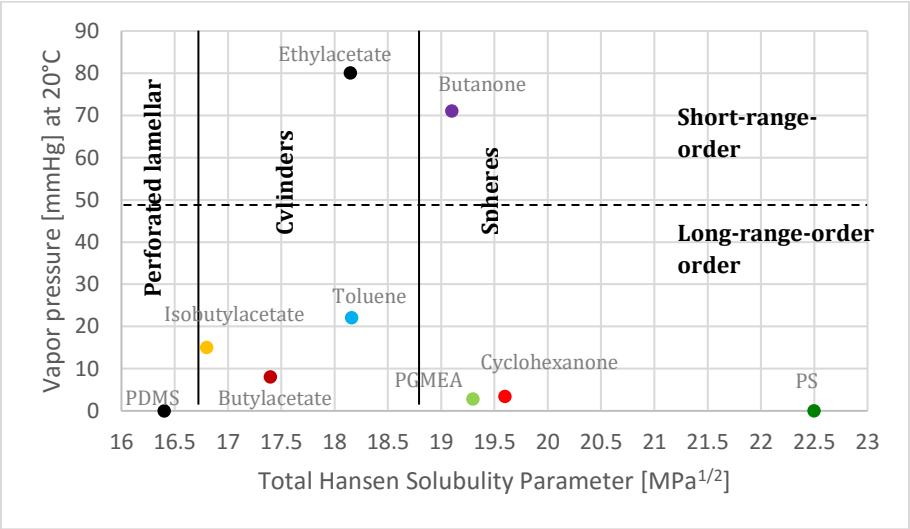

Figure 2-11: Cartography of morphologies and ordering that can be obtained with selected solvents in SD45

Our study shows that the vapor pressure and selectivity have both crucial influence on the final dried state of the BCP layer. The selectivity dictates as expected the morphology, while the ordering of the obtained structure depends on the vapor pressure of the solvent. For SD45, high vapor pressures lead to cylinders without long range order, while the quality of the cylinders depends on the selectivity. It seems likely that

higher PS-selectivity would lead to disorder spheres at vapor pressures above a certain threshold. Low vapor pressure solvents have the capability to align SD45 in long range order, while the selectivity changes the morphology from perforated lamellas, passing through the cylindrical area, to the final spherical state. With our cartography, it is possible to choose a desired morphology and adapt alignment quality via vapor pressure.

2.5 GISAXS *in-situ* Measurements of SVA on SD45

The precise knowledge of the structure in the swollen state is highly desirable when trying to understand how to connect the block copolymer solution structure to the dried polymer film structure. The understanding of when and what kind of structural transitions appear during swelling depend on the used conditions as observed before, but are not well established, most probably due to the difficulty to perform *in-situ* examinations on block copolymers. *In-situ* time resolved light scattering has been shown to study the thickness evolution of the BCP during SVA[28]. Also, *in-situ* Scanning Force Microscopy (SFM) has been reported to investigate the morphology transitions of polystyrene-b-poly(2-vinylpiridine) (PS-b-P2VP) and polystyrene-block-polybutadiene-block-polystyrene (SBS) in real time[29,30]. However, these methods only give topographical information about the mechanisms involved in SVA and SFM provides information of an area not larger than a few μm^2. For in-layer information, the only valuable method known is grazing incidence small angle X-ray scattering (GISAXS), which provides information of an area of several mm^2 throughout the entire film thickness. Several groups have reported on *in-situ* studies on solvent vapor annealing of different BCPs and have gained insight into the characterization of structural transition, reorientation and swelling and deswelling[6,31–36]. However, due to the poor contrast between the scattering domains, all of the reports show results for BCP layers several times as thick as the natural domain spacing of the BCP. This reflects non-realistic conditions that are usually not used in DSA processes. In order to be of interest for the semiconductor industry, the BCP should have monolayer thickness. This section deals with the study of the self-assembly process of SD45 in realistic conditions, i.e. using a monolayer of SD45, during solvent vapor annealing. The measurements were performed at the European Synchrotron Facility (ESRF) in Grenoble.

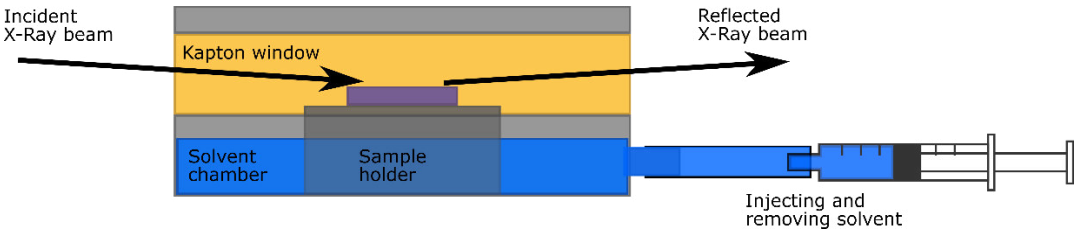

Figure 2-12: Schematic of the GISAXS setup for in-situ SVA measurements

The BCP films were prepared on plane SOC surfaces and placed in a custom-designed solvent vapor-annealing chamber to carry out real-time *in situ* GISAXS at room temperature (Figure 2-12). Kapton sidewalls allowed the x-rays to enter and exit the chamber. PGMEA or Toluene was introduced via an automated syringe setup as shown in Figure 2-12. The chamber volume and solvent surface and volume were chosen to reproduce the same experimental conditions used in the Petri dish set up.

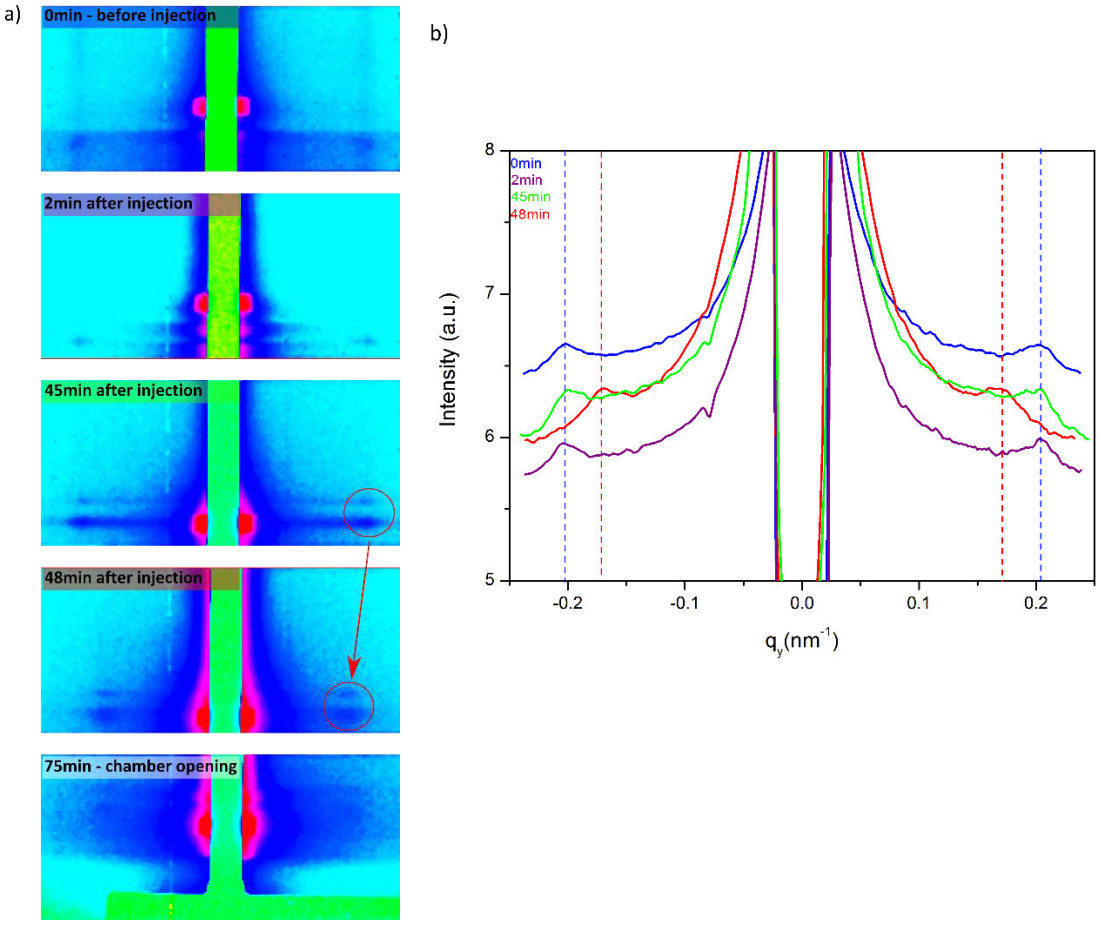

Figure 2-13 a) GISAXS intensity pattern and b) GISAXS intensity profile of SD45 during PGMEA vapor annealing

Obtained GISAXS data for PGMEA vapor annealing are presented in Figure 2-13. As shown in Figure 2-13a, at t=0 min, only two weak scattering spots were observed, most likely due to the very close optical index of PS and PDMS in the X-ray domain providing only a limited contrast in the condition of a thin-film measurement. Furthermore, the observations were made on monolayers, so the X-ray beam impinged only onto a small amount of matter. The scattering spots are not well defined and diffuse which indicates low order and only little developed morphology. No higher scattering orders are observed. The q_y position corresponds to a periodicity of 31.1 nm, which is much less than the equilibrium spacing of SD45 after SVA (≈35 nm). Furthermore, we observe thickness fringes in the q_z directions, which are most probably due to

the SOC underlayer as well as a reflection of the scattering spots in vertical direction. These propagation pins disappear right after solvent injection (t=0=, while the scattering spot intensity increases. It was shown that non-favorable block to block interactions can be increased when using a selective solvent. PGMEA is a PS selective solvent, consequently increasing the contrast of the two blocks and hence the pattern intensity[37–39]. Further solvent annealing leads to a change of the domain spacing after 45min of annealing. The period changes form 31.1 nm to 35.9 nm, which corresponds to fast fourier transform (FFT) values measured on ex-situ samples on planar SOC surfaces after SVA in PGMEA. We suggest that this change of period corresponds to the transition from the metastable micellar to the spherical ordered state. After swelling for 75min, the solvent was removed with the syringe and the chamber was opened to maximize the rate of evaporation of the solvent. The domain spacing kept constant at 36 nm and the intensity of the scattering spots decreased as a consequence of the decreased contrast between the two blocks due to the selective solvent removal.

In conclusion we observed that when swelled in PGMEA the system remains in an ordered state, confirming the assumption that the system does not pass the ODT. Also, the morphology transition seems to be a very prompt process that appears after a certain time in the swollen state.

In-situ GISAXS measurement of SVA in toluene vapor was also carried out, but due to its high vapor pressure, toluene evaporates faster under the X-ray beam. Structures were thus "frozen" and the evolution of GISAXS scattering could not be observed. Also the fact that it has a lower impact on the morphology might play a role in the signal contrast of the X-rays. It seems thus that the observation of toluene vapor annealing of thin films is impossible for GISAXS measurements.

Although the time at the ESRF pronounced itself as promising, the obtained results for *in-situ* measurements were not as conclusive as expected. A major issue was the destruction of the samples by the X-ray beam. During SEM analysis on areas where the beam hit the surface, a decomposition of the BCP layer was observed, which made it necessary to limit the exposure time to only a few seconds and to change exposure spots for each measurement. Furthermore, as toluene is toxic and highly suspected to be carcinogenic, safety requirements at the ESRF and the valuable limited time that we had at the beamline did not allow us to repeat experiments. Moreover, we chose to work in real conditions, meaning with thin monolayers, which made the signal of SD45 very weak. The signal was additionally weakened for *in-situ* measurements when the X-rays had to pass the kapton windows and solvent environment.

Further investigation of the obtained SD45 cylinders concerns the linewidth roughness and is presented in the following section.

2.6 Line Edge Roughness Measurements of SD45

The linewidth roughness (LWR) of a feature is the variation in the width over the length of the feature. The variation of the width on only one edge of a line is called line edge roughness (LER). The control of the roughness became important when feature sizes passed the 100 nm limit. LER and LWR are usually characterized as the 3σ deviation from a straight line. In order to guarantee the performances of semiconductor devices, the international technology roadmap for semiconductors (ITRS) requires a 3σ roughness to be smaller than 8% of the line width[18], whereas todays 193 nm lithography has generally a 3σ of 4%[40]. As the scaling down of feature sizes continuous, the line roughness becomes more and more important. Because high LER/LWR values are undesired and can degrade extremely the devices electrical performances, we have to analyze these values for BCP systems. The results were obtained from manual SEM measurements on PDMS cylinders formed in guiding trenches of 100 nm to 1.5 µm, before transfer etching but after revelation with oxygen plasma. The obtained values are mean values of ten measurements in the same guiding trench width. An illustration of a line width measurement on SD45 can be seen in Figure 2-14.

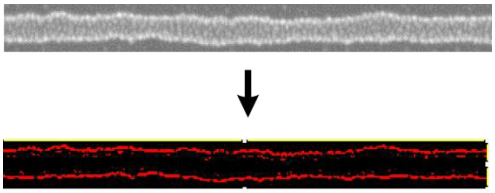

Figure 2-14: LWR measurement illustration on one line of SD45

Line edge roughness were found to be 3.4 ± 2.2nm on a mean critical dimension of 27 ±1.4 nm (12 %) and LWR were as low as 2.5 ±0.5 nm (7 %). It is known, that 193 nm lithography can have high intrinsic roughness that can be as high as 10 % of the critical dimension of the features. This roughness can be transmitted on to the BCP. In order to improve the LER values of the templating trenches, it has been suggested to perform post-lithography treatment on the resist in order to smoothen their edges. Among propositions are vacuum ultra violet (VUV), heat and plasma treatments[41–44]. In all cases a mixture of outgassing or cleavage of pendant groups form the main chain and cross-linking of the surface lead to a smoothening and better resistance towards subsequent etching. An improvement of LER values of up to 40% has been reported by these post-lithography treatments[45–47]. When applying one of these treatments to our SiArc/SOC substrates it is hoped to reduce the final LER of the by DSA obtained silicon lines drastically. Furthermore, it is known that oxygen plasma, depending on the plasma processing conditions, can create significant roughness on Si-containing polymer features[48–52]. During the revelation step of PDMS cylinders (explained in detail in chapter 5), the oxygen plasma could thus induce roughness on the edges of the cylinders. Precise control of the processing conditions could thus lead to a reduction of these values.

Interestingly for a future study would be to analyze the evolution of the LER/LWR during transfer etching. A smoothening step, as described for the lithography templates, might also be conceivable in BPC lines.
Finally, we want to emphasize that the presented results are preliminary and do not represent a statistical work. As SEM images were taken individually, differences in contrast and brightness of the images must have an influence on the final LER/LWR value. During this thesis the author did not have access to a critical-dimension scanning electron microscope (CD-SEM) with which a precise measurement of line edge roughness and line width roughness can be obtained for whole wafers. A CD-SEM provides extreme reproducibility and guarantees same image quality for each measurement by minimizing shot noises (caused by secondary electrons), visual misalignment, auto focus and brightness corrections variations[53]. For future work it would thus be necessary to use a calibrated CD-SEM in order to obtain comparable images. LER/LWR measurements are also discussed in chapter 3 and 4.

2.7 Conclusion

This chapter gives insights of the mechanisms involved in the directed self-assembly by solvent vapor annealing of SD45. First, the substrate-BCP interaction has been studied. It was shown that in order to work on plane silicon substrate, a brush treatment of the surface has to be done in order to obtain good alignment of SD45. PDMS brush complicates the transfer etching of the obtained patterns and is thus to be avoided; a good trade-off was found to be PS-brush. On patterned surfaces of SiArc/SOC stacks, we show that the treatment of a brush is not necessary as the SOC substrate favors naturally the wetting of the PS-block. It has been shown that not only the substrate chemistry but also the shape has great influence on the final pattern quality. Too deep trenches can create double patterning at the edges of the mesas which leads to uncontrolled ordering of SD45. Trench depth close to the natural domain spacing of the BCP gives consistent results. During solvent vapor annealing, numerous parameters play important roles on the self-assembly of the BCP. Mainly two parameters determine the final morphology and order quality of the sample. With the developed cartography of several solvents, we are able to predict the final ordering and morphology. This thesis concentrates particularly on the integration of PS-PDMS in industry which is why so called safe solvents have to be found. Butylacetate seems to be a good alternative to toluene for solvent annealing, but further optimization of the process has to be carried out in order to obtain PDMS cylinders aligned parallel to the guiding lines. Finally, *in-situ* GISAXS measurement of SD45 in PGMEA vapor has been presented. The obtained results are interesting but numerous constraints (safety issues, limited time, bulky set-up…) prevented us to perform an in-depth study that gave conclusive results. However, for a potential next session at the ESRF, concrete ideas for improvement have been proposed.
To conclude, the solvent vapor annealing is a very complex process that has to be meticulously controlled in order to obtain consistent results. Furthermore, the up-scaling of the annealing chamber is difficult and

has not been showed yet. Integrating SVA in manufacturing process does not seem likely to happen in the near future, which is why alternative solutions for BCP assembly have to be found.

Finally LER and LWR are analyzed by manual SEM imaging. Preliminary results show a high LER value that could be decreased by smoothening methods performed on lithography guiding trenches. Furthermore these results were obtained on oxygen plasma treated PDMS cylinders that were not yet transferred into the silicon substrate. It is suggested that the oxidation of PDMS leads to the roughening of the PDMS cylinders, which could be prevented by optimizing oxygen plasma conditions or compensated during transfer etching into the substrate. Future work includes the investigation of LER/LWR in a statistical way with a CD-SEM on larger surfaces that would give more reliable results. Also, the evolution of LER/LWR values after transfer etching would be interesting for a future work.

References

(1) Kathrein, C. C.; Bai, W.; Currivan-Incorvia, J. A.; Liontos, G.; Ntetsikas, K.; Avgeropoulos, A.; Böker, A.; Tsarkova, L.; Ross, C. A. Combining Graphoepitaxy and Electric Fields toward Uniaxial Alignment of Solvent-Annealed Polystyrene– B –Poly(dimethylsiloxane) Block Copolymers. *Chem. Mater.* **2015**, *27*, 6890–6898.

(2) Mokarian-Tabari, P.; Cummins, C.; Rasappa, S.; Simao, C.; Sotomayor Torres, C. M.; Holmes, J. D.; Morris, M. a. Study of the Kinetics and Mechanism of Rapid Self-Assembly in Block Copolymer Thin Films during Solvo-Microwave Annealing. *Langmuir* **2014**, *30*, 10728–10739.

(3) Qiang, Z.; Zhang, Y.; Groff, J. A.; Cavicchi, K. A.; Vogt, B. D. A Generalized Method for Alignment of Block Copolymer Films: Solvent Vapor Annealing with Soft Shear. *Soft Matter* **2014**, *10*, 6068–6076.

(4) O'Driscoll, B. M. D.; Kelly, R. A.; Shaw, M.; Liontos, G.; Ntetsikas, K.; Apostolos, A.; Petkov, N.; Morris, M. A. Achieving Structural Control with Thin Polystyrene- B-Polydimethylsiloxane Block Copolymer Films : The Complex Relationship of Interface Chemistry , Annealing Methodology and Process Conditions. *Eur. Polym. J.* **2013**, *49*, 3445–3454.

(5) Kihara, N.; Yamamoto, R.; Sasao, N.; Shimada, T.; Yuzawa, A.; Okino, T.; Ootera, Y.; Kamata, Y.; Kikitsu, A. Fabrication of 5 Tdot/in.2 Bit Patterned Media with Servo Pattern Using Directed Self-Assembly. *J. Vac. Sci. Technol. B* **2012**, *30*, 2166–2746.

(6) Sinturel, C.; Vayer, M.; Morris, M.; Hillmyer, M. a. Solvent Vapor Annealing of Block Polymer Thin Films. *Macromolecules* **2013**, *46*, 5399–5415.

(7) Gu, W.; Xu, J.; Kim, J.-K.; Hong, S. W.; Wei, X.; Yang, X.; Lee, K. Y.; Kuo, D. S.; Xiao, S.; Russell, T. P. Solvent-Assisted Directed Self-Assembly of Spherical Microdomain Block Copolymers to High Areal Density Arrays. *Adv. Mater.* **2013**, *25*, 3677–3682.

(8) Kim, S. H.; Misner, M. J.; Xu, T.; Kimura, M.; Russell, T. P. Highly Oriented and Ordered Arrays from Block Copolymers via Solvent Evaporation. *Adv. Mater.* **2004**, *16*, 226–231.

(9) Jung, Y. S.; Ross, C. A. Orientation-Controlled Self-Assembled Nanolithography Using a Polystyrene-Polydimethylsiloxane Block Copolymer. *Nano Lett.* **2007**, *7*, 2046–2050.

(10) Kim, E.; Ahn, H.; Park, S.; Lee, H.; Lee, M.; Lee, S.; Kim, T.; Kwak, E.-A.; Lee, J. H.; Lei, X.; *et al.* Directed Assembly of High Molecular Weight Block Copolymers: Highly Ordered Line Patterns of Perpendicularly Oriented Lamellae with Large Periods. *ACS Nano* **2013**, *7*, 1952–1960.

(11) Li, H.-W.; Huck, W. T. S. Ordered Block-Copolymer Assembly Using Nanoimprint Lithography. *Nano Lett.* **2004**, *4*, 1633–1636.

(12) Salaun, M.; Zelsmann, M.; Archambault, S.; Borah, D.; Kehagias, N.; Simao, C.; Lorret, O.; Shaw, M. T.; Sotomayor Torres, C. M.; Morris, M. A. Fabrication of Highly Ordered Sub-20nm Silicon Nanopillars by Block Copolymer Lithography Combined with Resist Design. *J. Mater. Chem. C* **2013**, *1*, 3544.

(13) Jeong, J. W.; Park, W. I.; Do, L.-M.; Park, J.-H.; Kim, T.-H.; Chae, G.; Jung, Y. S. Nanotransfer Printing with Sub-10nm Resolution Realized Using Directed Self-Assembly. *Adv. Mater.* **2012**, *24*, 3526–3531.

(14) Rockford, L.; Liu, Y.; Mansky, P.; Russell, T. Polymers on Nanoperiodic, Heterogeneous Surfaces. *Phys. Rev. Lett.* **1999**, *82*, 2602–2605.

(15) Kim, S. O.; Solak, H. H.; Stoykovich, M. P.; Ferrier, N. J.; Pablo, J. J. De; Nealey, P. F. Epitaxial Self-Assembly of Block Copolymers on Lithographically Defined Nanopatterned Substrates. *Lett. to Nat.* **2003**, *424*, 411–414.

(16) Segalman, R.; Yokoyama, H.; Kramer, E. Graphoepitaxy of Spherical Domain Block Copolymer Films. *Adv. Mater.* **2001**, *13*, 1152–1155.

(17) Jeong, S.-J.; Kim, J. Y.; Kim, B. H.; Moon, H.-S.; Kim, S. O. Directed Self-Assembly of Block Copolymers for next Generation Nanolithography. *Mater. Today* **2013**, *16*, 468–476.

(18) ITRS. International Technology Roadmap for Semiconductors. **2013**, http://www.itrs.net.

(19) Borah, D.; Rasappa, S.; Senthamaraikannan, R.; Kosmala, B.; Shaw, M. T.; Holmes, J. D.; Morris, M. A. Orientation and Alignment Control of Microphase-Separated PS-B-PDMS Substrate Patterns via Polymer Brush Chemistry. *ACS Appl. Mater. Interfaces* **2013**, *5*, 88–97.

(20) Harrison, C.; Chaikin, P. M.; Huse, D. A.; Register, R. A.; Adamson, D. H.; Daniel, A.; Huang, E.; Mansky, P.; Russell, T. P.; Hawker, C. J.; *et al.* Reducing Substrate Pinning of Block Copolymer Microdomains with a Buffer Layer of Polymer Brushes. *Macromolecules* **2000**, *33*, 857–865.

(21) Jung, Y. S.; Ross, C. A. . Solvent-Vapor-Induced Tunability of Self-Assembled Block Copolymer Patterns. *Adv. Mater.* **2009**, *21*, 2540–2545.

(22) Gotrik, K. W. Flow Controlled Solvent Vapor Annealing of Block Copolymers for Lithographic Applications, Massachusetts Institute of Technology, 2013.

(23) Dinachali, S. S.; Bai, W.; Tu, K.-H.; Choi, H. K.; Zhang, J.; Kreider, M. E.; Cheng, L.-C.; Ross, C. A. Thermo-Solvent Annealing of Polystyrene-Polydimethylsiloxane Block Copolymer Thin Films. *ACS Macro Lett.* **2015**, *4*, 500–504.

(24) Gotrik, K. W.; Ross, C. A. Solvothermal Annealing of Block Copolymer Thin Films. *Nano Lett.* **2013**, *13*, 5117–5122.

(25) Rasappa, S.; Schulte, L.; Borah, D.; Morris, M. A.; Ndoni, S. Sub-15nm Silicon Lines Fabrication via PS-B-PDMS Block Copolymer Lithography. *J. Nanomater.* **2013**, doi:10.1155/2013/831274.

(26) Huggins, M. L. The Solubility of Nonelectrolytes. By Joel H. Hildebrand and Robert S. Scott. *J. Phys. Chem.* **1951**, *55*, 619–620.

(27) Hansen, C. M. *Hansen Solubility Parameters*; 2008.

(28) Mokarian-Tabari, P.; Collins, T. W.; Holmes, J. D.; Morris, M. A. Cyclical "Flipping" of Morphology in Block Copolymer Thin Films. *ACS Nano* **2011**, *5*, 4617–4623.

(29) Horvat, A.; Knoll, A.; Krausch, G.; Tsarkova, L.; Lyakhova, K. S.; Sevink, G. J. A.; Zvelindovsky, A. V; Magerle, R. Time Evolution of Surface Relief Structures in Thin Block Copolymer Films. *Macromolecules* **2007**, *40*, 6930–6939.

(30) Knoll, A.; Lyakhova, K. S.; Horvat, A.; Krausch, G.; Sevink, G. J. A.; Zvelindovsky, A. V; Magerle, R. Direct Imaging and Mesoscale Modelling of Phase Transitions in a Nanostructured Fluid. *Nat. Mater.* **2004**, *3*, 886–891.

(31) Gowd, E. B.; Böhme, M.; Stamm, M. In Situ GISAXS Study on Solvent Vapour Induced Orientation Switching in PS- B -P4VP Block Copolymer Thin Films. *IOP Conf. Ser. Mater. Sci. Eng.* **2010**, *14*, 012015.

(32) Paik, M. Y.; Bosworth, J. K.; Smilges, D.; Schwartz, E. L.; Andre, X.; Ober, C. K. Reversible Morphology Control in Block Copolymer Films via Solvent Vapor Processing: An In Situ GISAXS Study. *Macromolecules* **2010**, *43*, 4253–4260.

(33) Gunkel, I.; Gu, X.; Sun, Z.; Schaible, E.; Hexemer, A.; Russell, T. P. An in Situ GISAXS Study of Selective Solvent Vapor Annealing in Thin Block Copolymer Films: Symmetry Breaking of in-Plane Sphere Order upon Deswelling. *J. Polym. Sci. Part B Polym. Phys.* **2016**, *54*, 331–338.

(34) Cummins, C.; Mokarian-Tabari, P.; Andreazza, P.; Sinturel, C.; Morris, M. a. Solvothermal Vapor Annealing of Lamellar Poly(styrene)-Block-Poly(d,l-Lactide) Block Copolymer Thin Films for Directed Self-Assembly Application. *ACS Appl. Mater. Interfaces* **2016**, *8*, 8295–8304.

(35) Bai, W.; Yager, K. G.; Ross, C. A. In Situ Characterization of the Self-Assembly of a Polystyrene–Polydimethylsiloxane Block Copolymer during Solvent Vapor Annealing. *Macromolecules* **2015**, *48*, 8574–8584.

(36) Gu, X.; Gunkel, I.; Hexemer, A.; Russell, T. P. Solvent Vapor Annealing of Block Copolymer Thin Films: Removal of Processing History. *Colloid Polym. Sci.* **2014**, *292*, 1795–1802.

(37) Lai, C.; Russel, W. B.; Register, R. A. Scaling of Domain Spacing in Concentrated Solutions of Block Copolymers in Selective Solvents. *Macromolecules* **2002**, *35*, 4044–4049.

(38) Wang, J.; Chen, W.; Roy, C.; Sievert, J. D.; Russell, T. P. Influence of Ionic Complexes on Phase Behavior of Polystyrene-B-Poly(methyl Methacrylate) Copolymers. *Macromolecules* **2008**, *41*, 963–969.

(39) Gu, X.; Gunkel, I.; Hexemer, A.; Gu, W.; Russell, T. P. An in Situ Grazing Incidence X-Ray Scattering Study of Block Copolymer Thin Films during Solvent Vapor Annealing. *Adv. Mater.* **2014**, *26*, 273–281.

(40) Mack, C. A. *Field Guide to Optical Lithography*; SPIE Press, 2006.

(41) Pargon, E.; Azarnouche, L.; Fouchier, M.; Menguelti, K.; Jussot, J. Smoothing Mechanisms Involved in Thermal Treatment for Linewidth Roughness Reduction of 193-Nm Photoresist Patterns. *J. Vac. Sci. Technol. B Microelectron. Nanom. Struct.* **2013**, *31*, 061203.

(42) Pargon, E.; Menguelti, K.; Martin, M.; Bazin, a.; Chaix-Pluchery, O.; Sourd, C.; Derrough, S.; Lill, T.; Joubert, O. Mechanisms Involved in HBr and Ar Cure Plasma Treatments Applied to 193 Nm Photoresists. *J. Appl. Phys.* **2009**, *105*, 094902.

(43) Pret, A. V.; Gronheid, R.; Foubert, P. Roughness Characterization in the Frequency Domain and Linewidth Roughness Mitigation with Post-Lithography Processes. *J. Micro/Nanolith. MEMS MOEMS* **2010**, *9*, 041203.

(44) Azarnouche, L.; Pargon, E.; Menguelti, K.; Fouchier, M.; Joubert, O.; Gouraud, P.; Verove, C. Benefits of Plasma Treatments on Critical Dimension Control and Line Width Roughness Transfer during Gate Patterning. *J. Vac. Sci. Technol. B Microelectron. Nanom. Struct.* **2013**, *31*, 012205.

(45) Chandhok, M.; Frasure, K.; Putna, E. S.; Younkin, T. R.; Rachmady, W.; Shah, U.; Yueh, W. Improvement in Linewidth Roughness by Postprocessing. *J. Vac. Sci. Technol. B Microelectron. Nanom. Struct.* **2008**, *26*, 2265–2270.

(46) Pret, A. V.; Gronheid, R.; Ishimoto, T.; Sekiguchi, K. Resist Roughness Evaluation and Frequency Analysis: Metrological Challenges and Potential Solutions for Extreme Ultraviolet Lithography. *J. Micro/Nanolithography, MEMS MOEMS* **2010**, *9*, 041308.

(47) Pargon, E.; Azarnouche, L.; Fouchier, M.; Menguelti, K.; Tiron, R.; Sourd, C.; Joubert, O. HBr Plasma Treatment Versus VUV Light Treatment to Improve 193 Nm Photoresist Pattern Linewidth Roughness. *Plasma Process. Polym.* **2011**, *8*, 1184–1195.

(48) Tserepi, A.; Gogolides, E.; Constantoudis, V. Surface Roughness Induced by Plasma Etching of Si-Containing Polymers. *J. Adhes. Sci. Technol.* **2003**, *17*, 1083–1091.

(49) Mori, S.; Morisawa, T.; Matsuzawa, N.; Kaimoto, Y.; Endo, M.; Matsuo, T.; Kuhara, K.; Sasago, M. Reduction of Line Edge Roughness in the Top Surface Imaging Process. *J. Vac. Sci. Technol. B* **1998**, *16*, 3739–3743.

(50) Oehrlein, G. S.; Phaneuf, R. J.; Graves, D. B. Plasma-Polymer Interactions: A Review of Progress in Understanding Polymer Resist Mask Durability during Plasma Etching for Nanoscale Fabrication. *J. Vac. Sci. Technol. B Microelectron. Nanom. Struct.* **2011**, *29*, 010801.

(51) Bruce, R. L.; Lin, T.; Phaneuf, R. J.; Oehrlein, G. S.; Bell, W.; Long, B.; Willson, C. G. Molecular Structure Effects on Dry Etching Behavior of Si-Containing Resists in Oxygen Plasma. *J. Vac. Sci. Technol. B Microelectron. Nanom. Struct.* **2010**, *28*, 751.

(52) Eon, D.; Poucques, L. De; Peignon, M. C.; Cardinaud, C.; Turban, G. Surface Modification of Si-Containing Polymers during Etching for Bilayer Lithography. *Microelectron. Eng.* **2002**, *62*, 901–906.

(53) Yamaguchi, A.; Nakagaki, R.; Kawada, H. CD-SEM Technologies for 65nm Process Node. *Hitachi Rev.* **2005**, *54*, 15–21.

Chapter 3 Pattern Generation of Lines and Dots via Thermal Annealing of PS-b-PDMS

3.1 Introduction

As explained in the previous chapter, PS-b-PDMS is characterized by the strong segregation regime and has a high diffusive energy barrier. Thermal annealing (TA) under normal conditions would need a considerable amount of time (up to several more than 10 hours) in order to achieve satisfactory phase separation. SVA has thus been adopted as the most common annealing method to promote microphase separation of PS-b-PDMS but is a complex method that requires careful control of various parameters and a up-scaling of a solvent containing annealing chamber for 300mm wafer seems unlikely. Hence, the best and simplest option for BCP assembly remains thermal annealing. It is a simple and well-known industrial method that can also easily be scaled up. This context gave the motivation to test novel techniques on PS-b-PDMS in order to promote the self-assembly by a thermal treatment, despite its high χ value.

Blending BCPs has been employed to influence the final morphology or domain size without any subsequent synthesis steps[1]. The addition of homopolymers[2–4], monomers[5] or salts[6] has already been reported in order to enhance the process time and kinetics of the self-assembly process of low-χ BCPs. Most of these proposed blending processes include the addition of a material that cannot be or is difficult to be removed, and thus permanently alters the functionality of the block copolymer for technological applications.

In this chapter, we will deal with the addition of plasticizer molecules in the high-χ PS-b-PDMS solution in order to lower its diffusive energy barrier and that can be removed without changing the obtained structures. Plasticizers are well known additives in the polymer industry. They are nonvolatile substances that are incorporated into rigid plastics to increase their flexibility. The plasticizer enters into the polymer network and expands its free volume by providing a lateral motion to the chains[7]. This process results in a decrease of the glass transition temperature (T_g) through reduction of intermolecular forces. In this case, we speak of physical or external plasticizers because they do not chemically react with the polymer.

Plasticizers have an influence on the morphology and chain movements of the polymer, but can be removed by annealing after alignment without altering the obtained nanopatterns. A good plasticizer candidate for a polymer requires a high degree of solvation power and compatibility with the polymer system, to decrease the glass transition temperature (T_g) efficiently[8].

A preview on industrial applications by blending PS-b-PDMS with plasticizers is shown in this chapter: our process was applied on standard industrial graphoepitaxial stacks, on large surfaces and in microelectronics clean room conditions (class 100). We finally show a complete process from deposition to pattern transfer by plasma etching of plasticizer blended PS-b-PDMS on 300 mm wafers. The experimental details of the process are explained in the following.

3.2 Experimental Details

PS-b-PDMS, SD42 (M_w = 31–11 kg mol^{-1}), SD45 (M_w = 30.5–14.5 kg mol^{-1}) and hydroxyl-terminated PS homopolymer (M_w = 3.5 kg mol^{-1}) were purchased from Polymer Source Inc. (Canada) and used as received. Propylene glycol monomethyl ether acetate (PGMEA) solvent and plasticizers bis(2-ethylhexyl) adipate (DOA) and bis(2-ethylhexyl) sebacate (DOS) were purchased from Sigma-Aldrich.

When working on silicon, before deposition of the BCP solution, the substrates were activated in O_2 plasma for 2 min before use and treated with a PS-brush. For the brush preparation, PS-homopolymer solution was deposited by spin-coating at 2000 rpm and the samples were immediately annealed at 200 °C for 5 min. Nonreacted PS-OH residues were rinsed off with PGMEA. The SiArc/SOC graphoepitaxy substrates were generated as described in chapter 2. After BCP deposition the samples were annealed and used for transfer etching as described previously for neat SD45.

After revealing the PDMS structures by CF4 and O2 plasma, the self-assembled morphologies could be investigated by SEM (Hitachi S-5000 or JEOL 7500F), FIB-STEM (Helios 450S – FEI) and GISAXS (beamline B02 at ESRF Grenoble) as described in chapter 2. In order to obtain information of the micellar state in the BCP solution in PGMEA solvent, Dynamic Light Scattering (DLS) measurements were performed. A He–Ne gas laser with a wavelength of 633 nm and a backscattering detector positioned at a scattering angle of 180° with respect to the laser was used. Thermogravimetric analysis (TGA) was performed in order to compare the thermal behavior of DOA and DOS: A TA Instrument Q105 was used with a heat rate at 10 °C min^{-1} from room temperature (RT) to 450 °C. Thickness measurements were obtained by ellipsometry measurements using a UVISEL ellipsometer from Horiba Scientific. Spectral range from 300 to 800 nm and a model composed by Si, SiO2, and the copolymer layer were used to measure the BCP film thickness. Finally, line edge roughness measurements were measured by SEM and using TerminalPC (cf. chapter 2).

3.3 Influence of Plasticizer Molecules on PS-b-PDMS (Mw = 42kg/mol)

By introducing the plasticizer in the solution before spin-coating we are able to obtain long-range ordered nanostructures after this single process step. The equilibrium morphology can then be obtained through an additional fast TA step where a transition occurs from its metastable morphology, which is trapped after spin-coating. Here, the influence of two selective plasticizers on PS-b-PDMS self-assembly was investigated for PS-b-PDMS with an overall molecular weight of M_w = 42kg/mol (SD42). Furthermore, morphological transitions were observed during thermal annealing.

PS-selective plasticizers widely used in industry such as dioctylsebacate (DOS) and diisooctyl adipate (DOA) were tested in order to study their influence on the self-assembly of PS-b-PDMS. Physical properties of BCP, solvent and plasticizers used in this study are listed in Table 3-1.

Table 3-1: Details of some useful physical properties of plasticizers 9 and solvents10

	Solubility parameter ($MPa^{1/2}$)	**Vapor pressure (Pa) at 25°C**	**χ-PS**	**χ-PDMS**
PGMEA	17.4	3.8	0.04	0.2
DOS	17.5	$1.5x10^{-4}$	0.1	0.7
DOA	17.8	$1.1x10^{-4}$	0.04	0.8

The entire procedure of self-assembly of plasticized high-χ BCPs is schematically shown in Figure 3-1and provides a preview of the obtained results. SD42 and DOS were solubilized in propylene glycol monomethyl ether acetate (PGMEA) having both 1 wt% concentration. The solution (DOS42) was spin-coated on a PS-brushed Si substrate as described in the experimental section, so that a BCP monolayer was spread out (Figure 3-1 1). During spin-coating, plasticizer molecules remain in the PS chains of the BCP ($\chi_{PS\text{-}DOS}$=0.1) due to their negligible vapor pressure of less than 1 mPa (Figure 3-1 2a). After spin-coating on functionalized Si substrates, a CF_4 followed by an O_2 plasma etching step was performed to remove the PDMS top layer and the PS matrix, respectively. This two-step plasma etching reveals an oxidized-PDMS sphere network having long-range order without any post-coating treatment (Figure 3-13a). A morphology transition from spheres to horizontal cylinders is obtained via ultra-fast TA treatment (30s) after spin-coating (Figure 3-1 2b). Finally, after pattern revelation by two-step plasma etching, a horizontal cylinder mask is obtained (Figure 3-1 3b). The stable morphology for SD42 is hexagonal cylinder packing, according to the phase diagram predicted by the self-consistent mean field theory. These mechanisms are expained in detail in the following.

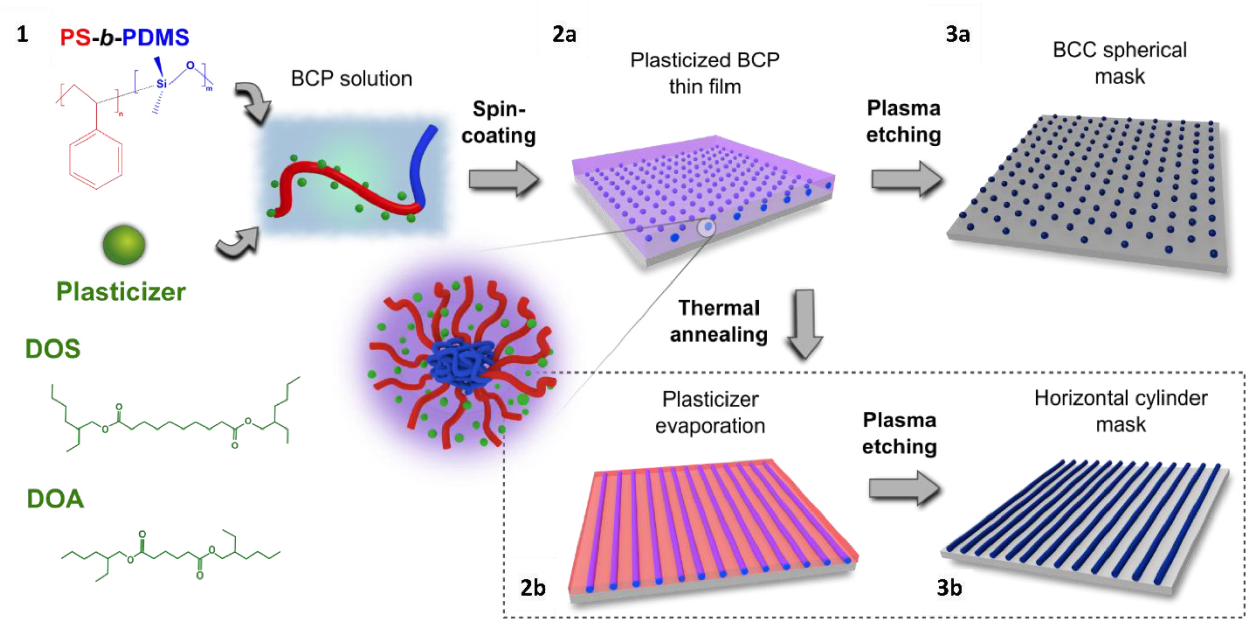

Figure 3-1: Schematic of the self-assembly of plasticized PS-PDMS 1) Plasticizers such as DOS or DOA are incorporated into the PS-PDMS solution. 2a) BCP solution is spread out on substrates. Low volatile plasticizers remain in the PS-PDMS thin films, giving mobility to micelles to induce self-assembly. 3a) CF4 followed by O2 plasma etching to remove the PDMS top-layer, PS matrix and oxidize PDMS spheres results in a one-step self-assembled mask without any post-annealing treatment. The as-spun film is subjected to 2b) an ultra-fast thermal annealing inducing plasticizer evaporation and a morphology transition from spheres to horizontal cylinders. 3b) Plasma etching reveals the oxidized-PDMS cylinders.

In order to understand the mechanism of the tested plasticizers on PS-b-PDMS self-assembly, the BCP was studied in the three steps involved in Figure 3-1 1) PS-b-PDMS-DOS (DOS42) system in PGMEA solution, 2) PS-b-PDMS-DOS thin film and 3) the final self-assembled PS-b-PDMS. In the first step, dynamic light scattering technique was used, to analyze the effect of DOS in DOS42 solution by measuring the hydrodynamic diameter (D_h) of PS-b-PDMS micelles. Adding a selective solvent to the BCP solution changes the PS volume fraction f_{PS}, leading to a shift of the micellar morphology[11]. PGMEA is a PS block-selective solvent and leads to the formation of PS_{corona} – $PDMS_{core}$ micelles in solution. As DOS is also PS-selective, spherical micellar formation is expected. Figure 3-2a shows the distribution of D_h of micelles in DOS42 solution indicating a monodisperse solution of PS-b-PDMS micelles, where mean D_h is calculated to be 35±1 nm. A slight difference was observed in mean D_h micelles of SD42 solution (D_h ~33±1 nm), suggesting an increase of the apparent D_h by the addition of DOS without structural modification of the PS-b-PDMS micelles.

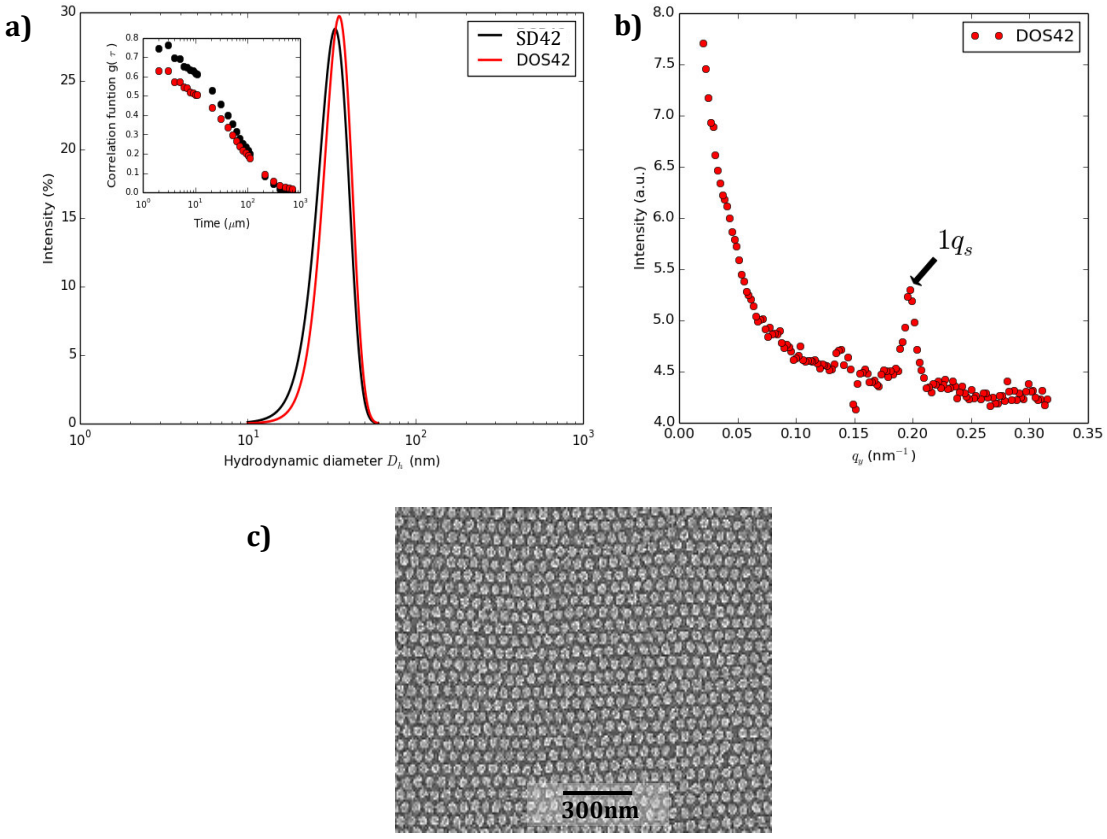

Figure 3-2: a) Dynamic light scattering measurements of PS-PDMS 42 kg/mol solution (SD42) and with the addition of DOS (DOS42 solution). Inset: the respective correlation functions. b) GISAXS intensity profile of a DOS42 thin film. c) SEM top-view observation of the same sample after the two-step plasma etching

When DOS42 solution is spin-coated on functionalized Si substrates, the PGMEA solvent evaporates and a plasticized BCP thin film is deposited. Figure 3-2b shows grazing-incidence small-angle X-ray scattering (GISAXS) profiles of the DOS42 thin film after spin-coating. First order reflections for the spherical structure appeared at 0.19 nm^{-1} corresponding to a domain length of $L_0 \sim 33$ nm. Figure 3-2c shows a top-view SEM image of the as-spun thin film after two-step plasma etching, as schematically shown in Figure 3-13a. This image shows the spherical lattice of oxidized-PDMS having L_0~33 nm, which is consistent with the GISAXS analysis. It was shown that micelle-micelle interactions drive the system to pack in an ordered array when the hydrodynamic diameter of the micelles is comparable to L_0[12]. In our case $D_h \sim L_0 \sim$33 nm, as is proven by DLS and GISAXS measurements, which is most certainly why we obtain a highly organized spherical morphology after BCP spin-coating. The interplay of PGMEA solvent and plasticizer is crucial for the good organization of the spheres after spin. Generally the BCP is trapped in a metastable state after spin, resulting in a poorly organized ordering, due to the fast evaporation of the solvent during spin-coating. When blended with plasticizers, the BCP remains plasticized even after solvent evaporation, due to

the low vapor pressure of plasticizers, which will be discussed more in detail further in the text. For comparison, an as-spun SD42 thin film is shown in Figure 3-3 without plasticizer addition from a PGMEA solution. Note that we refer to as-spun for samples on which no anneling step was performed, however in order to visualize the PDMS structures in SEM, a revealing plasma step by CF_4/O_2 is necessary.

A disordered and inhomogeneous system is observed, as the solvent is evaporated immediately during spin coating.

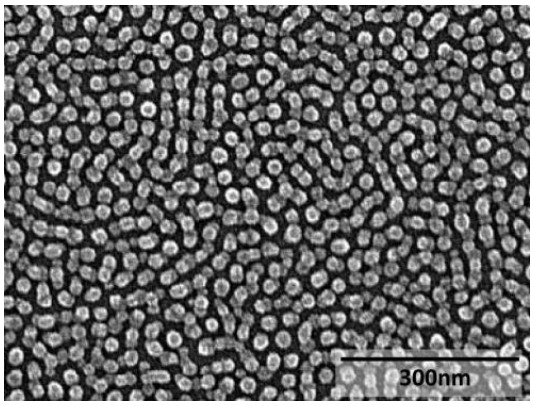

Figure 3-3: Top-view SEM image of as-spun SD42 thin film after the two-step revealing plasma etching

Due to the negligible vapor pressure of DOS and its good solubility with PS block (Table 3-1), retention of DOS molecules in the PS matrix after spin was considered. To characterize this, DOS42 thin films were then studied by in situ ellipsometry. We observed that the as-spun plasticized film is twice as thick as its reference without DOS at room temperature (Figure 3-5).

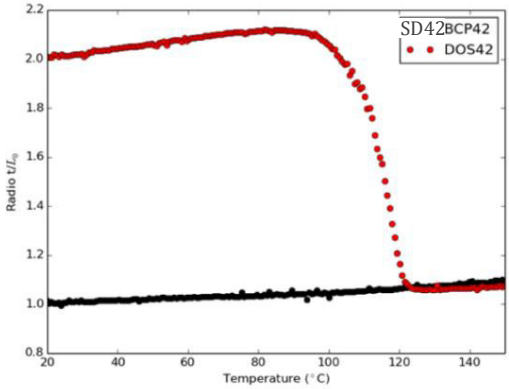

Figure 3-4: Temperature profile of SD42 and DOS42 film thickness by in-situ ellipsometry

As shown in Figure 3-4, the film thickness rapidly falls back to monolayer thickness in the case of DOS42. This film thickness decrease must be due to the evaporation of the plasticizer from 100°C on. In order to investigate this observation more closely, the evaporation of DOS was tested by thermal annealing on plasticized PS-b-PDMS thin films. DOS42 thin films were heated at different temperatures (110–140°C) for

60 s, and the thickness was measured in-situ by ellipsometry. Upon heating, the thin film thickness rapidly decreases after a first thermal expansion, suggesting an evaporation of DOS (Figure 3-5). Evaporation rates depend on the temperature, as demonstrated in Figure 3-5a. At 130°C and 140°C the PS-b-PDMS film rapidly drops from $2.2L_0$ to the monolayer thickness L_0, whereas at 110°C and 120°C DOS is not completely evaporated after one minute. In addition to the thickness measurements, the morphology state has been observed by SEM for 30 s and 60 s of TA (Figure 3-5b-g). A morphology evolution was observed in the DOS42 system from spheres to cylinders at 120 °C (Figure 3-5d-e) until reaching cylinder morphology after 60 s of TA. This suggests an upper limit of $\sim 1.6L_0$ to have a morphological transition. Then, faster transitions were found upon heating at 140 °C for 30 s.

The morphology obtained as-spun is trapped in an ordered metastable state. By heating, the plasticizer contained in the PS corona of the micelles starts to evaporate, thus increasing the PDMS volume fraction f_{PDMS}. According to the calculation of Liaw and co-authors[13], for a solvated BCP system, an increase in f_{PDMS} results in an increase of f_{core} and consequently triggers a morphology transition from spheres to cylinders when the system is already confined in a spherical packing. After calculations from ellipsometry measurements, a morphology transition occurs at $f_{PDMS} \approx 0.18$, when the BCP42 thin film is swollen by DOS, which is consistent with the cylinder-sphere transition in the BCP phase diagram at $\chi N=116$[14].

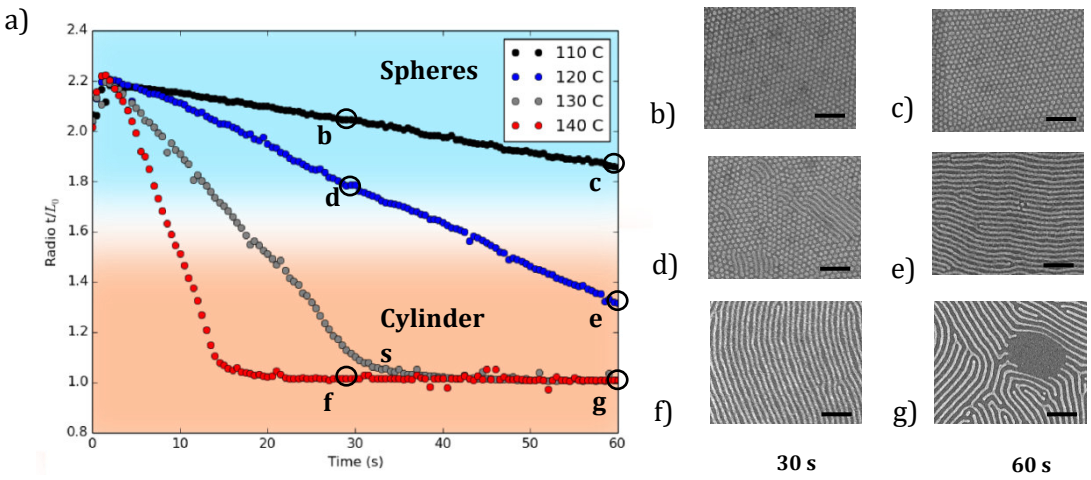

Figure 3-5: a) Kinetics of film thickness of PS-PDMS 42 kg/mol with DOS under thermal annealing for temperatures between 110–140 °C by in-situ ellipsometry. Top-view SEM images of PS-PDMS after 30 s (b,d,f) and 60 s (c,e,g) of thermal annealing in the range 110–140 °C. Scale bar corresponds to 200 nm.

As predicted by the plasticizer theory, DOS only increases the free volume of the PS block, and decreases its T_g to RT or lower[15]. Consequently, the PS volume fraction increases and the BCP system phase-separates in a spherical metastable morphology according to the phase diagram predicted by self-consistent mean field theory[16]. This mechanism is similar to a SVA treatment with PS-selective solvents. The solvent molecules enter into the PS chains, giving sufficient mobility to self-assemble by swelling selectively the PS matrix and

reducing its T_g[17]. Thus, the combination of PS selectivity and the low evaporation rate of plasticizer set the PS matrix in a glass-liquid state where PS-b-PDMS micelles have sufficient mobility. This reduces the kinetics of self-assembly drastically to the spherical morphology.

Figure 3-6 shows DOS42 as spun after plasma revelation. Spheres are well aligned, but DOS seems to misshape the interfaces between PS and PDMS. This is observed through the presence of residues around oxidized PDMS spheres, which could be troublesome for lithographic applications. The complete elimination of DOS from the BCP pattern is important to fabricate long-range ordered lithographic masks.

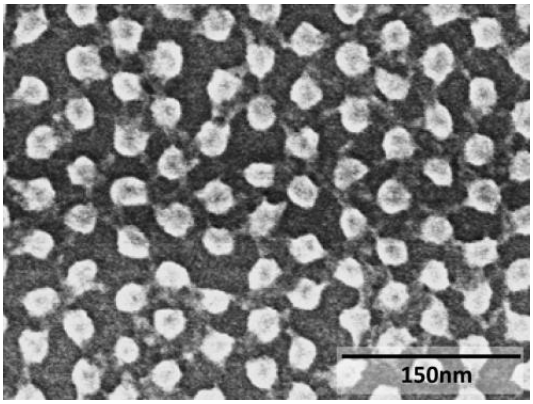

Figure 3-6: Top-view SEM image of as-spun DOS42 thin film after the two-step plasma etching.

Morphology transition is a direct consequence of DOS evaporation by the thermal effect. To prove this statement, DOS was evaporated by introducing a DOS42 thin film in a vacuum chamber (~ 13 mPa) without heating. After several minutes in the vacuum environment, DOS was completely evaporated and the characteristic monolayer thickness L_0 of SD42 was obtained. The resulting morphology was observed by SEM and depicted in Figure 3-7.

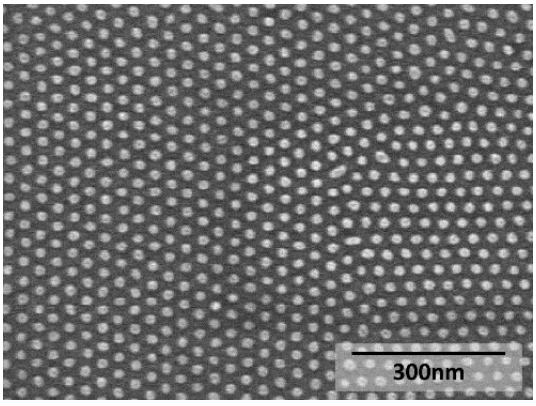

Figure 3-7: SD42 self-assembly by the DOS plasticizer effect. DOS was evaporated in a vacuum chamber (~13 mPa) for 5 minutes, immediately followed by the two-step plasma etching for PS removal and PDMS oxidizing

No morphology change could be observed: a microphase-separated network with well aligned spherical morphology was obtained with the absence of any residues.

Heating for 60 s at 140°C eliminates the PDMS residues on the cylindrical morphology, but dewetting appears at this stage (g). Since DOS was completely evaporated at ~15 s, the relaxation of the PS matrix is reduced. For longer annealing times above 30 s, PDMS residues tend to decrease contact forces with the PS block by diffusing to PDMS cylinders. This long-range residual stress from non-equilibrium chain conformations might play a role in the instability of the SD42 thin film, and dewetting occurs by the formation of holes[18,19].

To take advantage of plasticizer effects on PS-b-PDMS self-assembly while avoiding poor microseparated structures or dewetting issues, other plasticizers were tested on PS-b-PDMS. Among them was diisooctyl adipate (DOA) which, from its physical properties, is slightly more PS selective than DOS ($\chi_{PS\text{-}DOA}$=0.04 from Table 3-1). By thermogravimetric analysis (TGA), it was observed that DOA presents a faster evaporation rate than DOS (Figure 3-8).

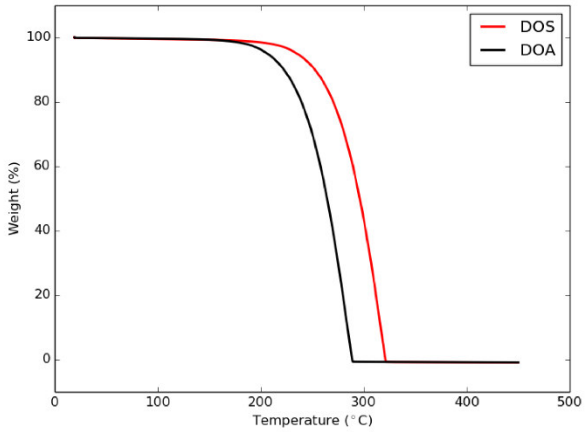

Figure 3-8: Evaporation rate of DOS and DOA plasticizers by thermogravimetric analysis (10°C min-1).

DOA and DOS both start to evaporate at ~175 °C, but DOA shows a greater evaporation rate. The lower bonding energy of DOA compared to DOS could be the origin of this difference. Although the molecules are very similar, DOA molecular weight is smaller, thus a smaller amount of energy is needed to evaporate these molecules.

Then DOA was tested in the same conditions as DOS and its effects on PS-b-PDMS self-assembly was studied.

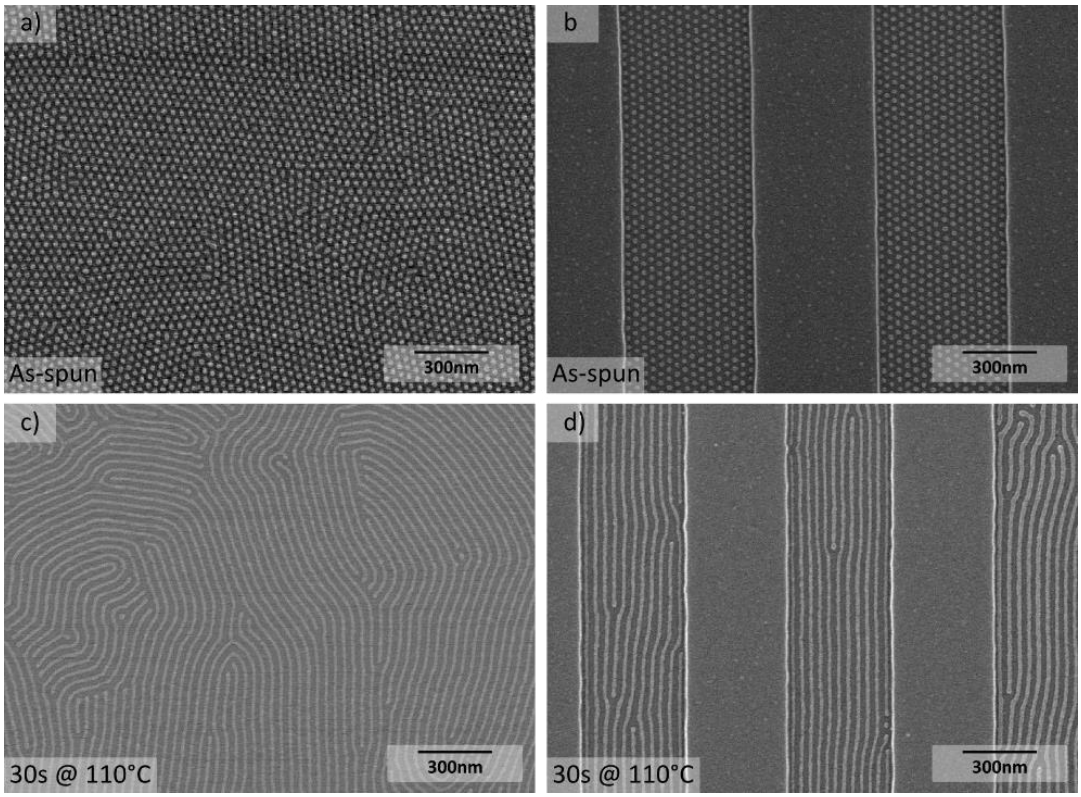

Figure 3-9: SEM top view images of as-spun DOA42 on a) plane surface and b) graphoepitaxial substrate. Rapid thermal annealing of DOA42 on (c) plane surface and (d) graphoepitaxy

A SD42 solution was diluted with DOA 1 wt% (DOA42) and spin-coated on PS brushed surfaces and subsequently plasma etched without any postcoating treatment. Figure 3-9a shows well-arranged spheres of oxidized-PDMS on a plane surface. As-spun images show microseparated structures without PDMS residues after plasma etching. The higher evaporation rate of DOA compared to DOS allows an instantaneous evaporation when inserted in a vacuum (~ 13 mPa): this fact was controlled by *ex-situ* ellipsometry measurements, where plasticized PS-b-PDMS thin films were shown to contract to L_0 when inserted in a vacuum chamber. The fast evaporation rate of the plasticizer allows us to process the samples directly in plasma without interruption between steps 2a and 3a in Figure 3-1, which is of main interest for high throughput. A SEM top-view image of the as-spun DOS42 thin film on a graphoepitaxial surface is shown in Figure 3-9b, where the directed self-assembly is demonstrated, maintaining the spherical morphology without postcoating annealing treatments. In this way, nanolithographic masks by self-assembly were fabricated effortlessly.

Similar to observations of DOS, DOA led to a transitional phase from spheres to cylinders by TA (Figure 3-9c-d). SD42 is located in the strong segregation limit with $\chi N=116$; therefore chain mobility is retarded and suffers from slow kinetics of self-assembly during TA. With the use of DOA, the PS-b-PDMS thin film remains swollen after spin-coating, which induces the spherical self-assembly. During TA, high PS

selectivity of DOA allows mobility in the PS matrix and greater relaxation times for PDMS chains to diffuse. Morphology transition occurs before the complete evaporation of the plasticizer, as was shown with DOS inFigure 3-5; the stable cylindrical morphology is trapped when the plasticizer is removed. Due to higher PS selectivity and evaporation rate of DOA compared to DOS, lower temperatures sufficed for phase transition (30 s at 110 °C). Consequently, dewetting phenomena were avoided and a good alignment retained.

In the free energy landscape, DOA minimizes the activation energy, thus allowing an easy exceeding of the free energy barrier to a new stable cylindrical state. The thermodynamics of the self-assembly process via microphase separation is represented by the Gibbs free energy equation $\Delta G_{SA} = \Delta H_{SA} - T\Delta S_{SA}$, where G is the Gibbs free energy required for self-assembly, H the enthalpy and S the entropy of the system at temperature T. This equation is in accordance to equation 1-4 of chapter 1.

In order to exceed the free energy barrier to reach the free energy minimum of the stable cylindrical morphology, the enthalpy changes have to be positive[20]. Since the as-spun micelles are already in a well aligned, the entropy contribution becomes negligible. The free energy required for the morphology transition depends mainly on the enthalpy change associated with the chain crossing over the interfaces of PS and PDMS[16]. These interactions appear only locally at the molecular scale (sharp PS-PDMS interfaces) when the BCP system is already ordered, and the PDMS chains easily diffuse into the swollen PS matrix via the interface diffusion mechanism. This phenomenon has already been observed by blending monomers with rod-coil block copolymers[5]. TA produces an excess of PS chain relaxation, which might explain the L_0 elongation that could be observed. Rapid evaporation of DOA retains the cylindrical morphology, and the BCP chains suffer from lower relaxation to self-assemble with its natural L_0 period. We calculated the same periodicity for free and graphoepitaxial surfaces (36.5 nm in Figure 3-9b, d).

PDMS chains diffuse from spheres to cylinders in the parallel direction of the guiding lines for the morphological transition. A transitional step is illustrated in Figure 3-10, where the passage from spheres to cylinders is observed, emphasizing the fact that the interface interactions related to the phase change are only local.

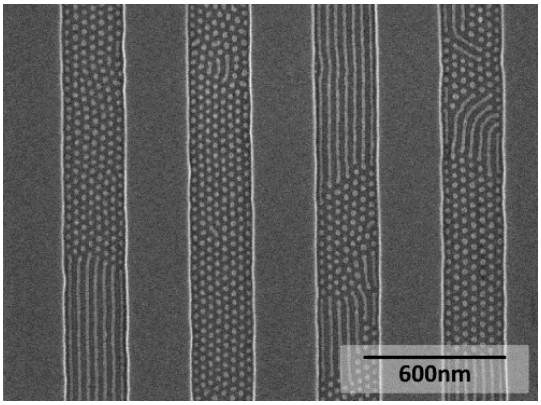

Figure 3-10: SD42 assisted self-assembly by the DOA plasticizer and thermally annealed for 60 s at 80 °C.

Despite fast cylinder formation, some defects were observed, mainly related to end-point defects[21]. This kind of dislocation appears mostly at grain boundaries, where a higher free energy barrier sets up and obstructs the rejoining of domains[22]. In the case of directed self-assembly, it is observed in Figure 3-10 that defects in topographical lines for graphoepitaxy could create defects in the starting structure, and then create end-point defects.

3.4 Graphoepitaxy and Application of SD45 on Large Area Surfaces

The applicability of BCP self-assembly lithography assisted with plasticizers is presented through the complete process from PS-b-PDMS deposition to the final pattern transfer etching. In order to eliminate defects and induce a long-range orientation during self-assembly, BCP lithography was combined with top-down lithography techniques using graphoepitaxy[23]. SD45 (f_{PDMS} = 32%) has very similar properties to SD42 (Mw=45.5 kg/mol, f_{PDMS} = 26%) and has been chosen for this applicational study due to its better commensurability with silicon-rich anti-reflective coating (SiArc)/spin-on-carbon (SOC)guiding lines. The directed self-assembly of SD45 plasticized with DOS (DOS45) is henceforth studied within standard SiArc/SOC guiding trenches[24]. The process flow is illustrated in chapter 2.

After the first etching for template design, DOA45 solution is deposited by spin-coating and the sample is thermally annealed if required. DOA is then either evaporated in vacuum or during TA, as explained above for DOS42 thin films. Transfer etching is performed in a two-step process. First, the nanopatterns are transferred into the remaining SOC layer and then into the silicon substrate by dedicated plasma etching processes (details of etching processes are given in chapter 5).

FIB-STEM images in Figure 3-11a-b compare the thicknesses of SD45 and DOA45 within SiArc/SOC trenches. PDMS domains are distinguished by the image contrast appearing as dark patterns. As can be seen, the SD45 (a) film is thinner than DOA45 (b), which is consistent with the thickness measurements of Figure 3-5. In both cases, the BCP spheres self-assemble on the bottom of the guiding patterns. DOA swells

the PS matrix in the direction perpendicular to the surface, driving PDMS spheres on the bottom. Even though a thicker layer was obtained (Figure 3-11b), the spheres arrange themselves like a monolayer, which was advantageous for the alignment quality. Furthermore, there was no need for any surface functionalization treatment, like a PS or PDMS brush, as the underlying SOC layer naturally favors the wetting of the PS block, as observed in chapter 2. Then, the SOC surface not only promotes the self-assembly and the good alignment of the PDMS spheres within guiding patterns, but also avoids the formation of a PDMS interlayer between copolymer and the SOC layer. Indeed, FIB-STEM images show the absence of a PDMS wetting layer at the interface, which is an advantage for pattern transfer etching (Figure 3-11a).

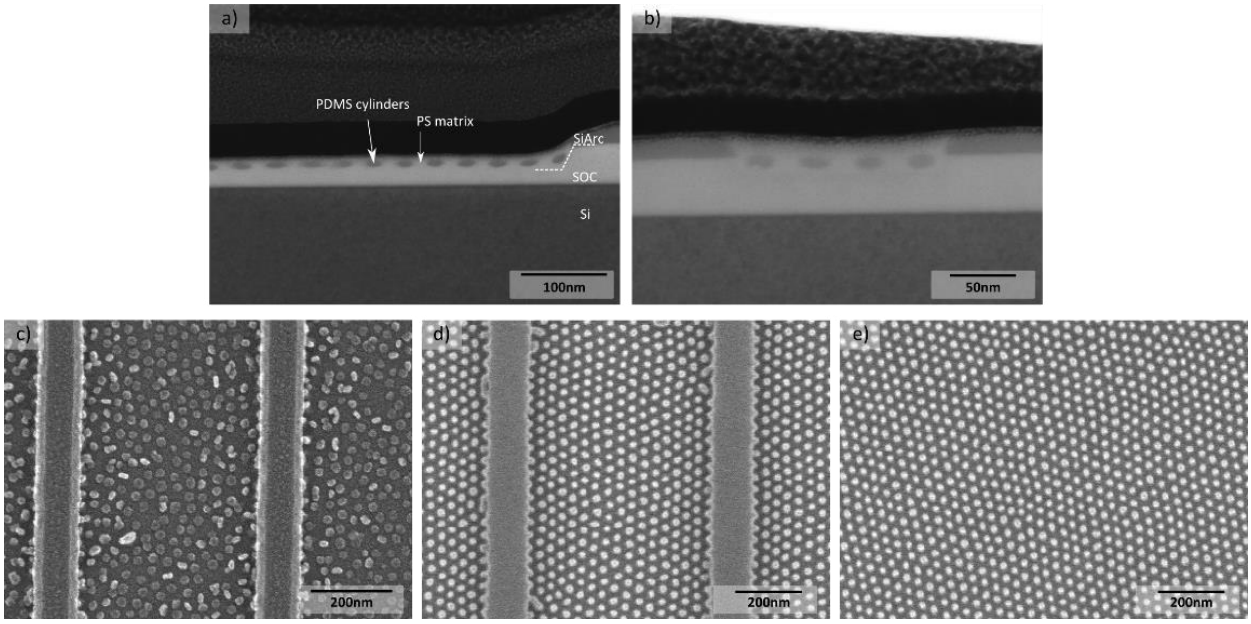

Figure 3-11: (top) STEM cross-sectional images of (a) SD45 and (b) DOA45 in SiArc/SOC guiding lines (bottom) SEM top view images of as-spun micelles of (c) SD45 and (d) DOA45 in SiArc/SOC guiding trenches and (e) DOA45 on plane SOC surface

Figure 3-11c-e shows SEM top view images of as-spun (c) SD45 and (d) DOA45 within SiArc/SOC guiding lines and (e) on plane SOC surface. In Figure 3-11c, micelles were disordered in the case of SD45 and form readily spheres with long-range order for DOA45 within SiArc/SOC guiding trenches and on plane SOC surfaces (Figure 3-11c). The DOA molecules, being non-volatile, act like a solvent and swell the PS block selectively. Due to the screening effect, chain mobility is increased, allowing a phase separation in a spherical metastable ordered packing without any annealing, which is consistent with the results obtained above for the SD42 on PS brushed surfaces (Figure 3-9). Under typical conditions, TA is not satisfied in reasonable processing time to self-assemble SD45[25,26]. Figure 3-12a-b shows SEM top view images of DOA45 and SD45 in SiArc/SOC trenches after a fast TA of 30 s at 110°C. In the SD45 case, there is no effect on the alignment; neither morphology shift nor ordering was observed. In such a short time, the relatively

low temperature does not provide enough energy to overcome the activation energy barrier to attain the equilibrium cylindrical morphology. On the other hand, when blended with DOA, DOA45 thin films readily generate self-assembled horizontal cylinders directed by the guiding lines (Figure 3-12b,c), which is again consistent with results observed for DOS42.

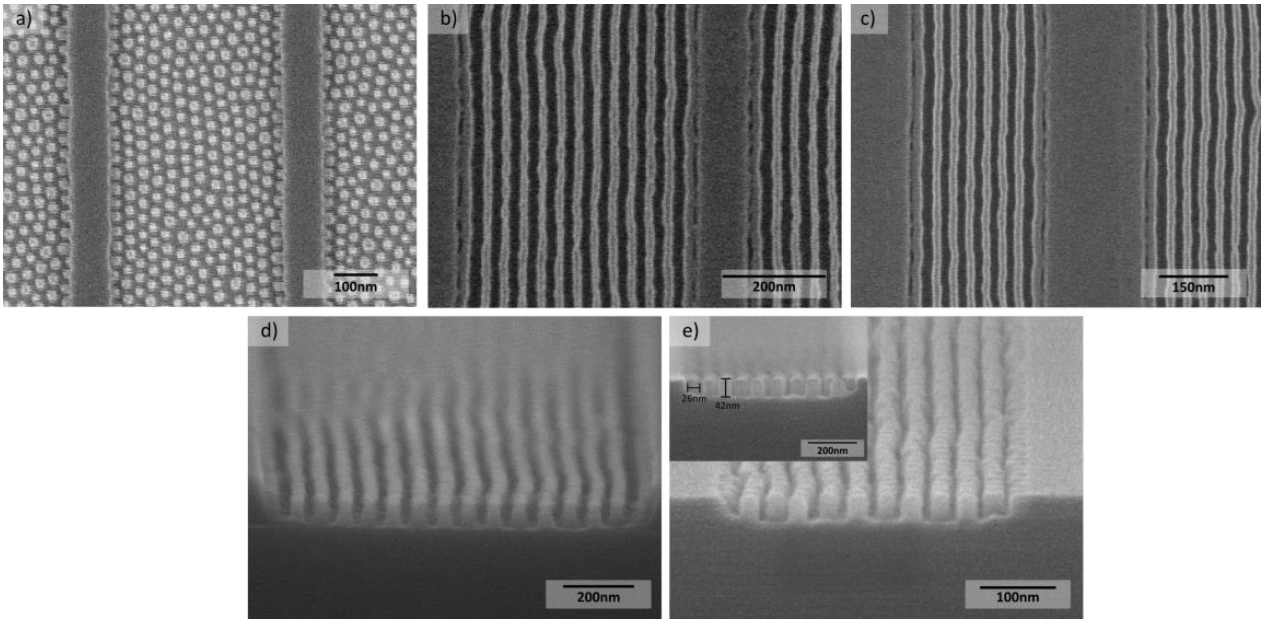

Figure 3-12: (top) SEM top view images of (a) neat SD45 and (b,c) DOA45 in SiArc/SOC trenches after 30s annealing at 110°C, (bottom) SEM cross-sectional images of (d) in SOC and (e) in Si transferred patterns of DOA45

The obtained patterns of DOA45 can be used as etching masks in order to transfer the long-range regular patterns into the silicon substrate. First, the PDMS top wetting layer at the air/BCP interface is removed by CF_4 plasma, and then HBr/O_2 plasma is applied to remove the PS matrix and transfer the pattern in the underlying SOC layer. Simultaneously, the PDMS mask is oxidized. Figure 3-12d,e show cross-sectional SEM images of spin-coated DOA45 after the SOC transfer step. 42 nm-height nanopillars were obtained with approximately 26 nm width for DOA45, which confirms a good CD control during etch. The Si transfer etching step is particularly challenging for the small etch mask of approximately 9 nm height. Transfer etching is performed with plasma recipes similar to those used typically for gate etching in industry. Plasma of $CHF_3/SF_6/Ar$ was used to etch Si selectively, relative to the SiOx/SOC mask. Chapter 5 gives further details on transfer etching processes. A successful proof of concept of the Si pattern transfer for DOA45 is shown in Figure 3-12e.

Finally, we demonstrate large-area pattern formation capability of this ultra-fast assembly process on 300 mm wafer substrates. The application of the DSA of PS-b-PDMS on full 300 mm is important in order to evaluate process feasibility and identify incompatible steps with industry requirements that have to be improved before transferring the process to the fab. DOA45 was spin coated on SiArc/SOC trenches,

annealed for 30 s at 110°C, and etched immediately. 300 mm wafers with 35 nm deep topographic trench patterns with several widths were printed by 193 nm lithography on SiArc/SOC stacks. $Ar/CF_4/CHF_3$ and HBr/O_2 chemistries are used for SiArc and partial SOC etching and the wafer was spin-coated with DOA45. Figure 3-13a shows an image of the wafer after spin. The spin coating resulted in a homogeneous layer, which is confirmed by the uniform color of the wafer; only at the far edges could we observe inhomogeneities in the layer thickness. After self-assembly by TA, eight chips were analyzed by SEM. Figure 3-13b shows the mapping of the wafer with corresponding SEM images. It can be seen that in this ultra-fast process, PDMS cylinders self-assemble with good alignment throughout the 300 mm wafer. Slight differences in the PDMS lines CD are most certainly due to slight differences in layer thicknesses, depending on the position on the wafer. As feature sizes of patterns decrease, the critical dimension uniformity (CDU), line edge and linewidth roughness (LER and LWR respectively) become critical. To evaluate pattern quality of DOA45 lines, the roughness on 9 SEM sample images was measured. The 3σ LWR is found to be of approximately 1.6 nm which is close to the standard requirements (8.7% of 19 nm pitch lines). The 3σ LER shows large variations and could reach 12 to 30% of the line width. High LER values of SiArc/SOC trenches (up to 11 nm) and or the oxygen plasma treatment of the PDMS lines may be the origin of these variations, as proposed in chapter 2. This problem could be solved by optimizing the oxygen plasma conditions and or smoothening treatments of the photoresist before etching the guiding trenches. These treatments may have a positive impact on the final DSA pattern and decrease the LER values drastically so that LER and LWR requirements can be met. Furthermore, film thicknesses variations could be avoided by improving the spin-coating deposition on 300mm wafers and so the variations of the CDU (Figure 3-13). In comparison to SD45 (12 % LER and 7 % LWR from line width) neither LER nor LWR of DOA45 increased drastically, which is expected since the plasticizer is removed and it does not modify the BCP pattern. However, a deeper statistical study is needed to give reliable information about LER/LWR behavior with and without plasticizer on 300 mm wafers. Despite these differences, we were able to show the feasibility of this ultra-fast assembly process of SD45 by plasticizer integration on one whole wafer sample. These results could open up profitable prospects for the microelectronic industry. A future study would contain further optimization of the 300 mm wafer process. In this study the results of one sample are presented, as the author does not have easy access to a manual 300 mm wafer spin-coater, which is not dedicated for this kind of experiments. Further work would include thus, a repetitive study of the 300 mm wafer processing, especially the spin-coating and the plamsa etching of guiding trenches in order to obtain smoother edges.

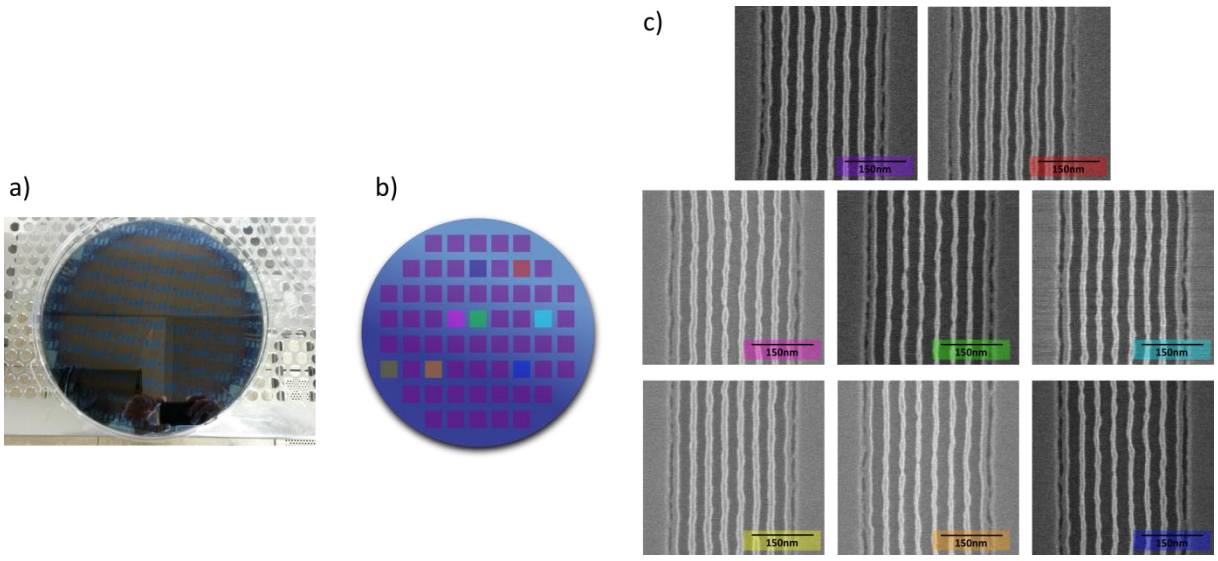

Figure 3-13: (a Photograph of DOA45 deposited on 300 mm wafer; (b mapping of the (c SEM images taken on 300 mm wafer. Samples were taken from eight selected locations throughout the wafer; the color code of the scale bar indicates the location on the wafer.

3.5 Conclusion

In summary, the influence of PS-selective plasticizers on the self-assembly process of PS-b-PDMS has been studied. The block copolymer forms PS-b-PDMS micelles in solution with a hydrodynamic diameter D_h commensurable with its natural period length L_0. This fact is due to the choice of selective plasticizers and solvent, PGMEA, used for solution preparation. The physical properties of plasticizers such as negligible vapor pressure and high PS selectivity promote high lateral motion of chains, and consequently a significant enhancement of the PS-b-PDMS self-assembly kinetics. The same BCP systems would under usual conditions (without blending with plasticizers) need either several days of annealing or extremely high temperature (in high- χ BCPs, the ODT transition is often above its degradation temperature, which is why it would sometimes even not be possible to assemble the system in TA). Here we obtain well-ordered spheres in a 30 s one-step coating process, without any post-coating annealing. This process reflects an increase of assembly kinetics of at least 3 orders of magnitude when counting annealing times of 2 days. SVA is often obtained in shorter process times, but the extreme sensitive process as well as its cumbersome up-scaling prospective make our method a concrete alternative annealing method that could be easily applied in industry.

Moreover it was found that the evaporation of plasticizer via thermal annealing allows a fast morphological transition from a metastable to its stable morphology. After 30 s of annealing, well-aligned cylinders were obtained. Among the tested plasticizers, diisooctyl adipate DOA resulted in the best trade-off between evaporation rate and PS-selectivity. In the view of potential industry integration, PS-b-PDMS blended with

DOA was tested on standard graphoepitaxy SiARC/SOC trenches, and pattern transfer into silicon substrates was successfully performed.

Finally, as a proof of concept, the process was applied on a whole 300 mm Si wafer. In this way, we have demonstrated a practical method to make block copolymers lithography a process with high throughput, and have shown the applicability to fabricate high-resolution structures on large surfaces. The process will be object to further optimization, but these results are already remarkably promising for the microelectronics industry, as well as for other fields needing resolved structures on large surfaces such as solar panels or photocathodes.

References

(1) Wright, D. B.; Patterson, J. P.; Pitto-Barry, A.; Lu, A.; Kirby, N.; Gianneschi, N. C.; Chassenieux, C.; Colombani, O.; O'Reilly, R. K. The Copolymer Blending Method: A New Approach for Targeted Assembly of Micellar Nanoparticles. *Macromolecules* **2015**, *48*, 6516–6522.

(2) Tanaka, H.; Hasegawa, H.; Hashimoto, T. Ordered Structure in Mixtures of a Block Copolymer and Homopolymers. 1. Solubilization of Low Molecular Weight Homopolymers. *Macromolecules* **1991**, 240–251.

(3) Hashimoto, T.; Tanaka, H.; Hasegawa, H. Ordered Structure in Mixtures of a Block Copolymer and Homopolymers. 2. Effects of Molecular Weights of Homopolymers. *Macromolecules* **1990**, 4378–4386.

(4) Yang, J.; Wang, Q.; Yao, W.; Chen, F.; Fu, Q. Effect of Added Homopolymer on Structures of Thin Films of PS-B-PDMS/PS Mixture under Solvent Vapor Annealing. *Appl. Surf. Sci.* **2011**, *257*, 4928–4934.

(5) Chun-Chih, H.; Shang-Jung, W.; Shih-Hsiang, L.; Seth B., D.; Wei-Fang, S. Kinetically Enhanced Approach for Rapid and Tunable Self-Assembly of Rod–Coil Block Copolymers. *Macromol. Rapid Commun.* **2015**, *36*, 1329–1335.

(6) Ghoshal, T.; Ntaras, C.; Shaw, M. T.; Holmes, J. D.; Avgeropoulos, A.; Morris, M. A. A Vertical Lamellae Arrangement of Sub-16nm Pitch (domain Spacing) in a Microphase Separated PS-B-PEO Thin Film by Salt Addition. *J. Mater. Chem. C* **2015**, *3*, 7216–7227.

(7) Immergut, E. H.; Mark, H. F. Principles of Plasticization. In *Plasticization and Plasticizer Processes*; American Chemical Society, **1965**; pp. 1–26.

(8) Csernica, J.; Brown, A. Effect of Plasticizers on the Properties of Polystyrene Films. *J. Chem. Educ.* **1999**, *76*, 1526.

(9) Wypych, G. *Handbook of Plasticizers*; William Andrew, **2013**; p. 800.

(10) Brandrup, J.; Immergut, E. H.; Grulke, E. A. *Polymer Handbook*; 4th ed.; Wiley-Blackwell: New York, NY, **1999**; Vol. 2, p. 2336.

(11) Fukumine, Y.; Inomata, K.; Takano, A.; Nose, T. Micellization Behavior of Diblock Copolymers in Solution near the Critical Micelle Temperature. *Polymer* **2000**, *41*, 5367–5374.

(12) Bennett, T. M.; Jack, K. S.; Thurecht, K. J.; Blakey, I. Perturbation of the Experimental Phase Diagram of a Diblock Copolymer by Blending with an Ionic Liquid. *Macromolecules* **2016**, *49*, 205–214.

(13) Liaw, C. Y.; Henderson, K. J.; Burghardt, W. R.; Wang, J.; Shull, K. R. Micellar Morphologies of Block Copolymer Solutions near the Sphere/Cylinder Transition. *Macromolecules* **2015**, *48*, 173–183.

(14) Cochran, E. W.; Garcia-Cervera, C. J.; Fredrickson, G. H. Stability of the Gyroid Phase in Diblock Copolymers at Strong Segregation. *Macromolecules* **2006**, *39*, 2449–2451.

(15) Schausberger, A.; Ahrer, I. V. On the Time-Concentration Superposition of the Linear Viscoelastic Properties of Plasticized Polystyrene Melts Using the Free-Volume Concept. *Macromol. Chem. Phys.* **1995**, *196*, 2161–2172.

(16) Bates, F. S.; Fredrickson, G. H. Block Copolymers—Designer Soft Materials. *Phys. Today* **1999**, *52*, 32.

(17) Bai, W.; Yager, K. G.; Ross, C. A. In Situ Characterization of the Self-Assembly of a Polystyrene–Polydimethylsiloxane Block Copolymer during Solvent Vapor Annealing. *Macromolecules* **2015**, *48*, 8574–8584.

(18) Damman, P.; Gabriele, S.; Coppée, S.; Desprez, S.; Villers, D.; Vilmin, T.; Raphaël, E.; Hamieh, M.; Akhrass, S. Al; Reiter, G. Relaxation of Residual Stress and Reentanglement of Polymers in Spin-Coated Films. *Phys. Rev. Lett.* **2007**, *99*, 036101.

(19) Sharma, A.; Reiter, G. Instability of Thin Polymer Films on Coated Substrates: Rupture, Dewetting, and Drop Formation. *J. Colloid Interface Sci.* **1996**, *178*, 383–399.

(20) Rubinstein, M.; Colby, R. H. *Polymer Physics*; OUP Oxford, **2003**.

(21) Simão, C.; Tuchapsky, D.; Khunsin, W.; Amann, A.; Morris, M. A.; Torres, C. M. S. Dimensional and Defectivity Nanometrology of Directed Self-Assembly Patterns. *Phys. status solidi* **2015**, *12*, 267–270.

(22) Li, W.; Müller, M. Defects in the Self-Assembly of Block Copolymers and Their Relevance for Directed Self-Assembly. *Annu. Rev. Chem. Biomol. Eng.* **2015**, *6*, 187–216.

(23) Girardot, C.; Böhme, S.; Archambault, S.; Salaün, M.; Latu-Romain, E.; Cunge, G.; Joubert, O.; Zelsmann, M. Pulsed Transfer Etching of PS–PDMS Block Copolymers Self-Assembled in 193nm Lithography Stacks. *ACS Appl. Mater. Interfaces* **2014**, *6*, 16276–16282.

(24) Weimer, M.; Wang, Y. Materials for and Performance of Multilayer Lithography Schemes. *Proc. SPIE* **2007**, *6519*.

(25) Jung, Y. S.; Ross, C. A. . Solvent-Vapor-Induced Tunability of Self-Assembled Block Copolymer Patterns. *Adv. Mater.* **2009**, *21*, 2540–2545.

(26) ITRS. International Technology Roadmap for Semiconductors. **2013**, http://www.itrs.net.

Chapter 4 Pattern Generation of High Resolution Lines via Thermal Annealing of a Cylindrical PS-b-PDMS

4.1 Introduction

After having showed long-range order results with SD45, we want to address now the challenges of the 14 nm technology node and beyond. In order to obtain this goal the performances of BCP lithography can be further increased by extending the range of available pattern dimensions to sub 10 nm. This chapter deals with the self-assembly of SD16, a cylindrical PS-PDMS system with an overall molecular weight of 16kg/mol (f_{PDMS} = 33%), thus a high-χ, low-N BCP. As described in the first chapter, the size and state of the ordered BCP are largely governed by the volume fraction of each block (f_i), the overall degree of polymerization (N, proportional to the molar mass) and the Flory-Huggins interaction parameter (χ). At fixed χ values, there is a minimum N value underneath the BCP remains disordered. Higher values for χ, allow for lower values of N and thus lower feature size. In theory one could descend to BCPs with feature sizes down to 2 nm, but the main challenge besides defect control, dewetting and stability, is the pattern transfer[1]. High aspect ratio feature sizes with dimension of 10 nm and less become extremely challenging to obtain via pattern transfer etching[2]. This chapter deals with the work on SD16 which has a theoretical feature sizes of approximately 8 nm. This chapter gives an overview of the potential of this polymer on graphoepitaxy substrates. Two different substrates were tested here, the one already described in chapter 2 (SiArc/SOC substrates) and a second one with trenches entirely made of silicon.

4.2 Experimental Details

Cylinder-forming PS-b-PDMS BCP (Mw = 16 kg/mol, f_{PDMS} = 33%) and hydroxyl-terminated polystyrene homopolymer h-PS (M_w = 3.2 kg/mol) were purchased from Polymer Source Inc. (Canada) and used as received. Microelectronic-grade propylene glycol methyl ether acetate (PGMEA) and toluene were purchased from Sigma-Aldrich and were used as the solution solvent for brush, BCP, and solvent vapor annealing. Cleaned Si and SiArc/SOC graphoepitaxy substrates were used in this study. O_2 plasma was used in order to activate the surface for the brush treatment. Hydroxy-terminated polystyrene was then grafted onto the Si cleaned surface after spin-coating deposition of a 1 wt% PGMEA solution at 1500 rpm; annealing at 200 °C during 5 min was performed to ensure the thermal grafting reaction. After a rinsing step in PGMEA to remove ungrafted homopolymer, a thickness of 3±1 nm is measured by ellipsometry. A precise optimization of the PS-brushing has been performed in the block copolymer team at LTM by Garnier and coworkers[3]. As described in this presentation, ellipsometry, AFM, XPS and water contact angle measurements were performed on different brush grafting techniques and the self-assembly of SD16 on different brushes led to the optimized parameters that are also used here. A homogeneous brush layer of 3 nm is obtained that leads to uniform wetting of the subsequent BCP layer. Concerning the BCP self-assembly, several experiments with changing parameters have been performed, however only limited results with optimum conditions are here presented. Solutions of 1 wt % dissolved in PGMEA solvent were

prepared and spin-coated (1500–3000 rpm) on cleaned substrate. Thicknesses were measured by ellipsometry on bare Si and SOC substrates and were estimated at approximately 17±1 nm on SOC substrates and 22±1 nm on PS-brushed Si substrates. Solvent vapor annealing, when applied, was carried out in a simple Petri dish setup, introduced in chapter 2, in toluene or PGMEA vapor. A hot plate was used for heat treatment at 150 °C for 15 min. The same characterization tools as described in chapter 2 were used (MEB, STEM, line width and edge roughness).

4.3 Effect of Substrate Wetting on PS-b-PDMS (M_w=16kg/mol)

As described in chapter 2, the polymer/substrate interface plays a very important role during self-assembly of block copolymers. Pattern generation of SD16 was obtained via graphoepitaxy in SiArc/SOC and Si trenches with native oxide that were coated with a hydroxyl-terminated PS-brush. The BCP films were treated with different annealing methods, depending on the substrate. We discuss here thermal and solvothermal annealing of SD16 in order to obtain a monolayer of PDMS cylinders, oriented parallel to the surface. As PDMS has lower surface tension compared to PS (γ_{PDMS} =20 mN/m and γ_{PS} = 40 mN/m) it preferentially wets the air/polymer interface. When annealed by thermal or solvent vapor annealing alone, the literature reports for this, or similar low molecular PS-PDMS systems, the formation of highly ordered spheres or cylinders only after several hours or even days of annealing [4–9]. Exotic methods like microwave annealing is one way to decrease processing time or the combination of microwave and solvent annealing was shown to lead to ordered phase separation in seconds to a few minutes[10–13]. Other, simpler methods have been introduced where the BCP sample is solvothermally annealing, i.e. the sample is either first exposed to solvent vapor and then to thermal annealing or the SVA chamber is heated simultaneously[14–17]. Jung et al. demonstrated further a rapid, large-area (200 mm wafer) solvent annealing of SD16 and SD45 with a solvent swollen polymer gel pad[18]. By bringing the pad closely to the BCP surface a proximity injection of solvent molecules leads to self-assembly in 1min. These setups however remain complex and difficult for whole wafer annealing and when solvents are used a risk of contamination of the wafer remains, which could be avoided by a simple thermal annealing. In this chapter we propose a way to successfully anneal SD16 solely by thermal annealing. First, the successive combination of solvent and thermal annealing which leads to a drastic reduction of process time is presented on Si substrates. Further thermal annealing is perfomed on SiArc/SOC graphoeptiaxy trenches. The mechanisms involved are explained in the following.

Figure 4-1 shows SD16 as-spun on planar SOC and PS-brush coated Si substrates in order to determine the morphology of the as-spun micelles.

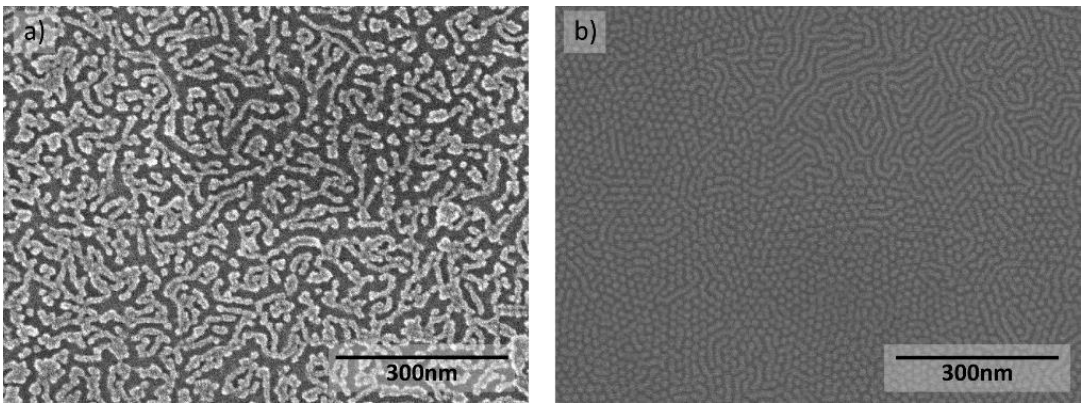

Figure 4-1 : SEM top-view images of SD16 as-spun on a) SOC substrate and b) PS-brushed Si substrate

Layer thicknesses were measured by ellipsometry and found to be 17 nm and 22 nm (± 1 nm) for SOC and PS-brush substrates, respectively. Besides a higher error in ellipsometry fit on the SOC layer, difference in the surface energies (PS-brush on Si ≈ 34 mN/m, oxidized SOC ≈ 41 mN/m) could be responsible for the slight thickness discrepancy using the same spin speed. On SOC substrates, micelle formation of SD16 differs from that of SD45 by forming worm like micelles instead of spheres in the case of SD45. A probable possibility is, that the influence of PGMEA on the morphology (described in chapter 2) is less significant in the case of SD16, due to its intrinsic higher PDMS amount compared to SD45 ($f_{PDMS\text{-}SD16}$ = 33%, $f_{PDMS\text{-}SD45}$ = 31%). On PS-brush coated Si substrates, SD16 forms a mixture of well-defined spheres and cylinders. It was shown that the layer thickness of cylinder forming BCP has great influence on the morphology[19,20]. The appearance of the cylinder formation in zones, suggests that there are undulations in the layer thickness driving the system to favor cylinder over spherical morphology. Furthermore it is noteworthy that the spheres and cylinders on PS-brush coated Si substrates are well-defined, homogeneous in size and show a beginning of ordering, which is unusual for as-spun structures[21–23]. A possible reason for this phenomenon is a better wetting of the PS block on the PS-brushed surface. Even though it was shown in chapter 2, that the SOC substrates prevents the formation of a PDMS wetting layer, the wetting of a PS-brushed surface should be even better for the PS block due to their high affinity to each other. It was shown by Harrison et al. that the BCP has more mobility when the majority part wets the surface, whereas it should have enough mobility in order to diffuse[24]. On too strongly interacting surfaces the block that wets the surface is "pinned" onto the surface and diffusion would be decreased. In our case, we think that the PS-brush lubricates the BCP chain movements slightly more than the SOC layer, which is why we obtain a better alignment right after spin-coating. Nevertheless, apart from as-spun organization, the SOC layer seems to provide as much mobility for chain movement during annealing as PS-brush coated Si. This will be discussed later.

We now concentrate on the layer composition and the interface SD16/substrate. Figure 4-2 shows cross section STEM images of annealed SD16 in SiArc/SOC and PS-brush coated Si trenches. Heavier atoms are displayed with darker contrast, PDMS patterns can thus be distinguished as dark spots in the layer. Self-assembly was obtained by solvothermal annealing in the case of Si substrate and thermal annealing in the case of SOC substrate. Detailed descriptions of the processes are given in the next section. It can be noticed that trench depth is not optimized for the silicon trenches, resulting in double layer formation at the edges of the trenches. Similar results were obtained for SD45 when the trench depth exceeded drastically the BCP characteristic domain length. In this case, the trench depth is of about 45 nm for Si trenches and 27 nm for SiArc/SOC trenches, which is why cylinder formation is more homogeneous in SiArc/SOC trenches, without the formation of double layers. Further, it can be noticed that both surfaces prevent the formation of PDMS interlayers, which is a precondition for pattern transfer etching.

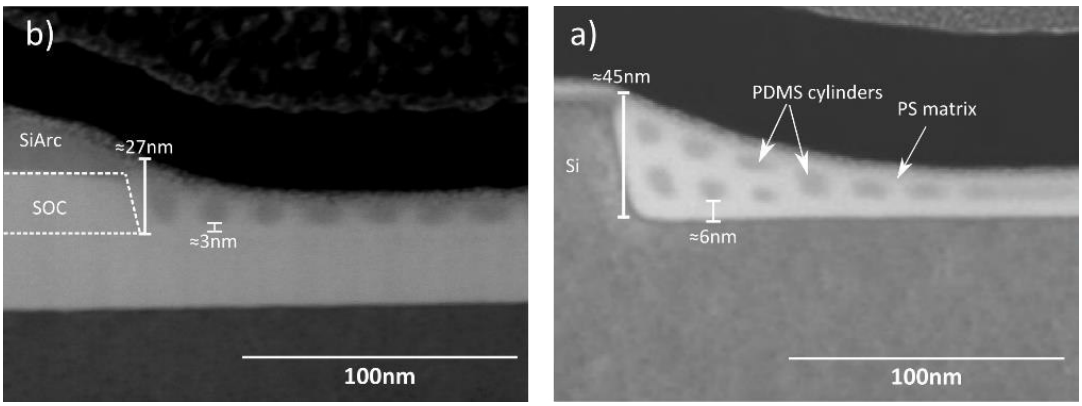

Figure 4-2 cross section STEM images of SD16 after annealing in a) SiArc/SOC and b) PS-brushed silicon trenches

We further discovered that the shape of the PDMS cylinders is round and not elliptic as it was for SD45. This is due to the fact that, in this case, the presented samples are thermally annealed. During solvent annealing the BCP layer swells about twice its initial thickness and collapses rapidly when the annealing chamber is opened and the solvent evaporates. Due to the fast compression, the PDMS cylinders collapse then into an elliptic form. The final cylinder shape might play a crucial role in pattern transfer etch, which will be discussed in chapter 5. A higher distance of the spheres to the substrate can be observed in the case of Si substrates (6 nm on Si vs. 3 nm on SOC), which is due to the additional PS-brush in the case of Si substrates.

4.4 Solvothermal Annealing of SD16 on Silicon Graphoepitaxy Substrates

As explained above, different annealing methods were performed on SD16 in order to find optimal conditions and decrease the process time. Two different graphoepitaxy substrates, PS-brushed Si trenches, that could have advantages during etching processes, and SiArc/SOC trenches that have been introduced in chapter 2, were used. In samples prepared on SiArc/SOC, the SOC layer serves as transfer layer, PDMS

cylinders are first transferred into the SOC layer and then into the Si substrate. For small feature sizes the SOC interlayer might become too high and cause pattern collapse during transfer etching. By preparing PDMS masks directly on Si or with only a small interlayer (the PS-brush is approximately 3 nm thick) these pattern collapse issues could be avoided. Further details of the etching process will be explained in chapter 5.

First, as solvent annealing was found to work for SD45, different solvent vapor annealing techniques have been tried on SD16. Although the film is homogeneous in height and composition before annealing, dewetting occurred during annealing as soon as 3 min annealing only. Figure 4-3a shows a SEM top view micrograph of a 5 min annealed sample in toluene vapor. It was observed that after a few seconds of annealing, holes appear in the layer, which grow over time and finally merge (images not shown). At the end islands are obtained, as shown in Figure 4-3a, in which the BCP material reaches multi-layers with increasing thickness and the rest of the surface is left clear of polymer. It can be found in the literature that the film breaks up due to capillary instabilities during height fluctuation caused by the swelling of the BCP layer[25,26]. It was also shown that this kind of dewetting depends on the composition and the initial thickness of the BCP. Higher thickness leads to slower dewetting[27]. This is the reason why SD45 with its different composition and higher layer thickness shows less dewetting issues in toluene vapor. As already explained in chapter 2, besides dewetting issues, toluene is a toxic solvent, which is prohibited in microelectronic fabs. Other safe solvents have to be introduced for the SD16 process. Dewetting could almost completely be avoided for SD16 when annealed shortly in PGMEA vapors. PGMEA has the advantages to be a safe solvent (see chapter 2) and to have low vapor pressure (P_{PGMEA} = 2.8 mmHg vs. $P_{Toluene}$= 22 mmHg at 20 °C). Phase separation and dewetting during SVA is influenced by a number of parameters like solubility, molecular weight and composition of the BCP, substrate interactions and film thickness[27]. The SVA chamber in toluene vapor is quickly saturated and the BCP film is swelled much faster than in PGMEA, due to the higher evaporation rate of toluene. The thickness fluctuation is then stronger and increased capillary instabilities lead to a quicker layer rupture. Figure 4-3b shows a SEM image of SD16 after 1min of SVA in PGMEA. The layer shows some dewetting on planar areas after only 1min annealing even with a low vapor pressure solvent. Inside the trenches the layer was however homogeneous as depicted in Figure 4-3c. Although we were able to produce good alignment solely in PGMEA vapor, the reproducibility of SVA samples is very poor. Despite its wide use, all mechanisms involved in the process of SVA are not fully understood yet, and often only some of the numerous parameter, influencing the final results, like swelling ratio and solvent removal rates, are taken into account during SVA[28,29]. However most certainly all are crucial for reproducibility. In order to control all parameters properly and reproduce the exact SVA cycle every time, a highly sophisticated setup has to be installed. This setup has then to be scaled

up for production which complicates the introduction of BCPs in industry. Therefore, other, simpler processes, like thermal annealing have been tested before engaging in an ambitious SVA chamber construction.

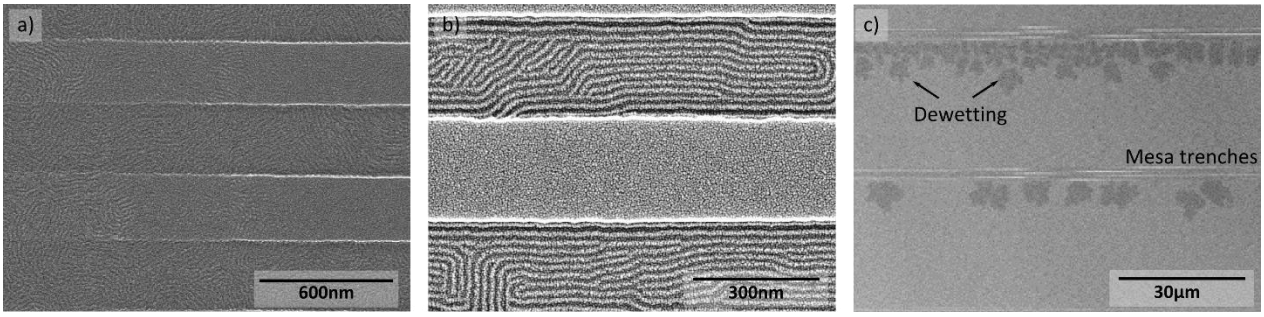

Figure 4-3 : SEM top view images of SD16 after solvent vapor annealing on Si graphoepitaxy substrates (a) 5min in Toluene and (b) 1min in PGMEA (c) low magnification of (b)

In thermal annealing the BCP is in general heated above its glass transition temperature (T_g) in order to approach the order-disorder transition temperature (ODT). Thermal annealing only of SD16 does not provide enough energy in reasonable time in order to obtain parallel aligned cylinders. Figure 4-4 shows top view SEM images of SD16 on Si substrates after 15min annealing at 150°C. We can find typical annealing times to obtain parallel alignment to be of 2h and more in the literature[30]. As this process time is not acceptable, our search for the best annealing method continues.

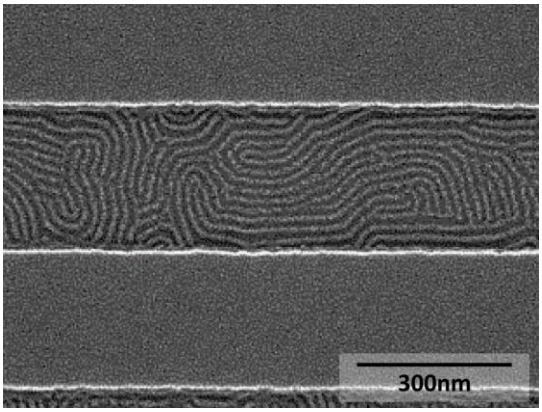

Figure 4-4 : SEM top view image of SD16 in Si graphoepitaxy trenches after 15min annealing at 150°C

A decrease in process time by microwave assisted solvent annealing for example, was already presented in the literature[10,31]. Kim et al. and Ross and coworkers showed the advantages of warm solvent annealing on defect quantity and process time[15,32]. As a high-χ BCP, PS-PDMS has a rather high interfacial energy barrier at the blocks interfaces that prevents the diffusion of the BCP by thermal activation. However, since it is a low molecular weight BCP, the kinetics of polymer diffusion in SD16 are faster than those of SD45. In combined processes where the sample is exposed to solvent vapor at the same time as it is heated, the solvent vapor pressure and the solubility of solvent in the film are changed by the temperature rise. In the

currently presented process, the sample is first annealed for 1min in PGMEA solvent vapor and is then transferred onto a hot plate where it is annealed for 15min at 150°C. Figure 4-5 shows SEM top view images of the annealed samples on PS-brushed Si trenches.

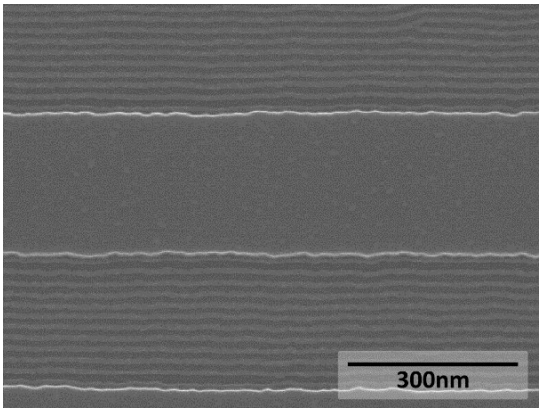

Figure 4-5 : SEM top view image of SD16 after 1min SVA in PGMEA followed by a TA of 15min at 150°C

In the first short solvent vapor annealing, the solvent has enough time to penetrate the BCP film providing sufficient energy for the polymer chains to start diffusion. By continuing the morphology change towards thermodynamic equilibrium via thermal annealing, dewetting is prevented. Solvent annealing for SD16 at room temperature was reported to need more than 1h for uniform alignement[4,14,33,34]. In our experiments such long annealing times led to the dewetting of the BCP layer. Pure thermal annealing fails to align the BCP satisfactorily on these PS-brushed substrates. Interestingly the process is not invertible. By inversing the process and performing first thermal annealing, the solvent that might be trapped in the polymer after spin-coating, is completely evaporated and cannot participate to the self-assembly process. The solvent vapor exposure after TA is too brief for the solvent molecules to be sufficiently absorbed by the completely dried BCP layer. By annealing first with solvent vapor, on the other hand, the solvent continues to contribute to the diffusion of polymer chains by evaporating slowly through the film upon heating, providing excellent cylinder alignment. It is thus proposed that a combination of solvent and thermal annealing is here the optimum treatment.

As described in chapter 2, solvent vapor annealing is a process that needs to be controlled meticulously in order to obtain continuously the same results. Furthermore the setup of a SVA chamber is rather complicated to be scaled up. Although we were able to obtain good results with a “safe” solvent PGMEA, it would be an advantage for manufacturing processes to be able to avoid SVA completely. In the following section, we present the alignment of SD16 by solely thermal annealing.

4.5 Thermal Annealing of SD16 on SiArc/SOC Graphoepitaxy Substrates

On SiArc/SOC trenches, we observe that it is not necessary to expose the sample to solvent vapor prior to thermal annealing. SEM micrograph of Figure 4-6 shows the perfect alignment of SD16 in SiArc/SOC trenches after 15min annealing at 150°C.

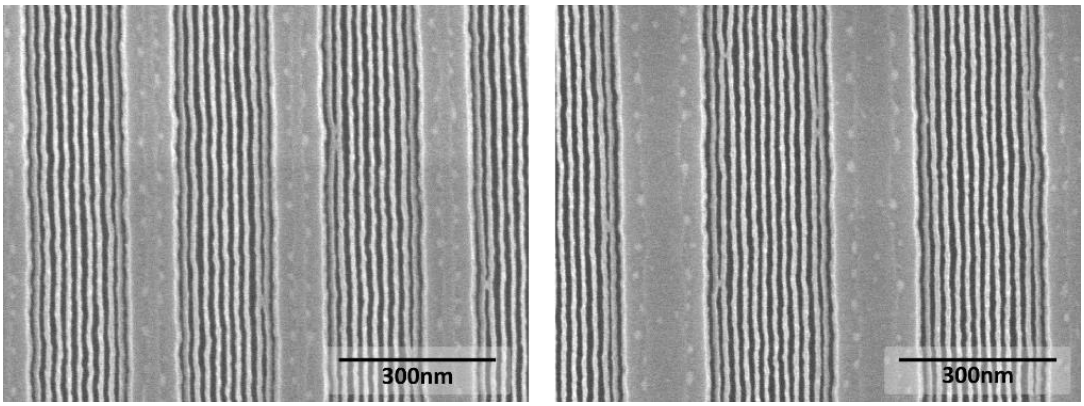

Figure 4-6 : SEM top view images of SD16 after 15min annealing at 150°C in different commensurability SiArc/SOC trenches

Here, the SOC substrate leads to solvothermal annealing of the SD16. The SOC substrate, a polymer based material[35], is permeable to solvents and can swell under solvent vapor. Figure 4-7 shows the swelling of a plane SOC substrate in a confined solvent vapor environment. In approximately 60min the SOC layer swells approximately 7%.

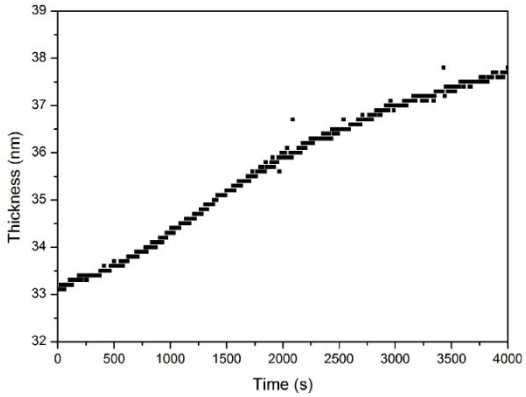

Figure 4-7 : Swelling rate of SOC substrate in solvent vapor

Here, during the deposition of SD16 by spin-coating, the solvent is partly absorbed by the SOC and retained until heated. The BCP is swelled from underneath as already explained for the PS-brushed Si substrates. Now that it is swelled, the diffusive energy barrier is below that of the unswollen BCP. Thus χ_{eff} is decreased and thermal annealing above T_g leads to polymer diffusion, whereas it would not be possible without the solvent. Moreover, the heating of the sample leads to the evaporation of the solvent, thus "quenching" of the BCP layer. It has been shown that the solvent removal step is of great importance during SVA. If the solvent

is reduced slowly it often leads to a decrease in defect density[36,37]. The sample has then more time to reach lower energy configurations while the solvent is still present[15]. In our case, as the solvent resides underneath the BCP layer, we presume that the evaporation, as the solvent has to diffuse through the SOC and the BCP layer, happens rather slowly. Considerable rearrangements of the BCP chains can appear when the sample is heated while the solvent is still present. On silicon substrates the PS-brush with its 3 nm thickness is not able to retain as much solvent as the SOC layer during spin coating. We are thus able to obtain perfectly aligned PDMS cylinders by solely thermal annealing which presents a strong potential over SVA for upscaling processes. The obtained PDMS patterns can be used as etch mask for FinFET production, as will be shown in chapter 5. After having created good etching masks, pattern quality, line edge roughness and line width roughness, should be characterized.

4.6 Line Edge Roughness Measurements of SD16

The line edge roughness of features is a crucial aspect in semiconductor industry. Defects resulting from roughnesses higher than ITRS specification can cause short circuits and will degrade device performances. If the roughness of BCP templates cannot be controlled within limits, the use of block copolymers in manufacture can be at risk. As of its high χ value, PS-b-PDMS exhibits sharper interfaces between the blocks, which is why its edge roughness should be decreased in comparison to lower χ value BCPs. This was described in the literature on PS-b-PDMS[17].

Here we measured the roughness of SD16 in order to determine its applicative potential in industry. The line edge roughness was measured with a commercial software on top view SEM images of SD16 after oxygen plasma treatment (Figure 4-8).

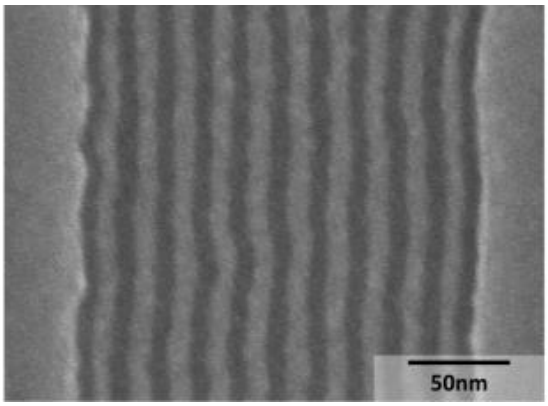

Figure 4-8 : High magnification SEM image of SD16 and corresponding LWR/LER and CD measurements. CD = 12.8 nm, 3σ (LWR) = 1.68 nm, 3σ(LER) = 4.12 nm

The obtained values are the result of 10 images taken in one trench of one sample on a manual SEM and are thus preliminary. The ITRS requirements state that the LWR should not exceed 8% of the critical dimension (CD) in order to guarantee the full performance of the device. As described in chapter 2, SD45 shows after

SVA a LER of 3.4 nm which is about 12% of the CD (~27 nm). When decreasing feature size to a CD of 12 nm (the discrepancy between measured CD and theoretical DC could be related to the plasma revealing techniques), the LWR becomes even more important (3σ = 4 nm, CD = 12 nm) and exceeds the requirements by far (30%). Jung et al. demonstrated LER/LWR values much lower than those measured here for the same BCP system [17]. As described in chapter 3, we think that our high LER/LWR values originate from the photolithography template which shows already high roughness values (3σ = 11 nm) and that are consequently transmitted into the BCP. This phenomena is highlighted in Figure 4-9 where a defect of the guiding trench is clearly mimicked by the PDMS cylinder.

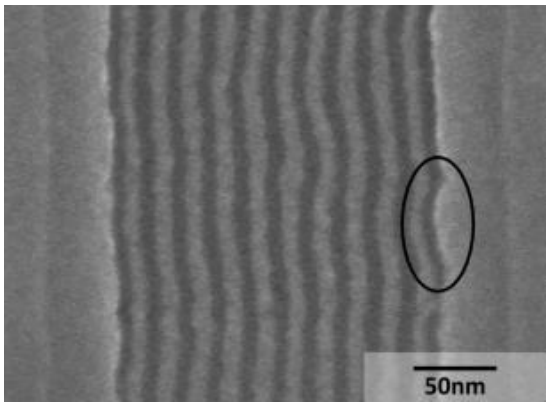

Figure 4-9 : High magnification SEM image of a defect of the lithography guiding trench transmitted onto the PDMS cylinders

It was demonstrated that BCP are able to "repair" defects of chemoepitaxy patterns. Particularly lamellae BCP have been investigated on their behavior on chemical templates [38–41]. However, Stoykovich et al. showed in experiments and simulations that the propagation of the roughness from the template into the BCP film is extremely dependent on the roughness geometry, wavelength and film thickness. The roughness in the BCP interfaces decays more rapidly in thick films than in thin films. Furthermore short LWR fluctuations were found to be mitigated very quickly in the polymer melt while long LWR wavelength damaged the BCP throughout its entire height [39]. The presented results were obtained on BCPs on chemoepitaxy substrates on which the healing process should be easier as there is no physical constriction. Contrary to the "healing" effect, Cheng and coworkers described that the guiding template pattern can induce defect formation[42]. The authors observed local vacancies in a spherical microdomain array, when sharp edge features were observed on the sidewall feature. In order to accommodate for the missing domain, the array extends or contracts to maintain the ordered arrangement. Similarly to this results, we suppose that defects in the trench walls can cause perturbations in the whole array of PDMS cylinders in order to compensate the induced defect. As described in chapter 2, the LER of the graphoepitaxy sidewalls can be improved by performing post-lithography smoothening treatments in VUV, heat or HBr plasma.

The oxygen revealing plasma treatment is known to induce roughness on PDMS lines. Optimization of the plasma revelation step could also reduce this roughening. Finally, similar smoothing steps as those, proposed for lithography trenches could be applied on the PDMS lines.

Interesting for a future work would be the statistical investigation of LER/LWR on a CD-SEM and to study the evolution of the CD uniformity after pattern transfer. Such a study will be facilitated when decontaminated polymers will be available that could be implemented on full 300 mm tools available in the LTM lab and in Leti's cleanrooms.

4.7 Conclusion

This chapter presents the behavior of SD16 on silicon and SiArc/SOC graphoepitaxy substrates. It was shown that differences in surface energies result in different wetting behavior depending on the substrate, so different layer thicknesses are obtained. Furthermore the as-spun morphology is dependent on the substrate surface. On PS-brushed Si surfaces the as-spun state is further "developed" than on SOC substrates, probably due to the slightly better wetting of the PS block on the PS brush than on the SOC. Best alignment on Si graphoepitaxy samples were achieved through a solvothermal annealing in which the sample is first exposed to PGMEA vapor and then transferred to a hot plate to anneal for 15 min at 150°C. On SiArc/SOC substrates, solely thermal annealing was sufficient to align the BCP inside the guiding trenches. Due to the thick layer of SOC, that is able to contain solvent like a sponge, the solvent desorbs by passing through the BCP during heating. The solvothermal annealing happens then in one single step, which is clearly an advantage when regarding upscaling processes. On silicon substrates, the PS-brush, with its 3 nm thickness cannot contain enough solvent which is why the sample has to be annealed shortly in solvent vapor prior to thermal annealing. Finally LER/LWR measurement were performed. It was shown that the values obtained for SD16 are far too high for any integration in the IC production. However, it is supposed that these values are partly due to the high LER values of the guiding trenches. The defects present after guiding trench etching, are then transmitted onto the BCP. The "healing" ability of BCPs, shown in different reports, does not account here for our graphoepitaxy self-assembly. Future work includes the smoothing of template trenches by post-lithography treatments in order to reduce the LER of the final silicon lines. Furthermore a statistical analysis of the aligned BCP by CD-SEM and a comparison of revealed and transferred patterns in order to determine the impact of transfer etching could be interesting.

References

(1) Sinturel, C.; Bates, F. S.; Hillmyer, M. a. High χ–Low N Block Polymers: How Far Can We Go? *ACS Macro Lett.* **2015**, 1044–1050.

(2) Borah, D.; Shaw, M. T.; Rasappa, S.; Farrell, R. A.; O'Mahony, C.; Faulkner, C. M.; Bosea, M.; Gleeson, P.; Holmes, J. D.; Morris, M. A. Plasma Etch Technologies for the Development of Ultra-Small Feature Size Transistor Devices. *J. Phys. D. Appl. Phys.* **2011**, *44*, 174012 (12pp).

(3) Garnier, J., Böhme, S., Girardot, C., Salaün, M., Arias-Zapata, J., Zelsmann, M. Polystyrene Brush Optimization for Directed Self-Assembly of High-Chi PS-B-PDMS Diblock Copolymers. In *Presentation at E-MRS Spring meeting*; **2015**.

(4) Jung, Y. S.; Chang, J. B.; Verploegen, E.; Berggren, K. K.; Ross, C. A. A Path to Ultranarrow Patterns Using Self-Assembled Lithography. *Nano Lett.* **2010**, *10*, 1000–1005.

(5) Tavakkoli K G, A.; Nicaise, S. M.; Gadelrab, K. R.; Alexander-Katz, A.; Ross, C. A; Berggren, K. K. Multilayer Block Copolymer Meshes by Orthogonal Self-Assembly. *Nat. Commun.* **2016**, *7*, 10518.

(6) Son, J.; Chang, J.; Berggren, K.; Ross, C. Assembly of Sub-10-Nm Block Copolymer Patterns with Mixed Morphology and Period Using Electron Irradiation and Solvent Annealing. *Nano Lett.* **2011**, 5079–5084.

(7) Jeong, J. W.; Park, W. I.; Do, L.-M.; Park, J.-H.; Kim, T.-H.; Chae, G.; Jung, Y. S. Nanotransfer Printing with Sub-10nm Resolution Realized Using Directed Self-Assembly. *Adv. Mater.* **2012**, *24*, 3526–3531.

(8) Xiao, S.; Yang, X.; Park, S.; Weller, D.; Russell, T. P. A Novel Approach to Addressable 4 Teradot/in. 2 Patterned Media. *Adv. Mater.* **2009**, *21*, 2516–2519.

(9) Kihara, N.; Yamamoto, R.; Sasao, N.; Shimada, T.; Yuzawa, A.; Okino, T.; Ootera, Y.; Kamata, Y.; Kikitsu, A. Fabrication of 5 Tdot/in.2 Bit Patterned Media with Servo Pattern Using Directed Self-Assembly. *J. Vac. Sci. Technol. B* **2012**, *30*, 2166–2746.

(10) Borah, D.; Shaw, M. T.; Holmes, J. D.; Morris, M. A. Sub-10 Nm Feature Size PS-B-PDMS Block Copolymer Structures Fabricated by a Microwave-Assisted Solvothermal Process. *ACS Appl. Mater. Interfaces* **2013**, *5*, 2004–2012.

(11) Mokarian-Tabari, P.; Cummins, C.; Rasappa, S.; Simao, C.; Sotomayor Torres, C. M.; Holmes, J. D.; Morris, M. a. Study of the Kinetics and Mechanism of Rapid Self-Assembly in Block Copolymer Thin Films during Solvo-Microwave Annealing. *Langmuir* **2014**, *30*, 10728–10739.

(12) Borah, D.; Senthamaraikannan, R.; Rasappa, S.; Kosmala, B. Swift Nanopattern Formation of PS - B - PMMA and PS - B - PDMS Block Copolymer Films Using a Microwave Assisted Technique. *ACS Nano* **2013**, *7*, 6583–6596.

(13) Zhang, X.; Harris, K. D.; Wu, N. L. Y.; Murphy, J. N.; Buriak, J. M. Fast Assembly of Ordered Block Copolymer Nanostructures through Microwave Annealing. *ACS Nano* **2010**, *4*, 7021–7029.

(14) Park, W. I.; Kim, K.; Jang, H.-I.; Jeong, J. W.; Kim, J. M.; Choi, J.; Park, J. H.; Jung, Y. S. Directed Self-Assembly with Sub-100 Degrees Celsius Processing Temperature, Sub-10 Nanometer Resolution, and Sub-1 Minute Assembly Time. *Small* **2012**, *8*, 3762–3768.

(15) Gotrik, K. W.; Ross, C. A. Solvothermal Annealing of Block Copolymer Thin Films. *Nano Lett.* **2013**, *13*, 5117–5122.

(16) Cummins, C.; Mokarian-Tabari, P.; Andreazza, P.; Sinturel, C.; Morris, M. a. Solvothermal Vapor Annealing of Lamellar Poly(styrene)-Block-Poly(d,l-Lactide) Block Copolymer Thin Films for Directed Self-Assembly Application. *ACS Appl. Mater. Interfaces* **2016**, *8*, 8295–8304.

(17) Kim, J. M.; Kim, Y.; Park, W. I.; Hur, Y. H.; Jeong, J. W.; Sim, D. M.; Baek, K. M.; Lee, J. H.; Kim, M.-J.; Jung, Y. S. Eliminating the Trade-Off between the Throughput and Pattern Quality of Sub-15 Nm Directed Self-Assembly via Warm Solvent Annealing. *Adv. Funct. Mater.* **2015**, *25*, 306–315.

(18) Jeong, J. W.; Hur, Y. H.; Kim, H.-J.; Kim, J. M.; Park, W. I.; Kim, M. J.; Kim, B. J.; Jung, Y. S. Proximity Injection of Plasticizing Molecules to Self-Assembling Polymers for Large-Area, Ultrafast Nanopatterning in the Sub-10nm Regime. *ACS Nano* **2013**, *7*, 6747–6757.

(19) Lyakhova, K. S.; Sevink, G. J. A.; Zvelindovsky, A. V.; Horvat, A.; Magerle, R. Role of Dissimilar Interfaces in Thin Films of Cylinder-Forming Block Copolymers. *J. Chem. Phys.* **2004**, *120*, 1127–1137.

(20) O'Driscoll, B. M. D.; Kelly, R. A.; Shaw, M.; Mokarian-Tabari, P.; Liontos, G.; Ntetsikas, K.; Avgeropoulos, A.; Petkov, N.; Morris, M. A. Achieving Structural Control with Thin Polystyrene-B-Polydimethylsiloxane Block Copolymer Films: The Complex Relationship of Interface Chemistry, Annealing Methodology and Process Conditions. *Eur. Polym. J.* **2013**, *49*, 3445–3454.

(21) Dinachali, S. S.; Bai, W.; Tu, K.-H.; Choi, H. K.; Zhang, J.; Kreider, M. E.; Cheng, L.-C.; Ross, C. A. Thermo-Solvent Annealing of Polystyrene-Polydimethylsiloxane Block Copolymer Thin Films. *ACS Macro Lett.* **2015**, *4*, 500–504.

(22) Wadley, M.; Hsieh, I.; Cavicchi, K.; Cheng, S. Solvent Dependence of the Morphology of Spin-Coated Thin Films of Polydimethylsiloxane-Rich Polystyrene-Block-Polydimethylsiloxane Copolymers. *Macromolecules* **2012**, *45*, 5538–5545.

(23) Lee, D.-E.; Je, N. J.; Yoo, S. Il; Lee, D. H. Directed Self-Assembly of Block Copolymer Micelles onto Topographically Patterned Surface. *Langmuir* **2015**, *31*, 12929–12936.

(24) Harrison, C.; Chaikin, P. M.; Huse, D. A.; Register, R. A.; Adamson, D. H.; Daniel, A.; Huang, E.; Mansky, P.; Russell, T. P.; Hawker, C. J.; *et al.* Reducing Substrate Pinning of Block Copolymer Microdomains with a Buffer Layer of Polymer Brushes. *Macromolecules* **2000**, *33*, 857–865.

(25) Xie, R.; Karim, a.; Douglas, J.; Han, C.; Weiss, R. Spinodal Dewetting of Thin Polymer Films. *Phys. Rev. Lett.* **1998**, *81*, 1251–1254.

(26) Vrij, A. Rupture of Thin Liquid Films Due to Spontaneous Fluctuations in Thickness. **1968**, *1*, 3074–3078.

(27) You, J.; Zhang, S.; Huang, G.; Shi, T.; Li, Y. Solvent Annealing Induced Phase Separation and Dewetting in PMMA/SAN Blend Film: Film Thickness and Solvent Dependence. *J. Chem. Phys.* **2013**, *138*, 244907.

(28) Gu, X.; Gunkel, I.; Hexemer, A.; Russell, T. P. Solvent Vapor Annealing of Block Copolymer Thin Films: Removal of Processing History. *Colloid Polym. Sci.* **2014**, *292*, 1795–1802.

(29) Gunkel, I.; Gu, X.; Sun, Z.; Schaible, E.; Hexemer, A.; Russell, T. P. An in Situ GISAXS Study of Selective Solvent Vapor Annealing in Thin Block Copolymer Films: Symmetry Breaking of in-Plane Sphere Order upon Deswelling. *J. Polym. Sci. Part B Polym. Phys.* **2016**, *54*, 331–338.

(30) Liu, Z.; Gu, X.; Hwu, J.; Sassolini, S.; Olynick, D. L. Low-Temperature Plasma Etching of High Aspect-Ratio Densely Packed 15 to Sub-10nm Silicon Features Derived from PS-PDMS Block Copolymer Patterns. *Nanotechnology* **2014**, *25*, 285301.

(31) Zhang, X.; Harris, K. D.; Wu, N. L. Y.; Murphy, J. N.; Buriak, J. M. Fast Assembly of Ordered Block Copolymer Nanostructures through Microwave Annealing. *ACS Nano* **2010**, *4*, 7021–7029.

(32) Kim, E.; Ahn, H.; Park, S.; Lee, H.; Lee, M.; Lee, S.; Kim, T.; Kwak, E.-A.; Lee, J. H.; Lei, X.; *et al.* Directed Assembly of High Molecular Weight Block Copolymers: Highly Ordered Line Patterns of Perpendicularly Oriented Lamellae with Large Periods. *ACS Nano* **2013**, *7*, 1952–1960.

(33) Jung, Y. S.; Ross, C. A. Well-Ordered Thin-Film Nanopore Arrays Formed Using a Block-Copolymer Template. *Small* **2009**, *5*, 1654–1659.

(34) Jung, Y. S.; Ross, C. A. Orientation-Controlled Self-Assembled Nanolithography Using a Polystyrene-Polydimethylsiloxane Block Copolymer. *Nano Lett.* **2007**, *7*, 2046–2050.

(35) Lin, G.; Rahman, M.; Caho, J.; Sahn, J. Development of Spin-on High Carbon Hard Masks for High Resolution Photolithography. *J. Photopolym. Sci. Technol.* **2011**, *24*, 503–510.

(36) Park, S.; Wang, J.; Kim, B.; Xu, J.; Russell, T. P. A Simple Route to Highly Oriented and Ordered Nanoporous Block Copolymer Templates. *ACS Nano* **2008**, *2*, 766–772.

(37) Sinturel, C.; Vayer, M.; Morris, M.; Hillmyer, M. a. Solvent Vapor Annealing of Block Polymer Thin Films. *Macromolecules* **2013**, *46*, 5399–5415.

(38) Stoykovich, M. P.; Daoulas, K. C.; Marcus, M.; Kang, H.; Pablo, J. J. De; Nealey, P. F. Remediation of Line Edge Roughness in Chemical Nanopatterns by the Directed Assembly of Overlying Block Copolymer Films. *Marcomolecules* **2010**, 2334–2342.

(39) Patrone, P.; Gallatin, G. Response of Block Copolymer Thin-Film Morphology to Line-Width Roughness on a Chemoepitaxial Template. *Macromolecules* **2014**, *47*, 4824–4829.

(40) Cheng, J. Y.; Rettner, C. T.; Sanders, D. P.; Kim, H.-C.; Hinsberg, W. D. Dense Self-Assembly on Sparse Chemical Patterns: Rectifying and Multiplying Lithographic Patterns Using Block Copolymers. *Adv. Mater.* **2008**, *20*, 3155–3158.

(41) Daoulas, K. C.; Müller, M.; Stoykovich, M. P.; Kang, H.; de Pablo, J. J.; Nealey, P. F. Directed Copolymer Assembly on Chemical Substrate Patterns : A Phenomenological and Single-Chain-in-Mean-Field

Simulations Study of the Influence of Roughness in the Substrate Pattern. *Langmuir* **2008**, *24*, 1284–1295.

(42) Cheng, J. Y.; Ross, C. A.; Thomas, E. L.; Smith, H. I.; Vancso, G. J. Templated Self-Assembly of Block Copolymers: Effect of Substrate Topography. *Adv. Mater.* **2003**, *15*, 1599–1602.

Chapter 5 DSA Pattern Transfer by Plasma Etching

5.1 Introduction

After obtaining DSA defined mask patterns, generally a pattern transfer into the semiconductor substrate is required for further applications in the microelectronics industry. In the beginning of the microelectronic revolution, the miniaturized structures of the integrated circuits (ICs) were produced by selective chemical "wet" etching. Chemical wet etching is isotropic, etching not only vertically but also horizontally into the substrate. As feature sizes were several hundreds of nanometers, slight undercutting was not considered a problem. With decreasing feature sizes, the lack of profile control coming from the isotropic wet etching became problematic and was replaced by dry plasma etching. Plasma etching is the most used method today for anisotropic etching, which means etching in vertical direction with no or little lateral etching. A comparison of isotropic and anisotropic etching is shown in Figure 5-1.

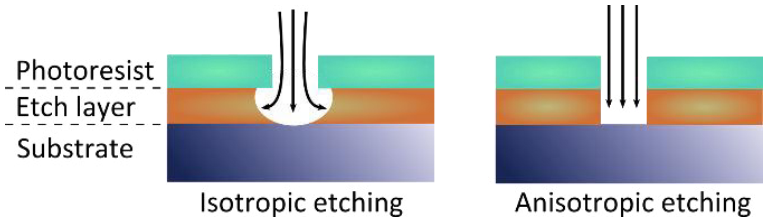

Figure 5-1: Comparison of isotropic and anisotropic etching

A plasma is a gaseous medium consisting of neutral species, charged particles (ions, electrons) and photons and presents the most common state of matter in the universe (~ 99 %). In order to generate etching plasmas, an externally imposed potential accelerates the few electrons that are present in an inert molecular gas. These accelerated electrons induce inelastic collisions with neutral gas species and produce electron-ion pairs (ionization) and reactive neutral species, known as radicals (dissociation). These reactions produce species in excited states which go back to their ground state by emitting photons (the so-called electrical glow discharge). The simplest form of an etch reactor operates in vacuum and the semiconductor wafer that is to be etched is positioned on one of two opposed parallel plate electrodes (Figure 5-2).

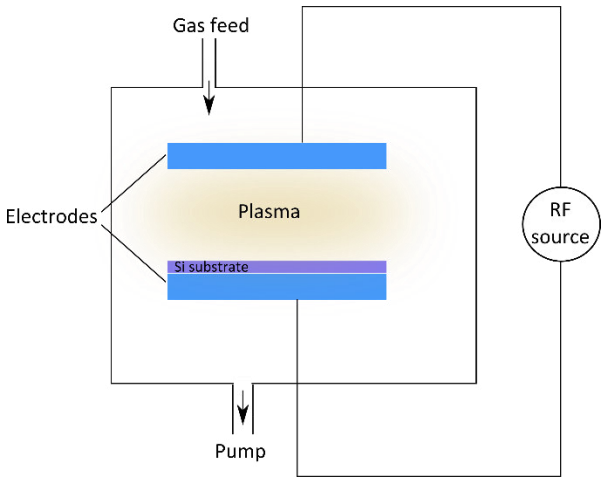

Figure 5-2: Schematic of a simple etching reactor containing two electrodes that are coupled to a radio frequency source.

The electric field is maintained with a continuously applied radio frequency (RF) or microwave power in order to compensate for electron-ion pair losses on the reactor walls. Furthermore, a feed gas is introduced to create the chemically active radicals and or ions that are used to remove material[1]. In inductively coupled plasma (ICP) etching, which is used in our applications, the RF power source is coupled with a high (ion) density source, a planar coil, through a dielectric window as schematized later in this chapter.

Plasma etching basically involves two types of etching: chemical etching which is caused by the radicals and sputter etching which results from ion bombardment. In chemical etching, radicals chemically react with the surface and produce volatile species. Chemical etching is isotropic. In sputter etching, atoms are ejected from the surface by high energy ions arriving on the surface. Sputtering has very low selectivity but is highly anisotropic. Consequently, etch rates are generally low and similar for different materials[2]. For both cases, the etch product has to be volatile so it can be removed. Ion assisted chemical etching combines these effects while finding a good trade-off between selectivity and anisotropy.

In BCP lithography, plasma etching is used after the directed self-assembly, in order to transfer the patterns into the semiconductor material. In order to obtain high fidelity processes, some criteria have to be respected. The transfer etch has to be highly anisotropic and selective, and the pattern transfer should have good dimensional control with a high etch rate. The selectivity is the ratio between the etch rate of the etched material and the masking material. Ideally the selectivity should be high enough to etch the substrate without completely removing the mask material. Further, for industrial applications, the etch process needs to have high etch rates in order to increase the throughput. However, the etch rate should not be too fast in order to be still able to control the process during thin film etching. Finally, it is important to control the CD uniformity and to precisely reproduce the mask into the underlying substrate, without modifying the shape or size of the initial features.

The etching of BCP is problematic, especially for sub 20 nm feature sizes. The global pattern transfer of BCPs consists of basically two steps: the first one consists of selectively removing one block while the other remains as a hard mask for the actual pattern transfer (second step). Purely organic BCPs have often low etching contrast, which is why several studies demonstrate the complexation of one block with heavier elements in order to increase the contrast[3]. A detailed description of such processes is given in chapter 6. When using blocks that contain inorganic elements, the etch contrast is intrinsically increased, as in PS-b-PFS (polystyrene- block –polyferrocenylsilane)[4] and PS-b-PDMS, and the etching is more straightforward. In PS-b-PDMS, the PDMS wetting layer that is formed at the BCP/air interface due to the lower surface tension of PDMS has to be removed before etching the PS block. Silica-like structures are often etched in fluorine rich chemistry; CF_4 plasma is then often used for PDMS etching[3,5–9]. Organic polymers can then easily be removed with O_2 plasma and, for silicon etching, halogen atom etchants (F, Cl, and Br) are often used[10]. As already detailed previously, due to the large surface tension differences between the blocks in PS-b-PDMS, it is important to carefully choose the substrate surface energy in order to prevent the formation of PDMS at the substrate/BCP interface. Several groups describe the increased mobility of PS-b-PDMS on PDMS-brush coated substrates but pay little attention to the subsequent transfer step[7,11–13]. A PDMS brush layer is problematic for the pattern transfer because of its higher resistance towards plasma etching. Borah et al. demonstrated the pattern transfer of PDMS cylinders by using SF_6/CHF_3 plasma. Due to the fact that a PDMS brush was used for alignment an intermediate etching step consisting of CHF_3/Ar plasma had to be used. This is a critical step, as it might attack the PDMS cylinders used as a hard mask. Consequently ≈ 14 nm silicon features with an aspect ratio of 1.3 were obtained. In a follow up study the group achieved to increase the aspect ratio of obtained Si nanowires to approximately 2.8, by functionalizing the substrate surface with silicon containing hexa-methyldisilazane (HDMS)[14]. Whether an additional PDMS wetting layer is formed at the BCP/HDMS interface remains unclear. Jung et al. demonstrated the pattern transfer of 16 nm wide ring-forming PDMS cylinders by sputtering a Co layer on top of the revealed structures[15]. The Co layer was then etched away using CF_4 plasma, which is a very slow process (> 20 min). When revealing the buried PDMS structures, the etch speed increased drastically leading to a reversed image of the original PDMS cylinders. The Ross group demonstrated several similar methods in which metals were used to create a reversed image of the PS-b-PDMS pattern[16,17]. Impressive work has been shown by Liu and coworkers, who demonstrated the challenging transfer etch of sub 10 nm PS-b-PDMS (M_w=15kg/mol) patterns by using a chromium interlayer[18]. Aspect ratios of 10:1 have been obtained. However, to our knowledge, no high aspect ratio greater than 3 have been reported for PS-b-PDMS without the use of a metal mask reinforcement other than by these authors[19]. In this chapter, we present the direct pattern transfer of oxidized PDMS nanostructures into Si substrates without the use of

any metal mask reinforcement. This is a great advantage regarding time and cost consummation but also regarding contamination issues that may arise from the use of metals in front-end of line microelectronics processes.

This chapter describes the etching processes involved in the pattern transfer of PDMS masks obtained by DSA of SD45 and SD16 into silicon substrates. As first described in chapter 2, PS-b-PDMS is aligned by graphoepitaxy on resist/SiArc/SOC trilayers. This configuration of a 193 nm photolithography resist on top of a silicon-containing hard mask with an underlying carbon containing layer is the most common in high resolution photolithography industrial applications. Indeed, a resist layer is used for pattern imaging with 193 nm photolithography. The SiArc and SOC layer are used in order to reduce substrate's reflectivity for improved resist imaging. The layers are prepared by spin coating and are both polymer based materials, with a high silicon content in the case of SiArc and high carbon content for the SOC layer. They should both be soluble in safe solvents (cf. chapter 2), and most importantly should have a good etching resistance during pattern transfer without wiggling or line distortion[20–22].

The first section of the chapter concentrates on the revealing of the PDMS nanostructures, which is generally the same process for both PS-b-PDMS resolutions (16k and 45k). Then, two different Si transfer techniques are presented for SD45, before coming to the challenging Si transfer etch of SD16. Finally SD16 pattern transfer is demonstrated on Silicon-on-Insulator (SOI) substrates which opens up the possibility to use DSA for fin field effect transistor (finFET) devices. The experimental details of the used reactors and etching conditions are described in the next section.

5.2 Experimental Details

Most of the experiments are carried out in a plasma reactor suited for 300 mm wafers. Nevertheless, during this thesis, the 300 mm wafer etch reactor was unavailable for almost 10 month due to a long duration maintenance operation. During this time etch experiments (particularly those on SOI) were taken out in a 200 mm wafer etch reactor with less tuning possibilities. The reactors are both commercially available AdvantEdge decoupled plasma sources (DPS) from Applied Materials, Inc. and are schematically depicted in Figure 5-3.

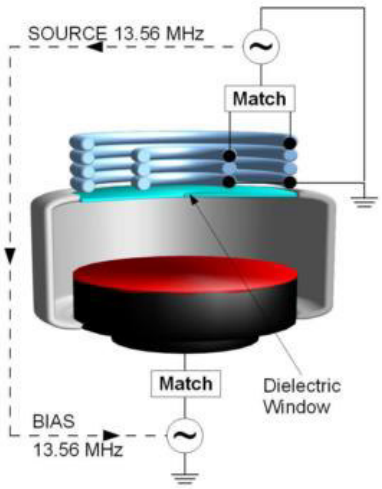

Figure 5-3: schematic of the plasma reactor used for PS-b-PDMS etching

The interior walls of the 300mm and 200mm wafer reactors are composed of Al_2O_3 and the chamber temperature is kept constant at 65°C and at low vacuum, in the order of some mTorr. The 300mm wafer reactor has a diameter of 50cm with 17.2cm height, while the 200mm reactor has a diameter of 35cm with a height of 20cm. For both reactors, two RF power generators are used to ensure the inductively coupled plasma. The "source" generator (source power from 0W to 3000W at 13.56MHz in the 300mm reactor and at 12.56MHz in the 200mm reactor) supplies the power for two ICP antenna coils that are situated on top of the reactor. The RF energy flowing in the antenna is transmitted to the plasma through a dielectric alumina window and induces a magnetic field in the plasma. This induces an oscillating electric field that accelerates electrons parallel to the reactor walls, making it possible to maintain the plasma at very low pressures (as low as 1mTorr) with high ion density (typically 10^{11} to 10^{12} ions/cm^3). The thermally regulated wafer holder, also called "chuck", is capacitively coupled to the second RF power supply (called "bias", power from 0W to 190W at 13.56MHz for both reactors). The bias power accelerates ions perpendicularly to the wafer. That way, a few hundreds of Volts can be obtained. When the bias generator is not used, a self-bias voltage of a few volts corresponding to the ion energy is established between the plasma and the wafer.

In order to increase the possibilities of the reactor and to better equilibrate the plasma chemistry and ion bombardement, the 300 mm wafer reactor allows pulsing the plasma. Pulsing the plasma means turning one of the generators on and off, at a pulsing frequency f (in the kHz region) and with a duty cycle $dc=t_{ON}/(t_{ON}+t_{OFF})$. A duty cycle, dc, of 1 indicates continuous wave (CW) plasma and dc<1 is characteristic for pulsed plasma. Plasma pulsing is interesting for high aspect ratio etching as it allows a precise control of the plasma chemistry and it tends to reduce or even eliminate charging of the features[23,24]. It also helps to overcome any charging by providing extremely energetic ions to the wafer compared to typical CW processes[25]. In the pulsed plasma system that we used, the RF power delivered to the ICP coil is modulated

ON and OFF periodically at 1 kHz (pulsing period of 1 ms) with a duty cycle of 20 %. All the other parameters (gas flow, temperature, pressure, bias power etc.) are kept constant.

The details of the etching processes that were used in this thesis are depicted in Table 5-1 and a detailed description of the recipes and samples is given in the concerning sections.

Table 5-1: Details of the etching process for pattern transfer of SD45 and SD16 on SiArc/SOC substrates in 300 mm and 200mm wafer reactors

Etching step	Sample type	Pressure [mTorr]	Gas flow [sccm]	Time [s]	Bias power [W]	Source power [W]
300mm wafer reactor						
1. PDMS surface layer (CW mode)	SD45+SD16 on SiArc/SOC	4	CF_4 100	5	20	700
2. PS, SOC etching & PDMS oxidation (CW)	SD45+SD16 on SiArc/SOC	5	HBr / O_2 70 / 30	5 - 25	120	500
3a. Si etching (Pulsed plasma, Duty cycle 20%)	SD45+SD16 on SiArc/SOC	20	HBr / O_2 200 / 5	10 - 250	100	750 (pulsed)
3b. Si etching (CW)	SD45+SD16 on SiArc/SOC	20	CHF_3 / SF_6 / Ar 50 / 20 / 60	8 - 20	75	450
4. SOC stripping (CW)	SD45+SD16 on SiArc/SOC	10	O_2 100	15	10	800
200mm wafer reactor						
1. Revelation PDMS surface layer	SD16 on SOI	10	CF_4 90	5	0	500
2. PS etching & PDMS oxidation	SD16 on SOI	5	O_2 90	5	0	400
3. Breakthrough	SD16 on SOI	10	Cl_2 100	10 - 250	100	800

4. Si etching	SD16 on SOI	5	HBr / He-O2 120 / 5	6 - 10	120	250

In our experiments, the small samples of approximately $1cm^2$ were patched on 300mm (or 200 mm) Si wafers in order to introduce them into the etching chambers. The carrier wafer type should be similar to the surface composition of the sample. The condition of the reactor walls can have a strong influence on the plasma process and consequently on the etch result, which is why cleaning, seasoning and conditioning steps were carried out before each etch experiment. At first, in the cleaning step, SF_6/O_2 plasma without bias is generated to etch silicon oxide layers or similar materials that remain from previous processes from the reactor walls. Subsequently, a two-step seasoning process deposits a SiO_2 layer on the clean reactor walls. The first step consists of a $SiCl_4/O_2$ plasma process which deposits chlorine rich SiOCl on the walls. A further oxidation in a pure O_2 plasma produces SiO_2(Cl) layers with a very low percentage of chlorine. Finally, in the conditioning step, the exact plasma process that is to be used on the sample is run in the chamber without the presence of the sample. During all of these steps, a dummy Si or SiO_2 wafer is placed on the wafer holder for protection.

To characterize the etch steps developed in this work, SEM and FIB-STEM observations were performed on Hitachi S-5000 or JEOL 7500F and Helios 450S – FEI respectively. Conditions for sample observation are similar to those described in chapter 2.

5.3 Revelation: Etching PDMS, PS and SOC

As explained in chapter 2, the stacks that were used for our experiments are composed of a thin PDMS layer formed at the air/BCP interface, horizontal PDMS cylinders in a PS matrix, a SOC layer and the silicon substrate. As a reminder, cross section STEM images of SD45 and SD16 in SiArc/SOC trenches are represented in Figure 5-4. Note that the PDMS surface layer is not distinguishable due to the deposited platinum layer for STEM observation that partly diffuses into the polymer. In order to get an impression of the layer composition, coloured highlights are introduced into the images.

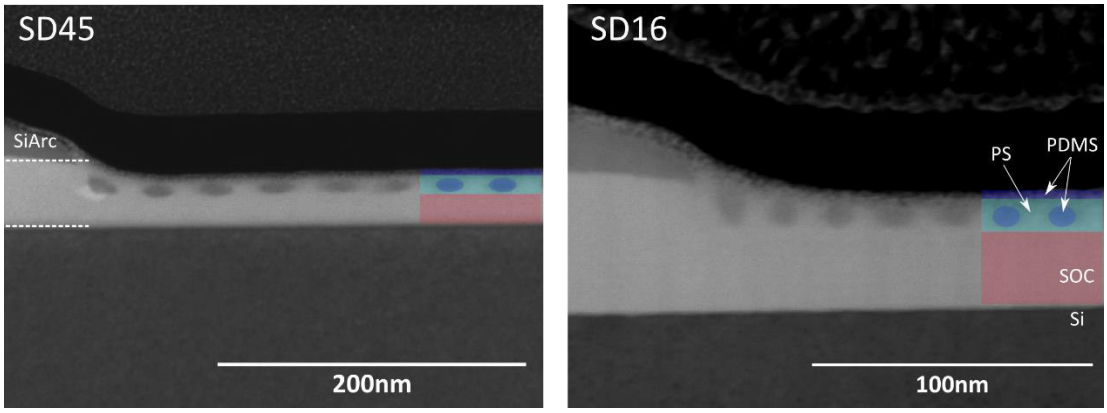

Figure 5-4: STEM cross section image of SD45 and SD16 in SiArc/SOC trenches

The revealing of the features consists thus of the removal of the PDMS surface layer, the PS matrix etching and simultaneous the SOC layer etching. These etching steps are all realized in CW mode (step 1 and 2 in Table 5-1). First, the PDMS wetting layer at the air/BCP interface is removed by CF_4 plasma (Step 1). This step has to be carefully controlled in order to prevent the etching of the PDMS cylinders, which could result from a too aggressive or too long CF_4 step. Figure 5-5 shows cross section SEM images of SD45 lines after step 1 of the etching process. It is noteworthy to say that for the sake of the SEM image, a very brief oxidation step was performed in order to enhance the contrast between SOC and PDMS.

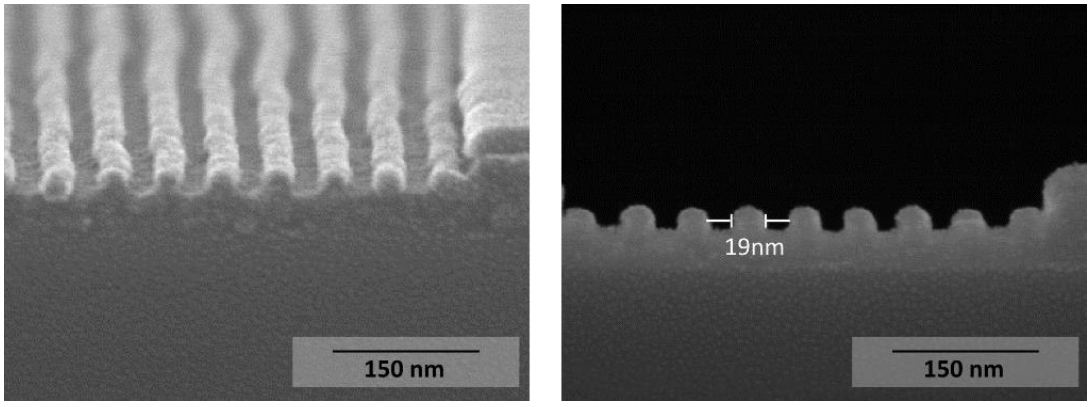

Figure 5-5: Cross section SEM images of SD45 lines after CF_4 and brief O_2 revealing etch step

This first CF_4 step was optimized prior to this thesis and adapted from previous work in the BCP group at LTM. Once revealed, the PDMS cylinders can be transferred into the SOC layer. The work on SD45 was partly performed in deeper trenches, with a remaining SOC layer of approximately 50 nm, and is compared here with those performed in thinner trenches with a remaining SOC layer of about 20 nm (cf. chapter 2). Figure 5-6 depicts the initial trench configuration with different SOC layer thicknesses.

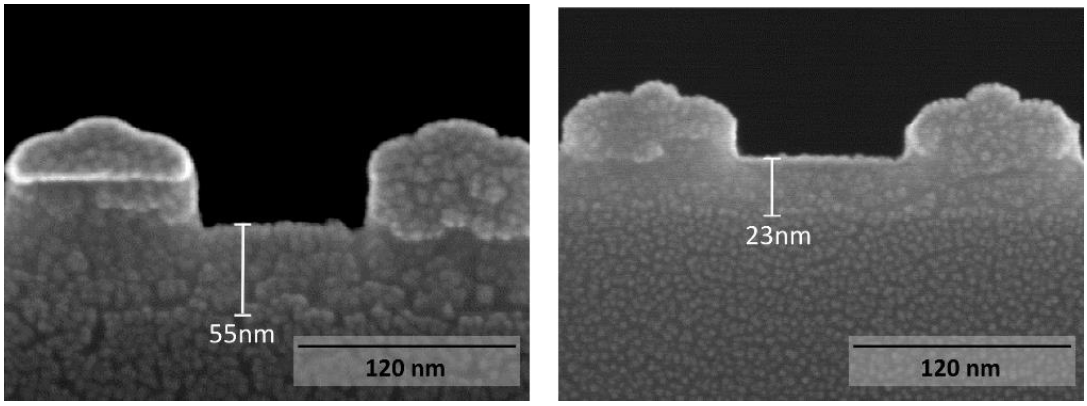

Figure 5-6: Cross-section SEM images of different SOC layer thicknesses

PS and SOC being essentially composed of carbon, they are removed with high selectivity during the HBr/O_2 process step compared to PDMS, while oxygen is responsible for etching and HBr for the passivation layer. This way, the etch is much more anisotropic compared to a pure oxygen etching process. Indeed, oxygen radicals react with the carbon of the PS/SOC layer to form CO_x volatile etch products. By introducing bromine, weakly volatile etch products such as $C_xH_yBr_z$ are formed which can redeposit on the feature sidewalls and form a thin protection layer. This passivation layer protects the sidewalls from lateral etching, allowing an excellent anisotropic etch of the lines. At the same time, the PDMS cylinders are oxidized and transformed into silicon oxy-carbide which was shown to have excellent robustness in oxygen plasma[26,27]. Ratios of O_2 and HBr have to be carefully chosen so that the passivation layer has the right thickness for anisotropic etching. Otherwise, if the passivation layer is too thin the etching becomes isotropic or if the layer is too thick the process could stop altogether or produce sloped features. 70sccm HBr to 30sccm O_2 seemed in our case to be the optimum ratio. Then, several etching times have been tested in order to obtain optimum results. When etched too long, it comes first to the overetching of the SOC layer, i.e the SOC layer starts to be etched underneath the PDMS and SiArc guiding lines. The PDMS mask “falls” then in an uncontrolled manner onto the Si substrate and the long-range order can be lost. Also, the SOC can no longer participate in the reinforcement of the mask during Si transfer etching. Finally, when the etching continues, the SOC will be completely consumed and the PDMS cylinders start being attacked, which makes them finally useless as a hard mask. On the other hand, too short process times are also disadvantageous as they do not open the SOC layer completely to the Si substrate. The remaining SOC layer

protects then the Si substrate during transfer etching. Figure 5-7 shows examples of too long and too short etching times that are not desired.

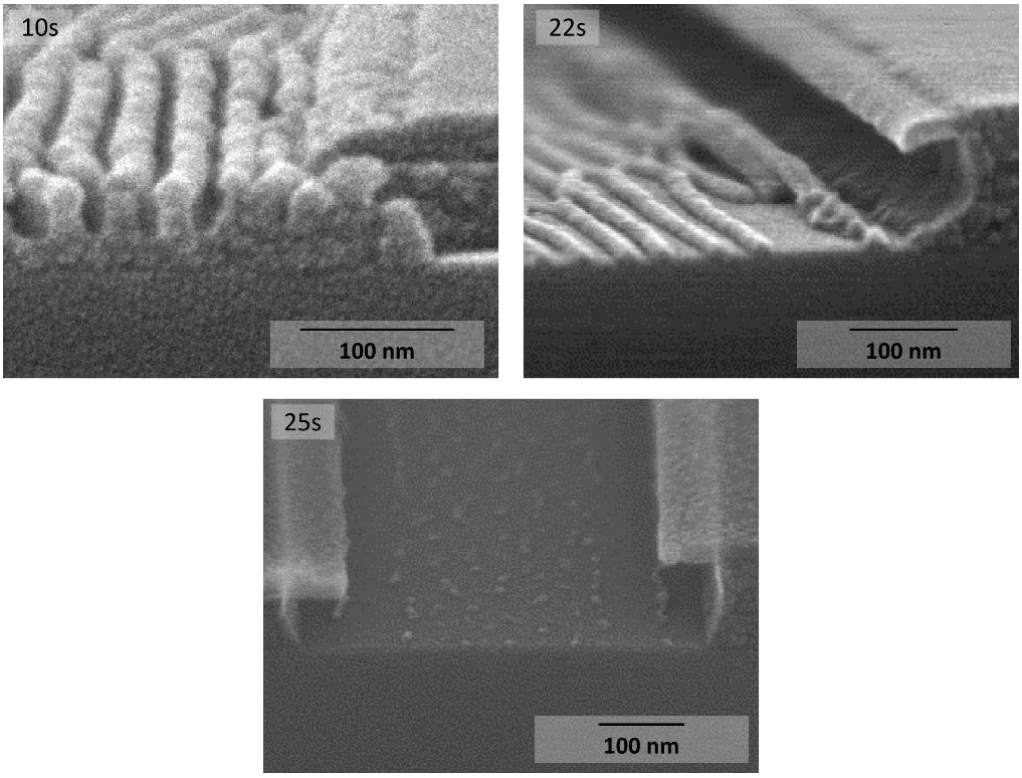

Figure 5-7: cross section SEM images of too short and too long SOC etching steps: after 10s the SOC layer is not completely open, one cannot continue with the following transfer etch; 22s the SOC is completely removed, the PDMS structure is still intact but long-range order is lost, 25s only residues of the PDMS mask is left, no pattern transfer is then possible

Optimized etching step durations have thus been identified to be 18s on thick SOC layers and 13s on thin layers. Examples of SEM cross-section micrographs of SD45 and SD16 on different SOC layer heights after this etching step are reported in Figure 5-8. As can be seen for SD45, high aspect-ratio lines with vertical sidewalls could be obtained, but the nanolines width is much smaller in the case of the higher SOC thickness. The longer etching time, that is necessary to etch the whole 55 nm thick SOC layer leads to a trimming (reduction of feature size) of the PDMS mask from initially 19 nm to 15 nm. The shorter etch time, which is sufficient to reveal the thinner SOC layers, retains the initial PDMS critical dimension almost perfectly (18 nm). SD16 on the other hand shows anisotropic etching results where some of the lines are collapsed. This phenomenon is known to appear in high aspect ratio features after wet etching due to capillary forces[28]. Here, no wet etching was used and the solvent is most certainly completely evaporated under vacuum conditions. We suggest that humidity might play a role here when the sample is exposed to air after etching. Another possibility is the intrinsic stress in the SOC layer that is relaxed in the thin etched lines.

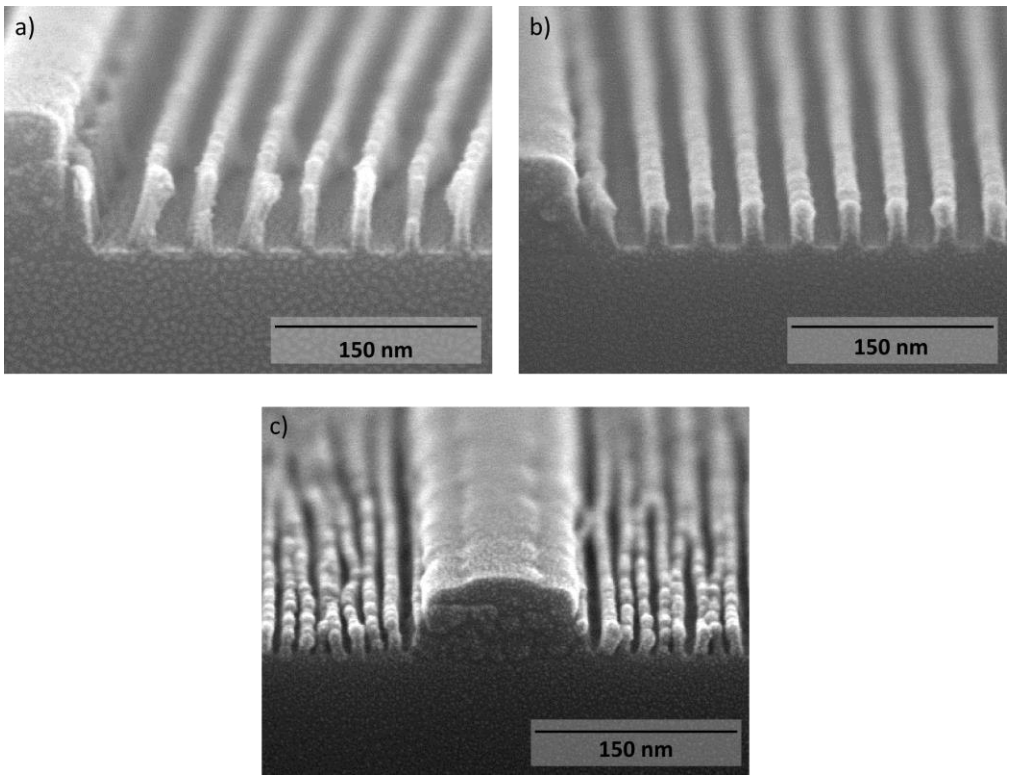

Figure 5-8: cross-section SEM micrographs after etching steps 1 and 2 on (a) SD45 on thick SOC layers, (b) SD45 on thin SOC layers and (c) SD16 on thin SOC layers, showing pattern collapse

5.4 HBr/O_2 Pulsed Plasma Transfer Etching of SD45 on Thick SOC Layers

The high aspect ratio of features makes the etching process into the silicon wafer difficult to control. In particularly, the collection angle of the plasma neutrals (as seen from the trench bottom or sidewalls) is restricted by shadowing of the adjacent features in high aspect ratio structures. The passivation layer is a very important factor that influences the slope of the final etch results. This layer is formed on the sidewalls either by deposition of low volatility etch by-products or by sputtering from the bottom of the feature. This layer is primordial for anisotropy as it protects features from lateral etching. In high aspect ratio feature however, the passivation layer thickness on the sidewalls becomes smaller with increasing aspect ratio. The lateral etching of features may become important leading to a lift-off (complete etching underneath the mask) effect of the mask. Furthermore, insulating materials such as oxidized PDMS (and probably passivated SOC) are known to accumulate electric charges. As a consequence, the top of the feature sidewalls charges negatively and the bottom positively as positive ions are directional while the plasma electrons have an isotropic velocity distribution function. As a result, ions are slowed down and deviated towards the sidewalls. Consequently, at the bottom of a high aspect ratio feature, the ion flux and energy is much lower than on plane substrates and etching can stop or become too slow to ensure a reasonable etching depth with the available mask thickness. To overcome those issues, we used pulsed plasma with a

baseline process composed of HBr / O_2 plasma with a low amount of oxygen. The basic phenomena taking place during the two RF power phases can be explained as follows. During the ON phase, the plasma ignites and the electron (and ion) density rises to form H_2O^+, O_2^+, HBr^+, Br_2^+ type reactive species in the plasma[29,30]. The ions are accelerated to high energy (about 250 eV) by the self-bias voltage that develops rapidly on the electrostatic chuck during this ON phase. Such a high energy allows them to reach the bottom of the trenches and assist the etching. Furthermore, the ion energy in pulsed plasma is high enough to sputter poorly volatile $SiBr_x$ species from the trench bottom. These species can redeposit on the feature sidewalls thus participating to their passivation[31]. This contribution is expected to be important. In the ON period, electron dissociation reactions produce reactive radicals (O, Br, H, $SiBr_x$) in the plasma which will stick on the sidewalls to form a protective $SiOBr_x$ passivation layer. However, it is known that in high aspect ratio features, due to shadowing effects, only the top of the features can be protected by the passivation layer but not the bottom (oxygen atoms have a high sticking probability and cannot diffuse deep into the features)[32]. The assistance of the SiBr species sputtered from the features bottom is expected to contribute significantly to form the sidewall passivation layers.

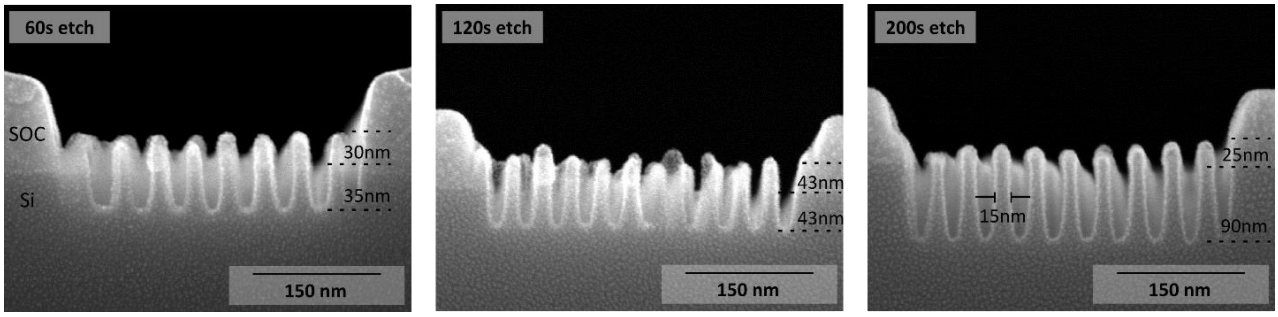

Figure 5-9: Cross-section SEM images of the transfer etching in silicon substrates of PDMS cylinders using pulsed HBr/O2 plasma with different etching times on thick SOC layers

Figure 5-9 shows the etching profiles obtained after different plasma etching times in the case of the thick SOC layer. From 60s to 200s the silicon etch depth was increased from 35 nm to 90 nm (+160%). Due to the shadowing effect in high aspect ratio samples, etching at the bottom of the features becomes slower with increasing aspect ratio. Consequently, we found the silicon etch rate to decrease during the process, at 60s the etch rate is ~0.6 nm/s while it decreases to ~0.4 nm/s after 200s. As the PDMS mask is consumed during such a long etching process, a thick layer of SOC is necessary to maintain the pattern profile. The SOC becomes then principal etching mask with a Si/SOC etching selectivity of about 2.5. In thick SOC layer samples, not all the SOC layer is consumed and a thin layer (25 nm) can be retained even after 200s of etching, protecting the upper part of the lines. The critical dimension (CD) of the lines is measured consistently to be approximately 15 nm, which corresponds to the SOC line dimensions produced in the second etching step.

5.5 SF_6/CHF_3/Ar Continuous Wave Plasma Transfer Etching of SD45 on Thin SOC Layers

As explained in chapter 2, thinner SOC layers are advantageous for the pattern alignment of PDMS cylinders. A better reproducibility is obtained when the trench depth is similar to the domain length of the BCP. In order to decrease this trench depth it was necessary to modify the SiArc/SOC stack to a 23 nm high SOC layer. For this thicknesses, the pulsed plasma process becomes problematic for the transfer etching process. Figure 5-10 shows a comparison of etching results after 60 s and 120 s of pulsed HBr/O_2 plasma etching.

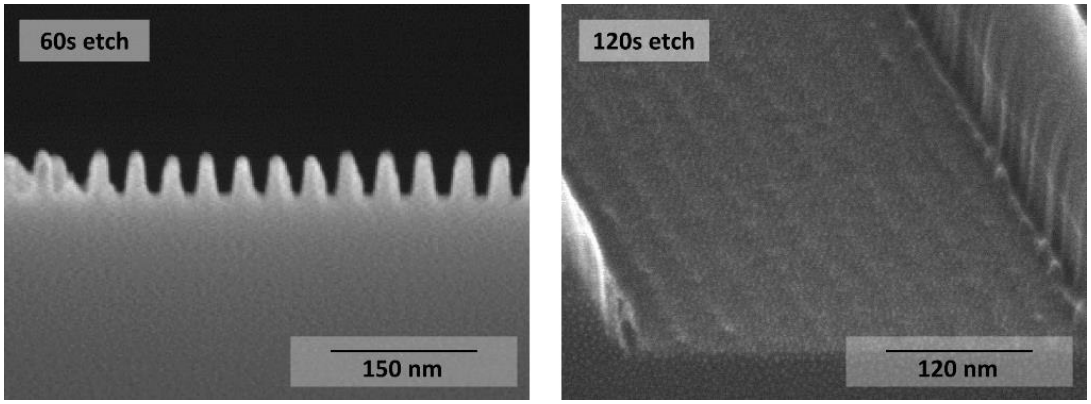

Figure 5-10: Cross section SEM image of PDMS on initially 20 nm high SOC, after 60s and 120s pulsed HBr/O_2 etching

60 s pulsed etching gives silicon lines with approximately 35 nm depth, which is consistent with earlier results, but the SOC mask is already completely consumed. As explained above, HBr/O_2 is used in the first step to etch the SOC layer, thus the selectivity of the pulsed plasma with the same gas composition is not good enough for thin SOC layers and hence is consumed too quickly. With this thin SOC layer, longer etching times (120s) lead to a full destruction of the mask (Figure 5-10).

In order to increase the anisotropy of the silicon lines and to avoid the quick loss of the PDMS etching mask, another etching gas composition has been tested. SF_6/CHF_3/Ar plasma is known as a typical gate etching recipe and was used here to etch in the regime of anisotropic ion enhanced inhibitor etching: F atoms, produced by dissociation of SF_6, etch silicon by forming SiF_x whereas inhibitor precursors like CF_3 or CHF_3 generate fluoro-carbon polymer films, passivating the feature sidewalls[32]. By finding a good trade-off between ion bombardment and etchant to inhibitor flux ratio this can result in a protective layer only on the sidewalls allowing the etch process to proceed at the trench bottom. Figure 5-11 shows SEM cross section micrographs of silicon lines obtained after this CW SF_6/CHF_3/Ar etching.

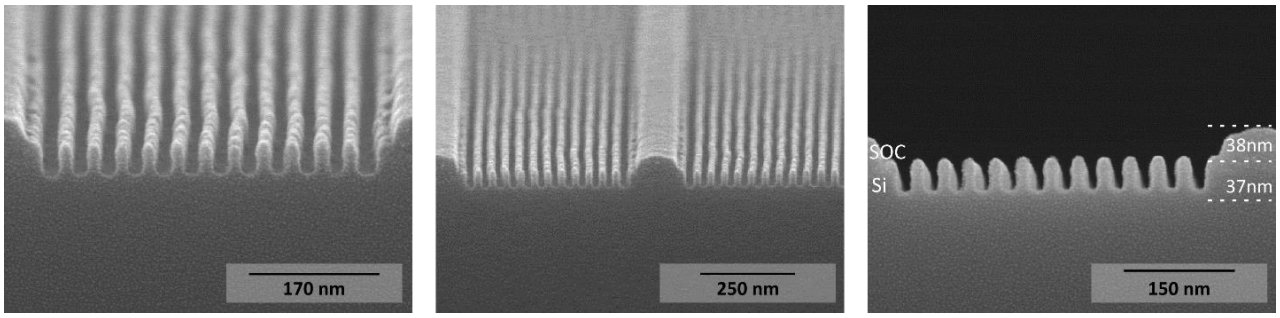

Figure 5-11: SEM cross section images of SD45 after 10s CW mode SF_6/CHF_3/Ar transfer etching

The nanolines show high regularity and anisotropy and are approximately 37 nm high and 18 nm wide, emphasizing the extremely good CD uniformity after etching with SF_6/CHF_3/Ar. Higher aspect ratios for this transfer were not achieved in the scope of this work.

5.6 Comparison of Pulsed and Continuous Wave Plasma on SD45

The silicon nanostructures, that were obtained with different etching techniques show considerably different shapes. One parameter that might influence the final results might be the mechanisms involved in the formation of the passivation layers. The layers in SF_6/ CHF_3/Ar plasmas are not formed from deposition of etch by-products coming from the gas phase as in the pulsed HBr/O_2 etching, but the passivating species are chemically sputtered from the bottom of the etched structures and coat the silicon sidewalls by line of sight deposition. Figure 5-12 compares STEM cross section images of SD45 after HBr/O_2 pulsed plasma and SF_6/CHF_3/Ar in continuous wave (CW) plasma.

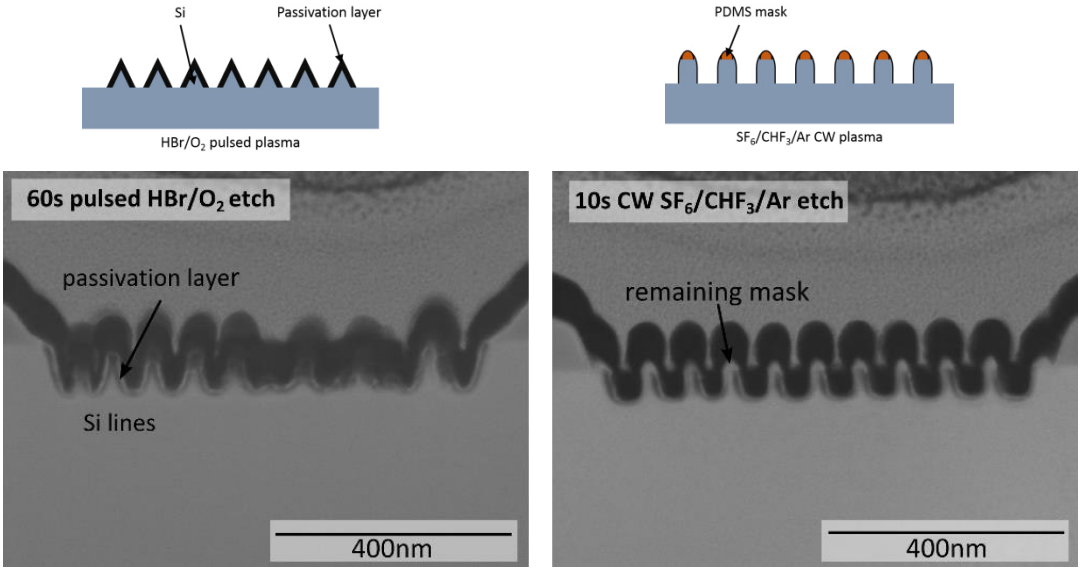

Figure 5-12: STEM cross section images of SD45 transferred into substrate by pulsed and CW mode etching and above schematic illustration thereof

The CW mode etching has a higher etching rate (approximately 3 nm/s) as we obtained 37 nm deep silicon lines in only 10s (vs 60s for pulsed plasma). Furthermore, the obtained features are much more homogeneous and anisotropic and it seems that the PDMS mask is still intact, leading to anisotropic Si nanowires. In HBr/O_2 plasma the passivation layer seems to be much thicker and only small parts of the wires are actually silicon, as depicted in the schematic of Figure 5-12.

Also, the results were found to be more reproducible than those obtained with pulsed plasma. Out of 10 etching tests in HBr/O_2, 5 would lead to the destruction of the features, while the $SF_6/CHF_3/Ar$ plasma achieved to work every time. On the STEM images it can be seen that there is no etching mask left in the case of pulsed plasma, which is why longer etching destroys the features. It was observed that the pulsed etching method was very sensitive and slight irregularities in the PDMS mask can destroy the resulting feature. Due to the rather low selectivity of HBr/O_2 plasma, the SOC is attacked very quickly when the protecting PDMS cylinder is too thin, destroying the feature. This is emphasized in the STEM micrograph, where some nanolines are collapsed, probably due to slightly thinner PDMS cylinders in the middle of the trenches. During spin-coating deposition, the block copolymer material tends to be slightly thicker in the edges than in the middle of the trenches, because the trench walls induce capillary wetting. This would explain the high rate of failure for this pulsed plasma samples.

In the case of CW etching, the mask is still present, resulting in the anisotropic etch. It seems that the passivation layer is also more homogeneous in the case of $SF_6/CHF_3/Ar$, but the investigation of such thin passivation layers is delicate and the fact that the samples were exposed to air has probably altered the results.

In conclusion, for samples on thick layers of SOC, the pulsed HBr/O_2 plasma process is a very efficient process that can achieve extraordinary high aspect ratio silicon lines. However its selectivity is rather poor (it attacks also the SOC layer) which is why, when thinner etching masks are used, it fails to work. Then, $SF_6/CHF_3/Ar$ etch process is a very promising alternative, without the need of pulsing the plasma. $SF_6/CHF_3/Ar$ CW mode plasma succeeded in etching anisotropic lines of up to 37 nm, six times faster than the pulsed plasma process for similar heights. Industry processes have to be kept as short as possible in order to increase the throughput. The $SF_6/CHF_3/Ar$ CW treatment yields anisotropic Si nanostructures with a reasonable aspect ratio considerably faster than the HBr/O2 pulsed plasma, which is why it is here the preferred process.

5.7 Transfer Etching of SD16

SD16, with its dense packing and small feature size, is particularly challenging for transfer etching. For the etching process, the mask has to be left sufficiently intact in order to successfully transfer patterns. The mask thickness and etching selectivity are crucial in this process. In SD16 however, the extremely small

lateral features dimensions means very thin masks that cannot or rather poorly compensate for a lack of selectivity. Ideally, from a pattern transfer point of view, lamellar microdomains of PS-b-PDMS would provide better etch robustness, as the height of the PDMS domains could be very high compared to its width. However, perpendicular orientation of lamellae BCP is problematic to obtain, even for low-χ BCPs, especially in topographical guiding patterns. Such orientation is even more challenging when using high-χ BCP, as block-to-block as well as BCP/substrate, BCP/air interactions are stronger and less easy to control. To our knowledge very few groups reported on large area perpendicular orientation of lamellar PS-b-PDMS microdomains[33].

Pattern transfer experiments on SD16 were conducted similarly to those of SD45, starting with HBr/O2 pulsed plasma. HBr/O_2 plasma has a limited selectivity, as it was shown on SD45 PDMS masks, and is even more problematic for the extremely thin mask of SD16. Figure 5-13 shows a SEM cross section micrograph of SD16 after a reduced time of 30 s pulsed HBr/O_2 etching.

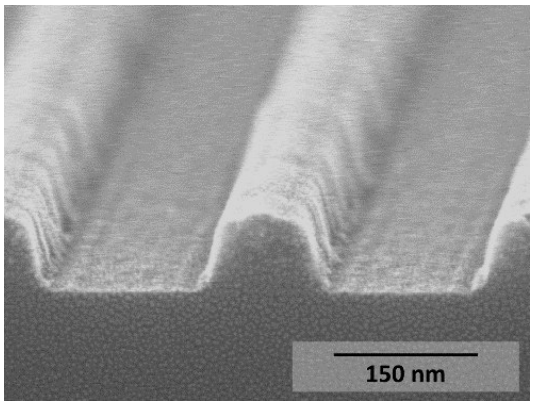

Figure 5-13: Cross section SEM image of SD16 after pulsed transfer etch of 30s

After only 30 s of etching, the mask is completely etched and only residues remain at the bottom of the trenches. Several tests on different parameters have been done to optimize this etching procedure for SD16, but no satisfactory results have been obtained. As it was shown on SD45, the HBr/O_2 pulsed plasma is sensitive to the PDMS etching mask uniformity and feature destruction was observed where PDMS cylinders were thinner. Cylinders of SD16 show a thickness of approximately 6 nm which is probably too thin to sufficiently protect the SOC layer from the HBr/O_2 pulsed etching. Furthermore the SD16 pattern is extremely dense which makes it difficult for the etchant to reach the bottom of the features. In order to increase selectivity, the SF_6/CHF_3/Ar CW mode plasma etching method was tested on SD16. As can be seen in Figure 5-14, 8 s etching was successful and approximately 30 nm high and 10 nm wide silicon nanowires were obtained.

As seen in Figure 5-8, SD16 showed pattern collapse at an intermediate state after SOC revealing and before Si transfer etch. Samples were removed from the vacuum of the etching reactor and exposed to

atmospheric pressure to take the SEM image, which may have introduced humidity and caused pattern collapse. This assumption is partly confirmed as Figure 5-14 was taken after a successive etching of SOC and Si transfer without exposure to atmospheric pressure. Pattern collapse seems to be reduced.

For a final product, the mask has to be completely removed in order to leave only the silicon substrate. Therefore a stripping with O_2 plasma was tested on SD 16 samples (see Table 5-1 for details). Figure 5-14 shows the results after stripping and it can be seen that the SOC has successfully been removed. Nevertheless, Figure 5-14b) shows that residues of SiArc trenches remain. These residues would need a more aggressive treatment, like hydrofluoric acid for example, to be completely removed.

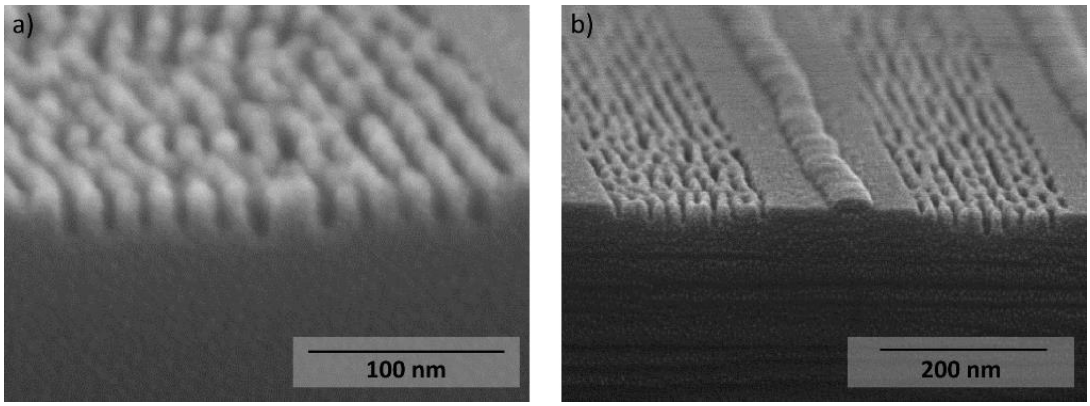

Figure 5-14: Cross section SEM images of SD16 transferred into the substrate by 8 s of SF_6/CHF_3/Ar CW mode plasma etching and subsequent O_2 stripping

In order to demonstrate a possible application of these silicon nanowires, trenches on SOI (silicon on insulator) wafers were designed for pattern transfer. SOI substrates are composed of a very thin silicon layer (here 30 nm) which is separated from the bulk silicon by a thin insulator layer (in our case 145 nm SiO_2) and were introduced in microelectronics in order to increase the performance of devices compared to bulk silicon devices[34,35]. In SOI substrates, the silicon drain and source junctions are built above an insulator (in general SiO_2 or sapphire), lowering parasitic capacitance and improving thus power consumption. The used stack for graphoepitaxy is composed of SiO_2 guiding trenches of approximately 40 nm depth. At the bottom of the trenches is a bare silicon layer of approximately 30 nm lying on the insulator layer of SiO_2. A sketch of the stack composition and the process flow can be seen in Figure 5-15.

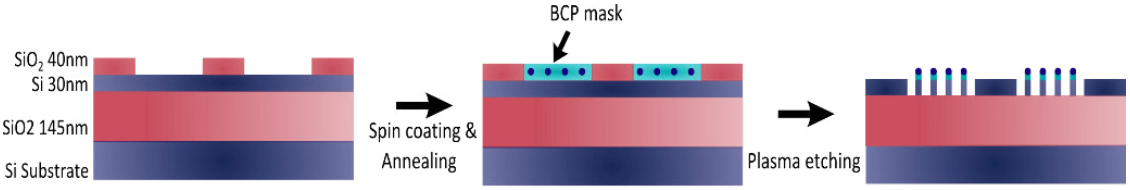

Figure 5-15: Sketch of the process flow of SD16 deposition and plasma transfer etching

Before depositing SD16, a thin layer of PS-brush is spin-coated on the substrate in order to obtain a PS attractive surface and prevent the formation of a PDMS interlayer (not shown in the sketch). In this case, the etching mask is considerably thinner than the SiArc/SOC stacks presented just before, consisting of 6 nm PDMS cylinders and only 3 nm PS-brush. As samples prepared on SOI were etched in the 200mm wafer etching reactor (cf. experimental section), different etching recipes have been developed that are detailed in Table 5-1 **Erreur ! Source du renvoi introuvable.**of the experimental section.

One possible application for patterning SOI substrates are fin field-effect transistor (finFET), where the transistor channel is wrapped from three sides by the gate. FinFETs have been introduced at the 22 nm node and show better electrostatic control than bulk devices[34]. Figure 5-16 shows SEM cross section images of the transferred PDMS lines.

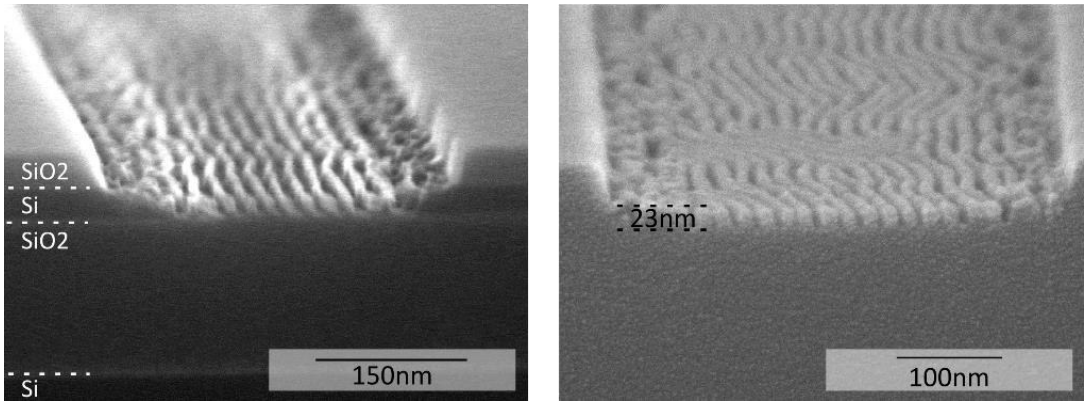

Figure 5-16: cross section SEM images of SD16 transferred into SOI substrate by HBr/He-O2 CW plasma

Due to the low aspect ratio, the transfer etch does not show any pattern collapse. The 200mm etching reactor does not have the possibility to pulse the plasma, but as the depth of etching is rather low, with an aspect ratio of only 2.3, the transfer etching is more staightforward and CW mode etching with HBr resulted in fins of ≈10 nm width and 23 nm height. Although the fins are only 23 nm high and the initial silicon thickness was 30 nm, it is considered that the Si layer is completely open. The height differences could be due to the consummation of the mask and height measurement errors. Additional morphological analysis (for example STEM) should be performed in order to exactly verify if the silicon layer has been completely etched.

5.8 Conclusion

We have generated periodic silicon line patterns by using transfer etching processes typically used in industry. Different etching methods have been investigated and optimized in order to obtain a good trade-off between anisotropy and aspect ratio. SD45 nanopatterns were transferred by using SiArc/SOC trilayer stacks. The SOC layer underneath the PDMS patterns serves as transfer layer, an additional mask thickness,

which makes it possible to obtain extremely high aspect ratio (≈6:1) features with pulsed HBr/O_2 plasma etching. For thinner SOC layers though, the selectivity of HBr/O_2 chemistry based plasmas is too low and it is favourable to use more selective $SF_6/CHF_3/Ar$ plasma in order to obtain even more anisotropic silicon lines. Anisotropic lines with virtually no slope and a reasonable aspect ratio of ≈2:1 were obtained. Finally, transfer etching of SD16 is challenging because of the extremely small etch mask of 10 nm width and only 6 nm height. After a first transfer into the SOC layer, patterns show some collapsing due to the high aspect ratio and high density of lines. HBr/O_2 plasma are not selective enough and did not show any satisfactory results while $SF_6/CHF_3/Ar$ etching achieves an aspect ratio of ≈3:1. For a future application of SD16 in, for example, finFETs, SD16 was deposited on SOI substrates, where PDMS masks are transferred directly into a Si layer, without using a transfer underlayer. The $HBr/He\text{-}O_2$ etch in CW mode was less critical than in the case of SiArc/SOC layers and Si nanofins on insulator of 10 nm width are obtained. These are promising results for a potential finFET application of BCP on SOI. In order to investigate the long-range integrity of the obtained nanofins, electrical measurements of the nanofins network could be performed. Then, such a process could be inserted into a fully industrial finFET fabrication flowchart and evaluated in terms of final electrical device performances.

References

(1) Borah, D.; Shaw, M. T.; Rasappa, S.; Farrell, R. A.; O'Mahony, C.; Faulkner, C. M.; Bosea, M.; Gleeson, P.; Holmes, J. D.; Morris, M. A. Plasma Etch Technologies for the Development of Ultra-Small Feature Size Transistor Devices. *J. Phys. D. Appl. Phys.* **2011**, *44*, 174012 (12pp).

(2) Kathrein, C. C.; Bai, W.; Currivan-Incorvia, J. A.; Liontos, G.; Ntetsikas, K.; Avgeropoulos, A.; Böker, A.; Tsarkova, L.; Ross, C. A. Combining Graphoepitaxy and Electric Fields toward Uniaxial Alignment of Solvent-Annealed Polystyrene– B –Poly(dimethylsiloxane) Block Copolymers. *Chem. Mater.* **2015**, *27*, 6890–6898.

(3) Nunns, A.; Gwyther, J.; Manners, I. Inorganic Block Copolymer Lithography. *Polymer.* **2013**, *54*, 1269–1284.

(4) Wang, X.; Winnik, M. A.; Manners, I. Synthesis, Self-Assembly and Applications of Polyferrocenylsilane (PFS) Block Copolymers. *Block Copolym. Nanosci.* **2008**, 151–168.

(5) Gu, X.; Gunkel, I.; Russell, T. P. Pattern Transfer Using Block Copolymers. *Philos. Trans. A. Math. Phys. Eng. Sci.* **2013**, *371*, 20120306.

(6) Gotrik, K. W.; Ross, C. A. Solvothermal Annealing of Block Copolymer Thin Films. *Nano Lett.* **2013**, *13*, 5117–5122.

(7) Lee, J.; Kim, Y.; Cho, J.; Yang, S.; Kim, J.; Yim, S.; Lee, H.; Jung, Y. In Situ Nanolithography with Sub-10nm Resolution Realized by Thermally Assisted Spin-Casting of a Self-Assembling Polymer. *Adv. Mater.* **2015**, *27*, 4814–4822.

(8) Hobbs, R. G.; Farrell, R. A.; Bolger, C. T.; Kelly, R. A.; Morris, M. A.; Petkov, N.; Holmes, J. D. Selective Sidewall Wetting of Polymer Blocks in Hydrogen Silsesquioxane Directed Self-Assembly of PS-B-PDMS. *ACS Appl. Mater. Interfaces* **2012**, *4*, 4637–4642.

(9) Jung, Y. S.; Ross, C. A. Orientation-Controlled Self-Assembled Nanolithography Using a Polystyrene-Polydimethylsiloxane Block Copolymer. *Nano Lett.* **2007**, *7*, 2046–2050.

(10) Lieberman, M. A.; Lichtenberg, A. J. *Principles of Plasma Discharges and Materials Processing: Second Edition*; **2005**.

(11) O'Driscoll, B. M. D.; Kelly, R. A.; Shaw, M.; Liontos, G.; Ntetsikas, K.; Apostolos, A.; Petkov, N.; Morris, M. A. Achieving Structural Control with Thin Polystyrene- B-Polydimethylsiloxane Block Copolymer Films : The Complex Relationship of Interface Chemistry , Annealing Methodology and Process Conditions. *Eur. Polym. J.* **2013**, *49*, 3445–3454.

(12) Wadley, M.; Hsieh, I.; Cavicchi, K.; Cheng, S. Solvent Dependence of the Morphology of Spin-Coated Thin Films of Polydimethylsiloxane-Rich Polystyrene-Block-Polydimethylsiloxane Copolymers. *Macromolecules* **2012**, *45*, 5538–5545.

(13) Jeong, J. W.; Hur, Y. H.; Kim, H.-J.; Kim, J. M.; Park, W. I.; Kim, M. J.; Kim, B. J.; Jung, Y. S. Proximity Injection of Plasticizing Molecules to Self-Assembling Polymers for Large-Area, Ultrafast Nanopatterning in the Sub-10nm Regime. *ACS Nano* **2013**, *7*, 6747–6757.

(14) Borah, D.; Rasappa, S.; Senthamaraikannan, R.; Holmes, J. D.; Morris, M. A. Graphoepitaxial Directed Self-Assembly of Polystyrene-Block-Polydimethylsiloxane Block Copolymer on Substrates Functionalized with Hexamethyldisilazane to Fabricate Nanoscale Silicon Patterns. *Adv. Mater. Interfaces* **2014**, *1*, 1300102.

(15) Jung, Y. S.; Jung, W.; Ross, C. A. Nanofabricated Concentric Ring Structures by Templated Self-Assembly of a Diblock Copolymer. *Nano Lett.* **2008**, *8*, 2975–2981.

(16) Tu, K.-H.; Bai, W.; Liontos, G.; Ntetsikas, K.; Avgeropoulos, A.; Ross, C. a. Universal Pattern Transfer Methods for Metal Nanostructures by Block Copolymer Lithography. *Nanotechnology* **2015**, *26*, 375301.

(17) Jung, Y. S.; Chang, J. B.; Verploegen, E.; Berggren, K. K.; Ross, C. A. A Path to Ultranarrow Patterns Using Self-Assembled Lithography. *Nano Lett.* **2010**, *10*, 1000–1005.

(18) Liu, Z.; Gu, X.; Hwu, J.; Sassolini, S.; Olynick, D. L. Low-Temperature Plasma Etching of High Aspect-Ratio Densely Packed 15 to Sub-10nm Silicon Features Derived from PS-PDMS Block Copolymer Patterns. *Nanotechnology* **2014**, *25*, 285301.

(19) Girardot, C.; Böhme, S.; Archambault, S.; Salaün, M.; Latu-Romain, E.; Cunge, G.; Joubert, O.; Zelsmann, M. Pulsed Transfer Etching of PS–PDMS Block Copolymers Self-Assembled in 193nm Lithography Stacks. *ACS Appl. Mater. Interfaces* **2014**, *6*, 16276–16282.

(20) Lin, G.; Rahman, M.; Caho, J.; Sahn, J. Development of Spin-on High Carbon Hard Masks for High Resolution Photolithography. *J. Photopolym. Sci. Technol.* **2011**, *24*, 503–510.

(21) Padmanaban, M. P.; Cho, J. Y.; Kudo, T.; Rahman, D.; Yao, H.; McKenzie, D.; Dioses, A.; Mullen, S.; Wolfer, E.; Yamamoto, K.; *et al.* Progress in Spin-on Hard Mask Materials for Advanced Lithography. *J. Photopolym. Sci. Technol.* **2014**, *27*, 503–509.

(22) Abdallah, D. J.; McKenzie, D.; Timko, A.; Dioses, A.; Houlihan, F.; Rahman, D.; Miyazaki, S.; Zhang, R.; Kim, W.; Wu, H.; *et al.* Spin-on Trilayer Approaches to High NA 193nm Lithography. *J. Photopolym. Sci. Technol.* **2007**, *20*, 697–705.

(23) Hwang, G. S.; Giapis, K. P. On the Origin of the Notching Effect during Etching in Uniform High Density Plasmas. *J. Vac. Sci. Technol. B Microelectron. Nanom. Struct.* **1997**, *15*, 70.

(24) Bodart, P.; Brihoum, M.; Cunge, G.; Joubert, O.; Sadeghi, N. Analysis of Pulsed High-Density HBr and Cl2 Plasmas: Impact of the Pulsing Parameters on the Radical Densities. *J. Appl. Phys.* **2011**, *110*, 113302.

(25) Brihoum, M.; Cunge, G.; Darnon, M.; Gahan, D.; Joubert, O.; Braithwaite, N. S. J. Ion Flux and Ion Distribution Function Measurements in Synchronously Pulsed Inductively Coupled Plasmas. *J. Vac. Sci. Technol. A Vacuum, Surfaces, Film.* **2013**, *31*, 020604.

(26) Chao, C.-C.; Wang, T.; Ho, R.-M.; Georgopanos, P.; Avgeropoulos, A.; Thomas E. L. Robust Block Copolymer Mask for Nanopatterning Polymer Films. *ACS Nano* **2010**, *4*, 2088–2094.

(27) Chao, C.-C.; Ho, R.-M.; Georgopanos, P.; Avgeropoulos, A.; Thomas, E. L. Silicon Oxy Carbide Nanorings from Polystyrene-B-Polydimethylsiloxane Diblock Copolymer Thin Films. *Soft Matter* **2010**, *6*, 3582.

(28) Tanaka, T.; Morigami, M.; Atoda, N. Mechanism of Resist Pattern Collapse during Development Process. *Jpn. J. Appl. Phys.* **1993**, *32*, 6059–6064.

(29) Petit-Etienne, C.; Darnon, M.; Vallier, L.; Pargon, E.; Cunge, G.; Boulard, F.; Joubert, O.; Banna, S.; Lill, T. Reducing Damage to Si Substrates during Gate Etching Processes by Synchronous Plasma Pulsing. *J. Vac. Sci. Technol. B Microelectron. Nanom. Struct.* **2010**, *28*, 926.

(30) Giapis, K. P.; Hwang, G. S. Pattern-Dependent Charging and the Role of Electron Tunneling. *Jpn. J. Appl. Phys* **1998**, *37*, 2291.

(31) Darnon, M.; Petit-Etienne, C.; Pargon, E.; Cunge, G.; Vallier, L.; Bodart, P.; Haass, M.; Banna, S.; Lill, T.; Joubert, O. Synchronous Pulsed Plasma for Silicon Etch Applications. *ECS Trans.* **2010**, *27*, 717–723.

(32) Luere, O.; Pargon, E.; Vallier, L.; Pelissier, B.; Joubert, O. Etch Mechanisms of Silicon Gate Structures Patterned in SF6/CH2F2/Ar Inductively Coupled Plasmas. *J. Vac. Sci. Technol. B* **2011**, *29*, 011028.

(33) Bai, W.; Gadelrab, K.; Alexander-Katz, A.; Ross, C. A. Perpendicular Block Copolymer Microdomains in High Aspect Ratio Templates. *Nano Lett.* **2015**, *15*, 6901–6908.

(34) Collaert, N.; Alian, a.; Arimura, H.; Boccardi, G.; Eneman, G.; Franco, J.; Ivanov, T.; Lin, D.; Loo, R.; Merckling, C.; *et al.* Ultimate Nano-Electronics: New Materials and Device Concepts for Scaling Nano-Electronics beyond the Si Roadmap. *Microelectron. Eng.* **2015**, *132*, 218–225.

(35) Hu, C. SOI (Silicon-On-Insulator) for High Speed Ultra Large Scale Integration. *Jpn. J. Appl. Phys.* **1994**, *33*, 356–369.

Chapter 6 Extended Functionalities for Block Copolymer

6.1 General Introduction

This chapter deals with innovative techniques for block copolymer self-assembly as an extension to the classical approach of directed self-assembly for IC production. The directed self-assembly of block copolymers has garnered a lot of attention throughout the last decade and tremendous progress has been made in terms of defect control, long-range ordering and process time. Innovative approaches on the other hand, like multipatterning in order to obtain complex structures or the selective metal inclusion for pattern transfer improvement have had little attention. This chapter presents double patterning approaches with PS-b-PDMS in order to obtain hierarchical structures and a straightforward metal infiltration technique for PS-b-PMMA in order to improve the etching capabilities of this widely used BCP.

6.2 Double Patterning of PS-b-PDMS

6.2.1 Introduction

Multilayer structures could enlarge the application fields for BCPs to other device fabrications than traditional planar transistor manufacturing, for example 3D devices, photovoltaic or bit-patterned media. Hierarchical structures are obtained by the sequential self-assembly of layers of a BCP with the same or different morphology and or size. By patterning several stacks of BCP layers, 3D nanostructures with various orientation could be obtained[1]. The preceding layer acts then as graophoepitaxy guiding structures for the following layer. In this section, we concentrate only on the double patterning of block copolymers, which paves the way for multi patterning. Moon and coworkers presented for example the directed self-assembly of a lamellar PS-b-PMMA with the help of a cylindrical PS-b-PMMA, oriented in photolithography guiding lines[2]. In that way, the authors were able to obtain a highly arranged array of lamellas without the trace of any photoresist guiding pattern. Ruiz and coworkers showed a similar approach, where additionally the correlation length of lamellar PS-b-PMMA, which is known to be quite low on flat substrates, was significantly increased by prepatterning the substrates with PS-b-PMMA[3]. Other multilayer structures have been presented by Kim et al. by cross-linking PS-b-PMMA structures and repatterning the same BCP on top of the cross-linked one[4]. This technique provides high-aspect ratio nanostructures with a variable height, depending on the number of deposited layers. A similar approach was shown by Jung et al. where a first layer of cylinder forming PS-b-PMMA is cross-linked and acts as a neutral layer for the second lamellar layer[5]. Thus, perpendicular orientation of the second layer is obtained. It was shown that these complex 3D structures could enhance the light efficiency of GaN light-emitting diodes by forming a graded refractive index layer. PS-b-PDMS multilayer approaches have also been proposed by several groups. Jeong et al. proposed an innovative nanoimprint technique in which PS-b-PDMS is aligned in PDMS molds and then transfer-printed onto various materials[6]. Sequential imprinting of two layers of PDMS in

perpendicular direction on Si substrates resulted in highly organized nanomesh structures of feature sizes as small as 8 nm. Very recently, Tavakkoli and coworkers showed the nanomesh formation by sequentially patterning of cylindrical SD45 and SD16 leading to the orthogonal orientation of the two or more cylinder layers[7]. The first layer was deposited on PDMS-brush coated Si substrates and the second layer did not need any further surface treatment. Circular and rectangular nanomesh structures have been obtained with great control. Jin et al. demonstrated an analogous study of mulitlayers of spherical PS-b-PDMS[8]. This way, a considerable density multiplication of hexagonal PDMS arrays could be achieved.

In this chapter, we combine several morphologies and sizes of PS-b-PDMS in order to obtain complex structures that have the possibility to be transferred into the underlying semiconductor substrate.

6.2.2 Experimental Details

The samples were prepared on SiArc/SOC graphoepitaxy substrates, as detailed in chapter 2. BCPs of cylindrical PS-b-PDMS with overall molecular weights of 45.5kg/mol and 16kg/mol, were purchased from Polymer Source, Inc. The solvents PGMEA and toluene were purchased at Sigma Aldrich. Phase separation was obtained via solvent vapor annealing in toluene (for cylindrical assembly of SD45) and PGMEA (for spherical assembly of SD45) or thermal annealing (for SD16) depending on the BCP (chapters 2 and 4). Spherical SD16 was obtained by blending the BCP solution with PS homopolymer. By adding PS homopolymer into a low molar-mass cylindrical PS-b-PDMS system, the morphology can be driven toward the spherical morphology and highly ordered PDMS nanodomains can be obtained by thermal annealing[9].

The first self-assembled layer of BCP was treated with 5s CF_4 and 3s O_2 plasma in order to remove the PDMS surface layer and partially the PS matrix. The oxidation of the PDMS structures made them resistant to the subsequent spin-coating and solvent annealing of the second layer. A PS-brush was grafted on the obtained structures by spin-coating a 1% solution of PS-OH in PGMEA at 1500rpm onto the surface. Annealing at 200°C for 5min was needed to graft the polystyrene homopolymer on the surface. The samples were then rinsed in PGMEA in order to remove excess, non-grafted PS-OH and subsequently dried in N_2. A second layer of BCP was then spin-coated and annealed depending on the BCP. Finally the structures were treated by plasma etching for revelation as described for layer one and observed in SEM (Hitachi S-5000 or JEOL 7500F).

6.2.3 Nanomesh Formation with Double Patterning of SD45

The formation of well-ordered linear cylinder patterns of SD45 in toluene vapor was already explained in chapter 2. By optimizing the surface interactions and vapor pressure conditions we were able to obtain defect free parallel cylinders in SiArc/SOC guiding trenches after 75 min annealing. Furthermore, it was explained that by varying the selectivity of the solvent towards the BCP, one can change the state of the

final dried morphology. When annealing in PGMEA vapor for the same amount of time, we were able to obtain well-ordered hexagonal packing of spheres with the same BCP. Figure 6-1 shows SEM top view images of PGMEA and toluene annealed SD45.

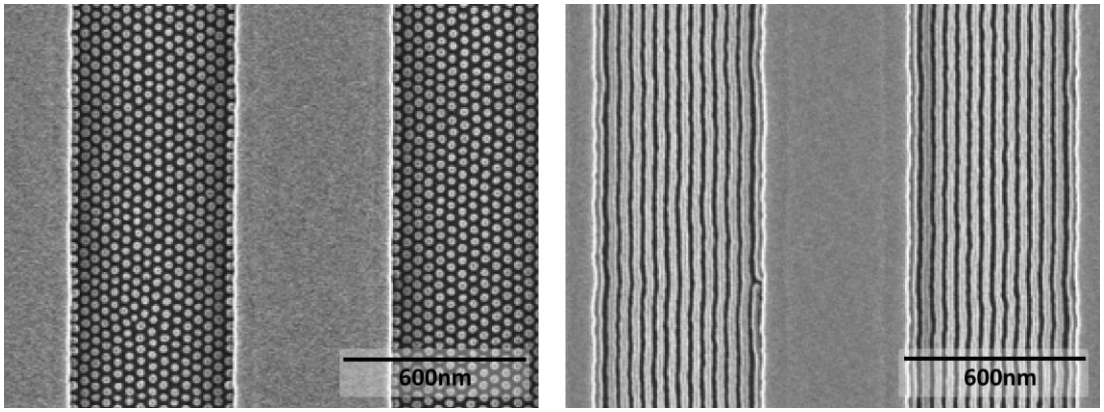

Figure 6-1: SEM top view images of SD45 after solvent vapor annealing for 75 min in (a) PGMEA and (b) toluene.

By combining these two morphologies, a nanomesh arrangement can be obtained. The process flow of the here proposed method is depicted in Figure 6-2.

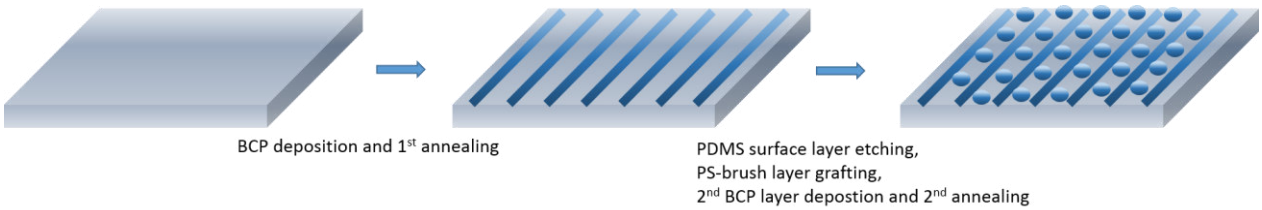

Figure 6-2: Process flow of the double patterning of PS-b-PDMS

The alignment of BCP can be guided by topographical or chemical substrate modifications. In our case the first layer of SD45 consists of cylinders that are aligned in SiArc/SOC graphoepitaxy templates. The obtained cylinders act then themselves as a template for the arrangement of the spherical SD45. The sequential patterning of different PS-b-PDMS systems has already been shown, but the layers of BCP were assembled without an intermediate etching step or by deposition of an intermediate PDMS layer[7,10]. A PDMS layer between the layers or at the substrate/BCP interface makes the pattern transfer etching process very problematic. A PDMS surface layer is naturally formed at the air/BCP interface due to the lower surface tension of PDMS compared to PS. In our approach an intermediate plasma etching step is performed before depositing the second BCP layer, in order to maintain the good transfer etching properties of the system. The PDMS layer is removed with short CF_4 plasma and the PS matrix is partly removed by O_2 plasma. The deposition of a PS-brush on top of this layer guarantees the homogeneous wetting of PS at the BCP/BCP interface. As it is desired to form mesh-like structures, the PDMS spheres of

the second layer should align inside the grooves of the first SD45 layer. The PS-brush prevents thus the preferential wetting of the PDMS spheres on top of the already aligned PDMS cylinders. After the grafting of the PS-brush, the second layer of SD45 is deposited and annealed for 75min in PGMEA solvent vapor. Figure 6-3 shows top view SEM images of the obtained results. The center-to-centre distances of both spheres and cylinders are uniformly 35 nm. Hexagonal symmetry of the dots are observed inside the parallel lines. The dimension of the obtained holes between spheres and cylinders is 17 x 23 nm^2.

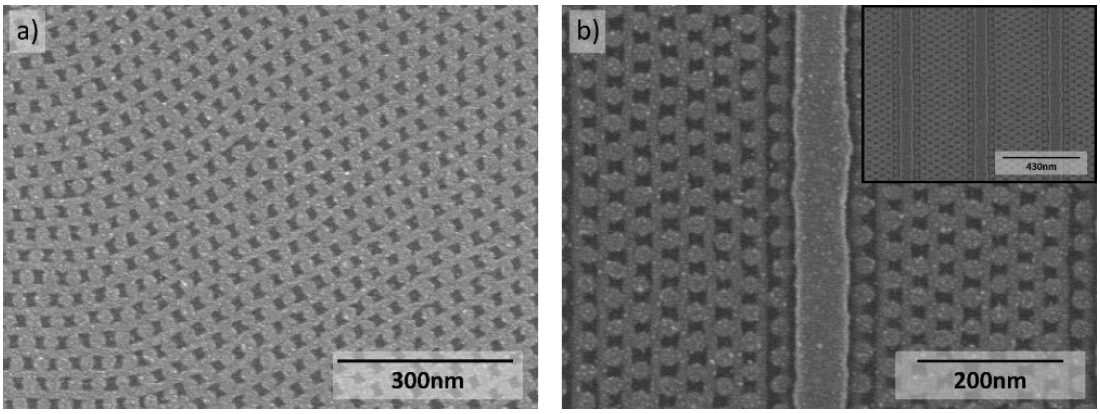

Figure 6-3: Nanomesh formation of two layers of SD45 on (a) plane surface and (b) in SiArc/SOC graphoepitaxy templates, inset: low magnification image

On plane silicon surfaces the templating of the first layer becomes evident. It can be seen how the second layer spheres orient themselves with respect to the SD45 template, following the "fingerprint" orientation of the cylinders (Figure 6-3 a). When oriented within graphoepitaxy lines, long range order nanomeshes can be obtained (Figure 6-3 b).

6.2.4 Nanomesh Formation with Double Patterning of SD16

The same experiment was performed on SD16. SD16 has intrinsically cylindrical morphology and a morphology change cannot be accessed by selective solvent annealing like we presented for SD45, as we use thermal annealing for SD16. However it was shown that the spherical morphology can be accessed by blending the solution with a PS-homopolymer[9,11–13]. By adding the PS homopolymer, the total volume fraction of PS in the BCP increases, while the one of PDMS decreases. By adjusting the amount of added PS-homopolymer, the desired morphology can be obtained. In our case, equal portions of a hydroxylterminated PS solution of 1 wt% and the BCP solution were mixed in order to obtain a final PDMS volume fraction of f_{PDMS} = 14% (for comparison, SD16 has initially f_{PDMS} = 22.4%)[9]. Figure 6-4a shows the obtained spherical structure in hexagonal symmetry and cylindrical morphology (in Si graphoepitaxy lines) after standard annealing of 15min at 150°C.

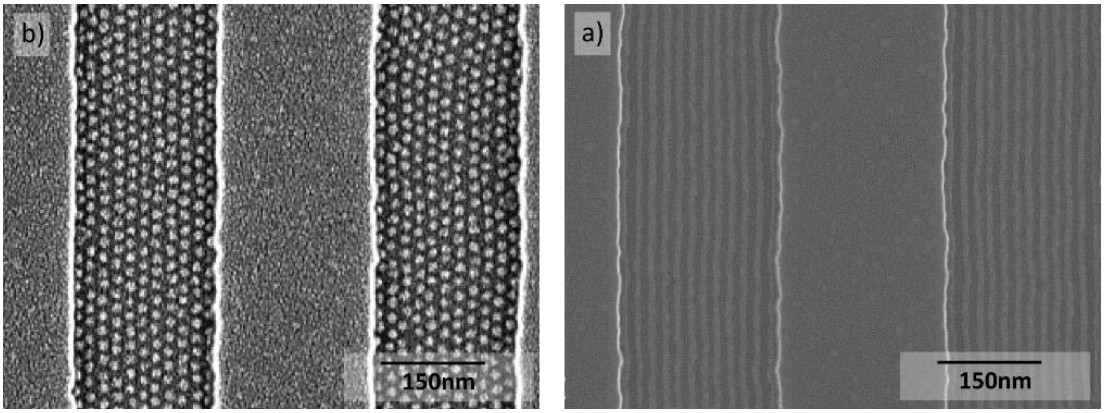

Figure 6-4: SEM top view image of (a) PS-OH blended SD16 and (b) neat SD16 after 15min annealing at 150°C

Similar to the process of SD45 the two layer of cylinders and spheres can be combined to obtain a mesh-like structure as shown in Figure 6-5.

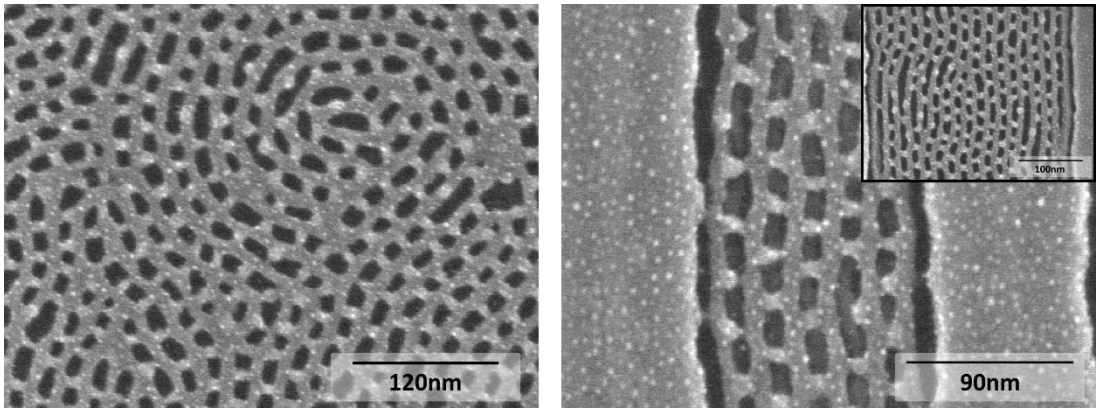

Figure 6-5: SEM top view images of SD16 after double patterning on (a) plane and (b) graphoepitaxy SiArc/SOC substrates

Nanocontainers with a dimension of 8 x 15 nm^2 have been obtained. The second layer of BCP, with spherical morphology, follows again the cylinder templates. It seems that the spheres elongate themselves in respect to the distance variations (induced by line width roughness of SD16) between the templating cylinders, thus showing chemical affinity towards the PDMS. However, the spheres elongate only to a certain amount, and when the distance between two cylinders is too high, the sphere arranges itself on top of the cylinder. Interestingly, the spheres are always sticking to the PDMS lines and are never arranged individually between the lines. The second PDMS dot layer is thus brought in a competition between chemical affinity towards PDMS (even treated with a PS-brush) and spatial confinement between two cylinders. Similar behavior was shown by Shin et al., where the thickness of the templating nanowires had great influence on the alignment of the second layer[14]. Differences in the line edge roughness of SD16 must be responsible for the alternating positioning of the dots on or in between the templating cylinders.

6.2.5 Density Multiplication by Double Patterning of Cylindrical SD45 and SD16

The combination of SD45 and SD16 features was also tested with our method, but on planar SOC substrates here (Figure 6-6).

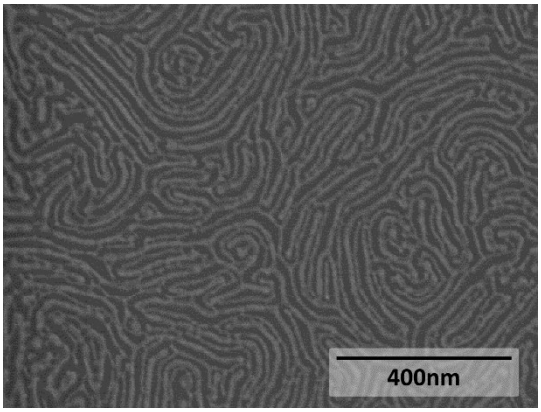

Figure 6-6: SEM top view image of double patterning cylindrical SD16 on cylindrical SD45

Due to the lack of guiding trenches, SD45 shows fingerprint orientation with short range order. Despite this fact, it can be seen that SD16 aligns perfectly parallel to SD45, obtaining a density multiplication of the features. This work demonstrates the ability of BCPs to create complex 3D structures with extremely small feature sizes in a low cost manner. Moreover, the here presented method for PS-b-PDMS has the ability to be transferred into the silicon substrate, as no PDMS wetting layers are obtained. Etching mechanisms as presented in chapter 5 should result in successful pattern transfer and complex Si structures. These constructed structures can find applications as interconnections or vias in transistor, as membranes, LEDs or photovoltaics device fabrication.

6.2.6 Conclusion

In conclusion, this section demonstrates the fabrication of innovative hierarchical nanostructures of SD16 and SD45 that are formed by double patterning of different PS-b-PDMS systems. During this process, the first layer of PS-b-PDMS acts as a templating layer for the second BCP. By aligning the first layer by graphoepitaxy one can obtain long range order structures. The second BCP aligns itself during this process with respect to the first layer. The dimension of the templating cylinders has influence on the position of the second layer structures. Too thin templating lines lead to the alignment of spheres on top of the cylinders. Therefore, this process allows a high level of control over the self-assembly of block copolymers. Especially small period BCPs can profit from this phenomenon and large scale sub-10 nm arrangement for lithography applications can be obtained. Furthermore, our process shows no PDMS interlayer between the BCP layers or at the substrate/BCP interface. The transfer etching of these features should thus be accessible via etching processes like those presented in chapter 5. It is imaginable that this double

patterning could be increased to multipatterning, obtaining three dimensional structures that could be used for interconnections or vias in the IC manufacturing or other 3D devices.

6.3 Fabrication and Characterization of Metal Oxide Nanowires

6.3.1 Introduction

The phase separation of block copolymers is dictated by the Flory-Huggins interaction parameter χ, the degree of polymerization N, and the volume fraction of each block. The Flory-Huggins parameter indicates the compatibility of the blocks, the higher the χ, the lower the miscibility. Besides high-χ BCP like PS-b-PDMS there are several low-χ BCP that are widely used. PS-b-PMMA remains the primary choice when using low-χ BCP, as it has been studied for nearly 20 years now[15]. Reasons for its widespread use are the ease in which it can be phase-separated and the high degree of familiarity of the homopolymers PS and PMMA in microelectronic manufacturing. The similarity of the surface tensions of PS and PMMA ($\gamma_{PS} \approx$ 40mN/m, $\gamma_{PMMA} \approx$ 41mN/m) prevents the formation of interfacial wetting layers. By controlling the film thickness and surface energy of the substrate (with neutral brush layers for instance), perpendicular structures can easily be obtained. Due to its higher miscibility, PS-b-PMMA is consequently easier to anneal than PS-b-PDMS. Thermal treatment above the glass transition temperature of the system is in general enough to obtain phase separation. Also, sophisticated methods have been introduced in order to decrease process time. Zhang et al. obtained phase separation in 1 minute by microwave annealing[16]. Yager and coworkers used laser illumination to generate localized thermal fields within a BCP thin film[17]. In this way, phase separation was obtained in seconds only in illuminated areas, allowing direct patterning via the incident light field.

Apart from the resolution issue related to low-χs, one of the main disadvantages of PS-b-PMMA is its low etch selectivity between the blocks. Pattern transfer becomes then difficult. Today, mainly two etching methods are used in the literature. Dry plasma etching with chemistries like argon, oxygen, carbon monoxide or polymerization gases like CHF_3[18–20] can be used. With oxygen-containing plasma, etching of carbon materials presents low selectivity between the blocks. When etching PS-b-PMMA in O_2/Ar plasma for example, for 2 nanometer of etched PMMA, one nanometer of PS is consumed. This makes the complete etching of PMMA and the transfer etching in the underlying layer without the loss of PS extremely difficult[19,21–23]. Another method is based on the wet development in acetic acid, with and without the use of UV irradiation[23,24]. When using acetic acid, we speak of surface reconstruction, as none of the polymer blocks is literally etched but rather relocated. Acetic acid is a non-solvent for PS and a good solvent for PMMA. It swells only the PMMA domains which then migrate up to the surface along the PS interface. Nanoporous surfaces can thus be obtained by a simple relocation of the PMMA chains when immersed into

acetic acid. However, PMMA residues remain inside the pores, possibly altering the critical dimension of features[25]. When using UV irradiation before the immersion in acetic acid, PS-b-PMMA bonds break, the PMMA chains degrade and can then be removed during the subsequent acid treatment. This way, the PMMA block is more efficiently removed[23]. The major concern in directed self-assembly of PS-b-PMMA is high fidelity pattern transfer. High aspect ratio features and small feature sizes (<15 nm) are extremely difficult to obtain. One solution in order to improve etch contrast is the integration of metal based materials in one of the blocks. Metals are chemically resistant to plasmas that are used to remove organic polymer materials or to etch silicon. Furthermore, metallic agents show high selectivity in silicon etching processes. Infiltration of metal agents into the block that is used as template has encouraging potential in order to raise etch resistance.

In chapter 1, BCPs that intrinsically contain inorganic atoms have been introduced. These types of BCP exhibit higher etch selectivity compared to purely organic BCPs. However, most of these BCPs are not well studied and their synthesis can be quite complex. Infiltration of the solution before spin-coating is another, less complicated solution for etch resistance enhancement. Kim et al. demonstrated the addition of metal salts into a PS-b-PEO (PS-Poly(ethylene oxide)) by simply mixing the BCP solution with a metal salt solution[26]. The salts coordinate then only with the polar PEO block. Due to its electron donating site, the metal ions are reduced to the corresponding metal, forming nanoscopic metal particles only within the PEO block. PS can then easily be etched away by an usual oxygen plasma. Since one block has to have electron donating sites in order to be altered by metals, this kind of experiments are restricted to only a narrow range of BCPs.

By infiltrating BCPs post self-assembly, one can retain the benefits of habitual BCP systems and the knowledge on their self-assembly methods. Several post assembly infiltration methods have been presented in the last few years, among them atomic layer deposition (ALD) sequential infiltration synthesis (SIS) and metal oxide inclusion via spin-coating[27]. ALD is a thin film deposition technique based on surface reactions of vapor phase precursors. The process is self-limiting as there are only a finite number of surface sites free for reaction with the precursor. That way, a thin film can be deposited with atomic level control[28]. The group of Thierry Baron at the LTM showed in 2010 the deposition of Al_2O_3 by ALD into the PMMA grooves of PS-b-PMMA after self-assembly and removal of the PMMA block. Obtained Al_2O_3 dots and stripes were then used for pattern transfer and high aspect ratio (>10) silicon pillars and wires were obtained by inductively coupled plasma etching[29,30]. Figure 6-7 shows a schematic of the whole process and corresponding SEM images of pattern transferred features.

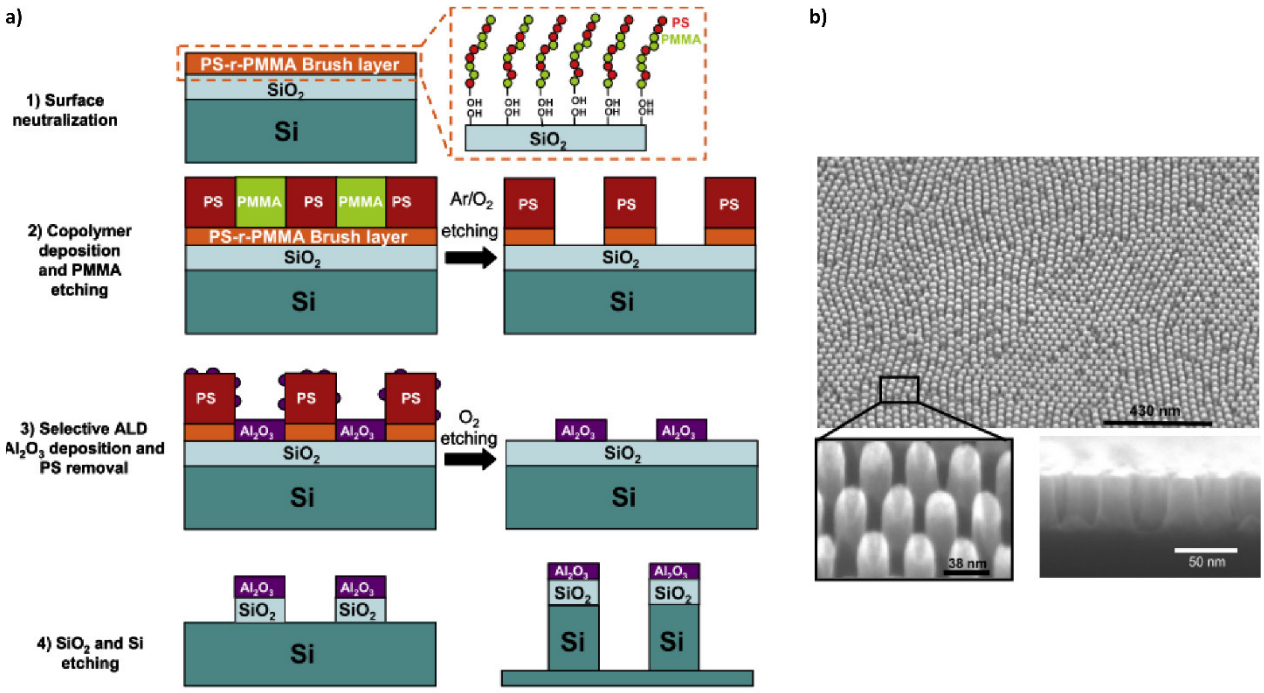

Figure 6-7: a) Strategy used for Al2O3 mask fabrication and subsequent nanopillar etching. b) corresponding SEM images after pattern transfer[29]

Other references show additional benefits of density multiplication by applying ALD on self-assembled BCPs[31,32].

SIS is a technique that is very similar to the processes presented using ALD, with the exception that the BCP does not have to be etched before applying ALD. One block serves as a growth site during ALD cycles. That way the metal is grown within the BCP and not at surfaces as it is the case in the ALD processes presented above. Secondly, the block removal, which is a critical step that can induce roughness and defects, can be avoided[27]. Peng and coworkers were the first to introduce SIS in 2010[33]. They infiltrated the PMMA block of a self-assembled PS-b-PMMA layer by exposing the sample to metal precursor vapor. Precursors, such as $TiCl_4$, $AlCl_3$, Al $(CH_3)_3$, which are Lewis acids, react selectively with the carbonyl-groups of the PMMA. Since this first report many others have followed enlarging the variety of BCPs and metal precursors that can be used[27]. However, this infiltration technique is complex and relies on the use of high-cost equipment. To further simplify this process, spin coating of metal salts on self-assembled BCPs has been introduced. In 2009 Son et al. presented a method to align nanomaterial arrays on reconstructed surfaces of PS-b-PMMA[34]. Relying on the principle of surface reconstruction, PS-b-PMMA is immersed in or exposed to selective solvents. Obtained nanostructures are then "filled" with inorganic salts by spin-coating. A lot of research on this subject has been reported by the research group of Mick Morris at the Trinity College Dublin [27,35–37] (formerly at the University College Cork) which is why this chapter was developed in close cooperation with this group. A collaboration in the framework of the Ulysses project has been developed,

funded by Campus France and the Irish Research Council to allow respective research visits by the author and Colm Keating, a PhD student within Morris' group. The infiltration by spin-coating of iron salt onto surface reconstructed PS-b-PMMA is presented. An analysis of the self-assembled, swollen and infiltrated system is given by grazing incident small angle X-ray scattering (GISAXS) measurements. Infiltrated patterns are then transferred by plasma etching into silicon, obtaining good etching contrast.

6.3.2 Experimental Details

Lamellar Poly(styrene)-block-Poly(methylmethacrylate) with an overall molecular weight of M_w=75kg/mol (f_{PMMA}=49, f_{PS}=51) and a natural period of 38 nm (named L38) and random PS-r-PMMA (with a similar global composition) was provided by Arkema France. Propylene glycol monomethyl ether acetate (PGMEA), Ethanol and $Fe_2(NO_3)_3 \cdot 9H_2O$ (iron(III) nitrate nonahydrate) were purchased from Sigma Aldrich and used without further purification.

Cleaned bare Si substrates were activated in O_2 plasma for 2min before use. For the brush preparation a random brush solution was deposited by spin-coating at 700rpm. Samples were immediately annealed at 200 - 230°C for 5 - 10min. Non-reacted brush residues were rinsed off with PGMEA and dried in N_2.

1-2 weight% solutions of PS-b-PMMA BCP were prepared in PGMEA and spin coated on brushed surfaces at 1500 rpm for 30seconds. Thermal annealing for phase separation was then applied on a hot plate at 210 – 230°C for 5 - 10min.

The surface reconstruction was carried out by placing the annealed PS-b-PMMA sample in a glass jar with ethanol vapors for 4 – 5 h at 40°C. After this vapor treatment, the sample was removed and left to dry at room temperature. This provided enough time for swelling of the PMMA domains to enable the reconstructed template to form for subsequent deposition of the metal nitrate solutions. Alternatively, PS-b-PMMA samples can be immersed in ethanol for this reconstruction. $Fe_2(NO_3)_3 \cdot 9H_2O$ solution of 2 wt% were prepared in ethanol and immediately spin-coated onto the reconstructed samples for 30 s at 3000 rpm. O_2 plasma treatment for 2 min was used to oxidize the precursor and remove polymer.

For pattern transfer, a 200mm AdvantEdge decoupled plasma sources (DPS) reactor from Applied Materials, Inc., described in chapter 5, was used. HBr/He-O2 plasma was used to transfer the iron oxide nanowires into the silicon substrate, similar to the etching process of SD16, presented in chapter 5. GISAXS measurements were performed on the BM02 beamline at the European Synchrotron Radiation Facility (ESRF) in Grenoble (France), using the experimental protocol described in chapter 2.

6.3.3 PS-b-PMMA Self-Assembly and Surface Reconstruction

Vertical lamellar of PS-b-PMMA (L38) are obtained by treating the surface with a random copolymer brush PS-r-PMMA. On bare silicon substrates, the lamellar BCP aligns parallel to the surface as the PMMA block

prefers the wetting of the natural oxide layer on Si substrates. When brushed with a random copolymer, which is composed of identical monomers, the preferential wetting can be canceled allowing perpendicular alignment[38]. After the grafting and rinsing of the random brush, L38 is spin-coated in order to obtain a layer of approximately 40 nm thick. The film is then annealed for 10min at 220°C in order to trigger phase separation. Since the electron contrast of PS and PMMA is very poor at this stage, SEM observations are challenging. Figure 6-8a shows top view SEM image of PS-b-PMMA after thermal annealing. Although the samples were sputtered with a thin Pd layer in order to enhance the contrast, PMMA lines are only vaguely visible. FFT measurements show a periodicity of 38 nm. Additional GISAXS measurements were obtained at the ESRF in Grenoble (Figure 6-8b). Although in SEM the electron contrast is quite low, X-ray contrast shows nicely defined scattering spots on the intensity image.

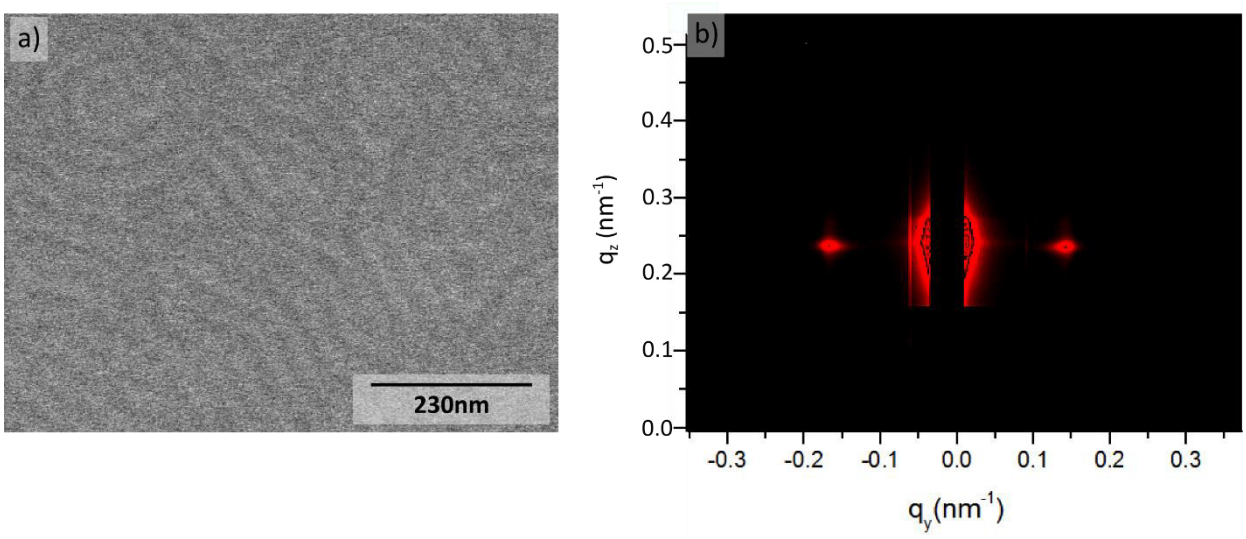

Figure 6-8: (a) SEM top view image of L38 after thermal annealing, (b) corresponding GISAXS intensity pattern

While PS-b-PMMA was already used as a template for nanoparticle infiltration[39,40], surface reconstruction in order to infiltrate one block by a spin-coating process has not been reported to our knowledge for PS-b-PMMA yet. In our case, the surface reconstruction of the sample was obtained with ethanol, based on experience within the Morris' group. It is suggested that the solvent swells the PMMA block as depicted in the schematic in Figure 6-9.

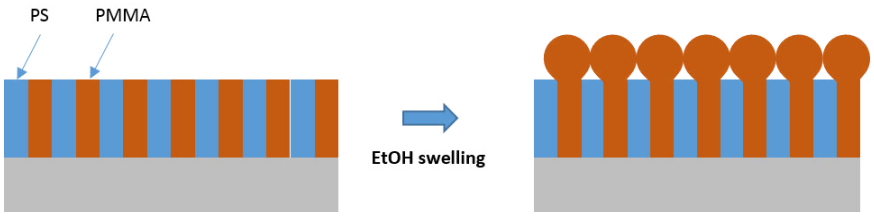

Figure 6-9: Schematic illustration of the swelling process of EtOH on PS-b-PMMA

Therefore, for good surface reconstruction the solvent has to be a good solvent for the block that is to be infiltrated and a non-solvent for the other block[35,41,42]. However, the exact mechanisms involved in surface reconstruction are not fully understood, yet. Especially when regarding the Hansen solubility parameters, we expect ethanol to be a poor solvent for both blocks (HSP_{PMMA} = 22.7 $MPa^{1/2}$, HSP_{PS} = 22.4 $MPa^{1/2}$, HSP_{EtOH} = 29.6 $MPa^{1/2}$)[43]. Yet, after exposure to ethanol vapor (Figure 6-10a) and immersion in ethanol (b) for 4h at 40 °C the electron contrast of the sample is drastically increased, indicating the successful swelling of PMMA.

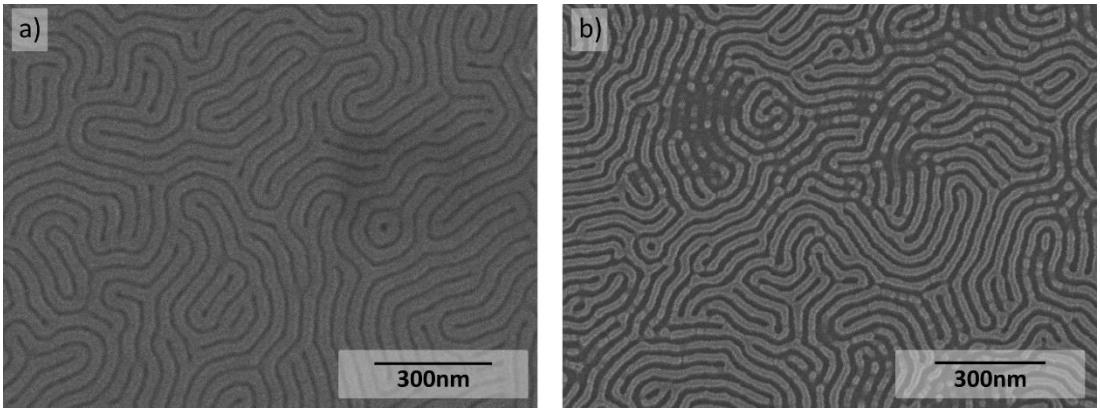

Figure 6-10: SEM top view image of L38 after self-assembly and subsequent 4h swelling in a) EtOH vapor and b) immersed in EtOH

Furthermore, the sample swollen in ethanol vapor shows homogeneous layer thickness and uniform wetting of the substrate. GISAXS measurements of this sample (Figure 6-11) reveal smaller, more defined scattering spots indicating well defined structures. Due to the enhanced contrast, caused by the relocation of PMMA, the intensity is slightly increased.

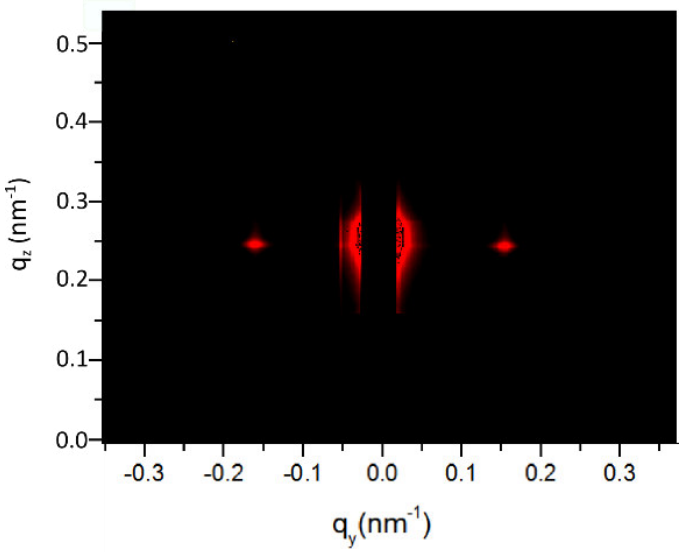

Figure 6-11: GISAXS intensity profile of L38 after swelling in ethanol vapor for 4h

The sample immersed in EtOH on the other hand shows some dewetting and or partial degradation of the BCP layer and the critical dimension compared to the sample exposed to EtOH vapor is decreased (22 nm when immersed and 28 nm in vapor). The swelling of the sample was certainly here too aggressive leading to a higher mobility of the PMMA domain. Due to capillary effects, the PMMA domain could be relocated partially on top of the PS lines. This makes clear that the full process of surface reconstruction is not fully revealed, but precise activation protocols have to be found in order to obtain good patterns for inclusion[35]. Interestingly, the swelled samples are stable over days, without deswelling. The simultaneous heating at 40°C combined with the ethanol leads clearly to a more complex mechanism than just solvent swelling.

6.3.4 Metal Salt Inclusion and Pattern Transfer Etching

The surface reconstructed patterns are then used as a template for metal oxide inclusion. Iron oxide Fe_3O_4 is known to be a robust etching mask for silicon transfer that allows the etching of high fidelity nanostructures[35]. The iron salt is diluted in ethanol and spin-coated on the activated BCP to fill out the nanoporous structure. The concentration of the metal solution is chosen to be quite low in order to prevent the overloading of the BCP. Iron nitrates starts by filling the PMMA block, but when an excess of iron nitrate is present it can form either agglomerates or start filling the PS block, which could cause problems during the substrate transfer etching[35,44]. After spin-coating, the samples were immediately oxidized in oxygen plasma for 2 min. This allowed the oxidation and cross-linking of the metal nitrate and a simultaneous etching of all organic material. The SEM top view images in Figure 6-12 shows the oxide nanowires after metal spin-coating and oxygen treatment of the two samples shown in Figure 6-10.

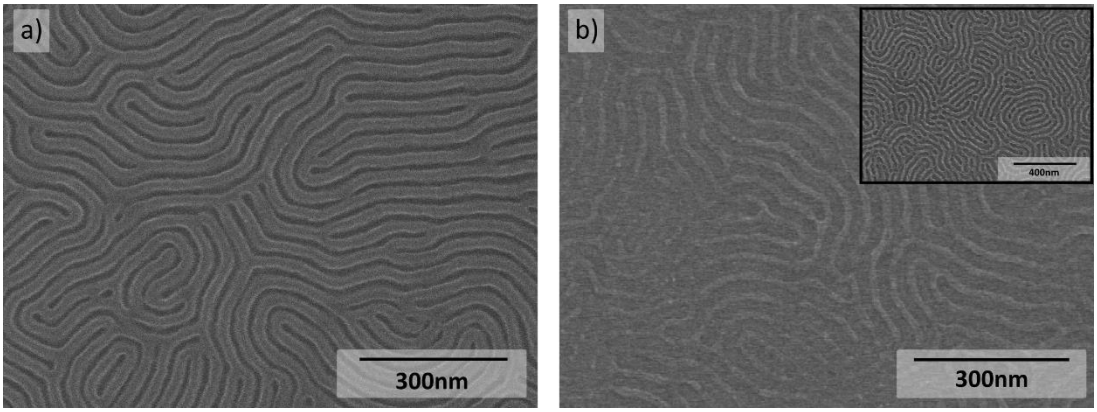

Figure 6-12: SEM top view images of Fe_3O_4 nanowires obtained after a) vapor swelling and b) immersion of self-assembled L38 samples in EtOH, inset low magnification image

The obtained nanowires mimic perfectly the templates obtained after swelling in EtOH. In the case of vapor swelled samples, the center to center spacing of the nanowires (and their width) are similar to those right after swelling (≈ 38 nm). On the other hand, the solvent immersed sample shows poor infiltration results, with partial destruction of the wires and high line roughness (Figure 6-12). This is most probably due to

the iron salt that infiltrates less defined PMMA domains that are partially relocated onto the PS domains due to uncontrolled swelling. The swelling step is thus primordial for optimal metal infiltration and, by controlling the swelling degree, and hence the degree of relocation, the quality of the final iron oxide wires can be tuned. Hence, we further worked with vapor swelled samples. The film morphology of the vapor swelled and infiltrated nanowires was further investigated by GISAXS (Figure 6-13). The scattering spots are now clearly increased in intensity, due to the etching of the organic polymers, leaving only iron-oxide structures. Now, first and second order diffraction spots can be observed, due to the high scattering intensity. The periodicity corresponds to 38.5 nm, which confirms a good CD control after inclusion and polymer etching.

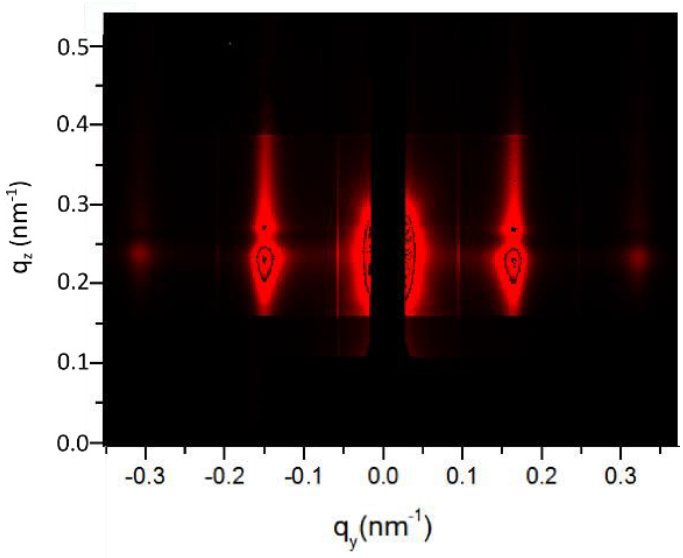

Figure 6-13: GISAXS intensity profile of L38 after iron nitrate inclusion and O_2 etching

The obtained Fe_3O_4 features can then act as efficient and selective hard masks in order to transfer the pattern into the silicon substrate. Cl_2 plasma was employed for the breakthrough, i.e. etching of the native oxide layer. The Si was then subject to HBr/He-O_2 plasma etch and after 15 s of etching, 35 nm deep nanowires are obtained (Figure 6-14). The transfer etch confirms that metal was deposited selectively in PMMA domains and that the PS domains were left free of metal

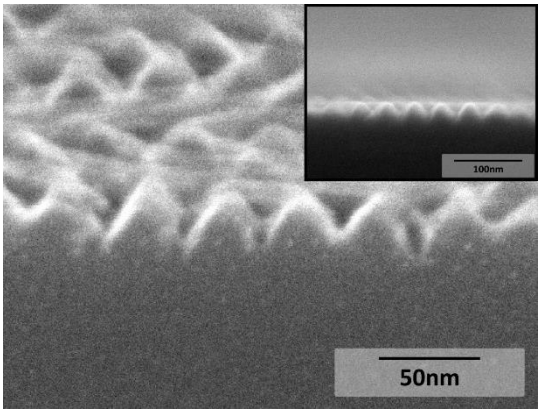

Figure 6-14: SEM cross section image at 80° of L38 after plasma transfer etching in HBr/He-O_2 for 10 s. Inset cross section image at 90°c

When comparing with neat PS-b-PMMA, the etching selectivity is considerable increased. Based on the research on PS-b-PMMA etching of a fellow PhD student at the LTM group, it is reasonable to say that a neat PS-b-PMMA would have shown much less selectivity and the pattern transfer would have been much more challenging[21]. Presented results were preliminary obtained on plane silicon substrates. Also, tests on the already presented graphoepitaxy SiArc/SOC substrates were made. The alignment of L38 in trenches did not result in long range order, due to the use of a random copolymer brush and to the fact that the trench size and depth was not optimized for the L38 system. However, inclusion could be obtained selectively in the PMMA part and SOC transfer etching was performed in HBr/O_2 plasma in order to reveal the metal nanowires and etch the SOC underlayer. The selective inclusion of iron in PMMA is confirmed by the successful etching of the SOC layer (Figure 6-15). The obtained nanowires are homogeneous and uniform in size.

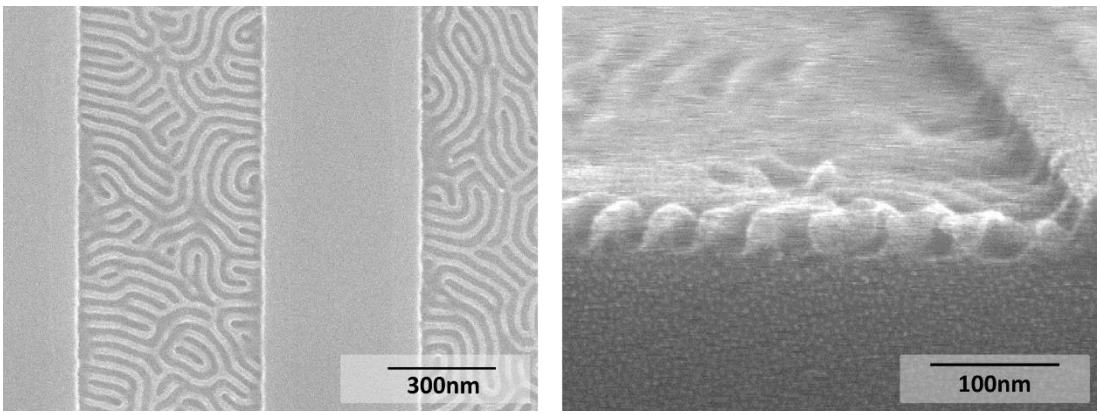

Figure 6-15: a) SEM top view and b) cross section image of pattern transferred Fe_3O_4 wires in SiArc/SOC guiding trenches

For pattern transfer, the 300 mm reactor could not be used du to contamination issues arising with the use of iron. The in chapter 5 presented process that was developed in the 200 mm etch reactor for SOI finFET etching was not adaptable for SiArc/SOC samples. In continuous wave on SiArc/SOC samples, the oxygen

present in the plasma underetches the SOC layer and causes a lift-off of the mask. As pulsed plasma is not available in the 200 mm reactor, SF_6/ CHF_3/Ar plasma was tested, but not optimized, leading to the fluorination of the surface. For the moment, no pattern transfer has been obtained, but a proper optimization of the SF_6/CHF_3/Ar plasma in the 200 mm reactor could lead to high fidelity pattern transfer.

6.4 Conclusion

This section presents a simple metal inclusion technique that improves transfer etching properties of low-χ BCPs. Due to the poor etch selectivity of low-χ BCP, they are often not suitable for certain IC manufacturing processes. By integrating metal oxide into one of the blocks it seems that the selectivity is increased and these BCP can be transferred into the underlying functional material. Low-χ BCP are limited in size but show interesting properties and are particularly well understood compared to some exotic high-χ BCPs, which is why the transfer etch of these BCP is interesting. In the presented approach, an iron salt solution is spin-coated on a self-assembled and surface reconstructed PS-b-PMMA. By exposing the obtained sample to O_2 plasma, the remaining organic polymer is removed and the metal nitride oxidized to iron oxide. This can be used as a robust etch mask for pattern transfer. On plane silicon, where the iron oxide was deposited directly on the substrate without a transfer layer, structures of 35 nm height could be obtained. When deposited on SOC layers, the etch mask could possibly be transferred into the substrate with high aspect ratio when optimizing the etching parameters

References

(1) Ross, C. A.; Berggren, K. K.; Cheng, J. Y.; Jung, Y. S.; Chang, J.-B. Three-Dimensional Nanofabrication by Block Copolymer Self-Assembly. *Adv. Mater.* **2014**, *26*, 4386–4396.

(2) Moon, H.-S.; Shin, D. O.; Kim, B. H.; Jin, H. M.; Lee, S.; Lee, M. G.; Kim, S. O. Large-Area, Highly Oriented Lamellar Block Copolymer Nanopatterning Directed by Graphoepitaxially Assembled Cylinder Nanopatterns. *J. Mater. Chem.* **2012**, *22*, 6307.

(3) Ruiz, R.; Sandstrom, R. L.; Black, C. T. Induced Orientational Order in Symmetric Diblock Copolymer Thin Films. *Adv. Mater.* **2007**, *19*, 587–591.

(4) Kim, E.; Shin, C.; Ahn, H.; Ryu, D. Y.; Bang, J.; Hawker, C. J.; Russell, T. P. Size Control and Registration of Nano-Structured Thin Films by Cross-Linkable Units. *Soft Matter* **2008**, *4*, 475–479.

(5) Jung, H.; Hwang, D.; Kim, E.; Kim, B.; Lee, W. B.; Poelma, J. E.; Kim, J.; Hawker, C. J.; Huh, J.; Ryu, D. Y.; *et al.* Three-Dimensional Multilayered Nanostructures with Controlled Orientation of Microdomains from Cross-Linkable Block Copolymers. *ACS Nano* **2011**, *5*, 6164–6173.

(6) Jeong, J. W.; Park, W. I.; Do, L.-M.; Park, J.-H.; Kim, T.-H.; Chae, G.; Jung, Y. S. Nanotransfer Printing with Sub-10nm Resolution Realized Using Directed Self-Assembly. *Adv. Mater.* **2012**, *24*, 3526–3531.

(7) Tavakkoli K G, A.; Nicaise, S. M.; Gadelrab, K. R.; Alexander-Katz, A.; Ross, C. a; Berggren, K. K. Multilayer Block Copolymer Meshes by Orthogonal Self-Assembly. *Nat. Commun.* **2016**, *7*, 10518.

(8) Jin, C.; Olsen, B. C.; Wu, N. L. Y.; Luber, E. J.; Buriak, J. M. Sequential Nanopatterned Block Copolymer Self-Assembly on Surfaces. *Langmuir* **2016**, *32*, 5890–5898.

(9) Garnier, J.; Arias-Zapata, J.; Marconot, O.; Arnaud, S.; Böhme, S.; Girardot, C.; Buttard, D.; Zelsmann, M. Sub-10nm Silicon Nanopillar Fabrication Using Fast and Brushless Thermal Assembly of PS-B-PDMS Diblock Copolymer. *ACS Appl. Mater. Interfaces* **2016**.

(10) Son, J. G.; Hannon, A. F.; Gotrik, K. W.; Alexander-Katz, A.; Ross, C. A. Hierarchical Nanostructures by Sequential Self-Assembly of Styrene-Dimethylsiloxane Block Copolymers of Different Periods. *Adv. Mater.* **2011**, *23*, 634–639.

(11) Tanaka, H.; Hasegawa, H.; Hashimoto, T. Ordered Structure in Mixtures of a Block Copolymer and Homopolymers. 1. Solubilization of Low Molecular Weight Homopolymers. *Macromolecules* **1991**, 240–251.

(12) Hashimoto, T.; Tanaka, H.; Hasegawa, H. Ordered Structure in Mixtures of a Block Copolymer and Homopolymers. 2. Effects of Molecular Weights of Homopolymers. *Macromolecules* **1990**, 4378–4386.

(13) Yang, J.; Wang, Q.; Yao, W.; Chen, F.; Fu, Q. Effect of Added Homopolymer on Structures of Thin Films of PS-B-PDMS/PS Mixture under Solvent Vapor Annealing. *Appl. Surf. Sci.* **2011**, *257*, 4928–4934.

(14) Shin, D. O.; Mun, J. H.; Hwang, G.-T.; Yoon, J. M.; Kim, J. Y.; Yun, J. M.; Yang, Y.-B.; Oh, Y.; Lee, J. Y.; Shin, J.; *et al.* Multicomponent Nanopatterns by Directed Block Copolymer Self-Assembly. *ACS Nano* **2013**, *7*, 8899–8907.

(15) Mansky, P.; Russell, T. P.; Hawker, C. J.; Mays, J.; Cook, D. C.; Satija, S. K. Interfacial Segregation in Disordered Block Copolymers : Effect of Tunable Surface Potentials. *Phys. Rev. Lett.* **1997**, *79*, 237–240.

(16) Zhang, X.; Harris, K. D.; Wu, N. L. Y.; Murphy, J. N.; Buriak, J. M. Fast Assembly of Ordered Block Copolymer Nanostructures through Microwave Annealing. *ACS Nano* **2010**, *4*, 7021–7029.

(17) Majewski, P.; Yager, K. Millisecond Ordering of Block Copolymer Films via Photothermal Gradients. *ACS Nano* **2015**.

(18) Farrell, R. a.; Petkov, N.; Shaw, M. T.; Djara, V.; Holmes, J. D.; Morris, M. a. Monitoring PMMA Elimination by Reactive Ion Etching from a Lamellar PS- B -PMMA Thin Film by Ex Situ TEM Methods. *Macromolecules* **2010**, *43*, 8651–8655.

(19) Ting, Y.-H.; Park, S.-M.; Liu, C.-C.; Liu, X.; Himpsel, F. J.; Nealey, P. F.; Wendt, A. E. Plasma Etch Removal of Poly(methyl Methacrylate) in Block Copolymer Lithography. *J. Vac. Sci. Technol. B Microelectron. Nanom. Struct.* **2008**, *26*, 1684.

(20) Yamamoto, H.; Imamura, T.; Omura, M.; Sakai, I.; Hayashi, H. Selective Etch of Poly (Methyl Methacrylate) in Block Copolymer Based on Control of Ion Energy and Design of Gas Chemistry for Directed Self Assembly Lithography of Ion Energy and Design of Gas Chemistry for Directed Self Assembly Lithography. *Japan Soc. Appl. Phys.* **2014**, *53*, 03DD03 (4 pp).

(21) Bezard, P. Développement de Procédés de Gravure Plasma Innovants pour les Technologies Sub-14nm par Couplage de la Lithographie Conventionnelle avec l'Approche Auto-Alignée par Copolymère à Blocs, **2016**.

(22) Liu, C.-C.; Nealey, P. F.; Ting, Y.-H.; Wendt, A. E. Pattern Transfer Using Poly(styrene-Block-Methyl Methacrylate) Copolymer Films and Reactive Ion Etching. *J. Vac. Sci. Technol. B Microelectron. Nanom. Struct.* **2007**, *25*, 1963.

(23) Gharbi, A.; Tiron, R.; Pimenta Barros, P.; Argoud, M.; Servin, I.; Chevalier, X.; Nicolet, C.; Navarro, C. PMMA Removal Options by Wet Development in PS-B-PMMA Block Copolymer for Nanolithographic Mask Fabrication. *J. Vac. Sci. Technol. B, Nanotechnol. Microelectron. Mater. Process. Meas. Phenom.* **2015**, *33*, 051602.

(24) Thurn-albrecht, B. T.; Steiner, R.; Derouchey, J.; Stafford, C. M.; Huang, E.; Bal, M.; Tuominen, M.; Hawker, C. J.; Russell, T. P. Nanoscopic Templates from Oriented Block Copolymer Films. *Adv. Mater.* **2000**, *12*, 787–791.

(25) Xu, T.; Stevens, J.; Villa, J. a.; Goldbach, J. T.; Guarini, K. W.; Black, C. T.; Hawker, C. J.; Russell, T. P. Block Copolymer Surface Reconstuction: A Reversible Route to Nanoporous Films. *Adv. Funct. Mater.* **2003**, *13*, 698–702.

(26) Kim, S. H.; Misner, M. J.; Yang, L.; Gang, O.; Ocko, B. M.; Russell, T. P. Salt Complexation in Block Copolymer Thin Films. *Macromolecules* **2006**, *39*, 8473–8479.

(27) Cummins, C.; Ghoshal, T.; Holmes, J. D.; Morris, M. a. Strategies for Inorganic Incorporation Using Neat Block Copolymer Thin Films for Etch Mask Function and Nanotechnological Application. *Adv. Mater.* **2016**.

(28) George, S. Atomic Layer Deposition: An Overview. *Chem. Rev.* **2009**, 111–131.

(29) Gay, G.; Baron, T.; Agraffeil, C.; Salhi, B.; Chevolleau, T.; Cunge, G.; Grampeix, H.; Tortai, J.-H.; Martin, F.; Jalaguier, E.; *et al.* CMOS Compatible Strategy Based on Selective Atomic Layer Deposition of a Hard Mask for Transferring Block Copolymer Lithography Patterns. *Nanotechnology* **2010**, *21*, 435301.

(30) Tallegas, S.; Baron, T.; Gay, G.; Aggrafeil, C.; Salhi, B.; Chevolleau, T.; Cunge, G.; Bsiesy, A.; Tiron, R.; Chevalier, X.; *et al.* Block Copolymer Technology Applied to Nanoelectronics. *Phys. Status Solidi* **2013**, *10*, 1195–1206.

(31) Moon, H.-S.; Kim, J. Y.; Jin, H. M.; Lee, W. J.; Choi, H. J.; Mun, J. H.; Choi, Y. J.; Cha, S. K.; Kwon, S. H.; Kim, S. O. Atomic Layer Deposition Assisted Pattern Multiplication of Block Copolymer Lithography for 5nm Scale Nanopatterning. *Adv. Funct. Mater.* **2014**, *24*, 4343–4348.

(32) Schelhas, L. T.; Farrell, R. a.; Halim, U.; Tolbert, S. H. Directed Self-Assembly as a Route to Ferromagnetic and Superparamagnetic Nanoparticle Arrays. *Adv. Funct. Mater.* **2014**, *24*, 6956–6962.

(33) Peng, Q.; Tseng, Y.-C.; Darling, S. B.; Elam, J. W. Nanoscopic Patterned Materials with Tunable Dimensions via Atomic Layer Deposition on Block Copolymers. *Adv. Mater.* **2010**, *22*, 5129–5133.

(34) Son, J. G.; Bae, W. K.; Kang, H.; Nealey, P. F.; Char, K. Placement Control of Nanomaterial Arrays on Surface-Reconstructed Block Copolymer Thin Films. *ACS Nano* **2009**, *3*, 3927–3934.

(35) Cummins, C.; Gangnaik, A.; Kelly, R. a; Borah, D.; O'Connell, J.; Petkov, N.; Georgiev, Y. M.; Holmes, J. D.; Morris, M. a. Aligned Silicon Nanofins via the Directed Self-Assembly of PS-B-P4VP Block Copolymer and Metal Oxide Enhanced Pattern Transfer. *Nanoscale* **2015**, *7*, 6712–6721.

(36) Cummins, C.; Gangnaik, A.; Kelly, R. A.; Hydes, A. J.; O'Connell, J.; Petkov, N.; Georgiev, Y. M.; Borah, D.; Holmes, J. D.; Morris, M. A. Parallel Arrays of Sub-10nm Aligned Germanium Nanofins from an In Situ Metal Oxide Hardmask Using Directed Self-Assembly of Block Copolymers. *Chem. Mater.* **2015**, *27*, 6091–6096.

(37) Chaudhari, A.; Ghoshal, T.; Shaw, M. T.; O'Connell, J.; Kelly, R. A.; Glynn, C.; O'Dwyer, C.; Holmes, J. D.; Morris, M. A. Fabrication of MoS2 Nanowire Arrays and Layered Structures via the Self-Assembly of Block Copolymers. *Adv. Mater. Interfaces* **2016**, *3*, 1500596 (9 pp).

(38) Huang, E.; Rockford, L.; Russell, T. P.; Hawker, C. J. Nanodomain Control in Copolymer Thin Films. *Nature* **1998**, *395*, 1–2.

(39) Darling, S. B. Mechanism for Hierarchical Self-Assembly of Nanoparticles on Scaffolds Derived from Block Copolymers. *Surf. Sci.* **2007**, *601*, 2555–2561.

(40) Darling, S. B.; Yufa, N. A.; Cisse, A. L.; Bader, S. D.; Sibener, S. J. Self-Organization of FePt Nanoparticles on Photochemically Modified Diblock Copolymers Templates. *Adv. Mater.* **2005**, *17*, 2446–2450.

(41) Bhoje Gowd, E.; Nandan, B.; Vyas, M. K.; Bigall, N. C.; Eychmüller, A.; Schlörb, H.; Stamm, M. Highly Ordered Palladium Nanodots and Nanowires from Switchable Block Copolymer Thin Films. *Nanotechnology* **2009**, *20*, 415302.

(42) Cummins, C.; Borah, D.; Rasappa, S.; Chaudhari, a.; Ghoshal, T.; O'Driscoll, B. M. D.; Carolan, P.; Petkov, N.; Holmes, J. D.; Morris, M. a. Self-Assembly of Polystyrene-Block-poly(4-Vinylpyridine) Block Copolymer on Molecularly Functionalized Silicon Substrates: Fabrication of Inorganic Nanostructured Etchmask for Lithographic Use. *J. Mater. Chem. C* **2013**, *1*, 7941.

(43) Hansen, C. M. *Hansen Solubility Parameters*; **2008**.

(44) Ghoshal, T.; Maity, T.; Godsell, J. F.; Roy, S.; Morris, M. a. Large Scale Monodisperse Hexagonal Arrays of Superparamagnetic Iron Oxides Nanodots: A Facile Block Copolymer Inclusion Method. *Adv. Mater.* **2012**, *24*, 2390–2397.

Conclusion and Perspectives

This thesis explored the capabilities of directed self-assembly (DSA) of cylindrical Poly(styrene)-b-Poly(dimethylsiloxane) (PS-b-PDMS) as a potential next-generation nanopatterning technique. Since the beginning of microelectronic industry, with the invention of integrated circuits, the technology progress was tremendous. Ever smaller transistors are built, increasing evermore the performance of chips. However, conventional photolithography, which has been for decades the key technique for micro and nanopatterning, is reaching its physical limit. Therefore, alternative nanopatterning techniques are desperately needed in order to keep the technology progress up. Block-copolymers (BCP) that have the unique ability to self-assembly into ordered structure seem to be a promising candidate to be used in future patterning techniques. Block copolymer with high incompatibility between their blocks exhibit a high Flory-Huggins interaction parameter χ and are capable of attaining feature sizes of a few nanometers. PS-b-PDMS has a relatively high χ parameter and, due to its very good etching properties, high resolution silicon structures can be obtained. However, in order to implement high-χ block copolymers in industry, reliable processes that meet the requirements of manufacturing standards, have to be established. During this thesis standard techniques and processes that are used today in research laboratories have been investigated and optimized in order to propose industry-compatible processes.

After having described the context of this topic in chapter 1, in chapter 2 we have seen that PS-b-PDMS (M_n = 45kg/mol, called here SD45) can be directed to self-assemble in graphopepitaxy stacks, that are currently used in 193 nm conventional photolithography processes, via solvent vapor annealing (SVA). The obtained guiding trenches are composed of silicon anti reflective coating (SiArc)/Spin-on-Carbon (SOC) layers whose depth was found to be crucial for self-assembly. Too deep trenches lead to a loss of self-assembly control and the obtained PDMS lines show fingerprint orientation. If the trench depth is close to the natural period on the other hand, large area, nicely aligned PDMS cylinders could be obtained after solvent vapor annealing in toluene. Nonetheless, toluene is a toxic solvent that could be complicated to be introduced into industry production lines. Therefore the annealing of SD45 with several “safe” solvents has been investigated in respect to vapor pressure and selectivity of the solvents. The selectivity dictates the morphology, while the ordering of the obtained structure was proven to depend mainly on the vapor pressure of the solvent. For SD45, high vapor pressures lead to cylinders without long range order, while the quality of the cylinders depends on the selectivity. Low vapor pressure solvents have the capability to align SD45 in long range order, while the selectivity changes the morphology from perforated lamellar, passing through the cylindrical state, to the spherical state. Higher vapor pressures, above a certain threshold, were found to lead to the same morphologies but with a loss in ordering. We were able to create a cartography of safe solvents for PS-b-PDMS which allows choosing desired morphology and adapt alignment quality via vapor pressure.

Further *in-situ* grazing incidence small angle X-ray scattering (GISAXS) measurements were performed at the European Synchrotron Radiation Facility (ESRF) in order to gain insight in the phase separation kinetics. During solvent vapor annealing in PGMEA, a change of the natural domain spacing could be observed by GISAXS analysis. However, due to safety restriction, decomposition of the BCP layer under X-ray beam and beam availability time restriction, the obtained results could not be exploited in-depth to obtain fully significant results.

Finally the line edge roughness of SD45 has been analyzed. As the scaling down of feature sizes continues, the line edge roughness has more and more impact of the final device performances. High line edge roughness (LER) and line width roughness (LWR) values are known to have a great impact on the device performances, which is why the International Technology Roadmap for Semiconductors (ITRS) set requirements of the 3σ roughness to be smaller than 8% of the line width. Line edge roughness were found to be 3.4 nm on a mean critical dimension of 27 nm (12 %) and LWR were as low as 2 nm (7 %). These values might be slightly too high with respect to the ITRS requirements but it is suggested that roughness of guiding trenches has a great impact on the BCP roughness. Several methods have been proposed to smooth guiding trenches roughness which will likely reduce the roughness of the BCP, too.

In the third chapter a method was presented that makes phase separation of high-χ BCPs possible without solvent vapor annealing. SVA is, as described, a complicated procedure that is unlikely to be used in industrial environment subjected to very strict rules in terms of health and safety. Thermal annealing remains the simplest method for self-assembly of BCPs but has to be optimized especially in terms of annealing duration that has to be compatible with industrial process throughput. PS-selective plasticizers have been introduced into the PS-b-PDMS solution before spin-coating and its influence on the BCP has been studied. As the plasticizer and the solvent, propylene glycol monomethyl ether acetate (PGMEA), are PS-selective, PS-b-PDMS forms micelles in solution. During spin-coating, enough mobility can be maintained due to the low vapor pressure of the plasticizers, even after solvent evaporation. That way, well arranged micelles are obtained right after spin. This already organized state is advantageous for the subsequent annealing step. The added plasticizer reduces sufficiently the diffusive energy barrier to obtain well aligned cylinders in only 30s of thermal annealing. Large area alignment could be obtained by directing the self-assembly in SiArc/SOC trenches. This process avoids solvent vapor annealing completely and decreases process time by at least a factor of 1000 when comparing to thermal annealing of high-χ, high-N BCPs without added plasticizers. Finally, as a proof of concept, the process was applied on a full 300 mm Si wafer. In this way, we have demonstrated a practical method of DSA that is actually realizable on industrial manufacturing tools.

The 4th chapter deals with more aggressive resolutions of PDMS feature sizes. A low molecular weight PS-b-PDMS, (M_w=16kg/mol, here called SD16) was investigated in terms of surface wetting and phase separation behavior. Two different graphoeptiaxy templates have been used. The first is composed entirely of bare Si substrate, where, via 193 nm lithography, trenches of varying sizes can be obtained. In this case the application of a PS-brush was necessary in order to prevent the wetting of the PDMS block at the BCP/silicon substrate interface. Since low molecular weight BCP have faster kinetics and higher chain mobility, a short annealing in solvent vapor, followed by thermal annealing, was shown to be sufficient for phase separation and long range order. As previously explained, SVA is unsuitable for mass production on full 300mm wafers. Therefore, the best option is to avoid SVA and use only thermal annealing. The SiArc/SOC trenches that were also tested for the DSA of SD16, were demonstrated to be able to retain solvent from the deposition by spin-coating. Later, during thermal annealing, this stocked solvent can then evaporate by diffusing through the BCP and participate in the phase separation of the BCP. That way, thermal annealing alone was enough to obtain long range ordered PDMS cylinders. Finally, the line edge roughness of with SD16 obtained nanopatterns was investigated and found to be relatively more important than that of SD45. Since the feature size is smaller, the roughness induced by the lithography templates is comparatively more important. However, on the basis of our various investigations, we are confident that this value can be decreased by smoothening techniques on the graphoepitaxy templates.

In chapter 5 we discussed the pattern transfer of the obtained nanostructures by plasma etching. Because of the variety of nanopatterns obtained by BCP's DSA process on various types of underlayers, several plasma ignition types and chemistries have been investigated. Etching processes with pulsed plasma of HBr/O_2, continuous wave (CW) plasma of $SF_6/CHF_3/Ar$ and CW plasma of $HBr/He\text{-}O_2$ were developed inside industrial standard reactors and their performances were evaluated by morphological analysis. Pulsed plasma was efficient for nanopatterns aligned on thick layers of SOC, as the etch mask is sufficiently high to compensate for low selectivity between Si and SOC etch. Extremely high aspect ratio features of up to 90 nm height and 15 nm width could be obtained. However, the CD control was shown to be rather low on thick SOC layers, as the nanostructures lose 20% of their initial thickness during the revelation step, where PS matrix and SOC layer are etched away. The obtained mask lines have then an aspect ratio of 3.6:1 which causes them partly to collapse, probably causing low reproducibility of the process. When reducing the thickness of the SOC layer, which is necessary for the good alignment of the BCP, the HBr/O_2 plasma is not selective enough and $SF_6/CHF_3/Ar$ was found to yield better results that were highly anisotropic with virtually no slope. Aspect ratio were reasonable of ≈2:1.

The transfer etching of SD16 was confirmed to be more challenging because of the extreme small PDMS etch mask of 10 nm width and only 6 nm height. After a first transfer into the SOC layer, the patterns were

shown to collapse due to the high aspect ratio (≈2:1) and extreme high density of lines. This phenomenon could be minimized by performing the whole etching process in one step, without exposing the samples to ambient pressure between PDMS revelation and the real transfer step. It is believed that humidity from the environment could be introduced into the SOC layer when retreating the sample from the vacuum chamber and being responsible of such modifications. HBr/O_2 plasma was not selective enough and did not show any satisfactory results for SD16. $SF_6/CHF_3/Ar$ etching however achieved to etch anisotropic silicon lines with an aspect ratio of ≈3:1. For a future application of SD16 in, for example, finFETs, SD16 was deposited on SOI substrates, where PDMS masks are transferred directly into a Si layer, without using any transfer layer. During this study, the 300 mm etch reactor used for pulsed HBr/O2 etching was unavailable which is why a third etching recipe, continuous wave $HBr/He\text{-}O_2$, was investigated. Here, where PDMS cylinders were deposited on only 3 nm thick PS-brush, the CW mode etching was less critical than on SiArc/SOC layers and 10 nm wide Si nanofins laying on silicon dioxide are obtained. These are promising results for a potential finFET application of BCP on SOI.

Chapter 6 regroups two innovative approaches for DSA of BCPs that extend the classical approach of directed self-assembly. In the first, multiple patterning of SD16 and SD45 leads to hierarchical, complex nanostructures that could be used for example in photovoltaic, LEDs or bit-patterned media. We assembled first cylinders of SD45 on graphoepitaxy templates and added as a second layer dot forming SD45. The difference in morphology was obtained by changing the annealing solvent from toluene, for cylinder formation, to PGMEA, for dot formation. The first layer acts then as a graphoepitaxy template for the second layer of PS-b-PDMS. Nanomesh like structures were obtained in which the dots oriented themselves perfectly in the cylinder template. The same structure could be obtained with SD16. Dot formation was here obtained by adding PS-homopolymer brush to the SD16 solution. It was found out that the roughness of the templating lines had great influence on the position of the second layer of dots. The second layer dots arranged themselves on top or between the templating lines, depending on the relative distance between these lines. When using SD45 cylinders as template for SD16 cylinders, the smaller cylinders aligned themselves, again perfectly in the templating lines. This multipatterning approach leads to a density multiplication and the controlled alignment of different structures, by using only one single photolithography step. Especially small period BCPs can profit from this phenomenon and large scale sub 10 nm arrangement for lithography applications can be obtained. Furthermore, our process shows no PDMS interlayer between the BCP layers or at the substrate/BCP interface. The transfer etching of these features should thus be accessible via etching processes like those presented in chapter 5. It is imaginable that this double patterning could be increased to multipatterning, obtaining three dimensional structures that could be used for interconnections or vias in the IC manufacturing.

The other innovative approach presented in the second part of chapter 6 deals with metal salt inclusion into conventional PS-b-PMMA BCP systems. Due to the poor etch selectivity of low-χ BCP, PS-b-PMMA is often not suitable for certain IC manufacturing processes. By integrating metal oxides into one of the blocks, the selectivity is significantly increased and these BCP can be transferred more easily into the underlying functional material. Low-χ BCP are limited in resolution but show interesting properties and are particularly well understood compared to some exotic high-χ BCPs, which is why the transfer etch of these BCP is interesting. Furthermore, this process could later be translated to other BCPs systems, which could be interesting especially for high-χ, low-N BCP, that are very challenging to be transferred in the substrate as seen in chapter 5. We chose to work with a straightforward spin-coating infiltration technique. PS-b-PMMA is first self-assembled via thermal annealing on polymer brush coated silicon substrates. The BCP layer is then exposed to ethanol vapor, which was observed to swell the PMMA block. PMMA is "reconstructed" leading to nanoporous structures in which iron salt can be introduced. The iron salt solution is then spin-coated on the reconstructed PS-b-PMMA, selectively integrating only the PMMA sites. The sample is then directly exposed to O_2 plasma in order to remove the remaining organic polymer and oxidize iron nitrate to iron oxide. Iron oxide is a robust etch mask for pattern transfer into silicon. On plane silicon, were the iron oxide was deposited directly in the BCP layer with no transfer layer, patterns of 35 nm height could be obtained. When deposited on SOC layers, the etch mask thickness is enhanced due to the SOC transfer layer and could possibly be transferred into the substrate with higher aspect ratio.

Future works on the directed self-assembly of PS-b-PMDS include a more detailed understanding of the mechanism of blending the BCP with plasticizers. *In-situ* GISAXS measurements of the spin coating process, could give valuable detailed knowledge about the mechanisms leading to an ordered arrangement of microdomains. The developed process could be used either right after spin for bit-patterned media or after ultra-fast annealing for lithography applications. Also, the blending with plasticizers could be expanded to other BCP systems and especially to smaller molecular weight BCPs. Ultra-small features on full-300mm wafers could thus be obtained within compatible industry processing time. Therefore the spin-coating process on 300 mm wafers should be further optimized in order to avoid thickness undulations. Before an implementation of PS-b-PDMS in microelectronics industry, though, a thorough, statistical analysis of line width roughness is crucial. Along with downscaling, the specifications concerning the dimensional control become more and more important and more and more restricted. Calibrated CD-SEM measurement will be here necessary in order to evaluate definitely the feasibility of DSA in microelectronics industry.

More in general it can be concluded that high-χ BCP present a promising route for future downscaling of integrated circuit feature sizes but a lot of work and understanding has to be undertaken before they can be implemented in real industrial environment. PS-b-PDMS has good etching resistance but as described,

when etched in oxygen plasma, it can create severe roughness which is problematic for IC integration, especially in the sub 10 nm region. Therefore, other high-χ materials that do not contain PDMS, like Polylactic acid (PLA) based or completely new BCPs, could be a better option for industry integration. When designing purely organic BCPs however, it has to be taken into account that a lack of etch selectivity has to be compensated, by for example using sequential infiltration synthesis (SIS).

Decreasing further the feature size means decreasing likewise the mask thickness, since both quantities scale with the BCP domain size. The thinner the etch mask, the smaller the etch resistance. Therefore, lamellar morphology should be preferred over cylindrical morphology for finFET fabrication for example. The thickness of vertical lamellar can be chosen individually high, showing thus a strong advantage for pattern transfer. However, today, the vertical orientation is difficult to achieve especially for high-χ BCP, which is why a lot of progress has to be made in terms of surface treatment.

Furthermore, for industry, the nanofins density on one wafer has to be as high as possible. When using graphoepitaxy templates, considerable space of the wafer is occupied by the guiding lines which have no use in the later process. Therefore, chemoepitaxy, where no space is wasted, should be improved in order to achieve higher density multiplication.

In the last decade, tremendous progress in the understanding and controlling of BCP self-assembly has been made. Although there are still a lot of challenges to be overcome, continuing the research promises an interesting future for the DSA of BCPs.

Résumé en Français

Cette thèse a exploré les capacités de l'auto-assemblage du Poly(styrène)-b-Poly(dimethylsiloxane) (PS-b-PDMS) cylindrique comme nouvelle technique de nanostructuration. Depuis le début de l'industrie microélectronique, avec l'invention des circuits intégrés, les progrès de cette technologie ont été énormes. Des transistors avec des tailles de plus en plus petites ont été construits, en augmentant toujours les performances des puces. Cependant, la photolithographie classique, qui est la technique clé pour la micro et nanostructuration, atteint aujourd'hui ses limites physiques en terme de résolution. Par conséquent, des techniques de nanostructuration alternatives, dont l'industrie a désespérément besoin afin de maintenir le rythme de l'avancement des performances, sont recherchées. Les copolymères à blocs (CPB), qui ont la capacité unique de s'auto-assembler en nanostructures ordonnées, semblent être des candidats prometteurs pour être utilisés comme future technique de lithographie. Les copolymères à blocs avec une forte incompatibilité entre leurs blocs, présentant un paramètre d'interaction de Flory-Huggins, χ, élevé, sont capables d'atteindre des tailles caractéristiques de quelques nanomètres. Le PS-b-PDMS a un paramètre χ relativement élevé et a de très bonnes propriétés de gravure. Des structures de silicium à haute résolution peuvent donc être obtenues. Toutefois, afin de mettre en œuvre des copolymères à blocs de haut χ dans l'industrie, des processus fiables qui répondent aux exigences des normes de fabrication doivent être établis. Au cours de cette thèse, les techniques et procédés standards qui sont utilisés aujourd'hui dans les laboratoires de recherche ont été étudiés et optimisés afin de proposer des procédés compatibles avec les contraintes de l'industrie.

Dans le chapitre 2, nous avons vu que le PS-b-PDMS (SD45, M_w = 45 kg / mol) peut être auto-organisé à longue portée grâce à la graphopepitaxie. Les motifs de guidage utilisés, fabriqués par photolithographie « 193 nm », sont composés de couches silicon anti reflective coating (SiArc) / Spin-on-Carbon (SOC) typiquement utilisés dans l'industrie. La profondeur de ces tranchées est cruciale pour l'auto-organisation. Des tranchées trop profondes conduisent à une perte de contrôle de l'auto-assemblage et les cylindres de PDMS sont organisés à courte portée. En revanche, si la profondeur des tranchées est proche de la période naturelle du CPB, des cylindres de PDMS bien alignés à grande portée peuvent être obtenus après le recuit sous vapeur de toluène. Néanmoins, le toluène est un solvant toxique qui est aujourd'hui proscrit des lignes de production industrielles. Par conséquent, le recuit du SD45 avec plusieurs solvants non-toxique a été étudié. Plus précisément, nous avons étudié l'influence de la pression de vapeur et de la sélectivité des solvants sur la séparation des phases du CPB. Il a été trouvé que la sélectivité induit une certaine morphologie, alors que la pression de vapeur du solvant influence le degré d'organisation des structures. Pour le SD45, des pressions de vapeur élevées conduisent à des cylindres sans ordre à longue distance, tandis que dans ce cas la qualité des cylindres dépend de la sélectivité du solvant. Des pressions de vapeur faible ont la capacité d'aligner le SD45 à longue distance, tandis que la sélectivité change la morphologie,

avec des structures en lamellaires perforées, cylindrique et sphériques. Au-delà d'un certain seuil de pression de vapeur, des morphologies identiques sont obtenues mais avec une perte d'alignement. Avec ces résultats, nous avons pu créer une cartographie des solvants non-toxiques avec lesquels il est possible de choisir une morphologie désirée et d'adapter la qualité de l'alignement par la pression de vapeur.

En outre des mesures de la diffusion des rayons X à l'incidence rasante (GISAXS) *in-situ* ont été réalisées à l'European Synchrotron Radiation Facility (ESRF) à Grenoble afin de mieux comprendre la séparation de phases de CPB. Pendant le recuit sous vapeur de PGMEA, un changement de la période a pu être observé, mais, en raison de restrictions de sécurité, de la décomposition de la couche CPB et de l'évaporation du solvant sous faisceau de rayons X et de limites de temps, les résultats obtenus n'ont pas mené à des conclusions significatives.

Enfin, la rugosité des lignes de SD45 a été analysée. Avec la diminution des tailles de motifs, la rugosité de bord de lignes devient de plus en plus critique. Des hautes valeurs de rugosités de bords de lignes (LER) et de largeurs de lignes (LWR) sont connues pour avoir un impact très important sur les performances des dispositifs, ce qui explique pourquoi l'International Technology Roadmap for Semiconductors (ITRS) exige une rugosité 3σ inférieure à 8% de la largeur de la ligne. Dans cette thèse, pour le SD45, une LER de 3,4 nm, sur une dimension critique moyenne de 27 nm (12%), et une LWR de 2 nm (7%) ont été trouvées. Ces valeurs semblent être légèrement trop élevées pour les industriels, mais il est suggéré que la rugosité des tranchées de guidage impacte la rugosité des lignes de CPB. Plusieurs méthodes ont été proposées pour lisser les lignes de guidage et donc très certainement baisser la rugosité des lignes de CPB.

Dans le troisième chapitre, un procédé a été présenté qui permet d'auto-organiser des CPB à haut χ sans l'utilisation d'un recuit sous vapeurs de solvant (RVS). En effet, ce type de recuit est une procédure compliquée qui est peu susceptible d'être utilisée dans l'industrie. Le recuit thermique reste la méthode la plus simple pour l'auto-assemblage de CPB. Dans la perspective de s'affranchir du recuit sous vapeur de solvant, des plastifiants sélectifs au bloc PS ont été introduits dans la solution de PS-b-PDMS. L'influence de ces plastifiants sur l'auto-organisation du CPB a été étudiée. Parce que le plastifiant et le solvant (propylène glycol mono méthyl éther acétate - PGMEA) sont sélectifs pour le bloc PS, le PS-b-PDMS forme des micelles en solution. Après l'étape de dépôt du polymère par centrifugation et l'évaporation du solvant, une mobilité importante peut être maintenue en raison de la faible pression de vapeur des plastifiants et des structures hexagonales compactes de sphères sont alors obtenues. Cet état déjà très organisé est avantageux pour l'éventuelle étape suivante du recuit et le plastifiant ajouté réduit également très certainement la barrière énergétique de diffusion dans le matériau. Ainsi, des cylindres bien alignés en seulement 30s de recuit thermique ont pu être obtenus sur surface plane et dans des tranchées de SiArc/SOC. Ce procédé évite complètement le recuit sous vapeurs de solvant et réduit le temps de recuit au moins d'un facteur 1000

comparé à un recuit thermique d'un CPB de haut χ et haut N sans plastifiants. Enfin, pour preuve de concept, ce procédé a été appliqué sur une pleine plaque de silicium de 300 mm de diamètre. De cette façon, nous avons démontré une méthode pratique de DSA qui est effectivement réalisable comme processus de fabrication industrielle.

Le 4ième chapitre traite d'un polymère PS-b-PDMS avec une résolution plus agressive car de plus faible masse moléculaire, (SD16, M_w = 16 kg / mol). Ce matériau a été étudié en termes de mouillage de surface et de séparation de phase. Deux substrats de graphoeptiaxie différents, réalisés par lithographie « 193 nm », ont été utilisés. Le premier, en silicium massif, présente des tranchées de différentes tailles et sa surface est traitée par application d'une brosse de PS, nécessaire afin d'éviter le mouillage du bloc PDMS à l'interface CPB/substrat. Les CPB de plus faible poids moléculaire ont une cinétique plus rapide et une mobilité des chaînes plus grande, c'est pourquoi un court recuit sous vapeur de solvant, suivi d'un recuit thermique, suffi pour générer la séparation de phases et l'ordre à grande distance. Cependant, comme expliqué précédemment, le RVS n'est pas pratique pour la production de masse, par exemple sur des plaques de 300 mm de diamètre. Par conséquence, la meilleure option est d'éviter le RVS et d'utiliser uniquement un recuit thermique. En utilisant des tranchées SiArc/SOC, nous avons montré qu'un recuit thermique seul était efficace pour générer l'auto-organisation du polymère. Ceci est certainement dû au fait que ce substrat est capable de retenir du solvant lors de l'étalement de la résine par centrifugation. Ainsi, au cours du recuit, le solvant stocké dans la couche SOC peut diffuser à travers le CPB et favoriser la séparation des phases. De cette façon, un recuit thermique de 15 min a été suffisant pour obtenir des cylindres couchés ordonnés à longue portée. Enfin, la rugosité de ligne du SD16 a été étudiée. Le ratio de rugosité par rapport à la période du CPB est plus important que dans le cas du SD45. Étant donné la plus petite taille caractéristique du SD16, la rugosité induite par les motifs lithographiés est relativement plus importante. Nous sommes convaincus que cette valeur peut être diminuée en lissant les motifs de graphoepitaxie avec des traitements thermiques ou plasma.

Dans le chapitre 5, nous discutons du transfert des nanostructures par gravure plasma. Plusieurs méthodes ont été étudiées: plasma pulsé de HBr/O_2, plasma continu de $SF_6/CHF_3/Ar$ et plasma continu de HBr / He-O_2. Le plasma pulsé a produit des bons résultats pour les échantillons alignés sur des couches de SOC épaisses. Dans ce cas le masque de gravure est suffisamment épais pour compenser la sélectivité réduite du Si à par rapport au masque PDMS/SOC. Des rapports d'aspect extrêmement élevés allant jusqu'à 6 (90 nm de hauteur et 15 nm de largeur) ont pu être obtenus. Toutefois, le contrôle des dimensions critiques (CD) et la reproductibilité sont plutôt faibles sur des couches de SOC épaisses à cause du fort facteur d'aspect du masque (3,6:1), qui peut entrainer l'effondrement de celui-ci par endroit, et de la sélectivité réduite, qui dégrade rapidement le très fin masque de PDMS. En réduisant l'épaisseur de la couche de SOC, ce qui est

nécessaire pour le bon alignement du CPB (comme observé dans le chapitre 2), un plasma continu plus sélectif à base de $SF_6/CHF_3/Ar$ a montré des meilleurs résultats. Des nanostructures extrêmement anisotrope, avec un rapport d'aspect de ≈2:1 et pratiquement sans pente ont été obtenues six fois plus vite qu'en plasma pulsé.

Le transfert par gravure de lignes plus résolues (SD16) est encore plus difficile car les motifs de PDMS sont extrêmement petits, avec une largeur de 10 nm et une hauteur de seulement 6 nm. Après un premier transfert dans la couche de SOC, un effondrement des motifs en raison du fort rapport d'aspect et de la forte densité est généralement observé. Ce phénomène a pu être réduit en traitant les échantillons en une seule étape de gravure, sans les exposer à la pression ambiante entre la révélation et le transfert de motifs. On suppose que l'exposition de l'échantillon à l'humidité ambiante pourrait modifier les propriétés mécaniques de la couche de SOC et également faire apparaitre des forces capillaires entre les nanostructures qui pourraient causer leur écroulement. La relaxation d'un stress mécanique intrinsèque au SOC après gravure pourrait également amplifier à ce phénomène.

En ce qui concerne le transfert de motif, le plasma pulsé HBr/O_2 n'a pas montré de résultats satisfaisants pour le SD16, ce qui était sans surprise car le SD16 est aligné sur des couches de SOC relativement épaisses pour cette résolution. La gravure avec le procédé $SF_6/ CHF_3/Ar$ est nettement plus satisfaisante et des lignes de silicium anisotropes avec un rapport d'aspect de ≈3:1 ont été obtenues. Pour une application future de SD16, par exemple pour la fabrication de FinFETs, le SD16 a été déposé sur des substrats silicon-on-insulator (SOI). Le masque de PDMS est alors transféré directement dans la couche de Si, sans utiliser de couche de transfert comme le SOC. Au cours de cette étude, le réacteur de gravure de plaque de 300 mm de diamètre, qui était utilisé jusque-là, était indisponible. C'est pourquoi une troisième recette de gravure, avec une chimie $HBr/He\text{-}O_2$ en mode continu, a été étudiée. Ici, les cylindres de PDMS ont été organisés sur seulement 3 nm d'épaisseur de brosse de PS comparé à ≈20 nm d'épaisseur de SOC dans l'étude précédente. Nous avons tout de même réussi à ouvrir complétement et de manière très anisotrope la couche de Si de 30 nm d'épaisseur pour créer des nano-fins isolés de 10 nm de largeur. Ce sont des résultats prometteurs pour une application des CPB dans la fabrication de finFETs. Les travaux futurs pourraient inclure la mesure électrique des nanofins obtenus.

Le chapitre 6 regroupe deux approches novatrices dans l'utilisation de CPB, afin d'étendre leurs fonctionnalités. Dans un premier temps, nous nous sommes concentrés sur des couches doubles de SD16 et SD45 pour obtenir des nanostructures hiérarchiques complexes qui pourraient être utilisés par exemple dans les cellules photovoltaïques, les LEDs ou dans les « bit patterned media ».

Une première couche de PS-b-PDMS est auto-assemblée par l'une des façons habituelles, présentées dans les chapitres précédents. Par exemple, nous avons assemblé premièrement des cylindres de SD45 sur les

motifs de graphoepitaxie et ajouté en deuxième couche des sphères de SD45. La différence de morphologie a été obtenue en changeant le solvant de recuit. Le toluène a été utilisé pour la formation des cylindres et le PGMEA pour celle des sphères. La première couche agit alors comme un motif de graphoepitaxie pour la deuxième couche de PS-b-PDMS. Des « nano-filets » ont pu être obtenues avec cette technique où les sphères s'orientaient parfaitement dans les tranchées entre les cylindres. La même structure peut être obtenue avec le polymère SD16. Dans ce cas, la morphologie de sphères a été obtenue en ajoutant un homopolymère de PS à la solution de SD16. Il a été découvert que l'espacement des cylindres de guidage avait une grande influence sur la position des sphères de la deuxième couche. Les sphères s'alignant sur le dessus de lignes de PDMS quand ces lignes étaient trop espacées et entre les lignes lorsque celles-ci étaient espacées d'exactement le diamètre des sphères. Lors de l'utilisation de cylindres des deux différentes tailles, les petits cylindres de SD16, qui formait la deuxième couche, se sont alignés parfaitement dans les lignes de guidage de SD45. Cette approche conduit à une multiplication de densité des structures et à l'orientation contrôlée de structures différentes, en utilisant une seule étape de photolithographie. Surtout, les petits CPBs peuvent profiter de ce phénomène et l'alignement de structures de taille inférieures à 10 nm à grande échelle peut être amélioré de cette manière dans de futures applications de lithographie. En outre, notre processus ne montre aucune couche de mouillage de PDMS entre les couches CPB ni à l'interface CPB/substrat. Le transfert par gravure de ces structures est donc possible avec les procédés de gravure habituels, comme ceux présentés dans le chapitre 5. Il est imaginable que ce « double patterning » puisse être étendu au « multi-patterning » pour réaliser des structures tridimensionnelles. De telles structures pourraient être utilisées pour les interconnexions ou trous d'interconnexion dans la fabrication de circuits intégrés, dans la photovoltaïque, les LEDs ou dans les disques durs.

La deuxième partie de ce chapitre se concentre sur l'inclusion de sels métalliques dans des systèmes PS-b-PMMA, le CPB le plus classique. En raison de la faible valeur de χ, la sélectivité de gravure de ce CPB est faible. C'est pourquoi il pourrait ne pas être adapté à certains procédés de fabrication de circuits intégrés. En intégrant des oxydes métalliques sélectivement dans l'un des blocs, la sélectivité de gravure peut être considérablement augmentée et ces CPB pourraient être transférés plus facilement dans le matériau fonctionnel sous-jacent. Ces CPBs avec une faible valeur d'incompatibilité et sont donc limités en résolution, mais présentent des propriétés intéressantes et sont particulièrement bien étudiés par rapport à certains CPBs « high-χ » exotiques. C'est pourquoi la gravure de ces matériaux est tout de même intéressante. Par ailleurs, une fois bien maitrisé, ce processus d'inclusion pourrait ensuite être appliqué sur d'autres systèmes, ce qui pourrait être intéressant pour des matériaux très haute résolution qui sont également difficile à graver. L'approche présentée est assez simple: Le PS-b-PMMA est auto-assemblé par recuit thermique sur un substrat de silicium. La couche de CPB est ensuite exposée à des vapeurs d'éthanol,

qui « reconstruit » le bloc PMMA à la surface du bloc PS et semble porosifier ce bloc PMMA. La solution de sel de fer est ensuite enduite par centrifugation sur le PS-b-PMMA « reconstruit » et s'introduit sélectivement dans le PMMA poreux. L'échantillon est ensuite exposé directement à un plasma O_2 afin d'éliminer les matériaux organiques restants et oxyder le nitrate métallique en oxyde. L'oxyde de fer est connu pour être un masque de gravure solide pour le transfert des motifs dans le silicium. Sur du silicium non-structuré, l'oxyde de fer est déposé sans couche de transfert et des structures d'une hauteur de 35 nm ont pu être obtenues. Lorsqu'il est déposé sur une couche de SOC, le masque de gravure est alors plus épais grâce à la couche de SOC et on pourrait imaginer que le transfert dans le substrat conduise à des rapports d'aspect plus hauts.

Au cours de cette thèse, nous avons vu que le PS-b-PDMS est un matériau prometteur pour l'industrie des semi-conducteurs. Différentes pistes pour son intégration dans des procédés industriels ont été explorées. Les travaux futurs sur l'auto-assemblage dirigé de PS-b-PMDS comprennent une compréhension plus détaillée du mécanisme de mélange du CPB avec des plastifiants. Des mesures de GISAXS *in-situ* lors du processus d'étalement par centrifugation pourrait donner des connaissances importantes sur les mécanismes conduisant à un arrangement ordonné des microdomaines. Ce procédé utilisant des plastifiants pourrait être utilisé soit directement après l'étape de dépôt résine pour des applications « bit patterned media » (morphologie sphérique) ou après recuit thermique pour des applications de lithographie de lignes (morphologie cylindrique). Le mélange avec des plastifiants pourrait également être élargi à d'autres systèmes CPB et en particulier aux systèmes plus résolus avec des poids moléculaires bas. Pour une application en grande surface, le dépôt sur des plaques de silicium de 300 mm de diamètre doit être optimisé afin d'éviter des ondulations d'épaisseur. En outre, avant une mise en œuvre du PS-b-PDMS dans l'industrie de la microélectronique, une analyse statistique approfondie de la rugosité des lignes est cruciale. Avec les tailles de motifs de plus en plus petits, les spécifications concernant le contrôle dimensionnel deviennent de plus en plus critiques. Des mesures CD-SEM (microscopie électronique pour la caractérisation statistique) sont nécessaires afin d'évaluer définitivement la faisabilité de l'auto-assemblage dirigé de copolymères dans l'industrie de la microélectronique.

De manière plus générale, on peut conclure que les CPB de haut-χ présentent une voie prometteuse pour l'avenir des circuits intégrés, mais beaucoup de travail et de compréhension sont encore nécessaires avant de pouvoir les mettre en œuvre dans un environnement industriel réel. Le PS-b-PDMS présente une bonne résistance à la gravure, mais comme décrit, lorsqu'il est gravé dans un plasma d'oxygène, des rugosités importantes peuvent être créées, ce qui est problématique pour les circuits intégrés, en particulier pour les motifs de taille inférieure à 10 nm. Par conséquent, d'autres matériaux de haut-χ qui ne contiennent pas de PDMS, comme ceux à base d'acide Polylactique (PLA) par exemple, ou des CPB complètement nouveaux,

pourraient être une meilleure option pour l'intégration dans l'industrie. Cependant, lors de la synthèse de CPB purement organiques, le manque de sélectivité de gravure doit être compensé, par exemple en utilisant la synthèse d'infiltration séquentielle (SIS).

Diminuer encore la taille caractéristique signifie diminuer également l'épaisseur du masque, puisque les deux quantités sont liées à la taille des domaines du CPB. Plus le masque de gravure est fin, plus la résistance à la gravure est faible. Par conséquent, la morphologie lamellaire doit être préférée à la morphologie cylindrique pour la fabrication de finFET par exemple. L'avantage des CPB avec une morphologie lamellaire est que l'épaisseur des lamelles verticales peut être choisie individuellement, augmentant donc les possibilités pour le transfert de motif. Néanmoins, aujourd'hui, l'orientation verticale est difficile à réaliser. En particulier pour les CPB de haut-χ, qui présentent des fortes interactions entre les blocs et avec les surfaces. C'est pourquoi beaucoup de progrès doivent être fait en termes de traitement de surface.

En outre, pour l'industrie, la densité de nanofins sur une plaque de silicium doit être aussi élevée que possible. Lors de l'utilisation de la graphoepitaxie, un espace considérable de la plaque est occupé par les lignes de guidage, qui n'ont aucune utilité par la suite. Par conséquent, la chemoepitaxie, où aucun espace n'est perdu, devrait être améliorée afin de parvenir à des multiplications de densité plus élevées.

Dans la dernière décennie, d'énormes progrès dans la compréhension et le contrôle des CPB ont été fait. Bien qu'il y ait encore beaucoup de défis à relever, la poursuite de la recherche fondamentale promet un avenir intéressant pour le DSA de CPB.